THESIS SUBMITTED FOR THE DEGREE OF DOCTOR OF PHILOSOPHY

博士論文

A numerical framework for simulations of gas-solid-liquid flows with complex geometries

(複雑壁面境界内の固気液三相流問題の数値解析)

Author
孫暁松
Xiaosong Sun
No. 37137143
Department of Nuclear Engineering and Management
Graduate School of Engineering
The University of Tokyo

Supervisor
酒井幹夫 准教授
Assoc. Prof. Mikio Sakai

平成27年6月
Jun. 2015

Abstract

The work in this thesis is dedicated to the numerical modeling of complex multiphase flows, specifically the gas-liquid flows and gas-solid-liquid flows interacting with general geometries. Those flows involving free surface, granular particles and complicated boundaries are widely encountered in industries including various mixing and grinding processes, e.g. agitation tank, wet beads or ball mill, and twin screw kneader (TSK). There is an urgent need for accurate, robust and efficient computational fluid dynamics (CFD) techniques that can assist engineers in designing and optimizing their operational conditions for those industrial problems.

From an engineering point of view, key factors affecting the process performance and product quality comprise the design of stirring paddles, rotation speed, fluid filling ratio and solid load of particles; for their counterparts in the numerical perspective, the considerations of boundary shape and movement, interfacial flow motion, solid behavior and fluid-particle interaction could be important. In these respects, numerical models that are able to provide integrated solutions have not been soundly established by past studies.

Therefore, the objective of the present study is to develop a numerical framework capable for predicting the macroscopic behaviors of two- and three-phase flows within complex geometries to facilitate their practical analysis. The current numerical framework provides systematic approaches to three types of flow problems with pragmatic relevance: (a) modeling of gas-liquid flows in complex geometries, (b) macroscopic large-scale modeling of gas-solid-liquid flows in complex geometries, and (c) microscopic direct numerical simulation (DNS) of gas-solid-liquid flows with full resolution of fluid-particle interactions. In our attempts to treat these problems of diverse complexities and scales, new computational technologies have been proposed and their validity has been tested thoroughly.

The first part of our main matter describes a computational method namely the VOF-IB method for the three-dimensional simulations of two-phase flows in general geometries. This method adopts a volume-of-fluid (VOF) approach to capture and advance the fluid interface, and it integrates the fluid solver with the immersed-boundary (IB) modeling of arbitrary-shaped walls and moving bodies. The shape and movement of general geometries are efficiently represented by an auxiliary signed distance function (SDF) field with local coordinate transformation. The VOF-IB method is a versatile two-phase solver allowing for a wide range of flow conditions as well as topological changes of the free surface. The simplicity and efficiency of its numerical algorithm are remarkable for real applications in comparison with

existing CFD models.

In the second part, an Eulerian-Lagrangian model, specifically the DEM-VOF method, is proposed to perform three-dimensional simulations of gas-solid-liquid flows, for which the fluid motion is solved by using the preceding computational techniques and the distinct particle phase is tracked by the discrete element method (DEM). The fluid-particle coupling is achieved by the volume-averaging approach wherein an empirical closure is employed for the description of interphase momentum transfer. In particular, the combination of the SDF representation and the IB method tackles the modeling of complex geometries that are in simultaneous interaction with the three-phase flow. A variety of model verification and validation tests are performed to show the capability of the DEM-VOF method to simulate macroscopic three-phase behaviors such as free surface deformation, water displacement, and configuration of solid beds. Results are also presented for its successful application to a laboratory TSK system.

The last development in this thesis is undertaken for the DNS method for the microscopic modeling of gas-solid-liquid flows. The discretization of the coupled system is accomplished by an improved IB method accounting for increased accuracy and generalized fluid actions. The VOF-based interface calculation is enhanced by the level set (LS) model to treat surface tension and contact angles on solid surface. Unlike the macroscopic model for large-scale simulations needing closure equations for unresolved terms, the DNS-based method can fully resolve the gas-solid-liquid interactions inclusive of both the fluid-particle hydrodynamic force and the particle-interface capillary force dominant in a typical three-phase flow system. Hence the DNS method is conceptualized as a supportive tool to validate and develop useful correlations for the large-scale simulations. Such an example is shown in this part to establish a preliminary link between the two levels of numerical modeling.

Contents

List of Figures

List of Tables

Chapter 1

Introduction

1.1 Background and motivation

The scope of this thesis covers the numerical modeling of gas-solid-liquid flows [1] which are defined as multiphase flows composed of gas and liquid phases separated by immiscible interfaces and solid granular particles; sometimes its concept also embraces the gas-liquid flows interacting with general solid boundaries in certain context [2]. Those flows are widely encountered in many environmental and industrial circumstances, at the largest scale of which are those common in nature such as erosion of river bank, transportation of sedimentation, pyroclastic and lava flow from volcano, tsunami and debris flows [3]. At the opposite end of these geophysical settings, three-phase phenomenon can scale down to the micro world where dust, bacteria and colloidal particles float and cluster on a fluid interface [4]. A typical industrial application of three-phase flow is the floatation machine used in mineral processing [5], which is able to separate ore particles effectively by aerating the liquid column with air bubbles. Another representative industrial three-phase system is the three-phase fluidized bed [6, 7].

Gas-solid-liquid flows are also ubiquitous in chemical engineering including many mixing, dispersion, classification and interface processes. Particularly in the author's group, interest of research has long been focused on the study of various mixing, blending and grinding processes. The agitation tanks are the first good example of the utilization of gas-liquid flows driven by specially shaped impellers to deliver continuous and efficient blending outputs. Three-phase flows could be found in many attrition-based devices, e.g. wet ball/beads mill [8, 9] and twin screw kneader (TSK). These instruments, usually equipped with spinning paddles in elaborate shapes to enhance work efficiency, stir to mechanically activate the gas-liquid or fluid-particle mixture inside, and hence the energetic impact and shear effects between solids (stir paddles or particles if involved) could serve to generate manufactured products (e.g. for mixing, size-reduction and improvement of micro particle dispersion state). Some key factors affecting the performance and product quality may include the design of stirring paddles, rotation speed, filling ratio of fluid and solid load of particles, for which the considerations of boundary shape and movement, flow motion, particle behavior and fluid-particle interaction could be important.

Traditionally such flows are mainly studied by experiments and empirical observations. In these problems, however, the lack of transparency for the internal movement and complicated phenomena will restrict the insight that could be obtained with experimental approaches. In addition, the cost of running experiments is another factor to be concerned. On the other hand, the alternative approach provided by the recent advent of computational fluid dynamics (CFD) techniques is gaining increasing attention, which has opened a new way of investigation into every details of the underlying system without the limitation of experimental conditions.

Therefore, development of accurate, robust and efficient numerical algorithms that can assist engineers in designing and optimizing their operational conditions is now becoming a pressing research topic in the nowadays computer-aided engineering (CAE) activities. This requirement for solution to practical problems, indeed, calls for a self-contained numerical framework able to predict the macroscopic behaviors of gas-solid-liquid flows with accurate computation of interface motion and fluid-particle interaction in a generality of complex systems, which has motivated our developments in the present study.

For gas-solid-liquid flow problems, numerical challenges mainly arise from complicated interactions among different phases. From an engineering perspective, the complexities could be decomposed into sub-problems (assuming they are separable) via a divide-and-conquer methodology and later integrated as a whole solver with proper coupling among different parts. This allows for effective extension of existing ideas and models to the maximum. Careful selection is needed for examining their suitability, as a matter of course.

Basically, a typical gas-solid-liquid flow involves fluid-fluid interaction (the evolving fluid interface and jumps in physical property), fluid-solid interaction (interphase momentum transfer mainly owing to the hydrodynamic and capillary forces) and solid-solid interaction (impact and friction during particle collision). In addition, the influence of arbitrary-shaped geometries and moving boundaries must be taken into consideration for practical simulations. In this study, problems related to these fundamental aspects are first discussed and addressed.

- The representation and advection of the fluid interface together with the modeling of binary fluids separated by it in a flow field;
- The way to calculate and track the motion of distinct solid particles;
- The discretization of fluid-particle system and how to achieve the coupling between them;
- The modeling of complex geometries and moving boundaries.

Prior to the introduction of our contributions to gas-solid-liquid problems, the section that follows will present a review of some past studies and related work, which is by no means exhaustive but intends to give an indication of potential numerical candidates, competitors and their limitations.

1.2 Previous studies and related work

1.2.1 Interface model

The history of computational efforts to model free surface and interfacial flows date back almost as long as that of the CFD itself. Up to now, two types of numerical approaches [10] have been adopted to model fluid interfaces, namely methods that use (a) boundary-fitted mesh conforming to the interface or (b) fixed-grid simulation with specific representation of the interface.

With accurate treatment of boundary conditions at the fluid interface, the boundary-fitted technique [11–14] is able to offer high accuracy for interface behaviors with lesser mobility such as steady rising of nearly spherical gas bubbles in viscous liquids. Its applications are mainly found for relatively simple geometries and interface configurations; however, for complex free surface flows involving violent interface motion, the mesh manipulation can be considerably complicated and expensive.

As an opposite, the latter methodology adopts a stationary Eulerian mesh to simulate the overall multiphase flow, which has greatly simplified the computational procedure with satisfactory accuracy for a wide range of flow conditions. Since an explicit representation does not exist for the fluid interface, special consideration must be made to somehow embed the interface on the fixed grid defined a priori. According to the way how interface is represented and connected to the underlying mesh-based computation, it can be further categorized into two classes of algorithms: interface tracking and interface capturing methods[1].

In an interface-tracking method, as its name implies, extra marker points are employed to explicitly represent the interface and track its movement in a Lagrangian manner. The marker-and-cell (MAC) method [18] is the earliest free surface model which employs massless dots to tag the domain occupied by the liquid. Its concept of using Lagrangian particles is still enlightening and has been extended in some modern interface models, e.g. the particle level set method [19, 20]. The front-tracking method [21] treats the infinitely thin interface by auxiliary meshes of $(N^{dim} - 1)$ dimensions, i.e. connected line segments in 2D and triangular surface elements in 3D. The Lagrangian modeling of the interface enables very exact calculation of the interfacial profile such as the surface normal and curvature; the front-tracking is also very gifted in modeling phase change problems such as evaporation, boiling and solidification [17]. However with this approach problems arise when large deformations of the interface occur: in order to maintain a well-defined front shape, a series of operations considerably complicated might be required to manipulate the front mesh, such as adjustment of node position and dynamic addition or deletion of some surface elements. Without the special operations, break-up and coalescence cannot be automatically handled by the front-tracking model. It is also difficult to treat three-phase contact lines in tracking methods because of the contradiction that the contact line explicitly defined by Lagrangian points does not move if their motions are subject to the non-slip boundary condition on solid surfaces, see [22].

The alternative approach consists in the fully Eulerian interface capturing methods, where an indicator function, C, is stored discretely on fixed grids provided as an implicit description of different phases separated by the interface. When the interface is to be evolved, unlike other Lagrangian models, a special advective transport equation is solved for C instead on the background fluid mesh to update the interface configuration. The conservative form of the advection equation is usually expressed by

$$\frac{\partial C}{\partial t} + \nabla \cdot (\boldsymbol{u} C) = 0 \tag{1.1}$$

with $\boldsymbol{u}$ the flow velocity. By utilization of the incompressibility condition $\nabla \cdot \boldsymbol{u} = 0$, a pure advection equation can be written for C as

$$\frac{\mathrm{D}C}{\mathrm{D}t} \equiv \frac{\partial C}{\partial t} + \boldsymbol{u} \cdot \nabla C = 0 \ . \tag{1.2}$$

---

[1] Note that the usage of terminology of "interface tracking" and "interface capturing" may be different in literatures under different contexts of definition, see [15, 16]. Their classification in this study generally follows the sense of Tryggvason et al. [17].

Different interface-capturing models adopt unique choices of the indicator function C and algorithms to solve the transport equation (1.2), which will be reviewed later.

The family of the interface capturing approach is composed of the most popular and commonly implemented algorithms for multiphase solvers, for instance, the volume-of-fluid (VOF) method [23], the level-set (LS) method [24], the constrained interpolation profile (CIP) method [25] and other diffuse interface model such as the phase field method (PFM) [26, 27], to cite a few. These methods, although not so accurate as the previous interface-tracking since the interface shape is not directly available, are conceptually simple and computationally efficient. They also inherently allows for high density ratios and complex interfacial phenomena such as large deformations, coalescence and breakup, making them handy to perform robust simulations of industrial flows. For this reason, we set our sights on two interface-capturing models, specifically the VOF method and the LS method.

Generally in the VOF method the liquid volume fraction ϕ which is actually the integral average of a Heaviside function across the interface is used as the indicator function. The value of ϕ is $\phi = 1$ in the liquid phase, $\phi = 0$ in gas phase and $0 < \phi < 1$ near the interface. For this sharp transition, the preceding advection equation (1.2) cannot be solved with general finite difference methods otherwise the interface will be severely smeared by numerical diffusion. For this reason, VOF methods usually feature a geometrical reconstruction and advection of the interface based on the volume fraction ϕ. The simplest approach is to approximate the interface by linear surfaces parallel to the boundaries of computational cells, viz. the simple line interface calculation (SLIC) [28]. A better choice for calculation of interface is recognized as the piecewise linear interface calculation (PLIC) [29,30] with sloped reconstruction of linear surfaces. The drawback of the PLIC approach is its complicated implementation in three-dimension. To overcome this, Yokoi [31] proposed the weighted line interface calculation (WLIC). In the WLIC, piecewise constant reconstruction similar to the SLIC is carried out along all coordinates separately, and then a weighted average of these components is calculated taking in account the local surface orientation. In comparison with the traditional PLIC, the WLIC could be implemented in three-dimensional space straightforwardly and it is able to capture the fluid interface with comparable accuracy in many scalar transportation tests. There are also other possible ways to treat the VOF function, such as that based on the algebraic function transformation [32, 33] and solution using high-order or high-resolution differencing schemes [16,34,35]. However, those methods are sometimes still too diffusive and may need compressive fluxes for anti-diffusion, e.g. the interFOAM solver contained in the open source OpenFOAM library[2]. Therefore, only those VOF models employing geometrical reconstruction techniques are considered in this study. A strict comparison of VOF-type methods could be found in [36].

In the LS method, a smooth function commutes the sharp marker function in the VOF method, for which the best practice is usually the signed distance function (SDF) ψ indicating the nearest distance to the interface although other choices may also be applicable (see e.g. [37]). Following the convections in many LS literatures [24, 38], the sign of ψ is negative in gas phase and positive in liquid phase, and hence the zero-contour of the LS function gives an implicit representation of the interface. Unlike the VOF function whose gradient $\|\nabla\phi\| \sim 1/\Delta x$ with Δx the grid spacing is steep, the property as a signed distance function ensures the gradient of ψ is well-defined,

$$\|\nabla\psi\| = 1 \ . \tag{1.3}$$

Thus the advection equation for ψ can now be treated as a typical hyperbolic one and get solved using the well-known ENO/WENO schemes [39, 40] and TVD-RK methods [41]. After the advection, it is known that ψ does not remain a distance function anymore, which can cause errors in interface calculation that follows. For this sake, the LS method usually comes with a reinitialization procedure [24, 38] to periodically regularize the interface. For the LS method its downside is the risk of loss of mass during the advection and reinitialization procedures, especially in cases where the interface is significantly distorted.

A problem existing in the VOF and LS methods has been the calculation of the surface tension force, for which it is common to rewrite the singular surface tension force as a body force, as done in the famous continuum surface force (CSF) model [42]. Later a continuum surface stress (CSS) model [43] is proposed to give an equivalent but conservative formulation of this body force. Other techniques developed to improve the computation of surface tension include the high-order reconstruction of interface [44] , height function based curvature calculation and balanced-force formulation [45, 46]. Another point worth noting is that these schemes (especially VOF with interface reconstruction) are originally designed for computation on rectangular, stationary grids, and thus special treatments are needed if complex geometries are to be modeled.

The VOF method is highly appreciated for its property of volume conservation (even up to machine precision with proper flux calculation), which is a virtue advantageous in long-time simulation of large-scale problems. On the

---

[2] OpenFOAM user guide, `http://cfd.direct/openfoam/user-guide/damBreak/`.

Table 1.1: Different approaches for the modeling of fluid-particle flows.

	Representation	Coupling	Target problem
TFM	Eulerian-Eulerian	Closure correlations	Large-scale flow structure
DEM-CFD	Lagrangian-Eulerian	Closure correlations	Macroscopic behavior
DNS	Lagrangian-Eulerian	Primary calculation	Flow details

other hand, holding the LS function during the simulation is beneficial for interface modeling because it directly tells the interface position, normal vector and curvature. A coupled LS and VOF (CLSVOF) method [47–49] combines them to complement the flavor of each other. However the CLSVOF algorithm that almost doubles the computational time and storage is still quite complex even in two dimensions, which is not realistic for engineering applications.

From the literature survey in this section, we find that the WLIC VOF advection scheme has the advantage of being reliably robust, reasonably accurate and technically simple, making it a good candidate for our numerical investigations of complex multiphase flows.

1.2.2 Modeling of fluid-particle flow

The numerical modeling of massive fluid-particle (liquid-solid or gas-solid) flows relevant in various industrial processes is a very interesting topic of research considering the multiscale nature of such systems. As figured out by Deen et al. [50] and van der Hoef et al. [51] in the context of fluid-particle fluidization, the requirements to resolve the flow behavior at different scales of phenomena with different details of information have diversified the numerical approaches ever adopted to aid their engineering. Since the fluid phase is naturally modeled as a continuum, numerical models can be roughly categorized according to the way to treat the dispersed particle phase, for which either continuous or discontinuous description has been employed, see Table 1.1.

An early and still attractive practice towards this problem by having a continuous solid phase is the well-known two-fluid model (TFM) [52, 53], where both the fluids and solids are treated as interpenetrating continua and get solved on stationary grids. Hence, it is commonly referred to as the Eulerian-Eulerian approach. In the TFM, a spatial filtering operation is applied to the mixture system with the local volume fraction of the solid phase indicating the phase configuration. The interaction between two separate phases is calculated based on empirical correlations which are generally written as the function of the local volume fraction and the mean slip velocity.

The major shortcoming in the TFM is that closure equations are also needed to describe the constitutive behavior of the solid bed, which is not only hard to be derived for solid behavior under generic circumstances but also has made it impossible to accurately evaluate the solid stress. For this sake, TFM-based simulations are not able to reflect some characteristic aspects of solid particles that might be important in engineering application, such as distribution of particle size, material properties and adhesive particles. In spite of this, the computational cost of the TFM is low and can be well scaled up, making it attractive for simulating industrial-size systems, see [54] for a review.

Insofar as the particle behavior is to be fully resolved, the Lagrangian methodology of the discrete element method (DEM) [55] or the discrete particle model (DPM) has proven to be a versatile tool. In the DEM where solid particles are modeled by distinct entities, the trajectory and velocity of particles could be calculated to high accuracy based on Newton's second law of motion. The particles are represented by soft spheres and the contact forces are derived from their overlap against others (or rigid walls) during a finite-time collision. For the contact force, usually a Voigt model combining linear springs, damping dashpots and friction sliders is used to produce a viscoelastic effect (Figure 1.1), for which the parameters can be calibrated numerically. The seemingly simple ideas employed by the DEM have performed surprisingly well in predicting behaviors of bulk granular flows, making it now a common practice to simulate powder and granular materials. The numerical strategy of DEM allows for specific particle properties and can be easily adapted to some new physics, e.g. non-spherical particles [56, 57], internal stress by coupling with finite element method (FEM) [58,59], nonlinear contact force [60, 61], plastic contact and deformation [62, 63] , cracking and fracture [64, 65], wet lubrication [66], van deer Waals force [67], etc. To further reduce the computational complexity that increases linearly with the particle number, the coarse grain model (CGM) has been proposed for the DEM by different authors, see [68–72].

The Lagrangian-Eulerian methodology couples the DEM with fluid simulation for the modeling of fluid-particle flows. Compared with the fully Eulerian description in TFM, the Lagrangian representation of particles is able to well resolve the solid force and alleviate the analytical and numerical difficulties when modeling dense solid beds. For this reason, numerical modeling based on the Lagrangian-Eulerian strategy is preferred in this study.

Within the Lagrangian-Eulerian framework, there are two types of algorithms classified by the calculation of the fluid-particle coupling term or the hydrodynamic force. In the first class of method referred to as the DEM-CFD method [73, 74], the fluid-particle coupling is established upon the volume-

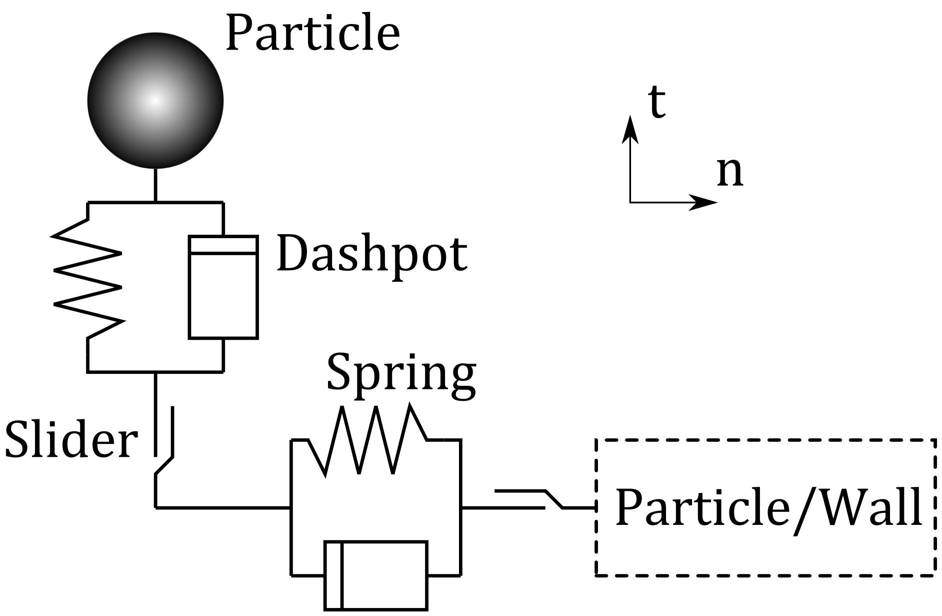

Figure 1.1: Contact force based on Voigt model in DEM.

averaging formulation [52] that has originated from the TFM. As illustrated in Figure 1.2 (a), the spatial resolution of the fluid phase is chosen coarser than the typical length of particle diameter, and the volume-averaged forms of equations of momentum and continuity are solved to determine the fluid motion. Similar to the TFM, the fluid-particle interaction terms are obtained with empirical correlations in terms of the local void fraction and flow conditions. The DEM-CFD method has broad applications in particle process engineering, see [75] for an extensive review.

Another category is the direct numerical simulation (DNS) of fluid-particle flows, where the fluid-particle interaction is directly calculated based on the primary solution of the governing equations with boundary conditions prescribed on the solid surface, and hence no model assumption is needed. In order to achieve this, it is necessary to have a sufficiently fine fluid mesh so that all relevant flow structures around the solid particle can be resolved properly, see Figure 1.2 (b). A variety of implementations of DNS models could be found in the literature, e.g. the body-fitted moving mesh method [76], the lattice Boltzmann method (LBM) [77], the distributed Lagrange multiplier-fictitious domain (DLM-FD) method [78] and the immersed boundary (IB) method [79, 80]. So far, the most impressive applications of them have been found in the DNS of pilot fluidization systems, see e.g. [81–84].

Apparently, the DEM-CFD method and DNS-based models have their targets in different directions: the former focuses on macroscopic fluid-particle

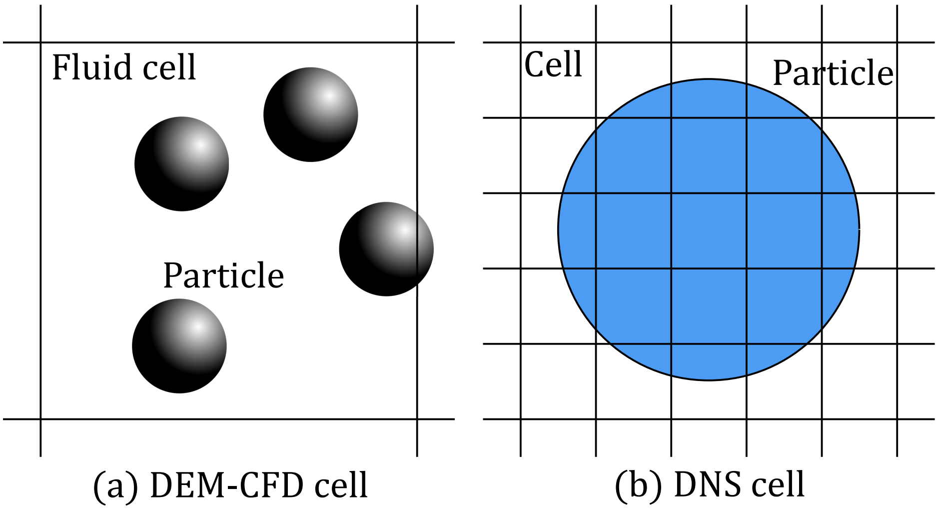

(a) DEM-CFD cell (b) DNS cell

Figure 1.2: Particle and cell configurations in DEM-CFD and DNS approaches.

behavior in average flow problems, while the latter tends to fully resolve the flow in detail at a microscopic level. In comparison with the DNS that is inherently computationally intensive, the DEM-CFD method based on the volume-averaging approach is less demanding and thus it is recognized as an affordable and pragmatic choice for simulating large-scale systems in the present study. From another point of view, the DNS method is able to provide a comprehensive understanding of the fluid-particle system from the first principle, which is helpful to develop improved closure models for the volume-averaged model, as documented by some literatures [85–89].

1.2.3 Modeling of complex geometry

Technically, the modeling of complex geometries treads a similar path to that of free surface falling in two classes of (a) body-fitted grid and (b) fixed grid methods, although the boundary condition therein is non-slip on the solid surface $\partial\Omega$ in place of the kinetic and dynamic boundary conditions at the fluid interface, that is,

$$\boldsymbol{u} = \boldsymbol{u}_B \quad \text{at } \partial\Omega \tag{1.4}$$

with $\boldsymbol{u}_B$ the wall velocity. In conventional finite-difference (FD) and finite-volume (FV) methods on curvilinear and unstructured grids [90,91], the task prior to the simulation is to generate a high-quality fluid mesh compatible with the boundary shape; for moving boundaries, it is also necessary to dynamically adjust the mesh in case of mesh distortion and overturning.

The consumption on those operations will significantly impose computational load for practical simulations. In addition, the implementation of the CFD algorithms is also considerably more complicated on these irregular grids.

In the light of the seminal work of Peskin [92, 93], the IB method is plausible for its simplicity and efficiently to treat arbitrary-shaped geometries and moving boundaries using stationary grids. Generally in IB methods, the model description of the fluid phase is extended to the whole computational domain including the "immersed" solid region, in which the governing equations for fluid motion are solved as well. Special techniques are applied to enforce the non-slip boundary condition on solid surface or the rigid motion within the solid domain. Compared with traditional body-fitted grids, the IB method is free of the mesh manipulation and is allowed to have almost unrestricted boundary motions.

In the original IB method by Peskin [92, 93] and others [94, 95], the immersed interface is tagged by Lagrangian marker points which actually compose a tessellation of the solid surface. The fluid-solid interaction $\boldsymbol{F}$ calculated from local relative velocity at those points is continuously scattered to surrounding fluid cells as a body force $\boldsymbol{f}$, which stylistically writes

$$\boldsymbol{f}_{ijk} = \sum_{l} \boldsymbol{F}_l \delta_{l,ijk} \Delta S_l \ , \tag{1.5}$$

in which $\delta_{l,ijk} \equiv \delta(\boldsymbol{x}_{ijk} - \boldsymbol{x}_l)$ is a generalized delta-function that converges with the grid spacing Δx and ΔS_l is the surface area associated with the point l. The δ-function is required to be normalized, i.e.

$$\sum_{ijk} \delta(\boldsymbol{x}_{ijk} - \boldsymbol{x}_l) \Delta x^3 = 1 \ . \tag{1.6}$$

Such a continuous forcing term shows up as an extra body force distributed smoothly within a band of cells covered by the support domain of the δ-function along the immersed interface. It is simple to implement but sometimes can give rise to a smeared near-wall flow and spurious flows in the solid interior, for which substantial improvement can be achieved with implicit calculation of the forcing term via an iterative procedure [96]. Another problem of the IB model based on continuous forcing is the generation of the point set representing the solid shape, of which the qualities (e.g. point number, spacing and uniformity) might finally affect the simulation results, see e.g. [80].

An alternative approach is developed in the IB formulation of Fadlun et al. [97] which is said to be the direct forcing. In their model, rather than introducing a continuous force term, the fluid velocity near the IB is directly

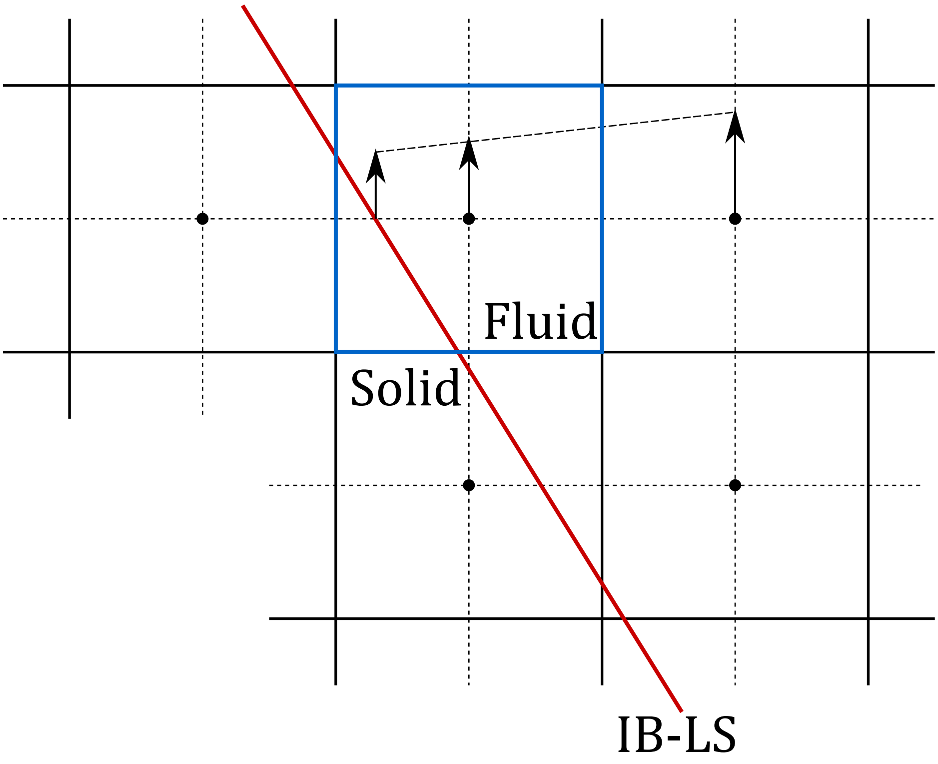

Figure 1.3: Velocity interpolation in the direct-forcing IB method.

modified to reflect the wall velocity. Usually it suffices to accomplish this direct forcing with an interpolation of the wall velocity and outer flow velocity based on the geometrical configuration of those points, see Figure 1.3 for a 2D illustration with linear interpolation. Higher-order interpolation has been described in [98] and truly multidimensional interpolation scheme is available in [99, 100]. In comparison with the continuous forcing approach, the direct forcing can result in a sharper representation of the immersed boundary, see [101] for a review.

A number of analytical and numerical investigations have been contributed to improve the performance of the direct forcing IB method. With respect to the model formulation, the accuracy of direct forcing used together with a projection method [102] for incompressible fluids is studied in [103]. New forcing terms considering the consistency between the IB interpolation procedure and surrounding fluid motion have been suggested by [104–106]. Kim et al. [107] proposed an extra mass sink/source term to improve the pressure solution yielded by the IB method. Other authors developed sharp-interface IB methods by using the cutting-cell technique [108–113] or stepwise truncation of the fluid domain [114] to achieve fully conservative modeling of fluid-solid interaction. We note that, all of the reports above require a well-defined shape of the solid surface, so that their interpolation stencils, added source terms and truncated cells or domain could be obtained without ambiguity. For this sake, they are best suited to simple IB geometries, but may become difficult and even render algebraic systems that are not solvable for complex shapes.

Kajishima et al. [79, 115] simplified the procedure in the direct forcing IB method. In their "volume-of-solid" approach, fluid and wall velocities are blended by using the solid volume fraction α as a weight function. This method is very robust, efficient and suitable for the situation where a single fluid point is affected by multiple solid objects. The advantages of this IB model are very appealing for an engineering method designed to simulate arbitrary-shape geometries and moving boundaries.

Another problem related to the modeling of complex geometry is the practical aspect of their representation in the actual implementation. For example, simple objects such as cube, sphere and cylinder can be described by their geometrical parameters with ease, and in principle, it is possible to provide appropriate approximation to all general shapes by using triangular meshes. However, those approaches are not suitable for practical usage: the generality is lacking in the former and the latter involves many inefficient operations of mesh elements. To this end, the arbitrary-shape wall boundary model developed by our group [116] is able to offer an efficient representation for general boundaries. It renders the solid object as a special SDF field ψ_B of which the zero-contour implicitly defines the surface shape. The rigid motion of the boundary is recorded by a corresponding transformation to the local coordinate space. Hence, it is guaranteed that complicated shapes and rigid motions are inclusively represented in a unified approach. Similar techniques utilizing the LS representation of IB objects (but with less delicate consideration of design, implementation and usability) have also been described in [117–119].

1.3 Objective and developments

In this section, the scope of this thesis on the numerical modeling of gas-solid-liquid three-phase flows will be discussed in detail. Particularly, our literature survey has helped us identify three major problems needing urgent solution for academic and engineering purpose.

Firstly, computational models have not been established for two-phase and three-phase flows in general geometries, which in fact comprises the theme of this thesis. Numerical studies of gas-liquid flows interacting with arbitrary shapes of boundaries seem to be restricted to stationary geometries or objects with simple motion such as spheres, cylinders, wedges and ship hulls, see e.g. [2, 117, 120–123]. Their application to rather complicated cases, including the stirring disks and paddles of considerable intricacy in beads mill and twin screw kneader, is however unknown. On the other hand, for gas-solid-liquid flows, the author is not aware of any general geometries other than a simple rectangular computational domain that has been ever treated in past studies. These facts imply that, the existing methods are not suitable to simulate three-phase flows interacting with arbitrary-shaped geometries or moving parts widely encountered in engineering applications. We would also like to emphasize that, a unified boundary model is desirable for conveniently treating the various interactions that dominate in a gas-solid-liquid system, which include the aspects of fluid-fluid (contact angle on solid surface), solid-solid (contact between particle and boundary structure) and fluid-solid (agitation of fluid by boundary movement) interactions.

Secondly, numerical studies are insufficient for the macroscopic modeling of gas-solid-liquid flows involving a dense particle phase and strong fluid-particle interaction as those found in mixing and grinding processes. In particular, this insufficiency resides in two ends of the numerical modeling: the model formulation and the computational capability. For the first point, as an engineering viewpoint is respected, models based on the volume-averaging approach aforementioned are preferable. However, the careful examination of literatures in three-phase flows has revealed that many of them adopted inconsistent formulations especially with respect to the fluid-particle interaction term, see e.g. [6, 124–126]. For this sake, unfortunately it is no point to expect that those computational models would balance the interphase momentum transfer between continuum and disperse phases and yield physically convincible results. For the second point, we have noticed that, previous studies are found within a rather limited scope of three-phase fluidization systems in dilute regime, see e.g. [127–130], where particle suspensions (typically below 10% solid volume fraction) passively follow the flow field and their influence to the fluid phase is not appreciable. It is thus not available in the past how the macroscopic flow structure (in particular the free surface) behaves in response to the motion of massive particles, which is oppositely the case in our scope of three-phase systems. For example, in mixing processes involving water entry and exit of solids (both stirring paddles and solid beds), some issues are to model the deformation of the free surface and the water displacement of the solid phase, in order to properly reflect the influence of operational conditions such as rotation speed and solid loading. These important considerations are lacking in previous studies. Consequently to all intents and purposes, the computational capability of existing models to recover the macroscopic behavior of three-phase flows is questionable.

Thirdly, the computational model that can directly simulate gas-solid-liquid systems without any empirical equations is absent in the current status. As commented by van der Hoef et al. [51] in their multi-scale philosophy of fluid-particle modeling, such a DNS approach is mainly conceptualized at the microscopic level, whose primary task is to supplement macroscopic models with effective and scalable closures for the description of unresolved and subgrid terms, rather than attempting to defeat complex problems using the brute numerical force of their own. To take the three-phase flow systems concerned in this study for instance, besides the dominant hydrodynamic effect, particles floatation on free surface and adhesion to wet wall owing to particle-interface capillary action can also be observed in our laboratory experiments for relatively fine particles with typical size $d_p < 1$ mm. For such effects having not been treated previously within a context of gas-solid-liquid flows, one might rely on the three-phase DNS in a representative system from which useful correlations could be extracted and then adopted in his/her larger-scale simulations. Similarly, another anticipatory application of the DNS-based study is the evaluation of validity for empirical drag correlations and the development of new ones. In this sense, a DNS model suitable to perform computations with fully-resolved interactions of hydrodynamic force and capillary force will fill the gap by aiming for the advancement of numerical modeling of gas-solid-liquid flows.

In order to address the aforementioned problems, the work presented in the current thesis is devoted to the development of an accurate and efficient computational framework that enables the numerical simulation of general gas-solid-liquid flow systems. As for the major objective, the numerical procedures are targeting towards the effective modeling and predicting the macroscopic flow behavior of three-phase systems in engineering problems, especially those encountered in various mixing and grinding processes including but not limited to wet beads milling, wet ball milling and twin screw kneading.

In the current numerical framework, a conventional finite volume method with Chorin's projection methodology [102] is used to compute the fluid motion. On discretized grids, the fluid interface is tracked by using the THINC/WLIC VOF method [31]. The DEM [55] is adopted to simulate distinct solid particles and their collisions. The IB method [79]) models complex geometries with the SDF representation [116]. These fundamental techniques are then combined as building blocks for more advanced simulators, which have comprised a set of numerical tools to treat diverse complexities and flow cases.

Specifically, our first step is made to develop a VOF-IB method for simulating two-phase flows in complex geometries. In this part a robust workhorse VOF model is implemented for gas-liquid flows interacting with arbitrary-shaped walls and moving boundaries modeled by the IB method. It is intended to provide flexibility and extensibility for more complicated flow problems as well as for the usage as a standalone fluid solver. Its development partly solves the first problem of complex geometry modeling for two- and three-phase flows.

In the second stage, the DEM-VOF method enlarges the computational window for three-dimensional simulation of gas-solid-liquid flows based on a volume-averaging approach. This method fully integrates the numerical techniques for three-phase flows and complex boundary modeling. It is also able to correctly recover the macroscopic flow behaviors for both the steady and unsteady states of gas-solid-liquid flows. The development of the DEM-VOF method satisfactorily achieves the main goal of this study with a settlement of both the first and the second problems. Simulation results of its application to a laboratory TSK system together with other test problems are presented to demonstrate its capability to model complex gas-solid-liquid flows.

The last part of this study describes a DNS method with direct calculation of two major effects in a representative three-phase flow, namely the hydrodynamic force and the capillary force exerted on solid particles. This DNS method finally furnishes the present framework by introducing a fully numerical approach to validate and develop closure model equations to enhance a large-scale simulation, as it is figured out by the third problem.

In this way, the numerical framework undertaken in this study utilized a systematic approach to treat gas-solid-liquid flows with complex geometries which is relevant in a large variety of engineering processes. In particular, the following *originalities and achievements* are thought to be the contribution of the present study.

- The VOF-IB method allows for a wide range of flow conditions and complex geometries. It presents a novel approach extending conventional VOF method to arbitrary-shaped computational domains. Its simplicity and efficiency are remarkable in comparison with existing two-phase models.

- The DEM-VOF method developed in this study, to the author's best knowledge, is the only one that can compute gas-solid-liquid flows interacting with non-trivial boundaries. Its development has filled the gap for a large variety of engineering problems.

- The three-phase DNS method is another important technology targeting the numerical solution of detailed gas-solid-liquid interactions.

Specifically, it is the first computational model based on VOF/IB methods with the ability to resolve the hydrodynamic and capillary actions in three-phase flows.

1.4 Outline of this study

The main matters of this thesis are organized as follows.

In Chapter 2, a numerical modeling of two-phase flows in complex geometries namely the VOF-IB method is presented. The essential concepts of the modeling of fluid motion, interface and general boundary are depicted and numerical tests are performed to show its validity.

In Chapter 3, this modeling is extended by the DEM-VOF method to gas-solid-liquid flows for which the fluid-particle interaction is defined via a volume-averaged approach. As the central element of the present numerical framework, this part describes a series of numerical techniques necessary for the proper calculation of three-phase interaction with the presence of non-trivial boundaries. The DEM-VOF method is successfully applied to the simulation of a laboratory TSK system, which highlighted its potential in tackling complicated gas-solid-liquid flow problems.

Chapter 4 describes developments to the microscopic end for the DNS of gas-solid-liquid flows, for which the fluid-particle interaction is fully resolved. Special treatments to discretize the entire system and to evaluate capillary effects are discussed. Numerical tests are performed to validate this DNS method. To exemplify the point in what way DNS results could be used to provide feedback to large-scale simulations based on averaged model, the evaluation of the validity domain of some empirical drag laws adopted by the DEM-VOF method is carried out by using the DNS.

Finally, overall conclusions and future investigations are summarized in Chapter 5.

Bibliography

[1] L.-S. FAN, *Gas-Liquid-Solid Fluidization Engineering.* Butterworth-Heinemann, 1989.

[2] J. Yang and F. Stern, “Sharp interface immersed-boundary/level-set method for wave—body interactions,” *Journal of Computational Physics*, vol. 228, pp. 6590–6616, 2009.

[3] R. M. Iverson, "The physics of debris flows," *Reviews of Geophysics*, vol. 35, no. 3, p. 245, 1997.

[4] P. Singh and D. D. Joseph, "Fluid dynamics of floating particles," *Journal of Fluid Mechanics*, vol. 530, pp. 31–80, 2005.

[5] M. Su, W. Han, Z. Zhang, R. Li, Q. Li, and W. Ma, "Numerical Simulation and Analysis of Gas-Solid-Liquid Three-Phase Flow in Mechanical Flotation cell," *Procedia Engineering*, vol. 31, pp. 850–856, 2012.

[6] Y. Li, J. Zhang, and L.-S. Fan, "Numerical simulation of gas—liquid—solid fluidization systems using a combined CFD-VOF-DPM method: bubble wake behavior," *Chemical Engineering Science*, vol. 54, pp. 5101–5107, 1999.

[7] E. Azimi, S. Karimipour, P. Nikrityuk, J. Szymanski, and R. Gupta, "Numerical simulation of 3-phase fluidized bed particle segregation," *Fuel*, vol. 150, pp. 347–359, 2015.

[8] Y. Yamada and M. Sakai, "Lagrangian—Lagrangian simulations of solid—liquid flows in a bead mill," *Powder Technology*, vol. 239, pp. 105–114, 2013.

[9] X. Sun, M. Sakai, M.-T. Sakai, and Y. Yamada, "A Lagrangian—Lagrangian coupled method for three-dimensional solid—liquid flows involving free surfaces in a rotating cylindrical tank," *Chemical Engineering Journal*, vol. 246, pp. 122–141, 2014.

[10] M. Sussman, "An Adaptive Mesh Algorithm for Free Surface Flows in General Geometries," in *Adaptive Method of Lines* (A. Vande Wouwer, P. Saucez, and W. Schiesser, eds.), Chapman and Hall/{CRC}, 2001.

[11] S. Takagi, A. Prosperetti, and Y. Matsumoto, "Drag coefficient of a gas bubble in an axisymmetric shear flow," *Physics of Fluids*, vol. 6, pp. 3186–3188, 1994.

[12] S. Takagi, Y. Matsumoto, and H. Huang, "Numerical Analysis of a Single Rising Bubble Using Boundary-Fitted Coordinate System.," *Transactions of the Japan Society of Mechanical Engineers Series B*, vol. 61, pp. 1976–1983, 1995.

[13] G. Ryskin and L. G. Leal, "Numerical solution of free-boundary problems in fluid mechanics. Part 2. Buoyancy-driven motion of a gas bubble through a quiescent liquid," *Journal of Fluid Mechanics*, vol. 148, p. 19, 2006.

[14] J. M. Boulton-Stone and J. R. Blake, “Gas bubbles bursting at a free surface,” *Journal of Fluid Mechanics*, vol. 254, p. 437, 2006.

[15] O. Ubbink, *Numerical prediction of two fluid systems with sharp interfaces*. Ph. d. thesis, Imperial College of Science, Technology and Medicine, 1997.

[16] O. Ubbink and R. Issa, “A Method for Capturing Sharp Fluid Interfaces on Arbitrary Meshes,” *Journal of Computational Physics*, vol. 153, pp. 26–50, 1999.

[17] G. Tryggvason, B. Bunner, A. Esmaeeli, D. Juric, N. Al-Rawahi, W. Tauber, J. Han, S. Nas, and Y.-J. Jan, “A Front-Tracking Method for the Computations of Multiphase Flow,” *Journal of Computational Physics*, vol. 169, pp. 708–759, 2001.

[18] F. H. Harlow and J. E. Welch, “Numerical Calculation of Time-Dependent Viscous Incompressible Flow of Fluid with Free Surface,” *Physics of Fluids*, vol. 8, p. 2182, 1965.

[19] D. Enright, R. Fedkiw, J. Ferziger, and I. Mitchell, “A Hybrid Particle Level Set Method for Improved Interface Capturing,” *Journal of Computational Physics*, vol. 183, pp. 83–116, 2002.

[20] S. E. Hieber and P. Koumoutsakos, “A Lagrangian particle level set method,” *Journal of Computational Physics*, vol. 210, pp. 342–367, 2005.

[21] S. O. Unverdi and G. Tryggvason, “A front-tracking method for viscous, incompressible, multi-fluid flows,” *Journal of Computational Physics*, vol. 100, no. 1, pp. 25–37, 1992.

[22] Y. Yamamoto, T. Ito, T. Wakimoto, and K. Katoh, “Numerical simulations of spontaneous capillary rises with very low capillary numbers using a front-tracking method combined with generalized Navier boundary condition,” *International Journal of Multiphase Flow*, vol. 51, pp. 22–32, 2013.

[23] C. Hirt and B. Nichols, “Volume of fluid (VOF) method for the dynamics of free boundaries,” *Journal of Computational Physics*, vol. 39, pp. 201–225, 1981.

[24] M. Sussman, P. Smereka, and S. Osher, “A Level Set Approach for Computing Solutions to Incompressible Two-Phase Flow,” *Journal of Computational Physics*, vol. 114, no. 1, pp. 146–159, 1994.

[25] T. Yabe, F. Xiao, and T. Utsumi, “The Constrained Interpolation Profile Method for Multiphase Analysis,” *Journal of Computational Physics*, vol. 169, pp. 556–593, 2001.

[26] D. M. Anderson, G. B. McFadden, and A. A. Wheeler, “Diffuse-interface methods in fluid mechanics,” *Annual Review of Fluid Mechanics*, vol. 30, pp. 139–165, 1998.

[27] D. Jacqmin, “Calculation of Two-Phase Navier—Stokes Flows Using Phase-Field Modeling,” *Journal of Computational Physics*, vol. 155, pp. 96–127, 1999.

[28] W. F. Noh and P. Woodward, *Proceedings of the Fifth International Conference on Numerical Methods in Fluid Dynamics June 28 — July 2, 1976 Twente University, Enschede*, vol. 59 of *Lecture Notes in Physics*. Berlin, Heidelberg: Springer Berlin Heidelberg, 1976.

[29] D. L. Youngs, “Time-dependent multi-material flow with large fluid distortion,” *Numerical methods for fluid dynamics*, vol. 24, pp. 273–285, 1982.

[30] G. Tryggvason, R. Scardovelli, and S. Zaleski, *Direct Numerical Simulations of Gas-Liquid Multiphase Flows.* Cambridge University Press, 1st editio ed., 2011.

[31] K. Yokoi, “Efficient implementation of THINC scheme: A simple and practical smoothed VOF algorithm,” *Journal of Computational Physics*, vol. 226, no. 2, pp. 1985–2002, 2007.

[32] F. Xiao, Y. Honma, and T. Kono, “A simple algebraic interface capturing scheme using hyperbolic tangent function,” *International Journal for Numerical Methods in Fluids*, vol. 48, pp. 1023–1040, 2005.

[33] F. Xiao, S. Ii, and C. Chen, “Revisit to the THINC scheme: A simple algebraic VOF algorithm,” *Journal of Computational Physics*, vol. 230, pp. 7086–7092, 2011.

[34] K. Sugiyama, S. Ii, S. Takeuchi, S. Takagi, and Y. Matsumoto, “A full Eulerian finite difference approach for solving fluid—structure coupling problems,” *Journal of Computational Physics*, vol. 230, pp. 596–627, 2011.

[35] S.-Y. Lin, Y.-H. Chin, C.-M. Wu, J.-F. Lin, and Y.-C. Chen, “A pressure correction-volume of fluid method for simulation of two-phase

flows," *International Journal for Numerical Methods in Fluids*, vol. 68, pp. 181–195, 2012.

[36] W. Aniszewski, T. Ménard, and M. Marek, "Volume of Fluid (VOF) type advection methods in two-phase flow: A comparative study," *Computers & Fluids*, vol. 97, pp. 52–73, 2014.

[37] E. Olsson and G. Kreiss, "A conservative level set method for two phase flow," *Journal of Computational Physics*, vol. 210, pp. 225–246, 2005.

[38] M. Sussman, E. Fatemi, P. Smereka, and S. Osher, "An improved level set method for incompressible two-phase flows," *Computers & Fluids*, vol. 27, no. 5, pp. 663–680, 1998.

[39] G.-S. Jiang and C.-W. Shu, "Efficient Implementation of Weighted ENO Schemes," *Journal of Computational Physics*, vol. 126, pp. 202–228, 1996.

[40] R. P. Fedkiw, T. Aslam, B. Merriman, and S. Osher, "A Non-oscillatory Eulerian Approach to Interfaces in Multimaterial Flows (the Ghost Fluid Method)," *Journal of Computational Physics*, vol. 152, pp. 457–492, 1999.

[41] S. Osher and R. Fedkiw, *Level Set Methods and Dynamic Implicit Surfaces(Google eBook).* Springer, 2002.

[42] J. Brackbill, D. Kothe, and C. Zemach, "A continuum method for modeling surface tension," *Journal of Computational Physics*, vol. 100, pp. 335–354, 1992.

[43] B. Lafaurie, C. Nardone, R. Scardovelli, S. Zaleski, and G. Zanetti, "Modelling Merging and Fragmentation in Multiphase Flows with SURFER," *Journal of Computational Physics*, vol. 113, pp. 134–147, 1994.

[44] Y. Renardy and M. Renardy, "PROST: A Parabolic Reconstruction of Surface Tension for the Volume-of-Fluid Method," *Journal of Computational Physics*, vol. 183, pp. 400–421, 2002.

[45] M. M. Francois, S. J. Cummins, E. D. Dendy, D. B. Kothe, J. M. Sicilian, and M. W. Williams, "A balanced-force algorithm for continuous and sharp interfacial surface tension models within a volume tracking framework," *Journal of Computational Physics*, vol. 213, pp. 141–173, 2006.

[46] M. Boger, J. Schlottke, C.-D. Munz, and B. Weigand, “Reduction of parasitic currents in the DNS VOF code FS3D,” *12th Workshop on Two-Phase Flow Predictions*, 2010.

[47] M. Sussman and E. G. Puckett, “A Coupled Level Set and Volume-of-Fluid Method for Computing 3D and Axisymmetric Incompressible Two-Phase Flows,” *Journal of Computational Physics*, vol. 162, no. 2, pp. 301–337, 2000.

[48] Z. Wang, J. Yang, B. Koo, and F. Stern, “A coupled level set and volume-of-fluid method for sharp interface simulation of plunging breaking waves,” *International Journal of Multiphase Flow*, vol. 35, pp. 227–246, 2009.

[49] K. Yokoi, “A practical numerical framework for free surface flows based on CLSVOF method, multi-moment methods and density-scaled CSF model: Numerical simulations of droplet splashing,” *Journal of Computational Physics*, vol. 232, pp. 252–271, 2013.

[50] N. Deen, M. Van Sint Annaland, M. Van der Hoef, and J. Kuipers, “Review of discrete particle modeling of fluidized beds,” *Chemical Engineering Science*, vol. 62, pp. 28–44, 2007.

[51] M. van der Hoef, M. van Sint Annaland, N. Deen, and J. Kuipers, “Numerical Simulation of Dense Gas-Solid Fluidized Beds: A Multiscale Modeling Strategy,” *Annual Review of Fluid Mechanics*, vol. 40, pp. 47–70, 2008.

[52] T. B. Anderson and R. Jackson, “Fluid Mechanical Description of Fluidized Beds. Equations of Motion,” *Ind. Eng. Chem. Fund.*, vol. 6, no. 4, pp. 527–539, 1967.

[53] D. Gidaspow, *Multiphase Flow and Fluidization: Continuum and Kinetic Theory Descriptions*. Academic Press, 1st ed., 1994.

[54] Zhou, “Two-Fluid Models for Simulating Dispersed Multiphase Flows-A Review,” *The Journal of Computational Multiphase Flows*, 2015.

[55] P. A. Cundall and O. D. L. Strack, “A discrete numerical model for granular assemblies,” *Géotechnique*, vol. 29, no. 1, pp. 47–65, 1979.

[56] A. Wachs, L. Girolami, G. Vinay, and G. Ferrer, “Grains3D, a flexible DEM approach for particles of arbitrary convex shape — Part I: Numerical model and validations,” *Powder Technology*, vol. 224, pp. 374–389, 2012.

[57] C. Boon, G. Houlsby, and S. Utili, “A new contact detection algorithm for three-dimensional non-spherical particles,” *Powder Technology*, vol. 248, pp. 94–102, 2013.

[58] A. Munjiza, T. Bangash, and N. John, “The combined finite—discrete element method for structural failure and collapse,” *Engineering Fracture Mechanics*, vol. 71, pp. 469–483, 2004.

[59] A. A. Munjiza, *The Combined Finite-Discrete Element Method.* John Wiley & Sons, 2004.

[60] C. Thornton, S. J. Cummins, and P. W. Cleary, “An investigation of the comparative behaviour of alternative contact force models during elastic collisions,” *Powder Technology*, vol. 210, no. 3, pp. 189–197, 2011.

[61] C. Thornton, S. J. Cummins, and P. W. Cleary, “An investigation of the comparative behaviour of alternative contact force models during inelastic collisions,” *Powder Technology*, vol. 233, pp. 30–46, 2013.

[62] L. Vu-Quoc and X. Zhang, “An elastoplastic contact force-displacement model in the normal direction: displacement-driven version,” *Proceedings of the Royal Society A: Mathematical, Physical and Engineering Sciences*, vol. 455, pp. 4013–4044, 1999.

[63] X. Zhang and L. Vu-Quoc, “An accurate elasto-plastic frictional tangential force—displacement model for granular-flow simulations: Displacement-driven formulation,” *Journal of Computational Physics*, vol. 225, pp. 730–752, 2007.

[64] M. D. Bolton, Y. Nakata, and Y. P. Cheng, “Crushing and plastic deformation of soils simulated using DEM,” *Géotechnique*, vol. 54, pp. 131–141, 2004.

[65] C.-Y. Wu, N. Weerasekara, M. Powell, P. Cleary, L. Tavares, M. Evertsson, R. Morrison, J. Quist, and R. Carvalho, “The contribution of DEM to the science of comminution,” *Powder Technology*, vol. 248, pp. 3–24, 2013.

[66] C. T. Crowe, M. Sommerfeld, and Y. Tsuji, *Multiphase Flows with Droplets and Particles.* Taylor & Francis, 1997.

[67] J. N. Israelachvili, *Intermolecular and Surface Forces: Revised Third Edition.* Intermolecular and Surface Forces, Academic Press, 3rd editio ed., 2011.

[68] Y. Feng and J. Loughran, “On upscaling of discrete element models: similarity principles,” *Engineering Computations*, vol. 26, pp. 599–609, 2009.

[69] L. Lu, J. Xu, W. Ge, Y. Yue, X. Liu, and J. Li, “EMMS-based discrete particle method (EMMS—DPM) for simulation of gas—solid flows,” *Chemical Engineering Science*, vol. 120, pp. 67–87, 2014.

[70] M. Sakai and S. Koshizuka, “Large-scale discrete element modeling in pneumatic conveying,” *Chemical Engineering Science*, vol. 64, no. 3, pp. 533–539, 2009.

[71] M. Sakai, Y. Yamada, Y. Shigeto, K. Shibata, V. M. Kawasaki, and S. Koshizuka, “Large-scale discrete element modeling in a fluidized bed,” *International Journal for Numerical Methods in Fluids*, vol. 64, no. 10 - 12, pp. 1319–1335, 2010.

[72] M. Sakai, M. Abe, Y. Shigeto, S. Mizutani, H. Takahashi, A. Viré, J. R. Percival, J. Xiang, and C. C. Pain, “Verification and validation of a coarse grain model of the DEM in a bubbling fluidized bed,” *Chemical Engineering Journal*, vol. 244, pp. 33–43, 2014.

[73] Y. Tsuji, T. Kawaguchi, and T. Tanaka, “Discrete particle simulation of two-dimensional fluidized bed,” *Powder Technology*, vol. 77, pp. 79–87, 1993.

[74] B. Xu and A. Yu, “Numerical simulation of the gas-solid flow in a fluidized bed by combining discrete particle method with computational fluid dynamics,” *Chemical Engineering Science*, vol. 52, pp. 2785–2809, 1997.

[75] H. Zhu, Z. Zhou, R. Yang, and A. Yu, “Discrete particle simulation of particulate systems: A review of major applications and findings,” *Chemical Engineering Science*, vol. 63, pp. 5728–5770, 2008.

[76] H. H. Hu, N. Patankar, and M. Zhu, “Direct Numerical Simulations of Fluid—Solid Systems Using the Arbitrary Lagrangian—Eulerian Technique,” *Journal of Computational Physics*, vol. 169, pp. 427–462, 2001.

[77] A. J. C. Ladd and R. Verberg, “Lattice-Boltzmann Simulations of Particle-Fluid Suspensions,” *Journal of Statistical Physics*, vol. 104, no. 5-6, pp. 1191–1251, 2001.

[78] R. Glowinski, T. Pan, T. Hesla, D. Joseph, and J. Périaux, "A Fictitious Domain Approach to the Direct Numerical Simulation of Incompressible Viscous Flow past Moving Rigid Bodies: Application to Particulate Flow," *Journal of Computational Physics*, vol. 169, pp. 363–426, 2001.

[79] T. Kajishima, S. Takiguchi, H. Hamasaki, and Y. Miyake, "Turbulence Structure of Particle-Laden Flow in a Vertical Plane Channel Due to Vortex Shedding," *JSME International Journal Series B*, vol. 44, pp. 526–535, 2001.

[80] M. Uhlmann, "An immersed boundary method with direct forcing for the simulation of particulate flows," *Journal of Computational Physics*, vol. 209, pp. 448–476, 2005.

[81] T.-W. Pan, D. D. Joseph, R. Bai, R. Glowinski, and V. Sarin, "Fluidization of 1204 spheres: simulation and experiment," *Journal of Fluid Mechanics*, vol. 451, pp. 169–191, 2002.

[82] J. J. Derksen and S. Sundaresan, "Direct numerical simulations of dense suspensions: wave instabilities in liquid-fluidized beds," *Journal of Fluid Mechanics*, vol. 587, pp. 303–336, 2007.

[83] A. Ozel, O. Masbernat, J.-L. Estivalezes, S. Vincent, M. Abbas, O. Simonin, and J. de Motta, "Fully Resolved Direct Numerical Simulation of a Liquid Fluidized Bed," in *8th International Conference on Multiphase Flow (ICMF 2013)*, (Jeju, South Korea), 2013.

[84] S. Vincent, J. C. Brändle de Motta, A. Sarthou, J.-L. Estivalezes, O. Simonin, and E. Climent, "A Lagrangian VOF tensorial penalty method for the DNS of resolved particle-laden flows," *Journal of Computational Physics*, vol. 256, pp. 582–614, 2014.

[85] R. J. Hill, D. L. Koch, and A. J. C. Ladd, "The first effects of fluid inertia on flows in ordered and random arrays of spheres," *Journal of Fluid Mechanics*, vol. 448, pp. 213–241, 2001.

[86] R. J. Hill, D. L. Koch, and A. J. C. Ladd, "Moderate-Reynolds-number flows in ordered and random arrays of spheres," *Journal of Fluid Mechanics*, vol. 448, pp. 243–278, 2001.

[87] R. Beetstra, M. A. van der Hoef, and J. A. M. Kuipers, "Drag force of intermediate Reynolds number flow past mono- and bidisperse arrays of spheres," *AIChE Journal*, vol. 53, pp. 489–501, 2007.

[88] S. Tenneti, R. Garg, and S. Subramaniam, “Drag law for monodisperse gas—solid systems using particle-resolved direct numerical simulation of flow past fixed assemblies of spheres,” *International Journal of Multiphase Flow*, vol. 37, pp. 1072–1092, 2011.

[89] Y. Tang, E. A. J. F. Peters, J. A. M. Kuipers, S. H. L. Kriebitzsch, and M. A. van der Hoef, “A new drag correlation from fully resolved simulations of flow past monodisperse static arrays of spheres,” *AIChE Journal*, vol. 61, pp. 688–698, 2015.

[90] J. H. Ferziger and M. Peric, *Computational Methods for Fluid Dynamics.* Berlin, Heidelberg: Springer Berlin Heidelberg, 3rd ed., 2001.

[91] H. K. Versteeg and W. Malalasekera, *An Introduction to Computational Fluid Dynamics: The Finite Volume Method.* Pearson Education Limited, 2007.

[92] C. S. Peskin, “Numerical analysis of blood flow in the heart,” *Journal of Computational Physics*, vol. 25, pp. 220–252, 1977.

[93] C. S. Peskin, “The immersed boundary method,” *Acta Numerica*, vol. 11, pp. 479–517, 2002.

[94] D. Goldstein, R. Handler, and L. Sirovich, “Modeling a No-Slip Flow Boundary with an External Force Field,” *Journal of Computational Physics*, vol. 105, pp. 354–366, 1993.

[95] A. M. Roma, C. S. Peskin, and M. J. Berger, “An Adaptive Version of the Immersed Boundary Method,” *Journal of Computational Physics*, vol. 153, pp. 509–534, 1999.

[96] T. Kempe and J. Fröhlich, “An improved immersed boundary method with direct forcing for the simulation of particle laden flows,” *Journal of Computational Physics*, vol. 231, pp. 3663–3684, 2012.

[97] E. Fadlun, R. Verzicco, P. Orlandi, and J. Mohd-Yusof, “Combined Immersed-Boundary Finite-Difference Methods for Three-Dimensional Complex Flow Simulations,” *Journal of Computational Physics*, vol. 161, pp. 35–60, 2000.

[98] N. Peller, A. L. Duc, F. Tremblay, and M. Manhart, “High-order stable interpolations for immersed boundary methods,” *International Journal for Numerical Methods in Fluids*, vol. 52, pp. 1175–1193, 2006.

[99] E. Balaras, “Modeling complex boundaries using an external force field on fixed Cartesian grids in large-eddy simulations,” *Computers & Fluids*, vol. 33, pp. 375–404, 2004.

[100] J. Yang and E. Balaras, “An embedded-boundary formulation for large-eddy simulation of turbulent flows interacting with moving boundaries,” *Journal of Computational Physics*, vol. 215, pp. 12–40, 2006.

[101] R. Mittal and G. Iaccarino, “Immersed boundary methods,” *Annual Review of Fluid Mechanics*, 2005.

[102] A. J. Chorin, “Numerical solution of the Navier-Stokes equations,” *Mathematics of Computation*, vol. 22, no. 104, pp. 745–745, 1968.

[103] R. D. Guy and D. A. Hartenstine, “On the accuracy of direct forcing immersed boundary methods with projection methods,” *Journal of Computational Physics*, vol. 229, pp. 2479–2496, 2010.

[104] T. Ikeno and T. Kajishima, “Finite-difference immersed boundary method consistent with wall conditions for incompressible turbulent flow simulations,” *Journal of Computational Physics*, vol. 226, pp. 1485–1508, 2007.

[105] K. Taira and T. Colonius, “The immersed boundary method: A projection approach,” *Journal of Computational Physics*, vol. 225, pp. 2118–2137, 2007.

[106] N. Sato, T. Kajishima, S. Takeuchi, M. Inagaki, and N. Horinouchi, “A Direct Discretization Approach near Wall Boundaries for a Cartesian Grid Method (Consideration of Consistency between Velocity and Pressure Fields),” *Transactions of the Japan Society of Mechanical Engineers Series B*, vol. 79, pp. 605–621, 2013.

[107] J. Kim, D. Kim, and H. Choi, “An Immersed-Boundary Finite-Volume Method for Simulations of Flow in Complex Geometries,” *Journal of Computational Physics*, vol. 171, pp. 132–150, 2001.

[108] J. Lee and D. You, “An implicit ghost-cell immersed boundary method for simulations of moving body problems with control of spurious force oscillations,” *Journal of Computational Physics*, vol. 233, pp. 295–314, 2013.

[109] M. Meyer, A. Devesa, S. Hickel, X. Hu, and N. Adams, “A conservative immersed interface method for Large-Eddy Simulation of incompressible flows,” *Journal of Computational Physics*, vol. 229, pp. 6300–6317, 2010.

[110] R. Mittal, H. Dong, M. Bozkurttas, F. M. Najjar, A. Vargas, and A. von Loebbecke, “A versatile shape interface immersed boundary method for incompressible flows with complex boundaries,” *Journal of computational physics*, vol. 227, pp. 4825–4852, 2008.

[111] J. H. Seo and R. Mittal, “A Sharp-Interface Immersed Boundary Method with Improved Mass Conservation and Reduced Spurious Pressure Oscillations.,” *Journal of computational physics*, vol. 230, pp. 7347–7363, 2011.

[112] J. Lee, J. Kim, H. Choi, and K.-S. Yang, “Sources of spurious force oscillations from an immersed boundary method for moving-body problems,” *Journal of Computational Physics*, vol. 230, pp. 2677–2695, 2011.

[113] H. Udaykumar, R. Mittal, P. Rampunggoon, and A. Khanna, “A Sharp Interface Cartesian Grid Method for Simulating Flows with Complex Moving Boundaries,” *Journal of Computational Physics*, vol. 174, pp. 345–380, 2001.

[114] S. Kang, G. Iaccarino, F. Ham, and P. Moin, “Prediction of wall-pressure fluctuation in turbulent flows with an immersed boundary method,” *Journal of Computational Physics*, vol. 228, pp. 6753–6772, 2009.

[115] T. Kajishima and S. Takiguchi, “Interaction between particle clusters and particle-induced turbulence,” *International Journal of Heat and Fluid Flow*, vol. 23, pp. 639–646, 2002.

[116] Y. Shigeto and M. Sakai, “Arbitrary-shaped wall boundary modeling based on signed distance functions for granular flow simulations,” *Chemical Engineering Journal*, vol. 231, pp. 464–476, 2013.

[117] M. Sussman, “A parallelized, adaptive algorithm for multiphase flows in general geometries,” *Computers & Structures*, vol. 83, pp. 435–444, 2005.

[118] J.-I. Choi, R. C. Oberoi, J. R. Edwards, and J. A. Rosati, "An immersed boundary method for complex incompressible flows," *Journal of Computational Physics*, vol. 224, pp. 757–784, 2007.

[119] M. Arienti and M. Sussman, "An embedded level set method for sharp-interface multiphase simulations of Diesel injectors," *International Journal of Multiphase Flow*, vol. 59, pp. 1–14, 2014.

[120] K. Kleefsman, G. Fekken, A. Veldman, B. Iwanowski, and B. Buchner, "A Volume-of-Fluid based simulation method for wave impact problems," *Journal of Computational Physics*, vol. 206, pp. 363–393, 2005.

[121] P. Lin, "A fixed-grid model for simulation of a moving body in free surface flows," *Computers & Fluids*, vol. 36, pp. 549–561, 2007.

[122] S.-Y. Lin and Y.-C. Chen, "A pressure correction-volume of fluid method for simulations of fluid—particle interaction and impact problems," *International Journal of Multiphase Flow*, vol. 49, pp. 31–48, 2013.

[123] H. S. Yoon, C. H. Jeon, J. H. Jung, B. Koo, C. Choi, and S. C. Shin, "Simulation of two-phase flow-body interaction problems using direct forcing/fictitious domain-level set method," *International Journal for Numerical Methods in Fluids*, vol. 73, pp. 250–265, 2013.

[124] Y. Li, G. Yang, J. Zhang, and L.-S. Fan, "Numerical studies of bubble formation dynamics in gas—liquid—solid fluidization at high pressures," *Powder Technology*, vol. 116, pp. 246–260, 2001.

[125] J. Zhang, Y. Li, and L.-S. Fan, "Discrete phase simulation of gas—liquid—solid fluidization systems: single bubble rising behavior," *Powder Technology*, vol. 113, pp. 310–326, 2000.

[126] J. Zhang, Y. Li, and L.-S. Fan, "Numerical studies of bubble and particle dynamics in a three-phase fluidized bed at elevated pressures," *Powder Technology*, vol. 112, pp. 46–56, 2000.

[127] C. Chen and L.-S. Fan, "Discrete simulation of gas-liquid bubble columns and gas-liquid-solid fluidized beds," *AIChE Journal*, vol. 50, pp. 288–301, 2004.

[128] M. van Sint Annaland, N. Deen, and J. Kuipers, "Numerical simulation of gas—liquid—solid flows using a combined front tracking and discrete particle method," *Chemical Engineering Science*, vol. 60, pp. 6188–6198, 2005.

[129] Y. Ge and L.-S. Fan, “3-D direct numerical simulation of gas—liquid and gas—liquid—solid flow systems using the level-set and immersed boundary methods,” *Advances in Chemical Engineering*, vol. 31, pp. 1–63, 2006.

[130] T. Can, L. Mingyan, and X. Yonggui, “3-D numerical simulations on flow and mixing behaviors in gas-liquid-solid microchannels,” *AIChE Journal*, vol. 59, pp. 1934–1951, 2013.

Chapter 2

The VOF-IB method for two-phase flows in complex geometries

2.1 Introduction

2.1.1 Background and related work

Incompressible gas-liquid flows interacting with complex geometries and moving bodies are ubiquitous in numerous natural and industrial circumstances. Their applications include wave impact problems in marine and costal engineering, liquid jets and atomization in engine designing, and high-viscosity or viscoelastic flows through kneader/extruder in chemical engineering. Efficient, accurate and robust computation of these flow problems are gaining increasing attentions in recent years. However, the physical intricacy and numerical difficulty have rendered such a problem highly challenging for computational methods.

As the simulation for two-phase flows within complex geometries is concerned, there are two major aspects defining the numerical method: the modeling of fluid-fluid interface and the modeling of fluid-solid interaction. Among a large variety of numerical models for solving two-phase problems (e.g. the marker-and-cell (MAC) method [1], the front tracking (FT) method [2], and the constrained interpolation profile (CIP) method [3]), the so-called " interface capturing "methods are good choices for predicting the motion of incompressible, viscous, and immiscible fluids involving complex fluid interface, large density ratio and general flow conditions. Basically, an interface capturing method follows an Eulerian description of fluid motion and has a fixed Cartesian grid covering the whole fluid domain. On that grid a field variable, viz. the indicator function, is discretized to identify and move the fluid interface. The volume-of-fluid (VOF) method [4] and the level set (LS) method [5] are the most famous and successful ones in the interface-capturing family. In the VOF method, the volume fraction of one fluid phase in each computational cell is adopted as the color function to distinguish different fluids. A typical procedure in a VOF method contains a geometrical reconstruction and advection of the binary interface using the volume fraction. To this end, several varieties of the VOF algorithm have been proposed [4,6–10]. The VOF method has good volume conservation properties, but it is difficult to exactly locate the interfacial point and compute the surface tension as pointed out by many past studies [11–13]. The LS method directly stores a signed distance field (i.e. the level-set function) whose zero contour corresponds to the fluid interface. High-order upwind methods for hyperbolic laws can be applied to the interface advection in a LS method [14]. However, the LS method is known to suffer from the loss of mass problem although this could be partly alleviated by using reinitializing operations [5,15]. Besides some improvements made individually to the VOF and LS methods, a coupled level set and volume-of-fluid (CLSVOF) method [13] has also been proposed to combine their advantages.

To model fluid-wall boundary interaction, the immersed boundary (IB) method is thought to be efficient. The term “immersed boundary” is now a collective designation of the techniques to represent geometrical shapes nonconforming to the fixed computational grids (see e.g. an overview [16]). Compared with traditional body-fitted grids, the IB method is free of the costly gridding procedure and is allowed to have almost unrestricted object motions. In general, existing IB methods could be categorized into two types in respect of the way how the flow field is modified near the immersed boundary. In the IB method originated by Peskin [17,18] and other researchers [19,20], the immersed interface is represented by distinct Lagrangian points and their actions to the fluid are scattered in surrounding fluid cells, calculated either explicitly or implicitly. The direct forcing IB method [21] adopts an alternative approach. The boundary velocity given by the interpolation based on local geometry profile is prescribed discretely at nearby fluid grids where the boundary is embedded. Kajishima & Takiguchi [22,23] proposed a simpler formulation of direct forcing IB method: at the fluid-solid interfacial cells, fluid and solid velocities are explicitly mixed by using the local solid volume fraction as a weight factor. This method is efficient and suitable for the situation when a fluid point is interacting with multiple solid objects. Different versions of the direct forcing IB method have been successfully applied to the numerical simulation of particulate flows [19,24], creature-induced air flows [25], and turbulent flows [26,27].

In the past, some numerical methods have been proposed for simulating two-phase flows in general geometries by connecting the VOF method and immersed boundary models in fixed Cartesian grids. Some attempts have been made for free-surface flows in wave impact problems where the influence of the gas phase is ignored [28, 29]. Kleefsman et al. [28] incorporated the VOF method into a finite volume code based on cutting-cell techniques. Lin [29] developed a two-dimensional VOF free-surface flow solver with special treatments for fluid-solid partial cells. An alternative approach is to solve the Navier-Stokes equation in the whole computational domain so that the gas motion is also taken into consideration, see [30]. Their two-phase VOF solver is further combined with discrete element method (DEM) [31] to simulate wave-particle-structure impact problems. However, they used an upwind-biased MUSCL scheme instead of a standard VOF advection algorithm, which may cause interface diffusion in long-time simulations. The treatment of contact-angle boundary condition is not specified in their work, either.

Similar to the VOF method, the LS method is also frequently adopted for simulating gas-liquid systems within general boundaries. Sussman [32,33] described a CLSVOF method for multiphase flows with application to ship hydrodynamics using three-dimensional adaptive mesh refinement (AMR) grids. To give the contact-angle boundary condition when the free surface intersects the solid wall, an iterative algorithm is developed based on a special advection equation of the LS function. By solving such an advection equation in pseudo-time iterations, the LS function defining the fluid interface is extended into the solid region subjected to a given contact angle, so that the contact-angle boundary condition could be satisfied without explicitly locating the three-phase contact line. Yang and Stern [34] developed a LS/IB method to simulate wave-body interactions. In their study, the density/pressure jump across the gas-liquid interface is treated by using a sharp interface model. At the solid surface, the LS function is directly modified in a way consistent with linear interface fitting to explicitly prescribe the contact-angle boundary condition. Yoon et al. [35] also proposed their computational model using the LS method. Degrees of freedom for rigid motion are added to their numerical model and the hydrodynamics force on solid objects is evaluated from the IB forcing term, allowing for simulating interaction problems between two-phase flows and floating bodies. Other numerical studies using a combination of the LS method and immersed boundary modeling of relatively simple geometries include two-dimensional bubble adherence [36], fluid-particle interaction [37], and three-dimensional jet atomization [38].

2.1.2 Developments in this study

In this study, a combined VOF-IB numerical method is developed to perform three-dimensional simulations of two-phase flows interacting with complex geometries. Its development is motivated by our interest to model some mixing devices used in chemical engineering, which usually have severely distorted free surfaces and highly complicated internal shapes and moving parts. Therefore, it is required in the VOF-IB method to simulate the generality of fluid interfaces and rigid boundaries (and their interactions) with good accuracy and efficiency. The originality of the present method different from known literatures lies in the following points.

- First, the THINC/WLIC scheme [10] is used for VOF interface reconstruction and advection, which could be implemented in 3D space more easily than traditional PLIC (piecewise linear interface calculation) method [7] while it is able to capture the fluid interface with comparable accuracy. Some possible improvements to the scheme are discussed. The convective momentum fluxes is computed by using a modified version of the hybrid scheme of Spalding [39] to avoid spurious wiggles at the free surface.

- Second, Kajishima's IB method [22, 23] is chosen for calculating fluid-solid interactions. In comparison with other direct forcing IB formulation with geometrical interpolation, its velocity blending based on volume fraction weighting provides a natural way to handle multiple moving bodies that might come close to each other.

- Third, the geometry boundary and immersed objects now have a special signed distance function (SDF) representation which is based on our arbitrary-shape wall boundary model developed in [40]. Not only could primary shapes such as spheres and cylinders be modeled but also very complicated ones are able to be imported from CAD (computer aided design) data. This programming module can also support rigid motions including translation and rotation with ease. Combined with the previous point, *our boundary modeling based on the SDF/IB approach is a major novelty of this study.* It does not only allow for flexible representation and computation of complex geometries, but is also critical for suppressing nonphysical interface attachment on wall boundaries. See Sections 2.5.2 and 2.5.3.

- Last but not least, we propose some simplified treatments within a VOF framework to apply the contact-angle boundary condition in gas-liquid-solid systems.

The problems of interest have a wide spectrum across many engineering problems, and we also hope our VOF-IB solver to be a generic, versatile tool for the prediction of various flow systems. In this study, we perform tests and provide comparison to analytical or numerical reference solutions in order to validate the proposed VOF-IB method.

2.2 Governing equations and grid system

We consider an incompressible Newtonian flow composed of two immiscible fluids confined by solid boundaries. Its computational model is governed by the Navier-Stokes equation (modified to reflect the immersed boundary) and the continuity equation:

$$\frac{\partial \boldsymbol{u}}{\partial t} + \nabla \cdot (\boldsymbol{u}\boldsymbol{u}) = -\frac{1}{\rho}\nabla p + \frac{\mu}{\rho}\nabla^2 \boldsymbol{u} + \frac{1}{\rho}\sigma\kappa\delta\boldsymbol{n} + \boldsymbol{g} + \boldsymbol{f}_B \ , \tag{2.1}$$

$$\nabla \cdot \boldsymbol{u} = 0 \ , \tag{2.2}$$

where $\boldsymbol{u}$ is fluid velocity, ρ is fluid density, μ is fluid viscosity, p is pressure, σ is coefficient of surface tension, κ is local mean curvature, δ is a delta function non-zero at the interface, $\boldsymbol{n}$ is the interface normal vector and $\boldsymbol{g}$ is gravity. Herein $\boldsymbol{f}_B$ stands for the external forcing on the fluid due to immersed boundary, whose role is to enforce the condition $\boldsymbol{u} = \boldsymbol{u}_B$ with $\boldsymbol{u}_B$ the boundary velocity. Hence, the terms on the right hand side of the Navier-Stokes equation 2.1 represent the effects of pressure gradient, viscosity, surface tension, gravity and wall boundary, respectively.

The VOF function ϕ is defined as the volume fraction of the "liquid" phase out of the binary fluid mixture. It works as a characteristic function whose value is 1 in "liquid", 0 in "gas", and $0 < \phi < 1$ at the interface. The temporal evolution of the fluid interface can be obtained by solving the passive advection equation:

$$\frac{\partial \phi}{\partial t} + \boldsymbol{u} \cdot \nabla \phi = 0 \ . \tag{2.3}$$

Using the VOF function, fluid density ρ and viscosity μ could be calculated from original physical properties of the liquid and gas phases as follows:

$$\rho(\phi) = \phi\rho_l + (1-\phi)\rho_g \ , \tag{2.4}$$

$$\mu(\phi) = \phi\mu_l + (1-\phi)\mu_g \ , \tag{2.5}$$

where the subscript l and g denote liquid and gas phases, respectively.

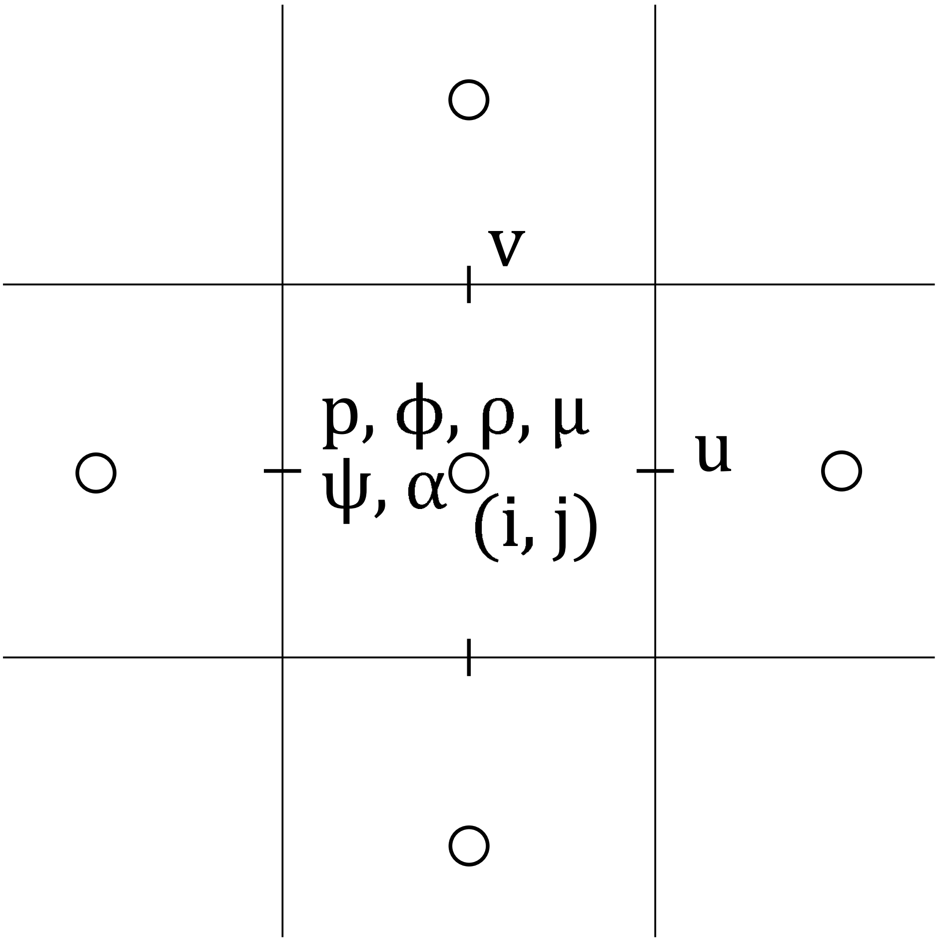

Figure 2.1: Staggered grid and variable configuration.

The fluid domain is discretized on a standard uniform staggered grid. As shown in Figure 2.1 (for clarity a 2D grid is used), components of velocity $\boldsymbol{u}$ are arranged at the corresponding staggered positions (face-centered), while other flow variables such as ϕ, ρ, μ, and p are defined at fluid cell centers (cell-centered).

2.3 Arbitrary-shape wall boundary representation

The arbitrary-shape wall boundary model developed in our previous study [40] is a highly reusable programming module that can provide a signed distance function (SDF) based representation of geometric shapes independent of the application context where it is deployed. The arbitrary-shape wall boundary model and its analogy have already been successfully applied to our previous Lagrangian particle simulations of granular materials [40] and solid-liquid granular flows [41–43]. A similar approach is that used by [38] in their CLSVOF simulation of injectors. For the sake of completeness, the basic concept, construction and utility about the arbitrary-shape wall boundary model is described in this section.

The solid boundary representation is based on the implicit zero-contour surface defined with a special SDF ψ_B. Following the convention in level set literatures, $\psi_B < 0$ in the region occupied by the solid body. Since ψ_B is a level set function, in principle, for a given point we can directly retrieve the shortest distance to the solid surface and get the boundary normal vector (pointing outwards from solid region to the fluid region) as

$$\boldsymbol{n}_B = \frac{\nabla \psi_B}{\|\nabla \psi_B\|} \ . \tag{2.6}$$

The original solid object is described by a surface mesh consisting of triangle elements, and we construct the SDF field within a box at least bounding all mesh nodes with some margin. The calculation of ψ_B value is equivalent to that for each grid point, find the minimal distance from all nodes, edges and elements in the original surface mesh. For better efficiency, the calculation is actually carried out in a limited range near the object mesh, and the remaining points are filled with a cutoff value instead. The input need not be a high quality mesh, as stretched elements are also allowable. However, for simplicity and correctness, it is desirable to have a closed object mesh without any hanging nodes.

One important point is that, ψ_B is independently calculated on a uniform grid which generally does not coincide with the fluid grid. In our case, this auxiliary grid has a resolution much finer than that used in fluid simulation (usually the grid size is a factor of 2 (or more) smaller than the fluid grid size). So that from the viewpoint of fluid solver, the boundary representation is almost precise. Once calculated, ψ_B could be cached for different simulations. When there are N objects, their SDF fields are built and kept separately as ψ_{B1}, ψ_{B2}, $\ldots$, ψ_{BN}. In fact, at the beginning of each step in our VOF-IB solver, the SDF values are transferred to the fluid cell $(i,\ j,\ k)$ and combined to be a single level set profile ψ:

$$\psi_{ijk} = \min\left(\psi_{B1}(\boldsymbol{x}_{ijk}),\ \psi_{B2}(\boldsymbol{x}_{ijk}),\ \ldots, \psi_{BN}(\boldsymbol{x}_{ijk})\right) \tag{2.7}$$

The combination of ψ_B by taking their minimum primarily has two reasons: (a) the resulting SDF field will give the closest distance to the wall in the

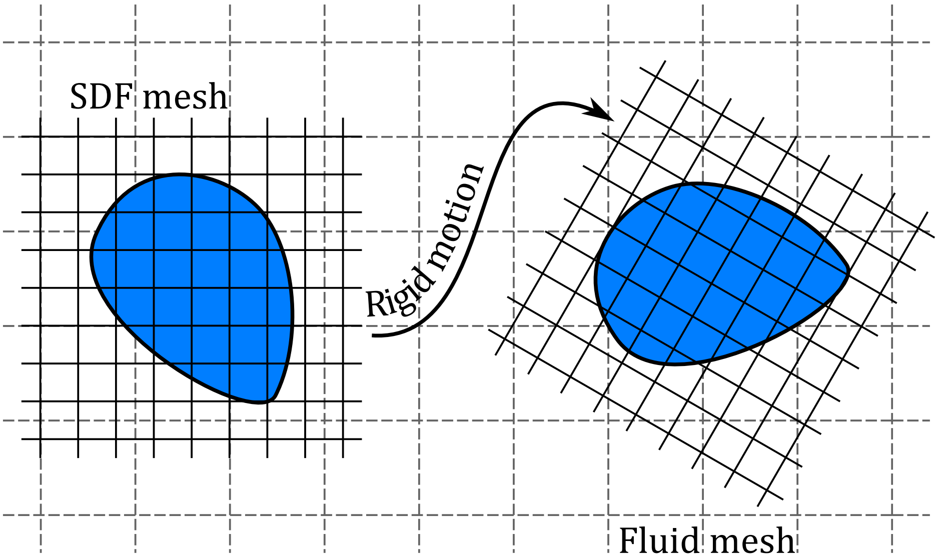

Figure 2.2: Translation and rotation represented by SDF coordinate transformation.

fluid and (b) any point with a negative SDF value must belong to the corresponding solid boundary.

A local coordinate is associated with each SDF field to reflect rigid body motion without re-evaluation of their values. The coordinate transformation is updated every time as translational or rotational motion occurs. If the SDF value at some point is requested, we will transform the point back to its position in the local coordinate system. Then we perform a trilinear interpolation on the SDF grid and return the obtained value. This procedure is illustrated in Figure 2.2.

From the SDF model, we can also obtain the solid volume fraction α_{ijk} which is a part of the IB treatment (see Section 2.5.2). In this study, each fluid cell is refined to $8 \times 8 \times 8$ finer volumes of which the SDF signs at the centers are checked. The volume occupied by the solid is then approximated by the ratio of non-positive fine volumes out of all subdivisions. Both the level set function, ψ, and the solid volume fraction, α, are defined as cell-centered variables (see Figure 2.1).

2.4 THINC/WLIC VOF interface advection

2.4.1 Standard WLIC scheme

We first describe the THINC/WLIC advection scheme [10] briefly. In this method, piecewise constant reconstruction of the interface similar to the SLIC (simple line interface calculation) [6] is carried out along x, y, and z-coordinates, respectively. All these three flat interfaces are used to determine the upwind, geometrical flux F across the cell face,

$$F_i = \int_{u_i \Delta t} \phi dV \quad \text{with } i = 1,\, 2 \text{ and } 3, \tag{2.8}$$

and a weighted average of the resulting fluxes is calculated taking in account the local surface orientation,

$$F = \sum_{i=1}^{3} F_i w_i \ . \tag{2.9}$$

Figure 2.3 provides a two-dimensional schematics of the WLIC interface reconstruction with corresponding weights.

To advance the fluid interface in time, the VOF advection equation 2.3 is written in the form

$$\frac{\partial \phi}{\partial t} + \nabla \cdot (\boldsymbol{u}\phi) - (\nabla \cdot \boldsymbol{u})\phi = 0 \ . \tag{2.10}$$

Then the operator split of the governing equation at time step n is performed as follows:

$$\phi^*_{ijk} = \phi^n_{ijk} - \frac{F^n_{i+1/2,j,k} - F^n_{i-1/2,j,k}}{\Delta x} + \Delta t \phi^n_{ijk} \frac{\Delta u}{\Delta x} \tag{2.11}$$

$$\phi^{**}_{ijk} = \phi^*_{ijk} - \frac{F^*_{i,j+1/2,k} - F^*_{i,j-1/2,k}}{\Delta y} + \Delta t \phi^n_{ijk} \frac{\Delta v}{\Delta y} \tag{2.12}$$

$$\phi^{n+1}_{ijk} = \phi^{**}_{ijk} - \frac{F^{**}_{i,j,k+1/2} - F^{**}_{i,j,k-1/2}}{\Delta z} + \Delta t \phi^n_{ijk} \frac{\Delta w}{\Delta z} \tag{2.13}$$

with

$$\begin{aligned} \Delta u &= u_{i+1/2,j,k} - u_{i-1/2,j,k} \ , \\ \Delta v &= v_{i,j+1/2,k} - v_{i,j-1/2,k} \ , \\ \Delta w &= w_{i,j,k+1/2} - w_{i,j,k-1/2} \ , \end{aligned}$$

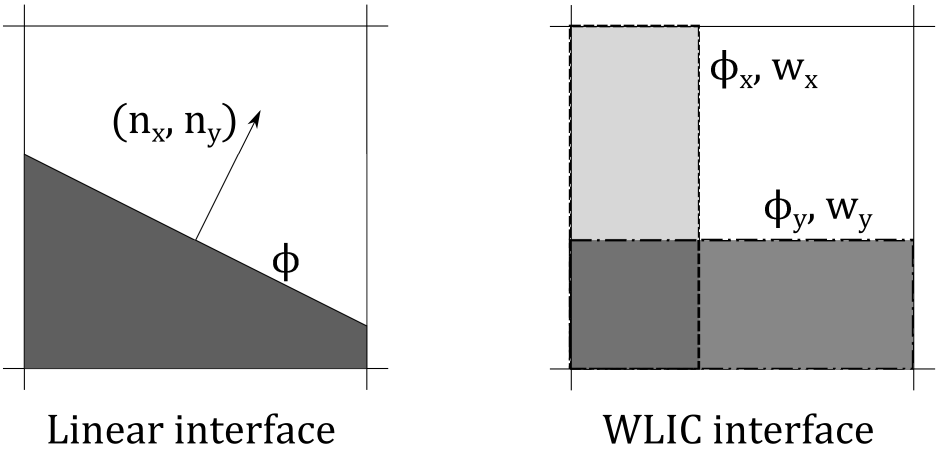

Figure 2.3: Schematic diagram of WLIC interface reconstruction. In this 2D example, an interface with surface normal vector $(\boldsymbol{n}_x,\ \boldsymbol{n}_y)$ is approximated by the sum of two simple line reconstructions ϕ_x (dashed line) and ϕ_y (dotted line) with different weights given by $w_x = \|\boldsymbol{n}_x\|/(\|\boldsymbol{n}_x\| + \|\boldsymbol{n}_y\|)$ and $w_y = \|\boldsymbol{n}_y\|/(\|\boldsymbol{n}_x\| + \|\boldsymbol{n}_y\|)$.

respectively. Herein F with different superscripts is the geometrical flux calculated from the VOF interface reconstruction at each split step. It is seen that all terms on the right hand side of the split equations contain only the variables from the previous stages. So this is thought to be an explicit updating of the VOF function ϕ. This method is conservative if the velocity field is discretely divergence free.

2.4.2 Modified WLIC schemes

In this study, we respect the interface reconstruction methodology from the original THINC/WLIC method. On the other hand, we explore alternative approaches for updating the VOF function.

Consider a two-dimensional flow case where the velocity is compressive in x-coordinate ($\Delta u < 0$) but expansive in y-coordinate ($\Delta v > 0$). One problem introduced by the above explicit scheme is that after a single sweep, overshoot in the value of ϕ may possibly occur because of the compressive one-directional velocities (see [8]), although it would be partially compensated by the following sweep in the expansive direction. This problem could be overcome by replacing the explicit scheme with a semi-implicit one as below:

$$\phi_{ijk}^{*} = \phi_{ijk}^{n} - \frac{F_{i+1/2,j,k}^{n} - F_{i-1/2,j,k}^{n}}{\Delta x} + \Delta t \phi_{ijk}^{*} \frac{\Delta u}{\Delta x} \tag{2.14}$$

$$\phi_{ijk}^{**} = \phi_{ijk}^{*} - \frac{F_{i,j+1/2,k}^{*} - F_{i,j-1/2,k}^{*}}{\Delta y} + \Delta t \phi_{ijk}^{**} \frac{\Delta v}{\Delta y} \tag{2.15}$$

$$\phi_{ijk}^{***} = \phi_{ijk}^{**} - \frac{F_{i,j,k+1/2}^{**} - F_{i,j,k-1/2}^{**}}{\Delta z} + \Delta t \phi_{ijk}^{***} \frac{\Delta w}{\Delta z} \tag{2.16}$$

It is not difficult to show that such a semi-implicit updating is conceptually equivalent to the "effective cell volume change" approach proposed by [8]. In addition, this scheme is made conservative by subtracting the velocity gradient terms from the operator-splitting algorithm, as done in [13]:

$$\phi_{ijk}^{n+1} = \phi_{ijk}^{***} - \Delta t \phi_{ijk}^{*} \frac{\Delta u}{\Delta x} - \Delta t \phi_{ijk}^{**} \frac{\Delta v}{\Delta y} - \Delta t \phi_{ijk}^{***} \frac{\Delta w}{\Delta z} \ . \tag{2.17}$$

Another approach used to advance the interface is a semi-Lagrangian propagation with directional split. Both forward [11] and backward-tracing [44] strategies are applicable to such a Lagrangian interface tracing. Our approach based on a backward-tracing is explained here.

Since the advection is done through separated one-directional sweeps, illustration for the x-coordinate case is sufficient. Consider a control volume CV_i on the interval $[x_{i-1/2}, x_{i+1/2}]$ with face velocity $u_{i-1/2}$ and $u_{i+1/2}$ at its two ends, respectively. We want to decide the VOF function ϕ_i^{n+1} for CV_i. Starting from the cell faces, we trace backward along the characteristic line, so we have a "departure cell" CVD mapped on the region

$$[x_{i-1/2} - u_{i-1/2}\Delta t,\ x_{i+1/2} - u_{i+1/2}\Delta t] \ .$$

In other words, the departure cell CVD shall be just fitted into the target control volume CV_i after the advection. So ϕ_i^{n+1} is set to the average value of the VOF function contained in CVD, which may involve multiple cells, as depicted in Figure 2.4. The same THINC/WLIC technique for evaluating the volume fluxes is adapted to integrate the VOF function in each intersected area separated by cell boundaries.

2.4.3 Comparative study of different schemes

In order to compare three different types of the THINC/WLIC method, we apply them to several two-dimensional scalar advection problems. We first consider the famous Zalesak disk [45] problem with rigid body rotation. In this test, the computational domain is set to a unit square and a notched

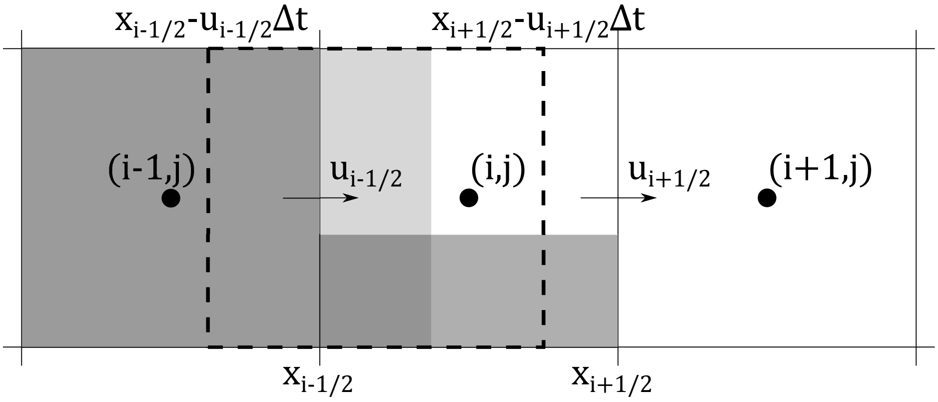

Figure 2.4: Semi-Lagrangian advection of VOF function with WLIC reconstruction. The departure cell for CV(i, j) is displayed as the rectangular region with dashed border.

disk whose radius is 0.17 is centered at (0.5, 0.75). The slit cutting into the disk is given by

$$|x - 0.5| \leq 0.03 \text{ and } y \leq 0.85 \ .$$

The VOF function inside the disk is initialized to one. An external velocity field is prescribed as

$$u = y - 0.5$$
$$v = 0.5 - x$$

After the simulation begins, the disk will rotate rigidly clockwise around the domain center. We run the computation on a 100 by 100 grid and complete one revolution in 2000 steps.

Figure 2.5 shows the computational results after one cycle of rotation. The original shape of the notched disk is clearly recovered by the results, except for some smearing and deformation at sharp corners, which could be improved by further refining the grids (results not shown here). It is seen that all three schemes can well predict the interface motion. Differences between different schemes are almost invisible for this rigid body rotation test.

Another problem, referred to as the Rider-Kothe vortex [46], is a more severe test featured by a large deformation of the interface. At $t = 0$, a circle with radius 0.15 is placed at (0.5, 0.75). A time dependent shearing flow is imposed as

$$u(t) = -U_0 \sin^2(\pi x) \sin(2\pi y) \cos(\pi t/T)$$
$$v(t) = +U_0 \sin^2(\pi y) \sin(2\pi x) \cos(\pi t/T)$$

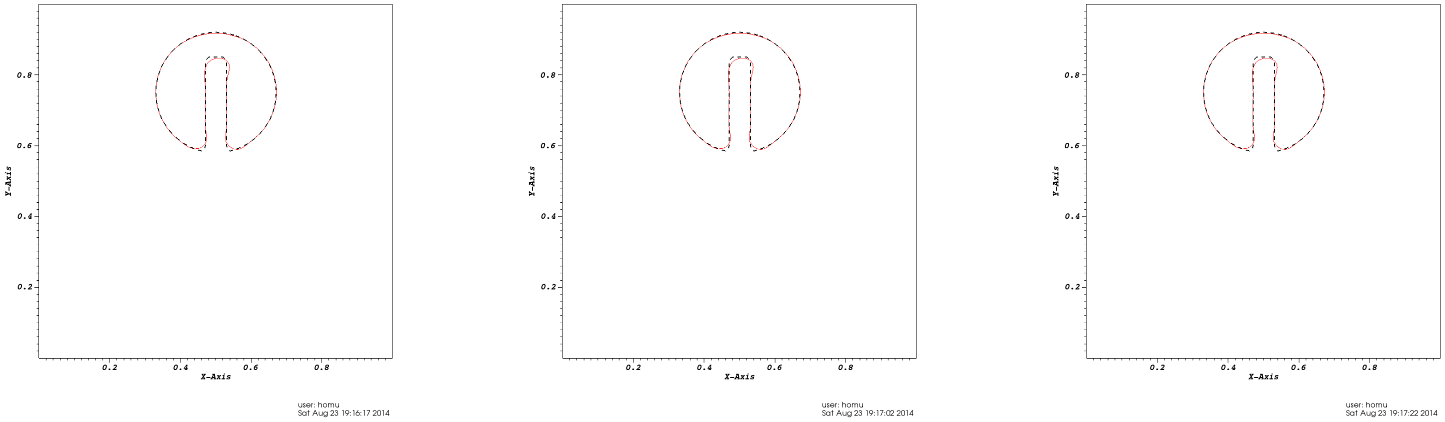

(a) Explicit updating

(b) Semi-implicit updating

(c) Semi-Lagrangian updating

Figure 2.5: Zalesak disk problem using different THINC/WLIC schemes. The red line shows the interface after one rotation and the black dashed line is the inital shape.

in which T is the time period for the circle returning back to its initial position. In this test, we have $U_0 = 1$ and $T = 8$. The (u, v) values are directly assigned to staggered velocity components at cell faces. We use a 200 by 200 uniform grid to discretize the computational domain of 1.0 by 1.0. A fixed time step of $\Delta t = 0.001$ sec is chosen to guarantee a mediate Courant number. After 8000 steps the simulation is finished. We also generate a reference solution by tracking the Lagrangian particles representing the front and integrate their motions using a fourth-order Runge-Kutta method.

Figure 2.6 shows the interface shapes of maximal deformation at $t = T/2$. The original circle has been stretched into a long filament along the vortex flow direction. At this stage, all three schemes yield comparable results in good agreement with the reference solution (Figure 2.6 (d)) except that some flotsam detached from filament tail which has becomes too thin to be resolved by the current computation.

When time comes to $t = T$, the circular shape should be exactly restored for a perfect advection. Figure 2.7 compares the simulation results with the initial state. It is observed that, however, there is a subtle phase lag between the interface calculated by the explicit scheme and the initial state. Such a discrepancy does not exist for the computation using the semi-implicit and semi-Lagrangian schemes. Hence, for flow cases with strong vorticity and large deformation of the interface, it is possibly more beneficial to use the VOF method together with a semi-implicit or semi-Lagrangian updating scheme.

In the fluid simulations reported in this study, the original THINC/WLIC interface reconstruction and propagation algorithm is used for its proven validity. The semi-implicit and semi-Lagrangian schemes discussed in this section are not pursued. Their performance in practice will be left for future research.

2.5 Numerical methodology

2.5.1 The Navier-Stokes solver

In this section, we first describe the basic implementation of the Navier-Stokes solver while ignoring the IB forcing term in the momentum equation. At the beginning of the n-th time step, all VOF related quantities at the new $(n+1)$-th step, i.e. ϕ^{n+1}, ρ^{n+1} and μ^{n+1}, are assumed to be known and they are referred with the superscript $(n+1)$ dropped.

Our discretization approximates the Navier-Stokes equation and satisfies the incompressible condition by using a classical first-order projection

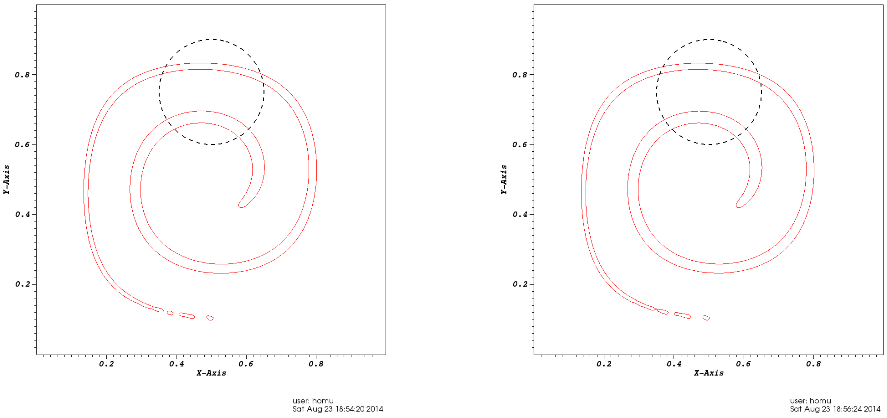

(a) Explicit updating

(b) Semi-implicit updating

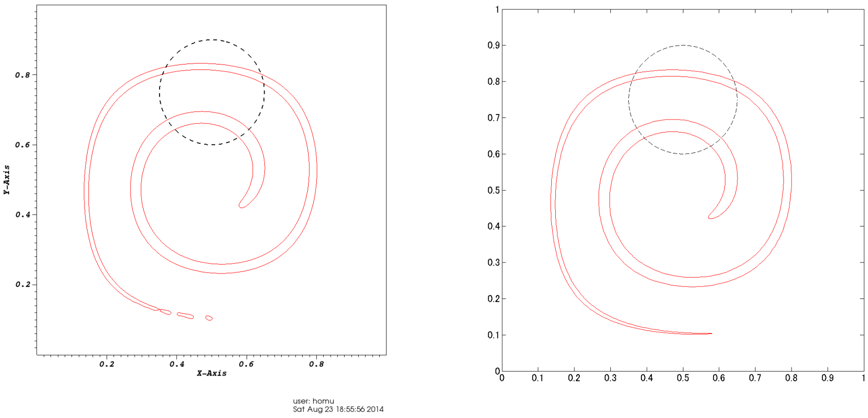

(c) Semi-Lagrangian updating

(d) Reference solution

Figure 2.6: Rider-Kothe vortex problem at $t = T/2$ using THINC/WLIC scheme. The red line shows the calculated interface and the black line is the original shape. The reference solution in (d) is obtained by tracking the motion of Lagrangian points.

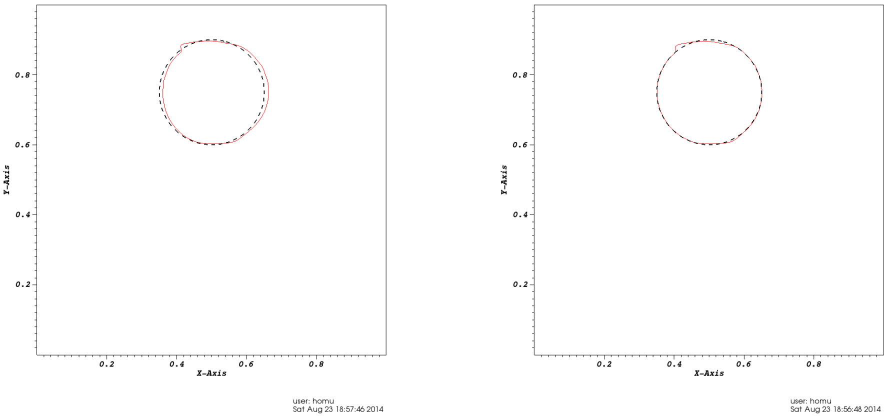

(a) Explicit updating (b) Semi-implicit updating

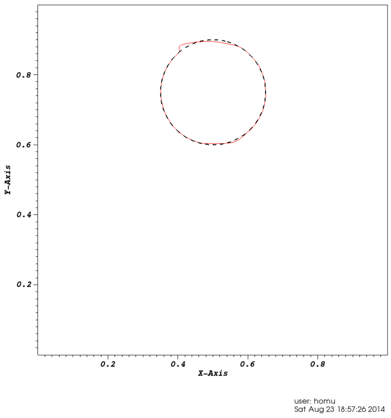

(c) Semi-Lagrangian updating

Figure 2.7: Rider-Kothe vortex problem at $t = T$ using THINC/WLIC scheme. The red line shows the calculated interface and the black line is the original shape.

method. In this method, the convective, viscous, gravity and surface tension terms are calculated explicitly. Next, a pressure Poisson equation is solved to obtain the pressure implicitly. Then the intermediate velocity is corrected to be discretely divergence free. The fractional-step algorithm is done by the following procedures.

1. Explicit Euler solve for predicting velocities:

$$\frac{\boldsymbol{u}^* - \boldsymbol{u}^n}{\Delta t} = -\nabla \cdot (\boldsymbol{u}\boldsymbol{u}) + \frac{\mu}{\rho}\nabla^2 \boldsymbol{u}^n + \frac{1}{\rho}\sigma\kappa\delta\boldsymbol{n} + \boldsymbol{g} \tag{2.18}$$

2. Implicit pressure Poisson equation with variable coefficients:

$$\nabla \cdot \left(\frac{1}{\rho}\nabla p^{n+1}\right) = \frac{\nabla \cdot \boldsymbol{u}^*}{\Delta t} \tag{2.19}$$

3. Pressure projection step for correcting velocities:

$$\frac{\boldsymbol{u}^{**} - \boldsymbol{u}^*}{\Delta t} = -\frac{1}{\rho}\nabla p^{n+1} \tag{2.20}$$

The resulting velocity field $\boldsymbol{u}^{**}$ will be further modified according to the IB treatment, see Section 2.5.2.

The following sections provide the spatial discretization schemes used in this study.

Grid variables

The fluid density and viscosity in each cell is computed thru the volume average in equations 2.4 and 2.5 using the VOF function collocated at the same position:

$$\rho_{ijk} = \phi_{ijk}\rho_l + (1 - \phi_{ijk})\rho_g \tag{2.21}$$

$$\mu_{ijk} = \phi_{ijk}\mu_l + (1 - \phi_{ijk})\mu_g \tag{2.22}$$

If their values are required at face or node position, they are obtained via a simple average of the neighboring values. For example,

$$\rho_{i+1/2,j,k} = \frac{1}{2}(\rho_{ijk} + \rho_{i+1,j,k}) \tag{2.23}$$

$$\mu_{i+1/2,j+1/2,k} = \frac{1}{4}(\mu_{ijk} + \mu_{i+1,j,k} + \mu_{i,j+1,k} + \mu_{i+1,j+1,k}) \tag{2.24}$$

Similar operations are done for staggered velocity components if necessary, e.g.:

$$u_{ijk} = \frac{1}{2}(u_{i-1/2,j,k} + u_{i+1/2,j,k}) \tag{2.25}$$

$$v_{i+1/2,j+1/2,k} = \frac{1}{2}(v_{i,j+1/2,k} + v_{i+1,j+1/2,k}) \tag{2.26}$$

Convective and viscous terms

For the non-linear convective term, a conservative discretization is used. For the u-component at staggered position $(i+1/2, j, k)$, it is given by

$$\nabla_x(uu)_{i+1/2,j,k} + \nabla_y(vu)_{i+1/2,j,k} + \nabla_z(wu)_{i+1/2,j,k} \ .$$

Let us take the second term with y-derivative for an example. It is written in finite difference form as

$$\frac{v_{i+1/2,j+1/2,k}U_{i+1/2,j+1/2,k} - v_{i+1/2,j-1/2,k}U_{i+1/2,j-1/2,k}}{\Delta y} \ ,$$

where v is the advection velocity obtained using linear interpolation as shown in the previous section. The quantities U in capital letters are u-velocities constructed at the faces of momentum control volume. In general, upwind-biased schemes should be used to avoid unphysical oscillations. A hybrid scheme of Spalding 's [39] with some modification is used to interpolate face values in this study. For the case of U velocity above, it can be determined using the hybrid scheme as

$$U_{i+1/2,j+1/2,k} = \begin{cases} u_{i+1/2,j,k} & \text{if } Pe > Pe^{stab}, \\ u_{i+1/2,j+1,k} & \text{if } Pe < -Pe^{stab}, \\ (u_{i+1/2,j,k} + u_{i+1/2,j+1,k})/2 & \text{otherwise,} \end{cases} \tag{2.27}$$

where the Peclet number (or cell Reynolds number), Pe, is chosen as the maximum value of two neighbor cells,

$$Pe = v_{i+1/2,j+1/2,k}\Delta y \max\left(\frac{\rho_{i+1/2,j,k}}{\mu_{i+1/2,j,k}}, \frac{\rho_{i+1/2,j+1,k}}{\mu_{i+1/2,j+1,k}}\right) \ . \tag{2.28}$$

Herein Pe^{stab} is the stability criterion for which we use $Pe^{stab} = 1.5$ in this study. The other terms are treated in a similar way. The hybrid scheme switches between first-order upwind difference scheme and second-order central difference scheme, depending on the local Peclet number. Although it tends to be more diffusive than other higher-order schemes often used in LS methods (e.g. the third-order QUICK scheme for convective term in [34]), the hybrid scheme is found to be a good company for a VOF method which can keep the consistency between momentum fluxes and mass fluxes and avoid spurious wiggles at the free surface.

The well-known central differences is applied for the viscous term while the variable fluid viscosity is computed at the midpoint. For example, its u-component is written as

$$\mu\nabla^2 u \approx \frac{\partial}{\partial x}\left(\mu\frac{\partial u}{\partial x}\right) + \frac{\partial}{\partial y}\left(\mu\frac{\partial u}{\partial y}\right) + \frac{\partial}{\partial z}\left(\mu\frac{\partial u}{\partial z}\right)$$

for which all the continuous derivatives are replaced by central differences, and the viscosity is estimated as mentioned in the previous section.

Surface tension

The famous continuum surface force (CSF) model [47] is used to compute the surface tension. In the CSF model, the original surface force is recast as a volume force within a narrow band across the free surface as follows:

$$\frac{1}{\rho}\sigma\kappa\delta\boldsymbol{n} \approx \frac{1}{\rho}\sigma\kappa\nabla\phi\ . \tag{2.29}$$

The interface unit normal vector $\boldsymbol{n}$ is computed by evaluating the finite-difference gradient of the VOF function

$$\boldsymbol{n} = \nabla\phi^s/\|\nabla\phi^s\|\ . \tag{2.30}$$

Here ϕ^s is a smoothed VOF function to improve the estimation of normal vectors. In this study, ϕ^s is obtained by smoothing the original ϕ twice using the filter suggested by [48]. The curvature κ is evaluated as the divergence of the surface unit normal:

$$\kappa = -\nabla\cdot\boldsymbol{n}\ . \tag{2.31}$$

In practice, we check the value of the VOF function and cutoff small, unstable values of normal vectors to ensure that the surface tension force is only calculated in the vicinity of the free surface.

Pressure projection

The left hand side of the pressure Poisson equation 2.19 is discretized by using a classical central difference scheme given by

$$\begin{aligned}\nabla \cdot \left(\frac{1}{\rho}\nabla p\right)_{ijk} &= \frac{1}{\Delta x^2}\left(\frac{p_{i+1,j,k} - p_{ijk}}{\rho_{i+1/2,j,k}} - \frac{p_{ijk} - p_{i-1,j,k}}{\rho_{i-1/2,j,k}}\right) \\ &+ \frac{1}{\Delta y^2}\left(\frac{p_{i,j+1,k} - p_{ijk}}{\rho_{i,j+1/2,k}} - \frac{p_{ijk} - p_{i,j-1,k}}{\rho_{i,j-1/2,k}}\right) \\ &+ \frac{1}{\Delta z^2}\left(\frac{p_{i,j,k+1} - p_{ijk}}{\rho_{i,j,k+1/2}} - \frac{p_{ijk} - p_{i,j,k-1}}{\rho_{i,j,k-1/2}}\right) .\end{aligned} \tag{2.32}$$

The matrix system defined by this discrete operator is thus symmetric.

The velocity divergence term at right hand side of the pressure Poisson equation can be easily calculated as

$$\begin{aligned}(\nabla \cdot \boldsymbol{u})_{ijk} &= \frac{u_{i+1/2,j,k} - u_{i-1/2,j,k}}{\Delta x} \\ &+ \frac{v_{i,j+1/2,k} - v_{i,j-1/2,k}}{\Delta y} \\ &+ \frac{w_{i,j,k+1/2} - w_{i,j,k-1/2}}{\Delta z} .\end{aligned} \tag{2.33}$$

Once the pressure is obtained, the fluid velocity (e.g. the u-velocity) could be corrected by

$$\frac{u^{**}_{i+1/2,j,k} - u^{*}_{i+1/2,j,k}}{\Delta t} = -\frac{1}{\rho_{i+1/2,j,k}} \frac{p_{i+1,j,k} - p_{ijk}}{\Delta x} . \tag{2.34}$$

To solve the discretized pressure equation, we use an algebraic multigrid-preconditioned conjugate gradient method from the HYPRE library[1] (namely the `PFMG-CG` structured grid solver in the HYPRE documentation). This solver is found to be efficient and robust through our numerical study even for gas-liquid flows with high density ratios (up to 1000 : 1). The convergence tolerance is set to 10^{-8} as a measure of the relative error.

2.5.2 IB treatment for flow field

The flow velocity at the wall is made consistent with the prescribed boundary velocity through the IB model. As mentioned in Section 2.3, each boundary wall has its own level set representation ψ_{Bm} ($m = 1, 2, \ldots, N$ in N objects),

---

[1] The Hypre library, `http://acts.nersc.gov/hypre/`.

and for the entire fluid domain, both a level set function ψ_{ijk} and a solid volume fraction α_{ijk} field will be generated from the boundary shape profile, see Figure 2.8.

Next the boundary velocity is to be projected from the Lagrangian wall objects to the Eulerian fluid mesh. The rigid velocity, $\boldsymbol{u}_{Bm}$, could be evaluated at a point $\boldsymbol{x}$ as follows:

$$\boldsymbol{u}_{Bm}(\boldsymbol{x}) = \boldsymbol{v}_{Bm} + \boldsymbol{\omega} \times (\boldsymbol{x} - \boldsymbol{x}_{Bm}) \ , \tag{2.35}$$

where $\boldsymbol{v}_B$, $\boldsymbol{\omega}_B$ and $\boldsymbol{x}_B$ are the linear velocity, angular velocity and reference point of rotation of the m-th wall, respectively. We note that the point $\boldsymbol{x}$ corresponds to a staggered velocity at cell face, so the components of $\boldsymbol{u}_B$ parallel to the cell face are actually discarded. The calculation of $\boldsymbol{u}_B$ is not only limited to the solid region inside the walls, but also expanded to a narrow band beyond the solid surface where the solid volume fraction α is non-zero.

For a momentum control volume intersected by multiple wall objects, special care should be taken. We first find out whether the fluid point is covered by any of these objects by checking the signs of the level set functions. If so, the rigid velocity of that wall is directly assigned to the fluid position; otherwise a weighted mean boundary velocity is calculated with the volume fraction of each wall used as the weight.

Then the velocity $\boldsymbol{u}^{**}$ yielded from the fluid solver (Section 2.5.1) could be readily corrected to take into account the solid motion by an explicit modification:

$$\boldsymbol{u}^{n+1} = (1-\alpha)\boldsymbol{u}^{**} + \alpha \boldsymbol{u}_B \tag{2.36}$$

which in return yields an expression for the IB forcing term

$$\boldsymbol{f}_B = \frac{\alpha(\boldsymbol{u}_B - \boldsymbol{u}^{**})}{\Delta t} \ . \tag{2.37}$$

Explicit evaluation of $\boldsymbol{f}_B$ is not necessary as only prescribed object motion is allowed. As illustrated in Figure 2.8, for a cell completely enclosed inside some solid subdomain ($\alpha = 1$), the present IB correction will directly inject the rigid velocity therein; while at the interface ($0 < \alpha < 1$), the velocities are continuously interpolated to form a boundary layer by which fluid and solid regions are smoothly connected. Similarly, in a physical sense, the IB forcing $\boldsymbol{f}_B$ could be related to the slip-velocity between solid and fluid phases in the interface boundary layer, whereas the forcing effect naturally vanishes in the fluid region ($\alpha = 0$).

Applying the IB correction to a staggered velocity variable still requires some more clarification. The face velocity that needs such a correction is

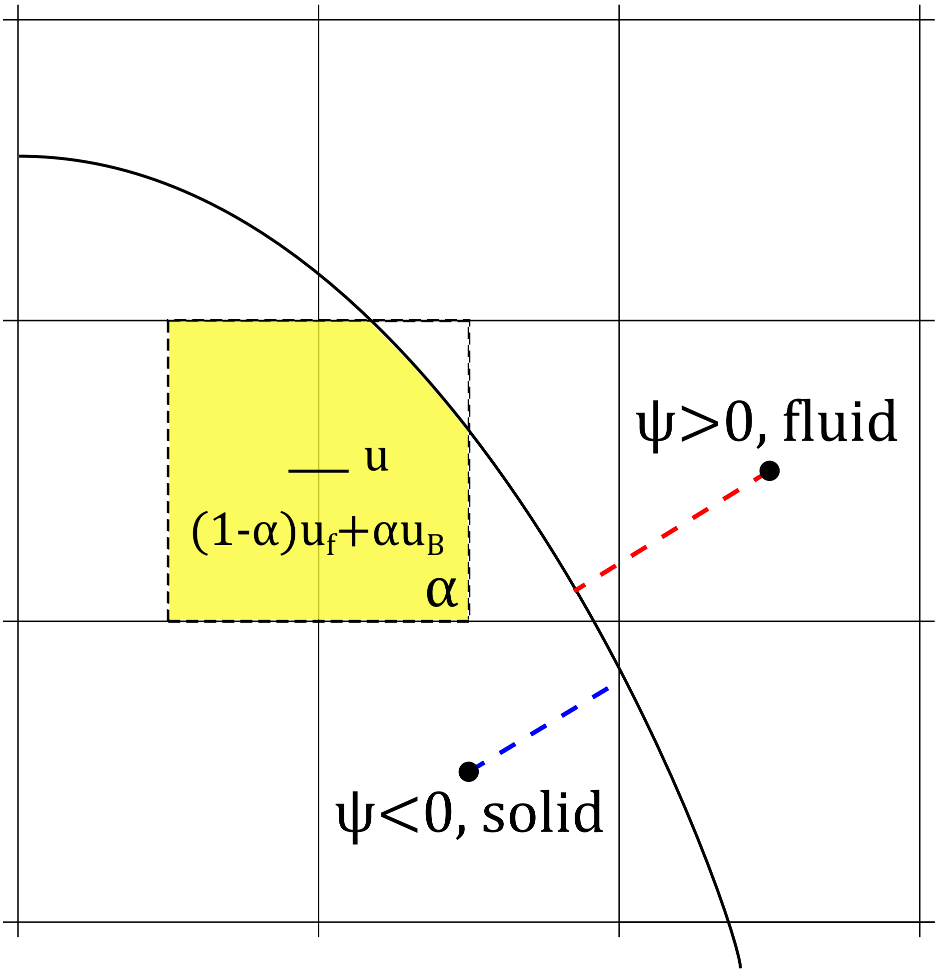

Figure 2.8: IB domain and fluid domain.

called an IB point, which is identified by that the wall level set function ψ is non-positive for at least one of the two adjacent cells. The determination of IB points is similar to that of finding interfacial points in some existing methods for fluid-fluid [49] and fluid-solid [25] interaction problems. Again, we choose the u-velocity $(i+1/2, j, k)$ as an example, see Figure 2.9. The values of ψ at adjoining cells sharing this face are first examined for

$$(\psi_{ijk} < 0 \text{ and } \psi_{i+1,j,k} < 0) \text{ or } \psi_{ijk} \cdot \psi_{i+1,j,k} \leq 0 \ . \tag{2.38}$$

In that case, the IB equation becomes

$$u^{n+1}_{i+1/2,j,k} = (1 - \alpha_{i+1/2,j,k}) u^{**}_{i+1/2,j,k} + \alpha_{i+1/2,j,k} u_{B,i+1/2,j,k} \ . \tag{2.39}$$

The solid volume fraction at face is given by the arithmetic average of two neighboring cells:

$$\alpha_{i+1/2,j,k} = \frac{1}{2}(\alpha_{ijk} + \alpha_{i+1,j,k}) \ . \tag{2.40}$$

We note that, using both SDF signs and IB fractions to identify IB points is a novel contribution by the proposed method in order to successfully simulate fluid interfaces within complex geometries. It is known that IB models generally introduce thickened artificial velocity boundary layer so that boundary and fluid domains are connected continuously. This is acceptable for single-phase flows but could be extremely problematic for two-phase flows within complex geometries. Based on our numerical test, the thickened boundary layer may cause the fluid interface to adhere to the wall surface spuriously, which is a peculiar problem that transpires only in the context of multiphase flows but not yet get addressed in existing IB literatures since their application to such flows is still very limited.

To solve this problem, the proposed SDF/IB approach is a useful remedy by restricting the thickness of artificial boundary layer to a minimal extent. We find this treatment is factually critical for suppressing the aforementioned spurious adherence of fluid interface on IB surfaces and subsequently can greatly improve the quality of numerical results. Its effect is demonstrated in the following example of a twin screw kneader (TSK) system which will be further discussed in the next chapter. Figure 2.10 shows fluid interfaces in a rotating TSK calculated by using the IB method with and without the SDF sign check. It is evident that the nonphysical attachment and entrainment of the gas-liquid interface on the paddle surface has spoiled the solution. One must be aware of the fact that those layers are mismatch to real liquid membranes sometimes observed on wall surfaces, as they are totally numerical artifacts and grid-dependent. When the current SDF/IB technique is

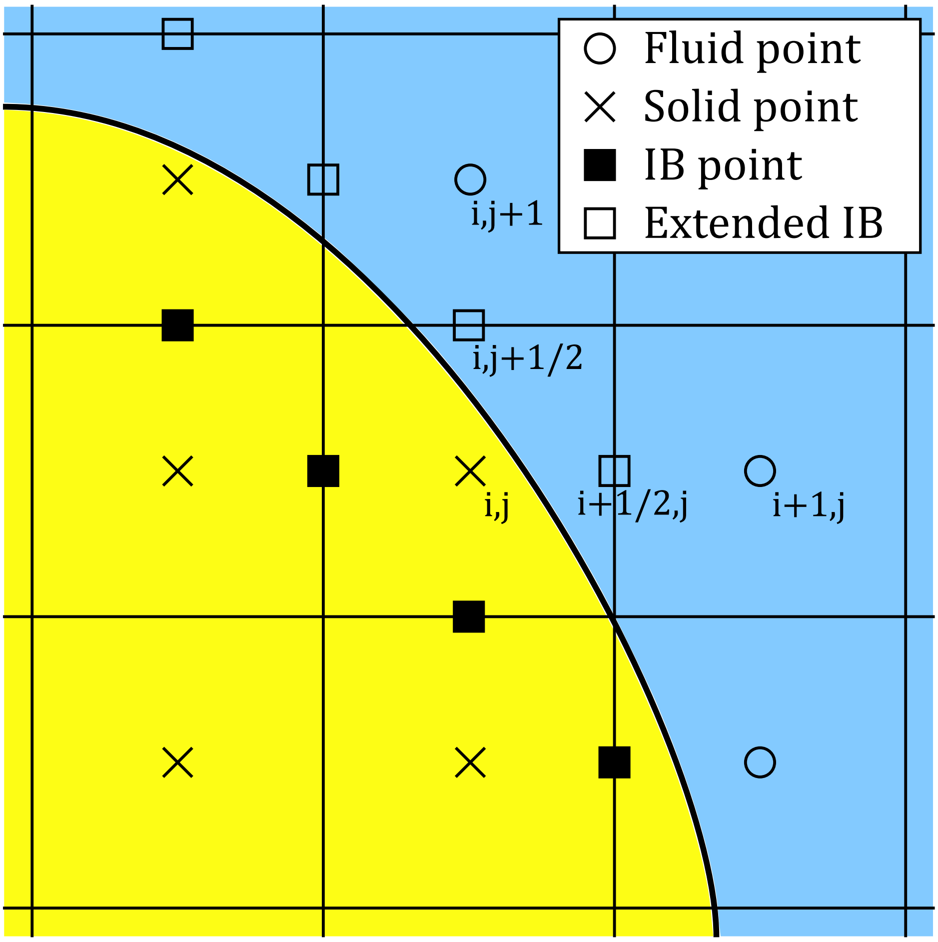

Figure 2.9: Selecting IB forcing points at staggered positions.

applied, such spurious phenomenon are satisfactorily eliminated and reasonable interface behavior is obtained.

Finally, a subsidiary problem is how to setup the boundary condition (BC) when the immersed boundary extends to the physical boundary, e.g. internal flows inside a tank. Based on our numerical test, at the boundary of the computational domain that is taken over by IB regions, one can apply some type of consistent fluid BCs, e.g. Dirichlet BC for velocity and homogeneous Neumann BC for pressure.

2.5.3 IB treatments for fluid interface

A typical IB method for fluid-solid problems takes care of the no-slip velocity BC, but an additional consideration arises when free surface calculation is

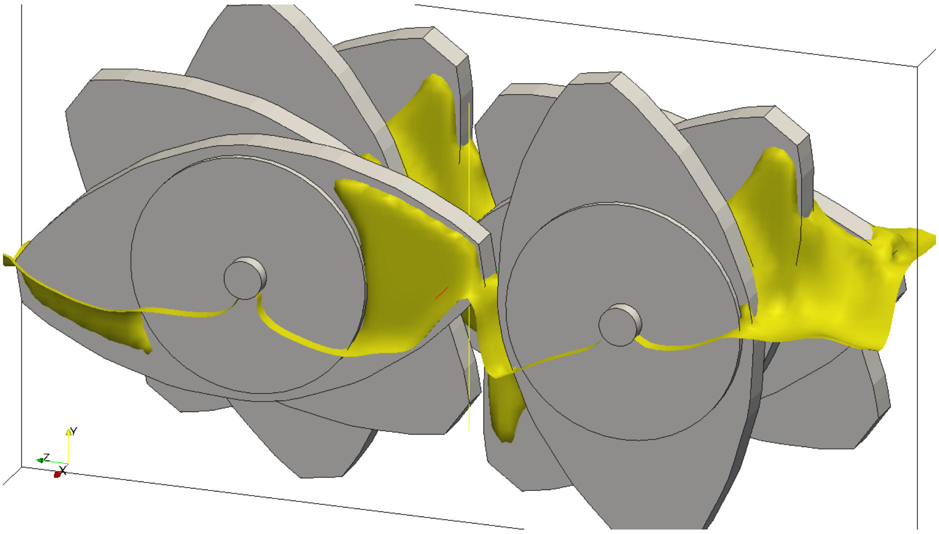

(a) IB interpolation without SDF sign check

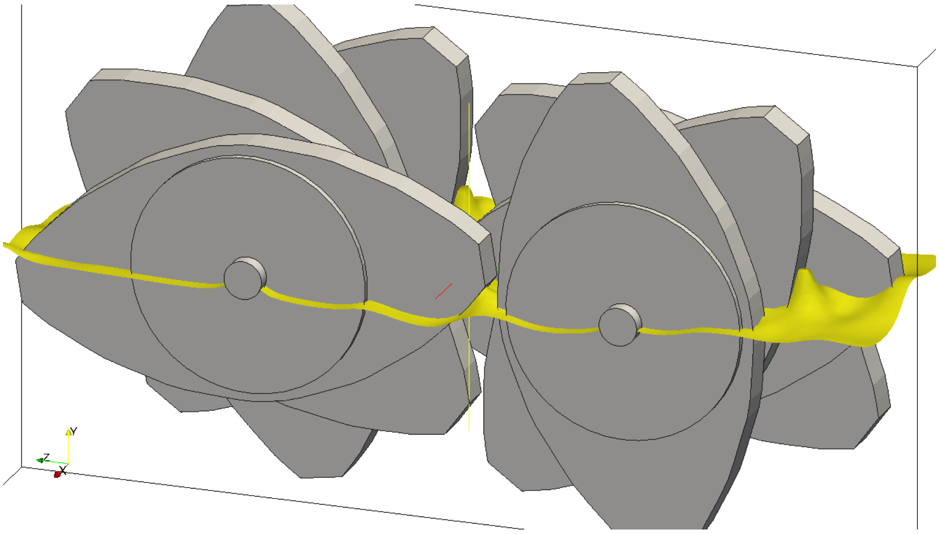

(b) IB interpolation with SDF sign check

Figure 2.10: Effect of the SDF/IB approach on interface behavior.

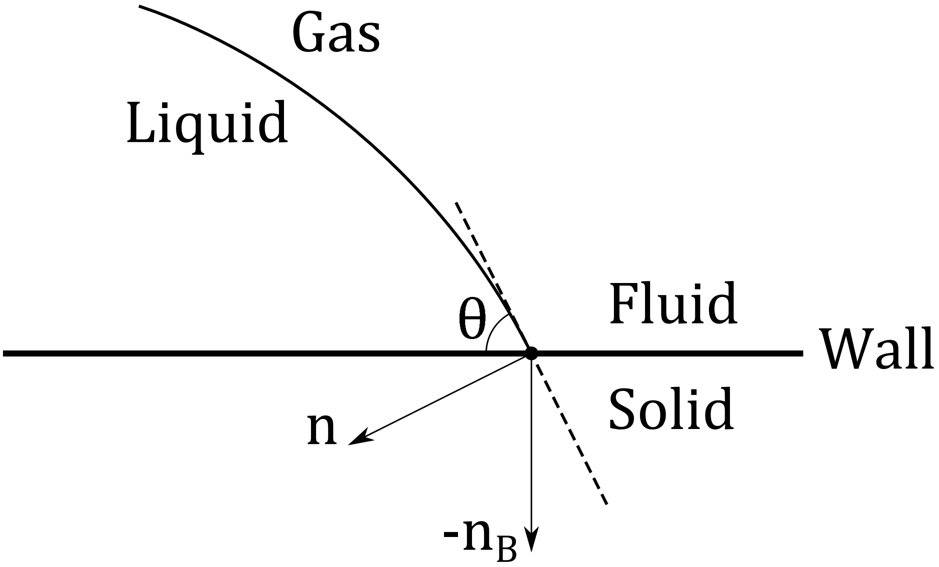

Figure 2.11: Schematic diagram of contact angle at a wall.

involved. Usually a special boundary condition has to be supplied to the intersection of the free surface and the solid wall, viz. the contact angle BC, which is given as follows with a contact angle θ_C:

$$\boldsymbol{n} \cdot (-\boldsymbol{n}_B) = \cos \theta_C \tag{2.41}$$

in which $\boldsymbol{n}$ is the interface unit normal pointing from gas region to liquid region and $\boldsymbol{n}_B$ is the boundary unit normal pointing from solid region to fluid region, as defined in preceding sections. Their relations is illustrated for a two-dimensional contact point in Figure 2.11.

Because the precise resolution of contact line dynamics is not the main aim, our discussion is restricted to the most basic case of a neutral contact angle, i.e. $\theta_C = \pi/2$. Consequently, the contact angle boundary condition is reduced to

$$\boldsymbol{n} \cdot (-\boldsymbol{n}_B) = -\frac{\nabla\phi}{\|\nabla\phi\|} \cdot \boldsymbol{n}_B = \cos(\pi/2) \text{ or } \nabla_B\phi = 0 \ . \tag{2.42}$$

It is thus shown that the reduced condition equals to a homogeneous Neumann BC for the VOF function at solid walls. In this study, two different approaches based on the extrapolation of the VOF function into the solid region are used to satisfy the contact angle BC.

The first way is a simple “dilation” operation which has been inspired by some sharp-interface methods that smoothly populate pressure [25, 50] or velocity [38, 51] into a fictitious fluid domain. In the beginning, all fluid cells ($\psi > 0$) are tagged and all solid cells ($\psi \leq 0$) are untagged. Next the VOF function inside an untagged cell will be assigned as the average value from tagged cells in its $3 \times 3 \times 3$ neighborhood with weight factors inversely proportional to the square of the distance between them. This procedure is repeated for n^{extend} times. Every time a cell is updated, it will be tagged and treated as known in the next iteration. In this way, the VOF front in the fluid region will grow into the solid region sequentially, by one layer of cells per iteration.

The second way consists in iteratively solving the "extension" equation proposed by [32]:

$$\frac{\partial \phi}{\partial \tau} + \boldsymbol{u}^{extend} \cdot \nabla \phi = 0 \ , \tag{2.43}$$

in which the extension velocity is the normal vector orthogonal to the solid surface:

$$\boldsymbol{u}^{extend} = -\boldsymbol{n}_B \ . \tag{2.44}$$

Although originally this method is proposed for level set methods, we apply it to VOF functions. It is solved at all the solid cells ($\psi 0$) for an artificial time duration $\tau^{max} = n^{extend} \Delta x$ with time increment $\Delta \tau = \Delta x$. A semi-Lagrangian advection scheme is used to find ϕ from its upwind position:

$$\phi_{ijk}^{\tau+\Delta\tau} = \phi^{\tau}(\boldsymbol{x}_{ijk} - \boldsymbol{u}^{extend} \Delta \tau) \tag{2.45}$$

in which the right hand side is evaluated by using a trilinear interpolation.

The dilation approach has the advantage in its simplicity that only the sign of the solid level set function is required, which makes it efficient and applicable to general geometry configurations. However, it must come with considerable smearing of the extrapolated interface. The extension approach reflects the solid surface orientation and thus can be adopted for arbitrary contact angles (see [32]), but finding the surface normal vector is sometimes ambiguous for under-resolved areas (e.g. consider a single cell influenced by two objects). Both methods are used in our numerical studies, case by case. The parameter n^{extend} is the total iteration number that controls the depth of front advancing into the solid region. Setting n^{extend} to zero is equivalent to omitting the contact angle BC. If not specified, we have $n^{extend} = 4$ in this study for both approaches.

It is noted that, in the present method, the THINC/WLIC interface advection (see Section 2.4) is performed for all computational cells ignoring immersed boundaries. And then the dilation or extension procedure is carried out to modify the VOF function in partial and full solid cells. This treatment is consistent with the IB methodology in an ignore-and-correct style, and it can circumvent the stringent time step restrictions caused by arbitrarily small cells, as figured out by [32]. However, the VOF advection is no longer conservative in the existence of the immersed boundary. A slight loss of mass (or overshoot) might occur in that case. If the volume conservation is desired, we choose to periodically reset the volume fractions of the liquid phase to compensate the mass error, which does not have an appreciable influence to the overall flow behavior.

2.5.4 Time-stepping algorithm

In the present method, the time step Δt is limited by the CFL condition, viscosity and surface tension:

$$\Delta t < C \cdot \min \left(\frac{\Delta x}{\|\boldsymbol{u}\|}, \frac{\rho \Delta x^2}{\mu}, \sqrt{\frac{\rho \Delta x^3}{2\pi\sigma}} \right) \tag{2.46}$$

where C is a positive constant sufficiently small. We perform simulations with a stable fixed time step chosen accordingly.

The overall time-stepping algorithm in a single sweep (from step n to $n+1$) is outlined as follows.

1. Update moving boundaries for the arbitrary-shape wall boundary model, see Section 2.3.
2. Transfer the boundary representation to the fluid grid, on which generate the solid wall level set ψ^{n+1} and volume fraction α^{n+1}, see Section 2.3.
3. Advance the VOF interface to ϕ^{n+1} using the THINC/WLIC scheme, see Section 2.4.
4. Extend the VOF function into the solid region, by using either the dilation or extension operation described in Section 2.5.3.
5. Compute the updated fluid properties ρ^{n+1} and μ^{n+1}, see Section 2.2.
6. Explicitly calculate the convective, viscous, gravity and surface tension terms listed in Section 2.5.1 to obtain a provisional velocity $\boldsymbol{u}^*$.
7. Solve the pressure Poisson equation for p^{n+1}, and correct the intermediate velocity to have $\boldsymbol{u}^{**}$, see Section 2.5.1.
8. Apply the IB treatment to enforce the velocity BC at the walls, and finally the flow velocity is updated as $\boldsymbol{u}^{n+1}$, see Section 2.5.2.

Now the current time step is completed.

2.6 Numerical results

In this section, we show three-dimensional numerical examples using the VOF-IB method. First, the fundamental part of the proposed method is validated in two quasi-steady systems, namely the parabolic surface in a rotating barrel and the relaxation of rods to static shape. Next the water exit of a cylinder is computed and compared with known solutions to show the effects of moving bodies. As a flow case with violent free surface motion, two dam break problems, where the flow either evolves freely or interacts with an obstacle, are investigated and validated against experimental data. Lastly, the simulation of the stirring process caused by two elliptical paddles rotating in a tank is conducted to show the ability of the present method to model complicated systems.

2.6.1 Water surface in a rotating barrel

The steady state of a free surface under rigid-body rotation, if ignoring the contact condition at the rigid wall, is given by a parabolic profile:

$$z = \frac{\omega^2}{2g} r^2 + (H - \frac{R^2}{4}) \ ,$$

where z is the surface elevation, r is the distance from rotation axis, ω is the angular velocity, g is gravity, H is the initial water depth, and R is the radius of the cylindrical container. See Figure 2.12.

In this test, we simulate a barrel with radius $R = 1$ and height $2H$ rotating with $\omega = 1$. The initial water depth H equals to 2 and the gravity is $(0, -1, 0)$. The computational domain is set to $2.4 \times 4.8 \times 2.4$ and the barrel is placed at the center of the domain with its pole aligned with the y-axis. The density and viscosity is $\rho_l = 1.0$ and $\mu_l = 0.01$ for the liquid phase, and $\rho_g = 0.001$ and $\mu_g = 10^{-5}$ for the gas phase, respectively. The computation is run up to steady state using four different resolutions, $18 \times 36 \times 18$, $24 \times 48 \times 24$, $36 \times 72 \times 36$ and $48 \times 96 \times 48$ cells, which serves as a grid convergence study involving the fluid interface. The extension approach described in Section 2.5.3 is used to treat the adhesion at walls.

Figure 2.13 shows the initial and final shapes of the interface obtained using the finest grid ($48 \times 96 \times 48$ cells). Due to centrifugal effects, the liquid has been pushed towards the wall side. Thus a concave surface forms and it is elevated from the initial position near the wall. In addition, as a 90-degree contact angle BC is applied, we can see that a flat extension of the interface is generated in the solid region on a plane orthogonal to the vertical wall.

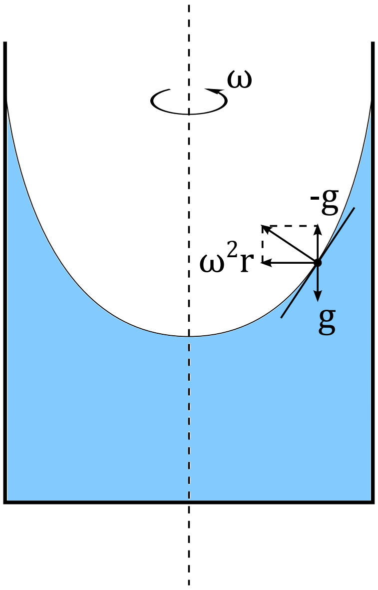

Figure 2.12: Rigid-body free surface vortex in a rotating barrel.

In Figure 2.14 the grid refinement study is shown in respect of the interface shape. Convergent results are obtained as grid is refined, and the interface shapes are also in good agreements with the analytical solution. Some difference between the simulation results and the parabolic profile is near the contact line at the wall. This is consistent with the application of the contact angle BC; however, this point is not considered in the analytical solution.

A numerical convergence study is performed for this test using the parabolic profile as the reference solution. Following the WLIC VOF paper by Yokoi [10], the L^1 error defined as

$$e^1 = \frac{\sum|\phi - \phi^{ref}|}{N} \tag{2.47}$$

is used for measuring the numerical error of interface shape in an average sense. Note that for immersed regions no analytical solution exists, so the evaluation of numerical error is only carried out in the fluid domain where $\psi > 0$. Figure 2.15 presents the estimates of numerical errors under different resolutions. From the slope in the error plot, a convergence rate close to 1 has been obtained, which is due to the first-order accuracy of the WLIC VOF scheme [10].

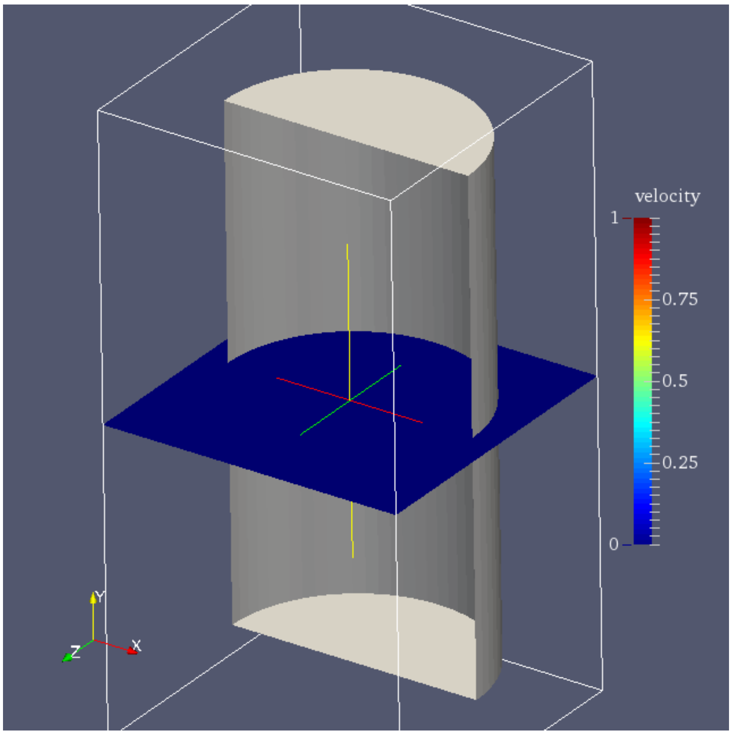

(a) Initial state

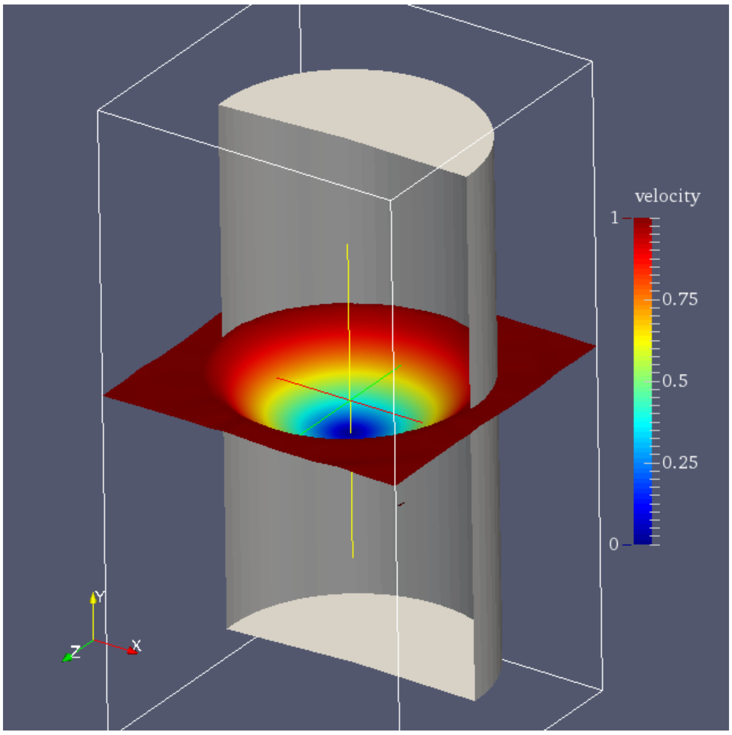

(b) Steady state

Figure 2.13: The interface shape in a rotating barrel. In this figure, the interface is calculated on the finest grid ($48 \times 96 \times 48$ cells) and is extrapolated from the solid surface using the extension algorithm.

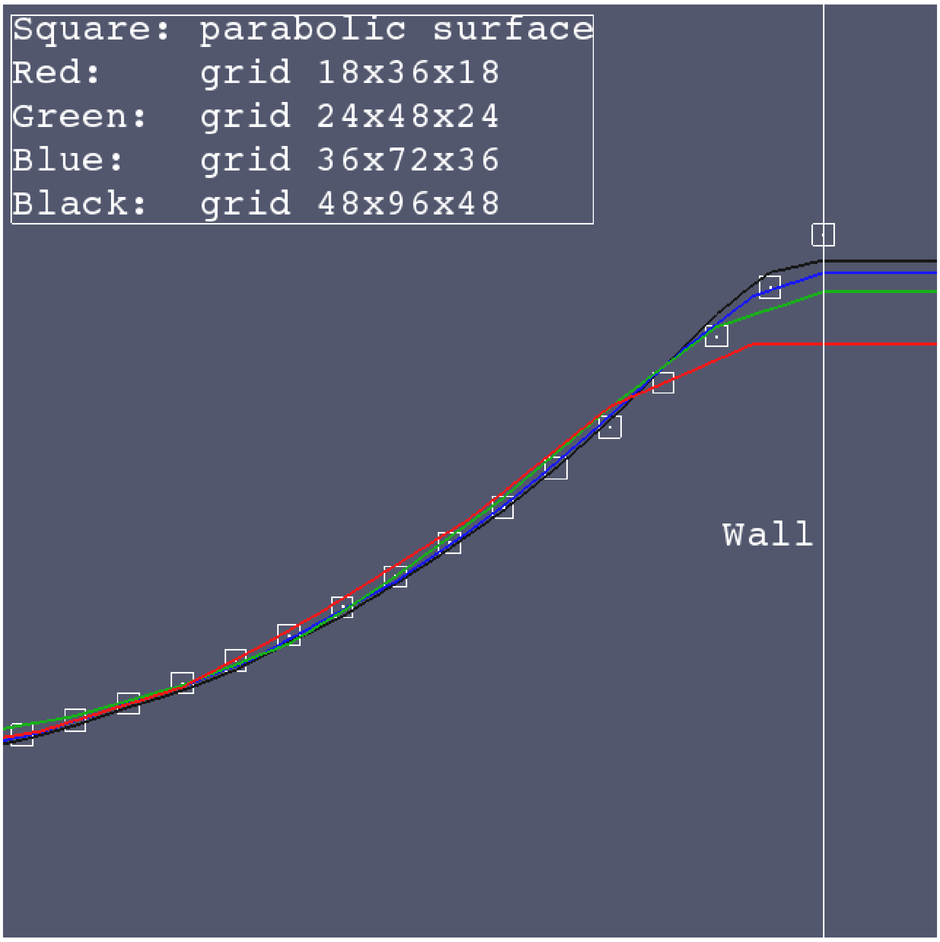

Figure 2.14: Comparison of the interface shape with grid refinement.

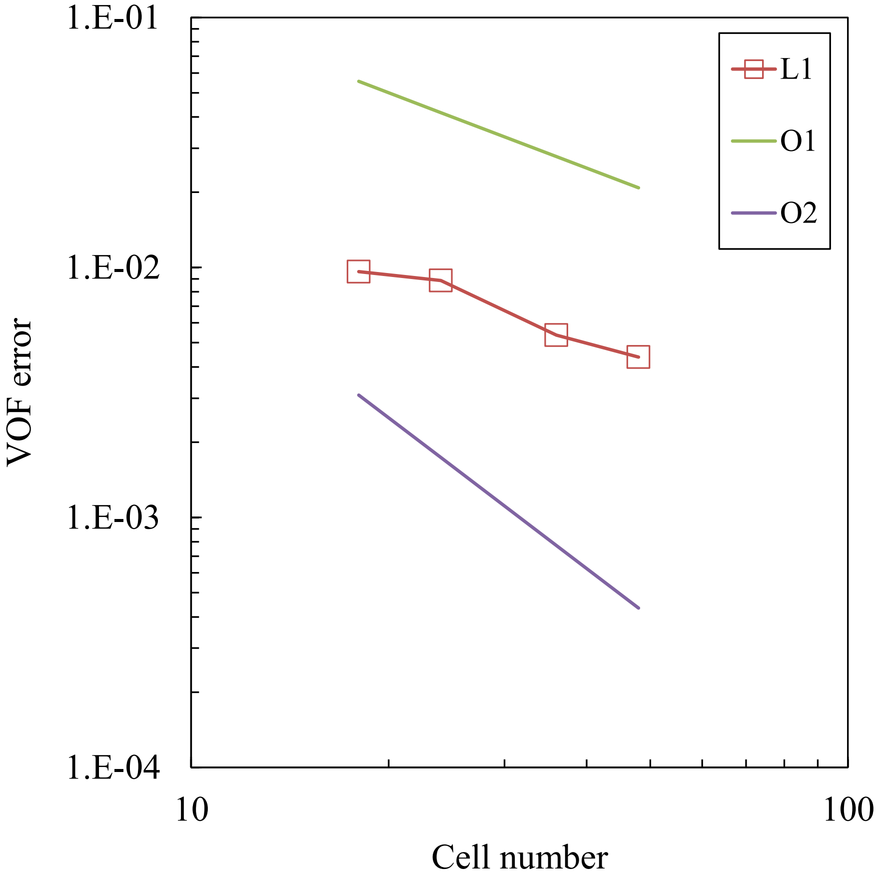

Figure 2.15: Convergence of VOF interface to the parabolic profile.

2.6.2 Relaxation of rods to static shape

In this section we validate the contact angle treatments described in Section 2.5.3 by studying relaxation of quasi-2D droplets (or rods) to static shape in different IB geometries.

Rectangular geometry

We first design a test case with straight walls. The computational domain is defined on $[-0.03, 0.03] \times [-0.06, 0.06] \times [-0.06, 0.06]$ with a discretization of $32 \times 64 \times 64$ cells. A box $[-L/2, L/2] \times [-L, L] \times [-L, L]$ is embedded as an IB geometry. The reference length L equals 0.05 m. The immersed boundary does not coincide with any cell boundaries under this problem setup. We initialize the VOF function to one in the area given by

$$y \leq 0 \text{ and } z \leq 0$$

and fill zero elsewhere.

In this study, we assume zero gravity, and have the parameters chosen as $\rho_l/\rho_g = 1$, $\mu_l/\mu_g = 10$ and $\sigma = 0.075$ N/m. Subject to the 90 ° contact angle condition, the initial shape will relax to a quarter of a cylindrical rod whose radius is computed as

$$a = 2L/\pi^{1/2} \approx 0.0564$$

and axis is at

$$y = z = -0.05 \; .$$

In Figure 2.16, we compare the computed interface shape (solid line) with the expected state (squares). Only a sectional view is shown for the two-dimensional nature of this test. It is confirmed that both the dilation and extension approaches are able to reproduce the analytical solution.

Curved geometry

Next we consider a system with curved boundaries. The parameters are totally the same as the previous test except that the IB geometry is replaced with a cylinder with radius $R = 0.05$. On a section plane, the static surface will theoretically be an arc whose tangents at the intersection points are perpendicular to the circular boundary (due to 90 ° contact angle). The central angle Θ subtending the arc (see Figure 2.17) can be obtained from the nonlinear equation

$$\frac{\pi - \Theta}{2} + \frac{\Theta}{2} \tan^2\left(\frac{\pi - \Theta}{2}\right) - \tan\left(\frac{\pi - \Theta}{2}\right) - \frac{\Theta_0}{2} = 0 \; .$$

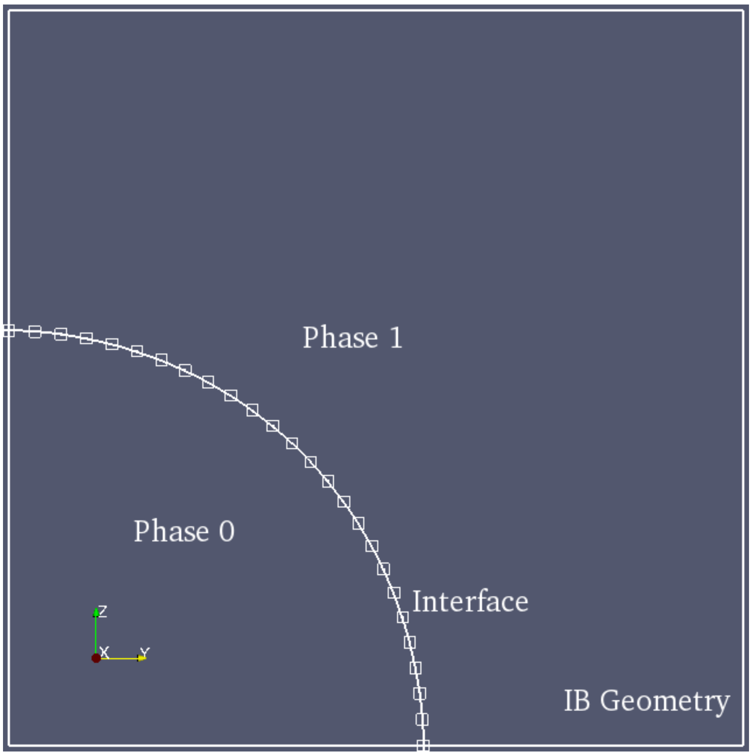

(a) Dilation approach

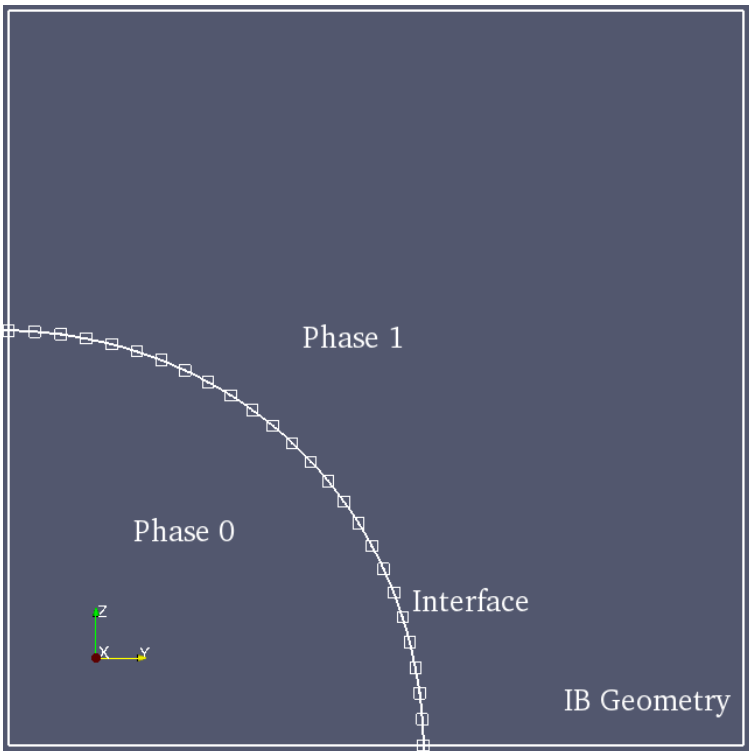

(b) Extension approach

Figure 2.16: Relaxation of rod to static shape in a box. The solid line shows the computed interface and squares represent expected solution.

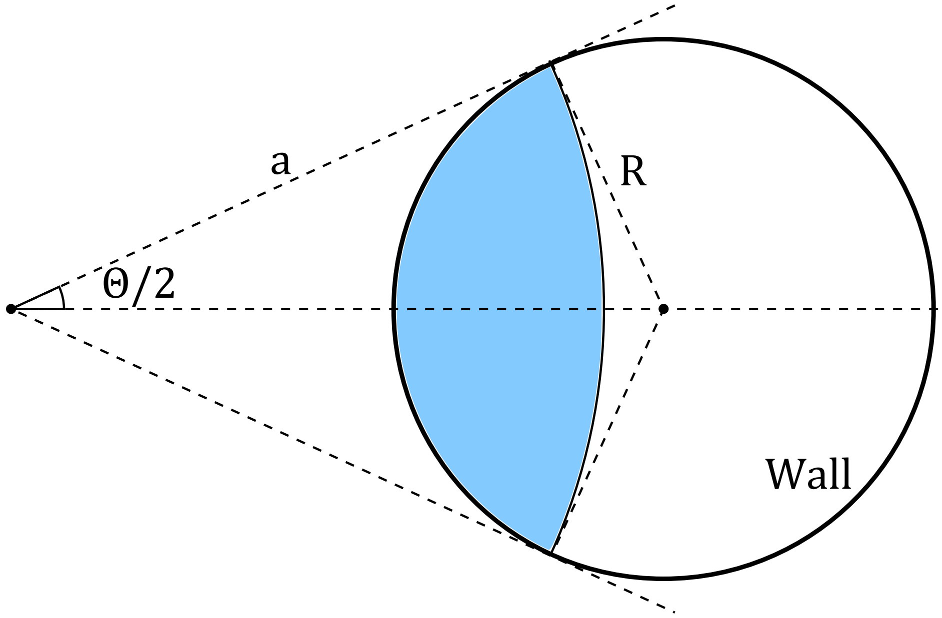

Figure 2.17: Meniscus shape in a cylinder.

Θ_0 depends on the initial configuration and is equal to $\pi/2$ in this problem. We solve this equation using Newton 's method and find that the value of Θ is approximately 69.28 degree. It is thereby easy to calculate the radius of the arc as

$$a = R \tan\left(\frac{\pi - \Theta}{2}\right) \approx 0.0724 \ .$$

Figure 2.18 shows the resulting interface in comparison with the expected shape. Again, both dilation and extension approaches can give satisfactory results in good agreement with the analytical solution. It also seems that the extension approach slightly outperforms that based on dilation operation in the vicinity of the immersed boundary. In the rest of this paper, the contact angle boundary condition is handled by the extension approach if not specified.

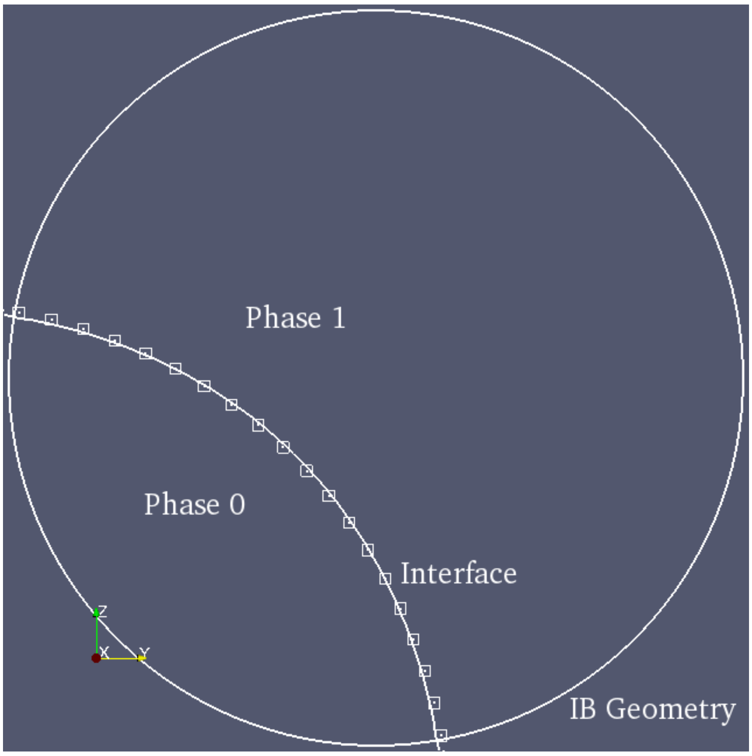

(a) Dilation approach

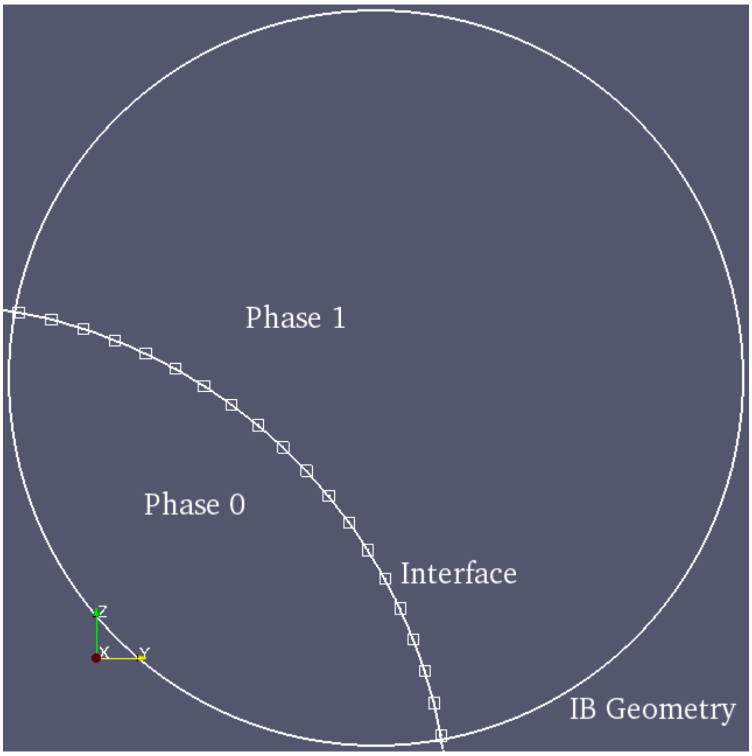

(b) Extension approach

Figure 2.18: Relaxation of rod to static shape in a cylinder. The solid line shows the computed interface and squares represent expected solution.

2.6.3 Water exit of a cylinder

The water exit problem of a cylinder has been studied as a test of free surface-moving body interaction by using various numerical approaches [28–30, 34, 35].

We setup this test in a fluid domain of $16R \times 16R \times 4R$ where $R = 1$ m is the cylinder radius. A $160 \times 160 \times 40$ grid is used to discretize the fluid domain, which gives a cell spacing $\Delta x = 0.1R$. The water depth is $12R$ and the cylinder is initially submerged beneath the water surface. The distance between the cylinder center and the surface is $H = 1.25R$. Physical properties of the water are $\rho_l = 1000$ kg/m^3 and $\mu_l = 0.001$ Pa·s, and those of the air are $\rho_g = 1$ kg/m^3 and $\mu_g = 10^{-5}$ Pa·s, respectively. The gravity is set to -1 kg m/s^2.

During the simulation, the cylinder rises at a constant upward velocity $V = 0.39$ m/s. The rising process is shown in Figure 2.19 against the dimensionless time

$$T = \frac{|V|t}{H} \ .$$

In early stages ($T < 0.6$), a growing curved surface arise due to the upward motion of the cylinder. At $T = 0.8$, the surface is broken by the emerging cylinder top and consequently surface waves are generated by the falling water from both sides around the cylinder ($T = 1.0$). As the cylinder moves on ($T > 2.0$), it completely exits the water surface. The behavior of the fluid interface obtained from our three-dimensional simulation agrees with other 2D reports (see e.g. [34]).

For a more precise comparison, Figure 2.20 shows the interface shapes at $T = 0.4$ and 0.6 in close-up together with the boundary element method (BEM) solution of [52]. The present results are in good agreements with the reference data.

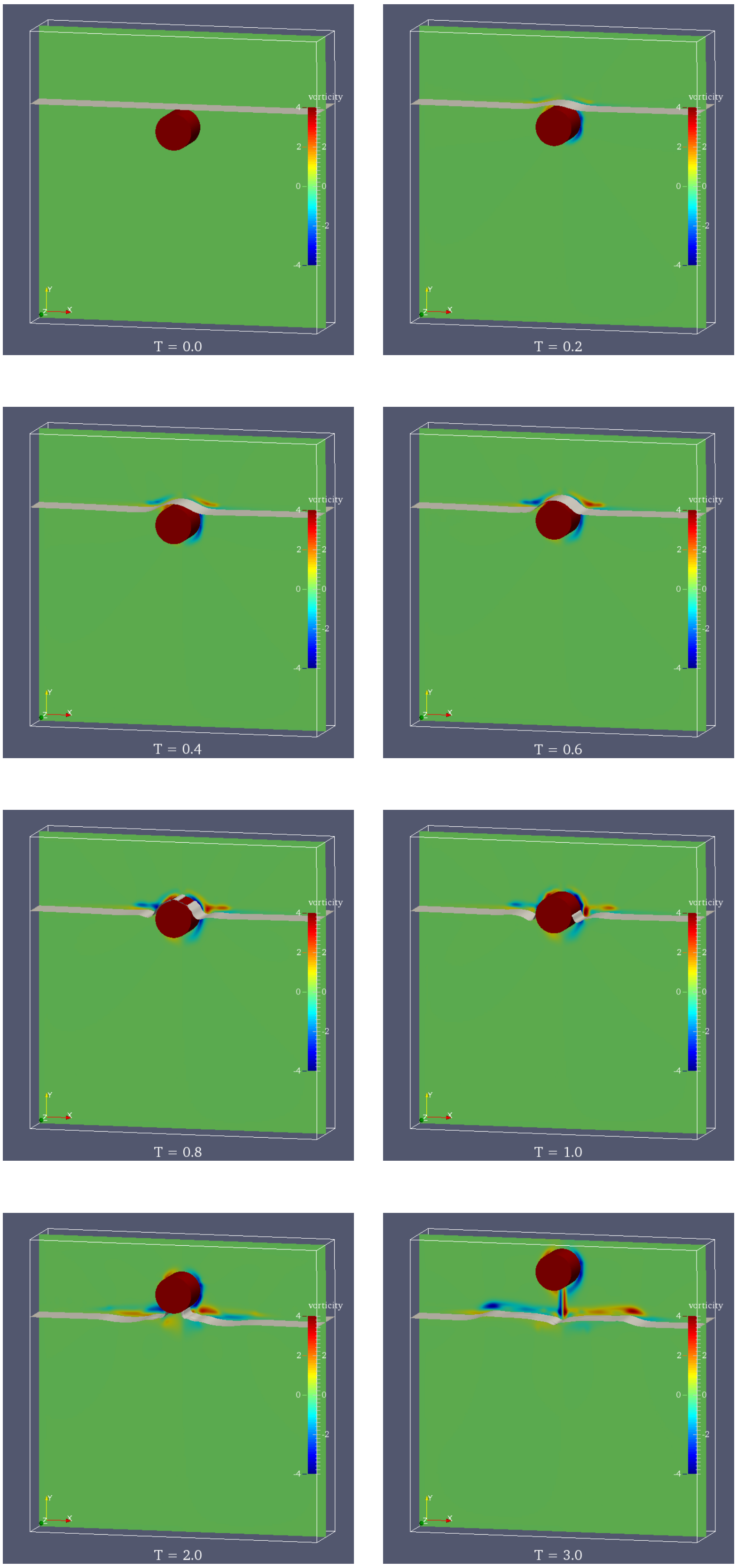

Figure 2.19: Water exit of a cylinder with vorticity contour.

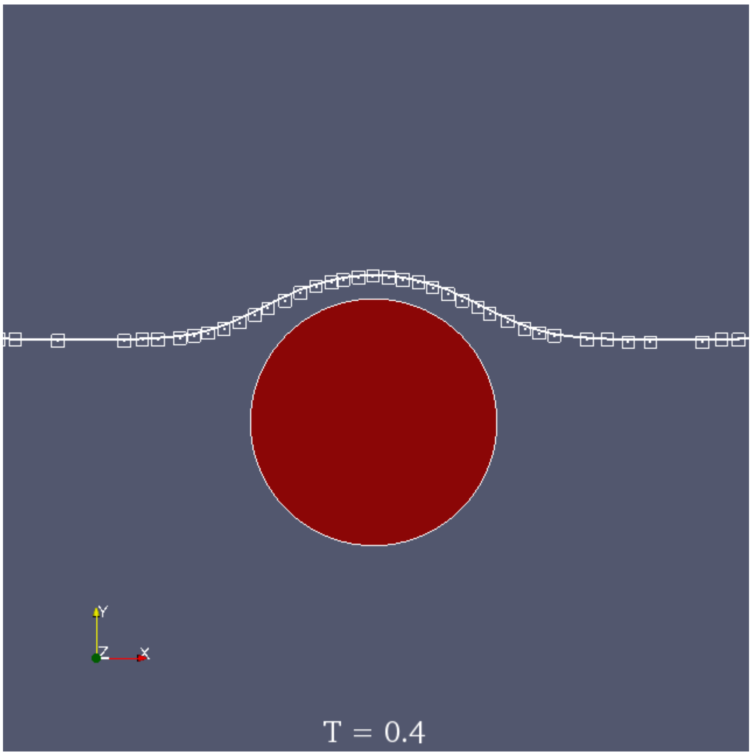

(a) $T = 0.4$

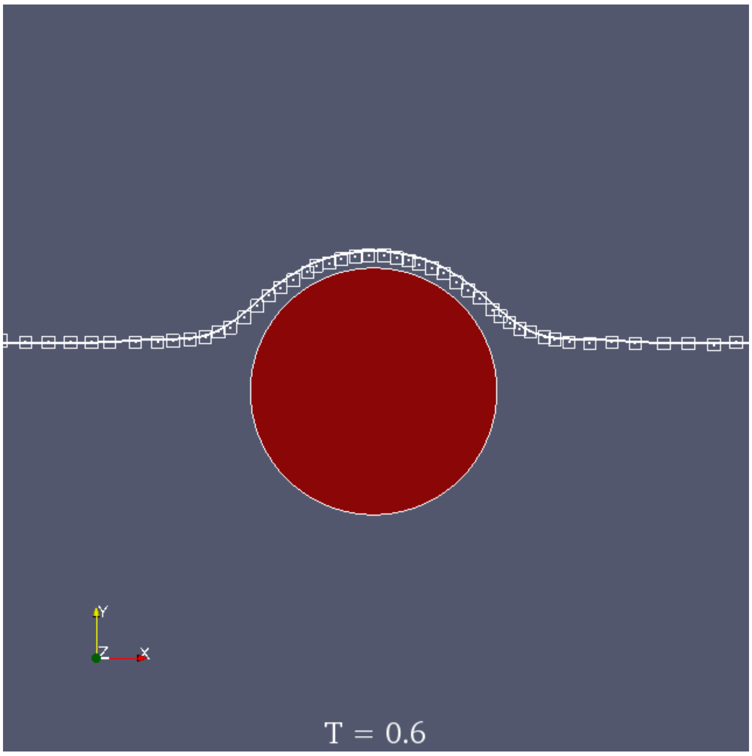

(b) $T = 0.6$

Figure 2.20: Water exit of cylinder: comparison of interface shapes.

2.6.4 Dam break flow

The dam break problem is a classical incompressible two-phase flow test case [53].

Conventional dam break

In this section, we first simulate a "standard" dam break flow in a 3D tank whose length, height and width are 1 m, 3 m and 2 m, respectively. The initial length and height of the reservoir are $a = 0.5$ m and $h = 2a$. Such a problem setup has been backed up by the experimental investigation of [54]. The water has density $\rho_l = 1000$ kg/m^3 and the air $\rho_g = 1$ kg/m^3, while their viscosities are $\mu_l = 0.001$ Pa s and $\mu_g = 10^{-5}$ Pa s. As usual the downward gravity is 9.8 m/s^2. Non-slip boundary conditions are applied to all walls except that the top of the tank is an outflow boundary. IB modeling is not activated for this problem.

Numerical simulations are computed using grids with different refinements: $20 \times 60 \times 40$, $30 \times 90 \times 60$ and $40 \times 120 \times 80$ cells. We have used the following non-dimensional quantities, see Figure 2.21.

$$\begin{aligned} \text{time } t^* &= t(2g/a)^{1/2} \\ \text{water front } z^* &= z/a \\ \text{dam height } y^* &= y/a \\ \text{pressure } p^* &= p/\rho g a \end{aligned}$$

As the simulation begins, the water dam will collapse under gravity and move along the floor. When it reaches the opposite wall, the splashed water rises high into the air. Figure 2.22 provides several snapshots showing the propagation and reflection of the water wave computed on the finest mesh.

The mesh-convergence behavior is demonstrated through Figure 2.23, in which the numerical solutions are compared at two different times before ($t^* = 2.505$) and after ($t^* = 3.757$) the arrival at the wall, respectively. Reasonable results have been obtained using all three grids. A general trend seems to be that both leading edge and rising tip of the water move faster on a fine mesh, but the overall difference between different grid refinements is not significant. Hence the current results are almost free of any grid dependency.

The computed positions of the leading front z^* at the floor and the receding edge y^* to the vertical wall before the impact are plotted against the non-dimensional time in Figures 2.24 and 2.25. Good agreements with the experimental data from Martin and Moyce [54] are apparent.

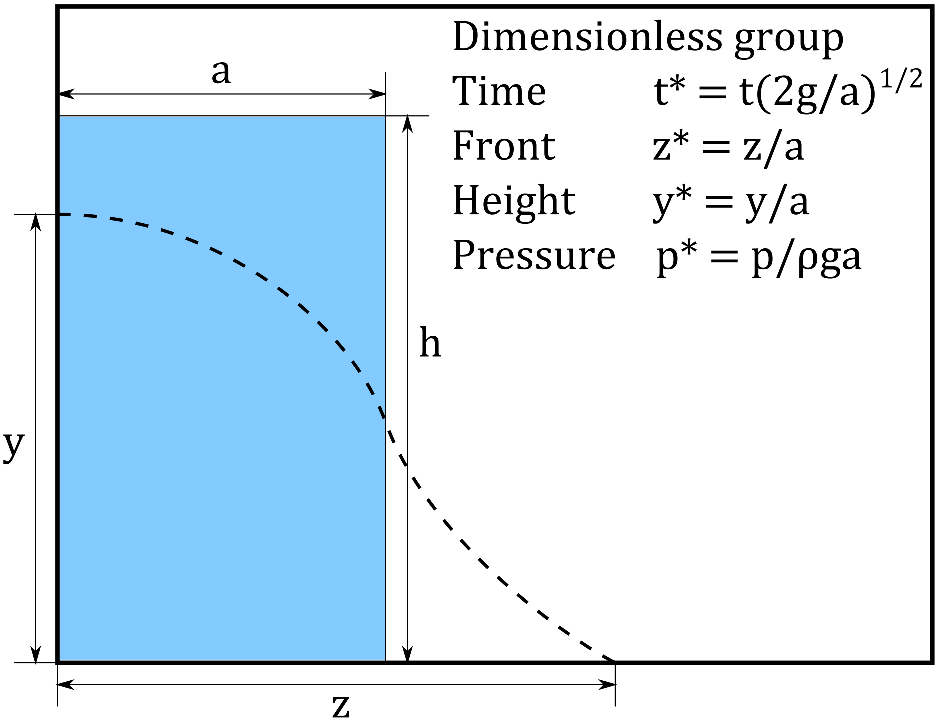

Figure 2.21: Schematic diagram of a dam break flow.

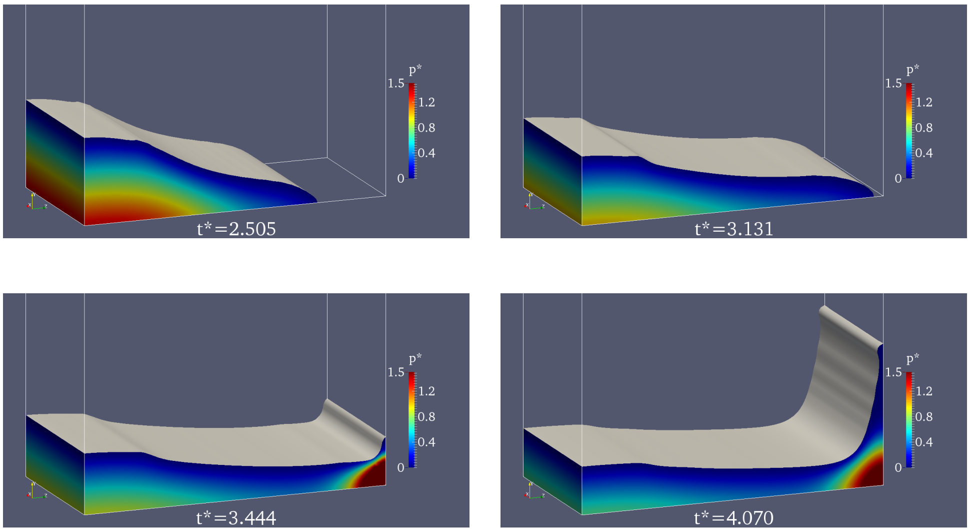

Figure 2.22: Dam break: snapshots of water surface and pressure contour.

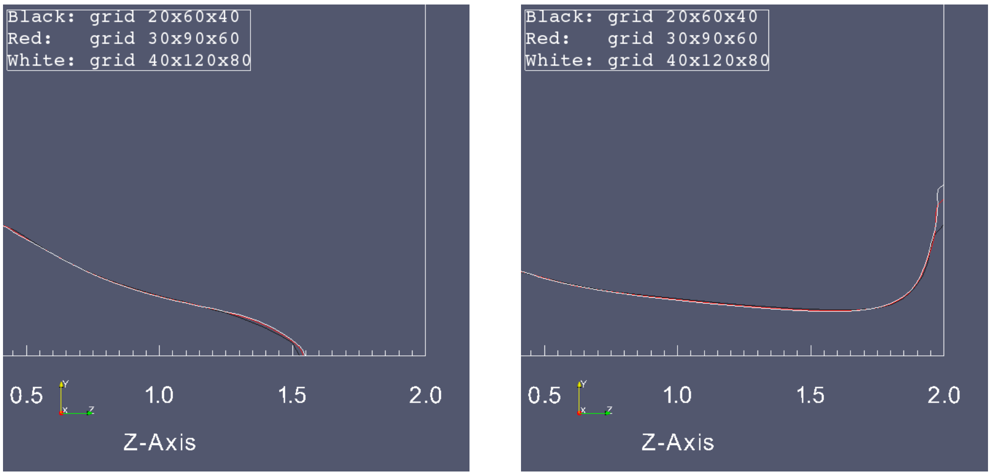

(a) $t^* = 2.505$

(b) $t^* = 3.757$

Figure 2.23: Dam break: comparison of interface shapes near the wave front with refinements.

Dam break with an obstacle

Next, we consider a more intense dam break problem in which the collapsing water hits on an obstacle before its impact against the wall. This test problem is suggested by Koshizuka et al. [55] and investigated therein both experimentally and numerically using a Lagrangian particle method. We follow the problem setup described in [55] and add a solid obstacle at the bottom of the tank. The obstacle is modeled by the IB method. We compute the solution with a uniform grid spacing $\Delta x = a/32$ and a fixed time step $\Delta t = 0.0001$ sec.

The calculated 3D fluid interface, colored by the velocity contour, is presented in Figure 2.26 at time instants $t = 0.2$, 0.3, 0.4 and 0.5 sec. Sliced views of these results are compared in Figure 2.27 with the experimental photographs[2]. We can see that the flow behavior has been drastically changed by the deflection at the obstacle. A strong, curved arm outspreads from the water body and flies towards the opposite wall ($t = 0.2$ and 0.3 sec). After the water arm hits the wall ($t = 0.4$ sec), a portion of air is trapped in the space enclosed by the water layer, tank and obstacle. As the water attached to the wall starts to fall ($t = 0.5$ sec), the air cushion is pushed to the obstacle side and tries to break through the water layer. At the same time,

---

[2] Experimental photographs are provided by courtesy of Professor Koshizuka.

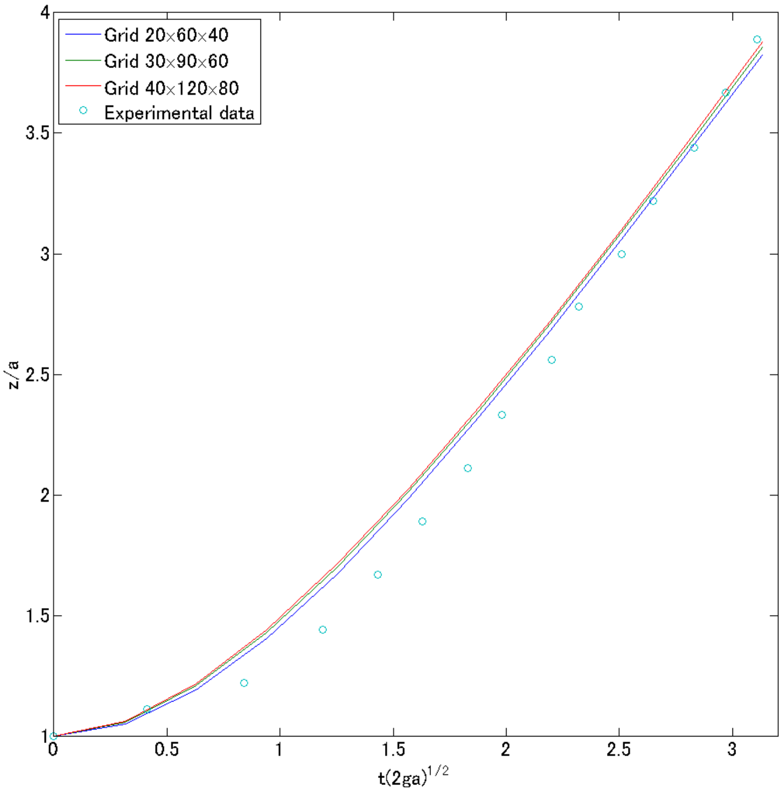

Figure 2.24: Dam break: time evolution of the water front at the bottom.

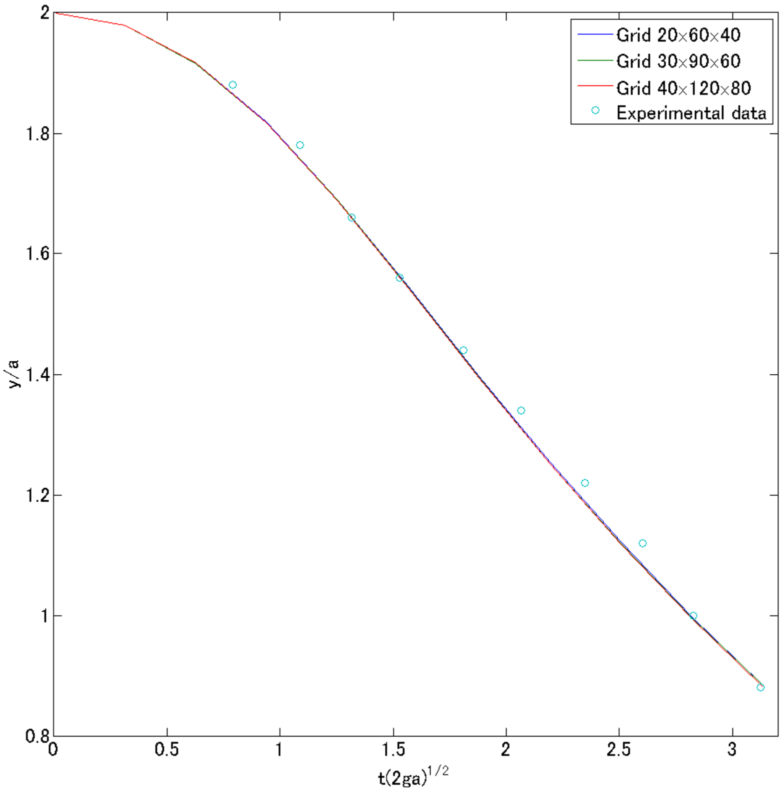

Figure 2.25: Dam break: time evolution of the water height at the wall.

a secondary water tip penetrates into the air region. From the comparative study in Figure 2.27, the computational results are likely to recover most interesting features in the experimental flow qualitatively, e.g. the water arm, impact against the wall, entrapment of air, deformation of water layer and the secondary water tip. On the other hand, some points less satisfactory may consist in flow details such as the splashing region above the water layer and the size of the secondary water tip.

Some differences could be found for the shape of the water tip at $t = 0.3$ sec. We are aware of this problem and ascribe its reason to the fact that in VOF- and LS-type interface capturing methods the motion of relatively thin jets, filaments and broken free surfaces with high density ratio is somehow prone to the accumulation of numerical errors depending on the grid resolution, discretization schemes (particularly the convection scheme) and boundary conditions adopted. As mentioned by some authors [56, 57], to some extent, discussion for such unsteady flow details is very hard and doubtful.

Figure 2.28 compares our simulation (the background picture) with other available VOF results. The triangular markers are the sketch of the jet shape in [58] which is calculated on octree-based adaptive grids by using a power law interpolation [59] for the convective term within a truncated domain at the top; the dots show the interface shape obtained with the opensource CFD software OpenFOAM[3] for which a fine mesh generation, an elongated computational domain and upwinded linear interpolation for the convection term have been used as the recommendation in its user document. The result of [58] generally conforms to the current one, while the OpenFOAM result is at a much leading position, which is plausibly explained for differences in their numerical aspects. Apart from those differences, the overall flow behavior has been satisfactorily recovered as shown in the comparison between simulation and experimental photographs.

---

[3] The OpenFOAM foundation, `http://www.openfoam.com/`.

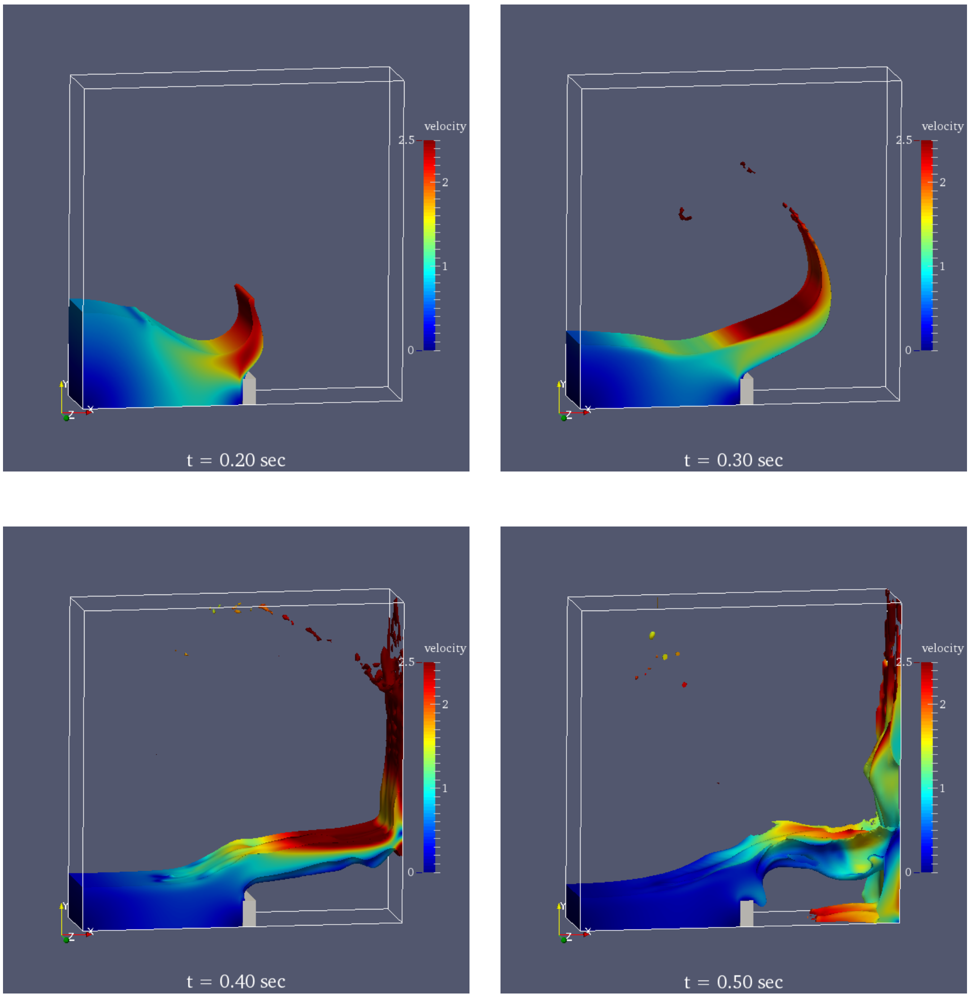

Figure 2.26: Dam break with an obstacle: free surface shape with velocity contour.

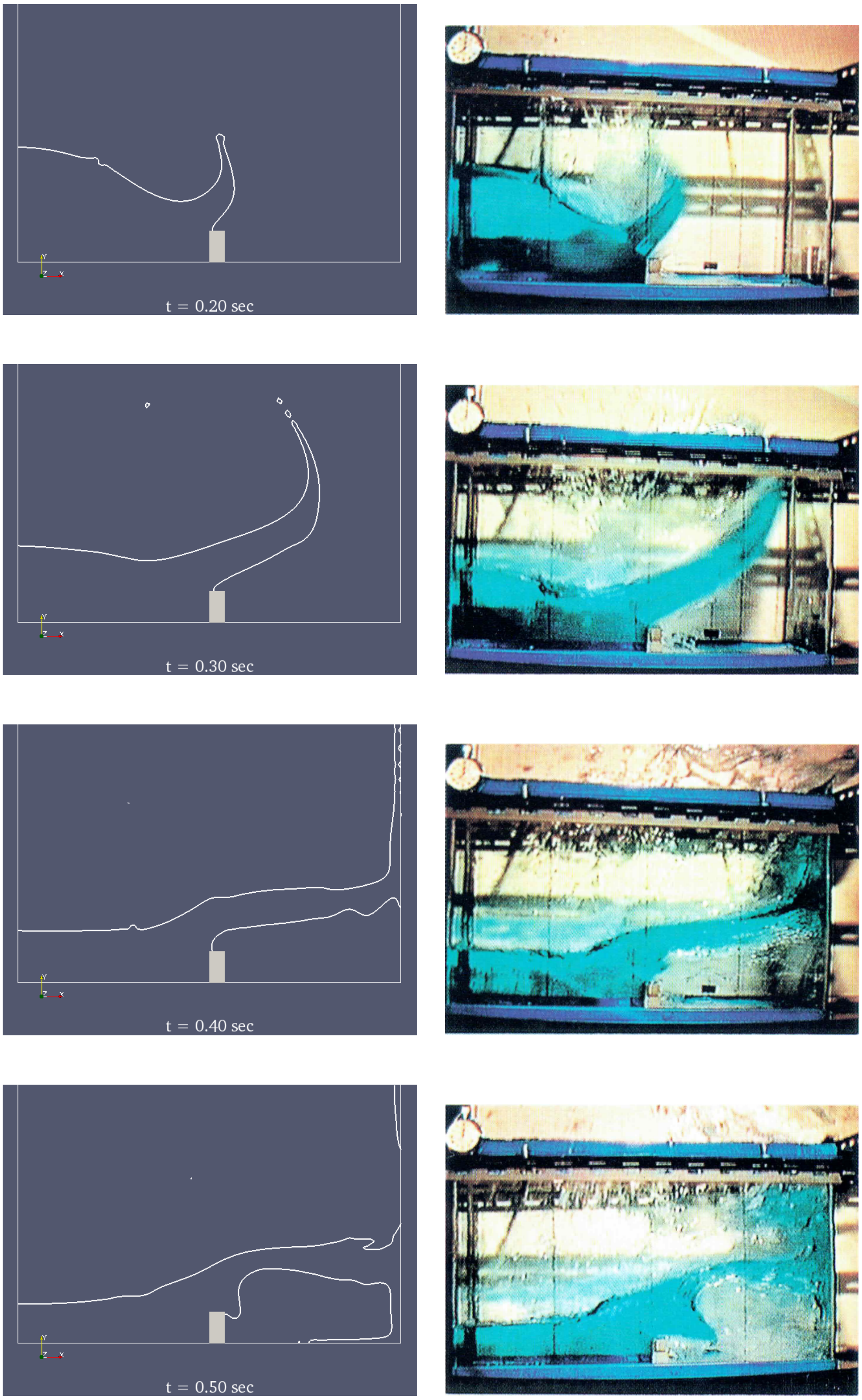

Figure 2.27: Dam break with an obstacle: comparison between the simulation (left column) and experiment [55] (right column).

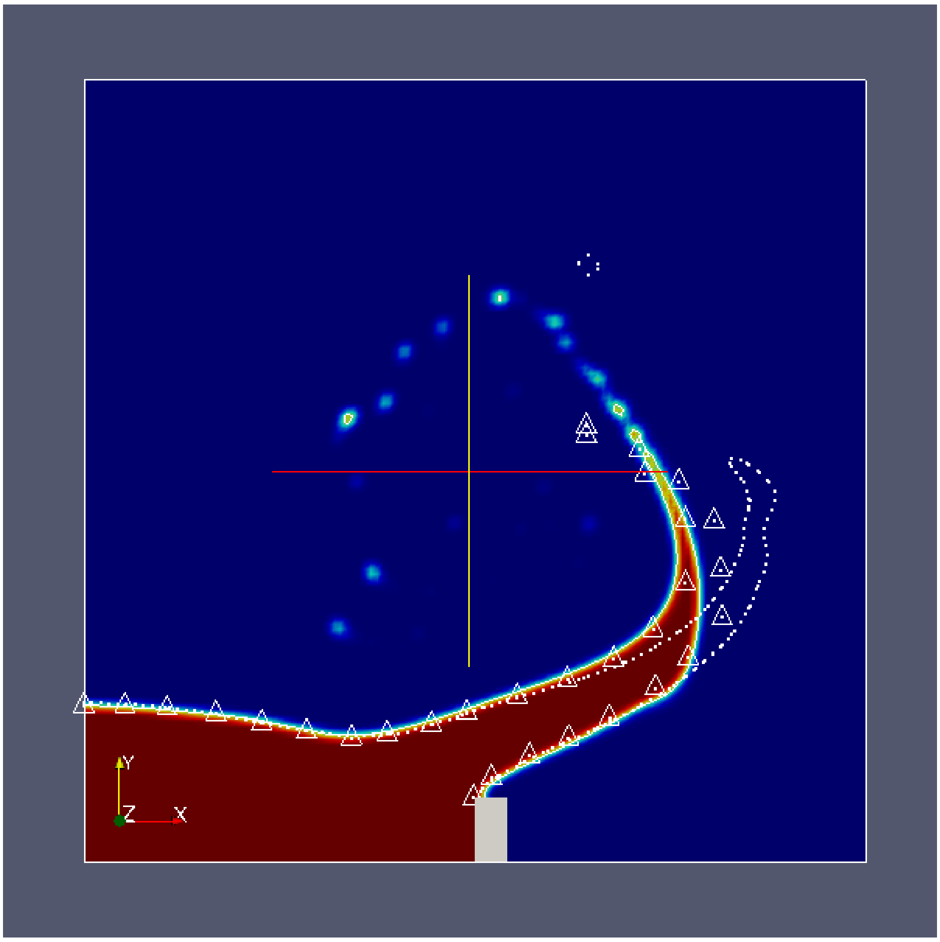

Figure 2.28: Comparison of jet shapes obtained in different studies. The background picture is the current VOF-IB simulation, the triangular marker is sketched up from [58] and the dots are results by the OpenFOAM solver.

2.6.5 Rotating elliptical paddles

The rotation of two ellipses in a water tank is numerically studied by [34] as a challenging test case with complicated behaviors of the free surface.

In this test, parameters similar to those given in [34] is used, but the problem setup is extruded to be a three-dimensional configuration. The computational domain is $4.0L \times 2.4L \times 2.4L$, and the reference length $L = 1.0$. The elliptical paddles have a semi-major axis of $0.9L$, semi-minor axis of $0.2L$, and a length $2L$. The constant angular velocity is $\omega = \pi/3$ rad/s for both paddles, but in opposite directions. The gravity is set to -9.8 m/s^2. The whole domain is discretized by using a grid of $80 \times 80 \times 48$ cells.

Figure 2.29 shows a series of three-dimensional snapshots of the air-water interface and velocity vectors under stirring of the elliptical paddles, for which the time is normalized by the rotation period $T = 2\pi/\omega$. A very noticeable phenomenon that takes place at $t/T = 0.25$ (and similarly at $t/T = 0.5$) is the upward jet caused by the squeeze between the paddle tip and the vertical wall, which is also observed in [34].

In order to further justify the current method, we compare the 3D simulation results with a reference solution obtained by using a 2D CLSVOF [13] code with direct forcing IB modeling [21]. This in-house code has been validated independently in many flow cases. The 2D simulation is performed using a much finer mesh of 320×192 cells. Their comparison is shown in Figure 2.30, in which the central plane of the 3D results are extracted for visualization. It is clearly seen that, although having a coarser resolution, the behavior of the fluid interface is still well predicted and the 3D results are in good agreement with the reference solution.

In the current 3D setup of the test problem, the liquid is allowed to escape through the gap between the paddles and the front and back walls, which does not occur for the 2D system. This difference helps balance the surface position in the 3D case and thus brings in some dimensional effects: (a) before captured by the downward moving ellipse tip, the water level between the paddle and the wall is higher than the 2D case (e.g. between the right side wall and paddle at $t/T = 0.4$) and (b) the liquid jets are weaker than their 2D counterparts (e.g. near the vertical walls at $t/T = 0.25$ and 0.5).

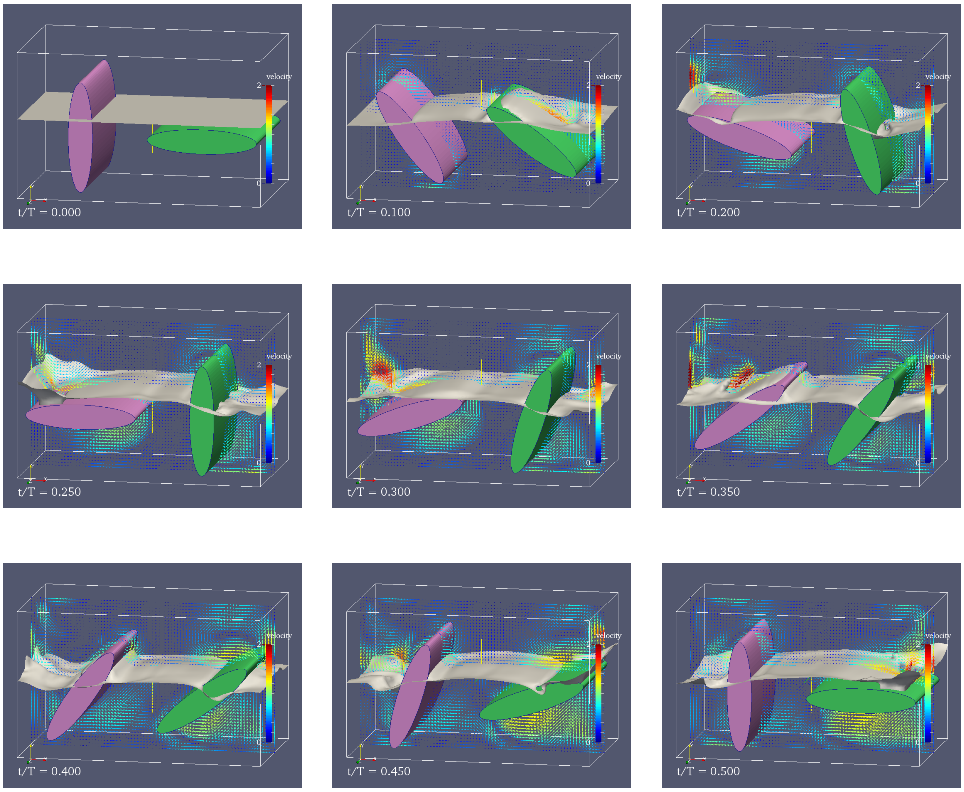

Figure 2.29: Rotating paddles: free surface with velocity vectors.

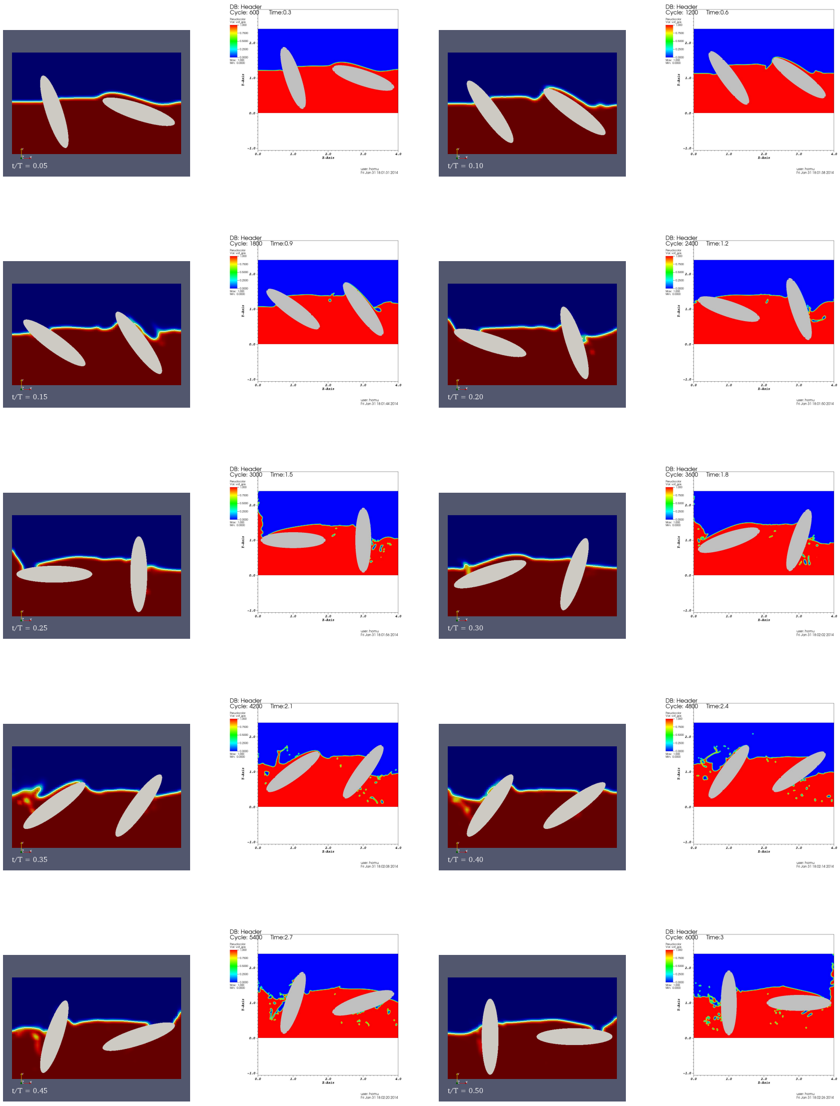

Figure 2.30: Rotating paddles: the present 3D VOF (left) vs. 2D CLSVOF solution (right).

2.7 Conclusions

In this study, we developed a numerical method for three-dimensional simulation of two-phase flows in complex geometries. The overall algorithm is based on the VOF method for two-phase flows and the IB modeling of wall boundaries. The shape and movement of general geometries are represented by an auxiliary level set function with local coordinate transformation. Numerical schemes are presented in detail to solve the interface advection, incompressible fluid dynamics, and the interaction with walls and moving objects. In addition, we describe and test two different ways to satisfy the 90° contact angle boundary condition. They are both usable and easy to implement in three-dimension.

Various numerical tests have been performed to validate the present method. They contains steady flow problems for grid convergence and wall contact (concave surface in rotating barrel and relaxation of rods to a state of rest), dynamic flow driven by moving objects (water exit of a cylinder), violent air-water flow (dam break without/with an obstacle) and complicated interactions with arbitrary shapes and movements (rotating elliptical paddles). The calculated results have been compared with known reference solutions and experimental data. Good agreements justify our numerical modeling. Hence, the numerical method developed in this study is shown to be suitable for simulating two-phase flows in complex geometries.

Bibliography

[1] F. H. Harlow and J. E. Welch, “Numerical Calculation of Time-Dependent Viscous Incompressible Flow of Fluid with Free Surface,” *Physics of Fluids*, vol. 8, p. 2182, 1965.

[2] S. O. Unverdi and G. Tryggvason, “A front-tracking method for viscous, incompressible, multi-fluid flows,” *Journal of Computational Physics*, vol. 100, no. 1, pp. 25–37, 1992.

[3] T. Yabe, F. Xiao, and T. Utsumi, “The Constrained Interpolation Profile Method for Multiphase Analysis,” *Journal of Computational Physics*, vol. 169, pp. 556–593, 2001.

[4] C. Hirt and B. Nichols, “Volume of fluid (VOF) method for the dynamics of free boundaries,” *Journal of Computational Physics*, vol. 39, no. 1, pp. 201–225, 1981.

[5] M. Sussman, P. Smereka, and S. Osher, "A Level Set Approach for Computing Solutions to Incompressible Two-Phase Flow," *Journal of Computational Physics*, vol. 114, no. 1, pp. 146–159, 1994.

[6] W. F. Noh and P. Woodward, *Proceedings of the Fifth International Conference on Numerical Methods in Fluid Dynamics June 28 — July 2, 1976 Twente University, Enschede*, vol. 59 of *Lecture Notes in Physics*. Berlin, Heidelberg: Springer Berlin Heidelberg, 1976.

[7] D. L. Youngs, "Time-dependent multi-material flow with large fluid distortion," *Numerical methods for fluid dynamics*, vol. 24, pp. 273–285, 1982.

[8] M. Rudman, "Volume-tracking methods for interfacial flow calculations," *International Journal for Numerical Methods in Fluids*, vol. 24, pp. 671–691, 1997.

[9] J. E. Pilliod and E. G. Puckett, "Second-order accurate volume-of-fluid algorithms for tracking material interfaces," *Journal of Computational Physics*, vol. 199, pp. 465–502, 2004.

[10] K. Yokoi, "Efficient implementation of THINC scheme: A simple and practical smoothed VOF algorithm," *Journal of Computational Physics*, vol. 226, no. 2, pp. 1985–2002, 2007.

[11] D. Gueyffier, J. Li, A. Nadim, R. Scardovelli, and S. Zaleski, "Volume-of-Fluid Interface Tracking with Smoothed Surface Stress Methods for Three-Dimensional Flows," *Journal of Computational Physics*, vol. 152, no. 2, pp. 423–456, 1999.

[12] M. Rudman, "A volume-tracking method for incompressible multifluid flows with large density variations," *International Journal for Numerical Methods in Fluids*, vol. 28, pp. 357–378, 1998.

[13] M. Sussman and E. G. Puckett, "A Coupled Level Set and Volume-of-Fluid Method for Computing 3D and Axisymmetric Incompressible Two-Phase Flows," *Journal of Computational Physics*, vol. 162, no. 2, pp. 301–337, 2000.

[14] S. Osher and R. Fedkiw, *Level Set Methods and Dynamic Implicit Surfaces(Google eBook)*. Springer, 2002.

[15] M. Sussman, E. Fatemi, P. Smereka, and S. Osher, "An improved level set method for incompressible two-phase flows," *Computers & Fluids*, vol. 27, no. 5, pp. 663–680, 1998.

[16] R. Mittal and G. Iaccarino, “Immersed boundary methods,” *Annual Review of Fluid Mechanics*, 2005.

[17] C. S. Peskin, “Numerical analysis of blood flow in the heart,” *Journal of Computational Physics*, vol. 25, pp. 220–252, 1977.

[18] C. S. Peskin, “The immersed boundary method,” *Acta Numerica*, vol. 11, pp. 479–517, 2002.

[19] M. Uhlmann, “An immersed boundary method with direct forcing for the simulation of particulate flows,” *Journal of Computational Physics*, vol. 209, pp. 448–476, 2005.

[20] K. Taira and T. Colonius, “The immersed boundary method: A projection approach,” *Journal of Computational Physics*, vol. 225, pp. 2118–2137, 2007.

[21] E. Fadlun, R. Verzicco, P. Orlandi, and J. Mohd-Yusof, “Combined Immersed-Boundary Finite-Difference Methods for Three-Dimensional Complex Flow Simulations,” *Journal of Computational Physics*, vol. 161, pp. 35–60, 2000.

[22] T. Kajishima, S. Takiguchi, H. Hamasaki, and Y. Miyake, “Turbulence Structure of Particle-Laden Flow in a Vertical Plane Channel Due to Vortex Shedding,” *JSME International Journal Series B*, vol. 44, pp. 526–535, 2001.

[23] T. Kajishima and S. Takiguchi, “Interaction between particle clusters and particle-induced turbulence,” *International Journal of Heat and Fluid Flow*, vol. 23, pp. 639–646, 2002.

[24] S.-Y. Lin, Y.-H. Chin, J.-J. Hu, and Y.-C. Chen, “A pressure correction method for fluid-particle interaction flow: Direct-forcing method and sedimentation flow,” *International Journal for Numerical Methods in Fluids*, vol. 67, pp. 1771–1798, 2011.

[25] J.-I. Choi, R. C. Oberoi, J. R. Edwards, and J. A. Rosati, “An immersed boundary method for complex incompressible flows,” *Journal of Computational Physics*, vol. 224, pp. 757–784, 2007.

[26] J. Yang and E. Balaras, “An embedded-boundary formulation for large-eddy simulation of turbulent flows interacting with moving boundaries,” *Journal of Computational Physics*, vol. 215, pp. 12–40, 2006.

[27] T. Ikeno and T. Kajishima, "Finite-difference immersed boundary method consistent with wall conditions for incompressible turbulent flow simulations," *Journal of Computational Physics*, vol. 226, pp. 1485–1508, 2007.

[28] K. Kleefsman, G. Fekken, A. Veldman, B. Iwanowski, and B. Buchner, "A Volume-of-Fluid based simulation method for wave impact problems," *Journal of Computational Physics*, vol. 206, pp. 363–393, 2005.

[29] P. Lin, "A fixed-grid model for simulation of a moving body in free surface flows," *Computers & Fluids*, vol. 36, pp. 549–561, 2007.

[30] S.-Y. Lin and Y.-C. Chen, "A pressure correction-volume of fluid method for simulations of fluid—particle interaction and impact problems," *International Journal of Multiphase Flow*, vol. 49, pp. 31–48, 2013.

[31] P. A. Cundall and O. D. L. Strack, "A discrete numerical model for granular assemblies," *Géotechnique*, vol. 29, no. 1, pp. 47–65, 1979.

[32] M. Sussman, "An Adaptive Mesh Algorithm for Free Surface Flows in General Geometries," in *Adaptive Method of Lines* (A. Vande Wouwer, P. Saucez, and W. Schiesser, eds.), Chapman and Hall/{CRC}, 2001.

[33] M. Sussman, "A parallelized, adaptive algorithm for multiphase flows in general geometries," *Computers & Structures*, vol. 83, pp. 435–444, 2005.

[34] J. Yang and F. Stern, "Sharp interface immersed-boundary/level-set method for wave—body interactions," *Journal of Computational Physics*, vol. 228, pp. 6590–6616, 2009.

[35] H. S. Yoon, C. H. Jeon, J. H. Jung, B. Koo, C. Choi, and S. C. Shin, "Simulation of two-phase flow-body interaction problems using direct forcing/fictitious domain-level set method," *International Journal for Numerical Methods in Fluids*, vol. 73, pp. 250–265, 2013.

[36] G. Son, "A level set method for incompressible two-fluid flows with immersed solid boundaries," *Numerical Heat Transfer, Part B: Fundamentals*, vol. 47, pp. 473–489, 2005.

[37] K. Yokoi, "Numerical Method for Interaction Among Multi-particle, Fluid and Arbitrary Shape Structure," *Journal of Scientific Computing*, vol. 46, pp. 166–181, 2010.

[38] M. Arienti and M. Sussman, “An embedded level set method for sharp-interface multiphase simulations of Diesel injectors,” *International Journal of Multiphase Flow*, vol. 59, pp. 1–14, 2014.

[39] D. B. Spalding, “A novel finite difference formulation for differential expressions involving both first and second derivatives,” *International Journal for Numerical Methods in Engineering*, vol. 4, pp. 551–559, 1972.

[40] Y. Shigeto and M. Sakai, “Arbitrary-shaped wall boundary modeling based on signed distance functions for granular flow simulations,” *Chemical Engineering Journal*, vol. 231, pp. 464–476, 2013.

[41] Y. Yamada and M. Sakai, “Lagrangian—Lagrangian simulations of solid—liquid flows in a bead mill,” *Powder Technology*, vol. 239, pp. 105–114, 2013.

[42] X. Sun, M. Sakai, and Y. Yamada, “Three-dimensional simulation of a solid—liquid flow by the DEM—SPH method,” *Journal of Computational Physics*, vol. 248, pp. 147–176, 2013.

[43] X. Sun, M. Sakai, M.-T. Sakai, and Y. Yamada, “A Lagrangian—Lagrangian coupled method for three-dimensional solid—liquid flows involving free surfaces in a rotating cylindrical tank,” *Chemical Engineering Journal*, vol. 246, pp. 122–141, 2014.

[44] Z. Wang, J. Yang, and F. Stern, “A simple and conservative operator-splitting semi-Lagrangian volume-of-fluid advection scheme,” *Journal of Computational Physics*, vol. 231, pp. 4981–4992, 2012.

[45] S. T. Zalesak, “Fully multidimensional flux-corrected transport algorithms for fluids,” *Journal of Computational Physics*, vol. 31, pp. 335–362, 1979.

[46] W. J. Rider and D. B. Kothe, “Reconstructing Volume Tracking,” *Journal of Computational Physics*, vol. 141, pp. 112–152, 1998.

[47] J. Brackbill, D. Kothe, and C. Zemach, “A continuum method for modeling surface tension,” *Journal of Computational Physics*, vol. 100, pp. 335–354, 1992.

[48] T. Yabe, K. Chinda, and T. Hiraishi, “Computation of surface tension and contact angle and its application to water strider,” *Computers & Fluids*, vol. 36, pp. 184–190, 2007.

[49] M. Sussman, K. Smith, M. Hussaini, M. Ohta, and R. Zhi-Wei, "A sharp interface method for incompressible two-phase flows," *Journal of Computational Physics*, vol. 221, pp. 469–505, 2007.

[50] J. Keating and P. D. Minev, "A fast algorithm for direct simulation of particulate flows using conforming grids," *Journal of Computational Physics*, vol. 255, pp. 486–501, 2013.

[51] Y. Wang, S. Simakhina, and M. Sussman, "A hybrid level set-volume constraint method for incompressible two-phase flow," *Journal of Computational Physics*, vol. 231, pp. 6438–6471, 2012.

[52] M. Greenhow and S. Moyo, "Water entry and exit of horizontal circular cylinders," *Philosophical Transactions of the Royal Society A: Mathematical, Physical and Engineering Sciences*, vol. 355, pp. 551–563, 1997.

[53] O. Mahrenholtz and M. Markiewicz, *Nonlinear water wave interaction.* WIT Press, 1999.

[54] J. C. Martin and W. J. Moyce, "Part IV. An Experimental Study of the Collapse of Liquid Columns on a Rigid Horizontal Plane," *Philosophical Transactions of the Royal Society A: Mathematical, Physical and Engineering Sciences*, vol. 244, pp. 312–324, 1952.

[55] S. Koshizuka, H. Tamako, and Y. Oka, "A particle method for incompressible viscous flow with fluid fragmentation," *Computational Fluid Dynamic Journal*, vol. 4, pp. 29–46, 1995.

[56] H. Wang, Y. Leng, Z. Wang, and X. Wu, "Application of image correction and bit-plane fusion in generalized PCA based face recognition," *Pattern Recognition Letters*, vol. 28, pp. 2352–2358, 2007.

[57] T. Ménard, S. Tanguy, and A. Berlemont, "Coupling level set/VOF/ghost fluid methods: Validation and application to 3D simulation of the primary break-up of a liquid jet," *International Journal of Multiphase Flow*, vol. 33, pp. 510–524, 2007.

[58] D. M. Greaves, "Simulation of viscous water column collapse using adapting hierarchical grids," *International Journal for Numerical Methods in Fluids*, vol. 50, pp. 693–711, 2006.

[59] J. H. Ferziger and M. Peric, *Computational Methods for Fluid Dynamics.* Berlin, Heidelberg: Springer Berlin Heidelberg, 3rd ed., 2001.

Chapter 3

The DEM-VOF method for three-phase flow simulation

3.1 Introduction

3.1.1 Background and related work

Gas-solid-liquid flows are widely encountered in chemical engineering. In particular, the motivation for our research focus is the pressing requirement for modeling gas-solid-liquid flows in wet ball/beads milling systems and twin screw kneaders (TSKs). In these problems, the complicated phenomena will restrict the observation and insight that could be obtained with experimental approaches. On the other hand, one may rely on accurate numerical simulations from which useful information could be extracted to help improve the designing and operating procedures.

For gas-solid-liquid flow problems, the numerical challenges mainly arise from interactions among different phases. Basically, a typical gas-solid-liquid flow involves fluid-fluid interaction (evolving fluid interface), fluid-solid interaction (fluid-particle momentum exchange), and solid-solid interaction (particle-particle collision). In addition, the influence of arbitrary-shaped geometries and moving boundaries must be taken into consideration for practical simulations. Prior to a systematic approach to complete gas-solid-liquid problems, some fundamental techniques have been established to solve those sub-problems independently.

Fluid-fluid interaction A variety of numerical models have been developed to describe the motion of two-phase flows separated by immiscible fluid interfaces, e.g. the volume-of-fluid (VOF) method [1] , the level set (LS) method [2], the coupled LS and VOF (CLSVOF) method [3], the front-tracking (FT) method [4] and the constrained interpolation profile (CIP) method [5]. Those interfacial models are known to have their own features and limitations, which has been discussed in the literatures.

Solid-solid interaction The discrete element method (DEM) [6] or the discrete particle model (DPM) is now a common practice to simulate powder and granular materials. Its numerical strategy by directly tracking distinct particle motion allows for specific particle properties and exact evaluation of solid forces. Due to the huge amount of particles in real-world industrial problems and a relatively limited computational capability and resources, the coarse grain model (CGM) has been proposed to release computational efforts by different authors, see [7–10].

Interaction with wall boundary The immersed boundary (IB) method [11–13] can efficiently model complex geometries non-conforming to the fluid grids, which has greatly alleviated the time-consuming mesh generation and regridding procedures in traditional computational fluid dynamics (CFD) techniques. On the other hand, DEM-type particle simulations usually adopt mesh-based models as is the exact wall shape. Recently, the author 's group has proposed an arbitrary-shaped wall boundary model [14] based on signed distance function (SDF) which can offer a unified wall boundary representation for both fluid and particle simulations.

When it comes to the numerical analysis of more complex, coupled gas-solid-liquid flow systems, two classes of approaches have been employed so far: the DNS and the local volume-averaging technique, of which the former intends to resolve microscopic flow behaviors and the latter mainly focuses on macroscopic average flow problems. As opposed to the DNS that requires fine grids to resolve all relevant flow structures, the volume-averaging approach is less computationally demanding and thus it could be an affordable and pragmatic choice for simulating large-scale systems. The volume-averaging approach has its theoretical origin in the famous two-fluid model (TFM) [15, 16], where a spatial filtering operation is applied to the mixture system and the interaction between two distinct phases is calculated based on empirical correlations.

At present, the DEM-CFD method is among the most popular and successful numerical techniques for simulating fluid-solid flows based on a volume-averaging approach. In the DEM-CFD method, The discrete particle phase is simulated by DEM-type particle-tracing Lagrangian methods and the fluid phase is computed on Eulerian meshes by using CFD. Hence such a coupling method is said to be an Eulerian-Lagrangian methodology. Compared with traditional TFM Eulerian description, this combination can overcome the analytical and numerical difficulties when modeling dense solid beds. The DEM-CFD method is now widely used to simulate solid-gas and solid-liquid fluidization systems. Review of DEM-CFD simulations of fluidized beds could be found in [17–19].

Despite the successful application of the volume-averaging Eulerian-Lagrangian model to two-phase fluidization systems, its power is not fully explored for gas-solid-liquid three-phase flows. Zhang and Ahmadi [20] performed 2D simulation of slurry bubble columns in which motions and trajectories of disperse phases (bubbles and particles) are calculated by Lagrangian analysis procedure. As a result, there arises a dependency on empirical closure model to define the fluid-bubble interaction. Wen et al. [21] described an interesting approach to model large-scale three-phase fluidization systems by combining DEM for particle phase and TFM for bubbly flows, where liquid-bubble interaction still relies on constitutive correlations. The fluid-particle momentum exchange is seemingly not balanced as different drag closures have been adopted in continuum and disperse phases separately. Additionally, their formulation is provided for axisymmetric coordinate but the DEM particle model is ambiguous in that case.

Fan's group has contributed some important results to the simulation of three-phase fluidization systems with direct computation of bubble motions. In [22–25], the authors proposed a 2D method combining the VOF method and a hard-sphere DPM in which a special close-distance interaction (CDI) model is included in the particle-particle collision process. Unfortunately, their formulation of gas-solid-liquid fluidization suffers from an inconsistent fluid-particle interaction model, as pointed out by [26]. Later in their 3D studies [27, 28], the LS method is used instead of the VOF method for the interface description. A review of their studies on gas-liquid-solid fluidized beds and bubble formation from nozzle in three-phase system is given by [29].

A combination of FT method and hard-sphere DPM has been proposed in [30] to simulate bubble rising and particle entrainment. However their study is restricted to the case of dilute particle suspensions (up to maximum 4% solid volume fraction) where the influence to fluid phase is not appreciable. The authors of [31] incorporated distinct particle tracing into a commercial VOF package for simulation of microchannel flows. Although the fluid-particle interaction is considered to be balanced, the interactions among solid particles are not included in their implementation. In [32] a DEM-CIP coupling method is developed to calculate liquid droplet impingement on powder bed. They described a sub-grid scale model for the capillary action when the fluid interface penetrates into the solid layer, and the authors argued that this modeling can compensate the overestimated pushing effect due to drag force during the granular wetting process.

As briefly reviewed above, previous studies are found within a rather limited scope. Many of them are simple DEM-CFD extensions to three-phase fluidization systems in dilute regime. Particularly, we wish to identify several points that may obstruct the application to real engineering problems.

- First of all, more or less flaws could be found in many models concerning the formulation of the fluid-particle interaction term. This problem exists especially for some relatively early attempts, e.g. the VOF-DPM method by [22]. It is no coincidence that such a model fails to verify the momentum balance between continuum and disperse phases.

- Secondly, it is not clearly documented in the past how the free surface behaves in response to the particle motion. For example, in mixing processes involving water entry and exit of solids, common issues are to model the deformation of the free surface disturbed by particles and the water displacement of the solid phase, of which the former is mainly credited with the dynamic fluid-particle interaction and the latter corresponds to the overall volume conservation property of the numerical approach. These vital considerations are, however, incidentally lacking in previous studies. Therefore the applicability of existing models to recover the macroscopic behavior of gas-solid-liquid flows in such problems is unknown.

- Lastly, it is found that no general geometries other than a simple rectangular computational domain have ever been treated throughout our literature survey. This means that the existing models cannot simulate three-phase flows interacting with curved geometries or moving parts widely encountered in engineering applications. One must be aware that, there is no trivial solution to this point because the influence of general geometries is an essential aspect in gas-solid-liquid flow modeling, which is extensively involved in respects of fluid-fluid (contact line and angle on wall surface), solid-solid (particle-structure collision) and fluid-solid (interphase coupling term) interactions.

3.1.2 Developments in this study

In this study, we developed a novel Eulerian-Lagrangian coupling method for the numerical simulation of gas-solid-liquid flows. The proposed model is referred to as the DEM-VOF method. The continuum fluid phase composed of two immiscible fluids separated by a fluid interface is simulated by using a WLIC/THINC VOF scheme [33] which is able to offer a simple implementation, good volume conservation property and capability to treat topological change of interface shapes. The particle phase is tracked by the DEM as discrete entities, which allows for exact evaluation of solid collisions in the system. The fluid and solid phases are coupled by the volume-averaging technique wherein the calculation of fluid-particle interaction is based on the empirical closure for the description of hydrodynamic forces. The present method enables modeling of complex geometries by incorporating the IB method [12, 34] with SDF representation of arbitrary wall shapes [14]. Necessary adaptations when applying the IB method to gas-solid-liquid flows are also noted in the paper.

Special efforts have been made to address the aforementioned problems in the present numerical method. Compared with existing models, the DEM-VOF method is thought to have the originalities as follows. Firstly, its formulation is based on the consistent model equations by [35] and the fluid-particle interaction term is carefully distributed to balance the interphase momentum exchange. Next, it is able to accurately predict the macroscopic behavior of three-phase flow systems including large deformation of the free surface and motion of the solid bed, as well as the liquid displacement of submerged solids. Finally, the ability to model arbitrary-shaped wall boundaries has distinguished it from all other competitive methods by allowing practical simulations in chemical engineering.

Prior to the main results, model verification is performed to justify the interphase coupling in the DEM-VOF method. After that, it is validated against various gas-solid-liquid flow problems. The water entry of a particle block is first simulated to examine the interface advancement and overall volume conservation property. Next simulation results are presented for a three-phase dam break flow, which is a dynamic system involving violent free surface and particle motions. In the third test, the DEM-VOF method is applied to the quasi-steady gas-solid-liquid flow in a rotating cylindrical tank. This problem is provided as a validation test for modeling of curved boundaries in constant motion. We will talk about the special treatments required by this deceptively “simple” system to correctly compute the fluid-particle interaction, which is conceived as prerequisites for our ongoing research towards more complicated three-phase problems. By comparing the simulation results with reference solution and experimental data, we have obtained good agreements for all validation tests in respect of the macroscopic behaviors of the three-phase flow system. Finally, we present its application to gas-liquid flows within a laboratory twin screw kneader as an example involving highly complex geometries and rotating parts.

In this way, the novelty of this study is highlighted by the good applicability to real gas-solid-liquid problems involving complex fluid-particle motions and general geometries. To the authors' best knowledge, *the present method is the first report which successfully couples the DEM to a VOF solver and offers support for non-trivial wall boundaries.*

3.2 Model specification

In this section, theoretical model equations are described individually for an Eulerian-Lagrangian model of a gas-solid-liquid flow system involving general geometries. Some fundamental concepts are then introduced to facilitate a primary understanding of the present model.

3.2.1 Particle motion equations

According to the Newton's law of motion, the following equations describe the translational and rotational motions of a spherical particle immersed in fluid:

$$m_p \frac{\mathrm{d}\boldsymbol{v}}{\mathrm{d}t} = \boldsymbol{F}^C + m_p \boldsymbol{g} + V_p \nabla \cdot \sigma + \boldsymbol{F}^S + \boldsymbol{F}^p \ , \tag{3.1}$$

$$I_p \frac{\mathrm{d}\boldsymbol{\omega}}{\mathrm{d}t} = \boldsymbol{T}^C \ . \tag{3.2}$$

Herein on the left-hand side, m_p, $\boldsymbol{v}$, I_p and $\boldsymbol{\omega}$ are the particle mass, velocity, moment of inertia and angular velocity; on the right-hand side, V_p is the particle volume, and $\boldsymbol{F}^c$, $\boldsymbol{g}$, σ, $\boldsymbol{F}^s$, $\boldsymbol{F}^p$ and $\boldsymbol{T}^c$ stand for the actions of contact force, gravity, fluid stress, surface tension, fluid-particle interaction force and torque of contact force, respectively.

Basically the fluid stress action is separable to be a pressure gradient term and a viscous stress part [36]:

$$V_p \nabla \cdot \sigma = -V_p \nabla p + V_p \nabla \cdot \tau \ , \tag{3.3}$$

where p is the pressure and τ is the deviatoric viscous stress tensor of the fluid. The far-field pressure gradient actually includes (but not limited to) the buoyant effect counteracting the particle gravity. The viscous stress part is often dropped from numerical modeling because of the negligible effect of viscosity in most fluidization systems, see e.g. [26], which gives that

$$V_p \nabla \cdot \sigma \approx -V_p \nabla p \ , \tag{3.4}$$

Our numerical test also displayed affirmative results to this convention[1], so it is respected in the present study.

$\boldsymbol{F}^s$ corresponds to the capillary force induced by the curved gas-liquid interface, whose effect is integrated as a part of the total fluid stress. Its modeling will be further explained in subsequent sections.

The fluid-particle interaction $\boldsymbol{F}^p$ may contains various coupling terms such as the drag, lift and virtual mass forces. The fluid drag force is relatively dominant while the other hydrodynamic forces are sometimes neglected, see e.g. [37]. This statement is also supported by the numerical study of [38]. Therefore, we will only accept a drag-related term as the fluid-particle interaction:

$$\boldsymbol{F}^p = \boldsymbol{F}^{drag} \ . \tag{3.5}$$

$\boldsymbol{F}^{drag}$ is an effective drag force calculated from some analytical or empirical correlation. The pairwise particle lubrication force is also ignored, similar to [28, 39].

3.2.2 Fluid hydrodynamic equations

The fluid phase motion is described using the well-known volume-averaged forms of governing equations [15], i.e. the continuity equation

$$\frac{\partial \varepsilon}{\partial t} + \nabla \cdot (\varepsilon \boldsymbol{u}) = 0 \tag{3.6}$$

and the momentum equation

$$\begin{aligned} \rho_f \left(\frac{\partial (\varepsilon \boldsymbol{u})}{\partial t} + \nabla \cdot (\varepsilon \boldsymbol{u}\boldsymbol{u}) \right) &= -\varepsilon \nabla p + \varepsilon \nabla \cdot (\mu_f (\nabla \boldsymbol{u} + \nabla \boldsymbol{u}^T)) \\ &\quad + \varepsilon \rho_f \boldsymbol{g} + \varepsilon \boldsymbol{f}^s + \boldsymbol{f}^p \ . \end{aligned} \tag{3.7}$$

In these equations, ε is the void fraction, ρ_f, $\boldsymbol{u}$ and μ_f are the fluid density, velocity and viscosity, respectively. The surface tension force $\boldsymbol{f}^s$ is located near the fluid interface, and $\boldsymbol{f}^p$ is the reaction force of the fluid-particle interaction term 3.5.

In the past different forms of equations have been ever used. Concerning the model consistency, particularly the way how the fluid stress and coupling

---

[1] Rigorously speaking, the viscous force is still indispensable in some hypothetical flow cases. For example, consider the steady motion of a test particle in a pressure-driven Poiseuille flow or vertical channel. In that case, the pressure gradient must be balanced by the viscous force so that the particle can reach a steady state. See Appendix A. We thank Professor S. Takagi (The University of Tokyo) and Professor T. Kajishima (The University of Osaka) pointing out this problem in private communication.

term are posed, a good series of discussions about the formulation can be found in [26, 40, 41]. Recently, Zhou et al. [35] carried out a thorough examination and comparison of different approaches, and our choice of model formulation is kept compatible with their arguments.

3.2.3 Gas-liquid interface

The configuration of binary fluid interface is described by a color function ϕ indicating the volume fraction of the liquid phase. Its value is 1 in liquid, 0 in gas and $0 < \phi < 1$ across the interface. The interface motion is then given by the advection equation of ϕ based on the fluid velocity:

$$\frac{\partial \phi}{\partial t} + \boldsymbol{u} \cdot \nabla \phi = 0 \ . \tag{3.8}$$

Being an analogy to the volume-averaging fluid equations, Washino et al. [32] also introduced a “volume-averaged” form of the interface advection:

$$\frac{\partial (\varepsilon \phi)}{\partial t} + \nabla \cdot (\varepsilon \phi \boldsymbol{u}) = 0 \ .$$

We note that, by substitution of the continuity equation (3.6), it could be easily reduced to the standard form of Eq. (3.8), so their equivalence is apparent. In this study, the fluid interface is reconstructed and moved by using the WLIC VOF scheme [33]. Our implementation and improvement of this algorithm has been discussed and tested in the previous chapter. The fluid density and viscosity are derived from the physical values of different phases by a linear interpolation with the color function:

$$\rho_f(\phi) = \phi \rho_l + (1 - \phi) \rho_g \tag{3.9}$$

$$\mu_f(\phi) = \phi \mu_l + (1 - \phi) \mu_g \tag{3.10}$$

The subscripts l and g denote liquid and gas phases, respectively.

Contact angle on rigid walls

At contact lines where the gas-liquid interface intersects with the wall surface, a static 90° contact angle boundary condition is enforced, see the previous chapter. The reason of choosing a neutral contact angle is mainly for simplicity and efficiency, and it also stands on the fact that the bulk flows in the scope of this study are not affected by local motions driven by surface tension, c.f. [42].

Free surface in solid bed

In [32], a sub-grid scale model is proposed for capillary effects when a droplet penetrates into a dense particle bed. Such microscopic capillary interaction is also neglected for the particle phase in the present study; instead of that, the additional force induced by the macroscopic interface curvature is considered in Section 3.3.1. Similar to the aforementioned reason, it is because that the problem scale of interest is considerably larger than that of nucleation processes in wet granulation. Therefore compared with capillary effects, the hydrodynamic force is thought to be the dominant fluid-particle coupling term.

3.2.4 Arbitrary-shaped wall boundary

The arbitrary-shape wall boundary model developed in our previous study [14] is deployed in this study to offer a unified representation of boundary shape for both Lagrangian particle and Eulerian fluid sides. Unlike an explicit representation of shapes by surface mesh, this model uses a special SDF field whose zero contour implicitly defines the boundary shape. A local coordinate transformation is associated with the SDF field to record the boundary motion. It is thus highly simple and efficient to model complicated shapes and unlimited rigid motions.

The SDF-based model has been first described in detail for granular particles in [14]. Next in our VOF-IB method, it becomes the essential ingredient to compute two-phase flows in complex geometries. Similar approaches have been adopted in our Lagrangian particle simulations as well, see [43–45].

3.2.5 Configuration of the fluid-particle system

The configuration of the Eulerian-Lagrangian modeling of the fluid-particle system is illustrated for a computational cell in Figure 3.1. It is apparently seen that the cell size is selected larger than the typical size scale of particle diameter. Such a configuration, sometimes referred to as a mesoscale grid, is required for a meaningful volume-averaging model.

Figure 3.1 shows a representative situation where the computational cell is occupied by the wall geometry, fluids and particles. This simply implies a volume summation:

$$V^{cell} = V^{geom} + V^{fluid} + V^{particle} \ , \tag{3.11}$$

where $V^{cell} = \Delta x \Delta y \Delta z$ is the cell volume with Δx the cell size. Due to the impenetrability of the wall boundary, we first introduce the geometry volume fraction

$$\alpha = \frac{V^{geom}}{V^{cell}} \ . \tag{3.12}$$

The volume fraction of solid particles accommodated in this cell is then calculated as

$$\varepsilon^{particle} = \frac{V^{particle}}{V^{fluid} + V^{particle}} = \frac{V^{particle}}{(1-\alpha)V^{cell}} \ . \tag{3.13}$$

For a particle lying on the cell boundaries, it is approximated by a cube and only the cut volume chopped by the cell boundary is taken into account, that is,

$$V^{particle} = \sum \gamma_p^{cell} V_p \ . \tag{3.14}$$

Herein the weight γ_p^{cell} indicates the ratio of truncated particle volume. It is evident that $\gamma_p^{cell} = 1$ for a particle completely enclosed by the cell and $0 < \gamma_p^{cell} < 1$ if the particle intersects with the cell boundary. The void fraction ε is then given by the complement of the solid particle volume fraction, that is,

$$\varepsilon = 1 - \varepsilon^{particle} \ . \tag{3.15}$$

One is thus able to compute the volume of fluids in the remains of the cell:

$$V^{fluid} = (1-\alpha) \cdot \varepsilon \cdot V^{cell} \ . \tag{3.16}$$

Recalling the color function ϕ indicating the volume fraction of liquid in a two-phase flow, it is also possible to estimate the volume for liquid and gas phases in the current cell:

$$V^{liquid} = (1-\alpha) \cdot \varepsilon \cdot \phi \cdot V^{cell} \tag{3.17}$$

$$V^{gas} = (1-\alpha) \cdot \varepsilon \cdot (1-\phi) \cdot V^{cell} \tag{3.18}$$

3.3 Numerical method

3.3.1 Particle phase

Contact force

In the DEM, the particle-particle or particle-wall contact force is determined from their overlap during a finite collision time. In this study, a simple force model composed of linear spring, viscous dashpot and friction slider is used to represent a viscoelastic collision process. The contact force is first

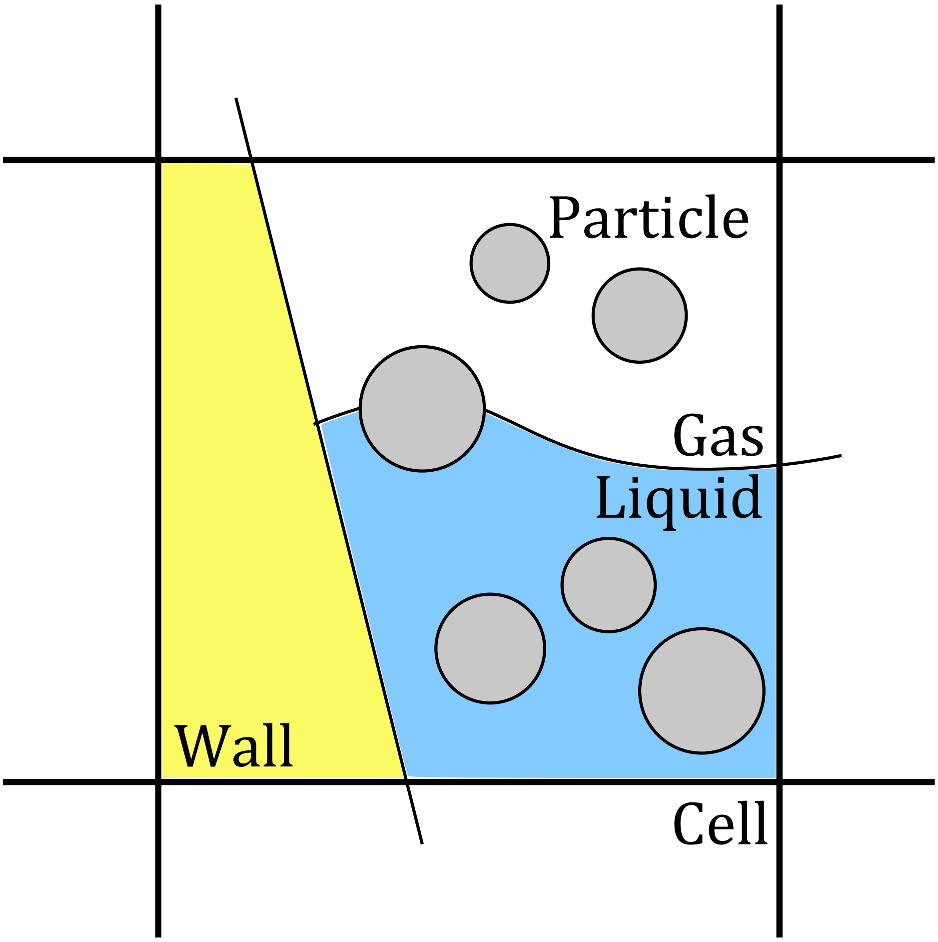

Figure 3.1: Configuration of wall geometry, fluid interface and particles in a computational cell.

decomposed with respect to the contact surface into normal and tangential directions:

$$\boldsymbol{F}^C = \boldsymbol{F}_n^C + \boldsymbol{F}_t^C \ , \tag{3.19}$$

in which the subscripts n and t denote the normal and tangential components, respectively. The normal component is computed as a combination of elastic spring with damping:

$$\boldsymbol{F}_n^C = -k\boldsymbol{\delta}_n - \eta\boldsymbol{v}_n \ , \tag{3.20}$$

where k, η, $\boldsymbol{\delta}_n$ and $\boldsymbol{v}_n$ are, respectively, the spring constant, damping coefficient, displacement vector and relative velocity in the normal direction. The tangential force is treated in a similar manner, but it is first tested whether the surfaces in contact have reached the maximum static friction:

$$\boldsymbol{F}_t^{trial} = -k\boldsymbol{\delta}_t - \eta\boldsymbol{v}_t \tag{3.21}$$

$$\boldsymbol{F}_t^C = \begin{cases} \boldsymbol{F}_t^{trial} & \text{if } \|\boldsymbol{F}_t^{trial}\| \leq \mu\|\boldsymbol{F}_n^C\|, \\ -\mu\|\boldsymbol{F}_n^C\| \cdot \boldsymbol{v}_t/\|\boldsymbol{v}_t\| & \text{otherwise,} \end{cases} \tag{3.22}$$

where $\boldsymbol{\delta}_t$ and $\boldsymbol{v}_t$ are the displacement vector and relative velocity in the tangential direction, and μ is the friction coefficient. The damping coefficient η is derived as follows:

$$\eta = -2\ln e\sqrt{\frac{km^*}{\ln^2 e + \pi^2}} \ , \tag{3.23}$$

in which e is the restitution coefficient, and m^* is the reduced mass of the contact pair. The torque $\boldsymbol{T}^C$ is calculated based on the contact force $\boldsymbol{F}^C$ and the distance vector connecting particle center and contact point.

This numerical procedure is repeated for all particle-particle and particle-wall pairs in direct contact. We note that, it is straightforward to detect the contact between the particle and the rigid boundary represented by an SDF model, because the SDF value at the particle position directly yields the distance to the nearest point on the wall. This approach integrates well with the DEM contact force model and is highly efficient.

Drag force

The drag force acting on a solid particle is given by the following general form:

$$\boldsymbol{F}_p^{drag} = \frac{\beta V_p}{1-\varepsilon}(\boldsymbol{u} - \boldsymbol{v}) \ . \tag{3.24}$$

Herein the local void fraction ε is equal to the value in the fluid cell that contains the particle, and the flow velocity $\boldsymbol{u}$ is found by linear interpolation at the particle center. The choice of an accurate and versatile correlation for the coefficient β is critical. In this study, a combination of the equations of Ergun [46] and Wen-Yu [47] suggested by [16] is adopted.

$$\beta = \begin{cases} 150\frac{(1-\varepsilon)^2}{\varepsilon}\frac{\mu_f}{d_p^2} + 1.75(1-\varepsilon)\frac{\rho_f}{d_p}\|\boldsymbol{u}-\boldsymbol{v}\| & \varepsilon \leq 0.8 \\ 0.75C_D\frac{\varepsilon(1-\varepsilon)}{d_p}\rho_f\varepsilon^{-2.65}\|\boldsymbol{u}-\boldsymbol{v}\| & \varepsilon > 0.8 \end{cases} \tag{3.25}$$

where d_p is the particle diameter. C_D is the drag coefficient of a single sphere given by

$$C_D = \begin{cases} \frac{24}{Re_p}(1+0.15Re_p^{0.687}) & Re_p \leq 1000 \\ 0.44 & Re_p > 1000 \end{cases} \tag{3.26}$$

The particle Re number Re_p is defined as

$$Re_p = \frac{\varepsilon\rho_f d_p\|\boldsymbol{u}-\boldsymbol{v}\|}{\mu_f} \ . \tag{3.27}$$

The Gidaspow's correlation has been commonly used in DEM-CFD simulations of fluidization systems as a drag model valid for a wide range of flow conditions. Other drag models (e.g. the Di Felice correlation [48]) are also available.

Pressure gradient and surface tension terms

As described in Section 3.2.1, other fluid actions on the particle include the pressure gradient term

$$\boldsymbol{F}^{\nabla p} = -V_p\nabla p \tag{3.28}$$

and the surface tension term (also see next section for its computational model)

$$\boldsymbol{F}^{s} = V_p\sigma\kappa\nabla\phi \tag{3.29}$$

with the surface tension coefficient σ and interface curvature κ. For a particle submerged by a single fluid, a partial effect of the former term is the hydrostatic buoyancy while the latter one vanishes. In the vicinity of the fluid interface, the particle is affected by both terms. Let us consider a static drop, for which according to the Laplace formula the jump of the pressure across its interface is $\Delta p = \sigma\kappa$. Hence in this case the pressure gradient term near the interface tends to push a test particle toward the outside of the drop. On the other hand, the surface tension term pointing inward will result in a capillary attraction to balance the repulsive effect. In the simulation, both terms are calculated on the fluid grid and then interpolated for each particle by simple averaging.

Updating particle states

The aforementioned force calculation is performed explicitly at each time step n. Once the contact force, gravity force and fluid hydrodynamics forces have been computed for a particle, their net force is used to determine the acceleration $\boldsymbol{a}$. The particle states of velocity and position are then updated to the next time step by using the symplectic Euler scheme:

$$\boldsymbol{v}^{n+1} = \boldsymbol{v}^{n} + \Delta t \boldsymbol{a}^{n} \tag{3.30}$$

$$\boldsymbol{x}^{n+1} = \boldsymbol{x}^{n} + \Delta t \boldsymbol{v}^{n+1} \tag{3.31}$$

The angular velocity is treated in a similar way; if necessary, the rotated orientation of the particle could be updated by using quaternion operations, see e.g. [49].

3.3.2 Fluid phase

The modeling of the fluid phase basically follows our previous numerical study of two-phase flows in general geometries, see the previous chapter for details. For the sake of completeness, the numerical procedure is outlined here.

Spatial discretization

The computational domain is discretized on a uniform, staggered grid [50]. The velocity components are defined at corresponding cell faces and other variables are centered in each cell. The governing equations are solved with a classical finite-volume method, where the spatial derivatives in the viscous and pressure gradient terms are calculated by central differences, and field values required at undefined places are obtained by using linear interpolation. For the discretization of the convective term, either a modified hybrid scheme of [51] or a TVD upwind scheme like [52] is used. Numerical tests show that they can give equivalent results.

Surface tension

The singular surface tension term is introduced by using the continuum surface force (CSF) model [53] as a volume force spreading over the interfacial region:

$$\boldsymbol{f}^{s} = \sigma \kappa \nabla \phi \tag{3.32}$$

with the curvature $\kappa = -\nabla \cdot \boldsymbol{n}$. The normal vector $\boldsymbol{n}$ is computed as the gradient of the color function ϕ as

$$\boldsymbol{n} = \frac{\nabla\phi}{\|\nabla\phi\|} \,. \tag{3.33}$$

In a VOF method, it is also common to replace the original color function ϕ with a smoothed field ϕ^s to facilitate the calculation of normal vectors and curvatures. In this study, two sequential sweeps of the smoothing operation based on the compact filter suggested by [54] are used.

Fluid-particle interaction

The fluid-particle interaction force $\boldsymbol{F}_p$, as described in the preceding section, is first evaluated for distinct particles based on local flow conditions and particle states. From the point of view of the continuum fluid, their reaction force becomes a cloud of point source term $\boldsymbol{f}_p$ appended to the right-hand side of the volume-averaged Navier-Stokes equation (3.7). In the fluid solver, those scattered point forces are gathered from particles and distributed as a volume force for each computational cell. This operation can be written by

$$\boldsymbol{f}^p = -\frac{\sum \gamma_p^{cell} \cdot \boldsymbol{F}^{p,cell}}{V^{cell}} \,, \tag{3.34}$$

in which the minus sign indicates the effect of reaction. We note that the weight $\gamma_p^{cell} \in [0, 1]$ is the fraction of the partial volume of a particle inside the current cell, see Section 3.2.5.

Pressure solution

The fluid solver follows the fractional-step algorithm of a projection method [55]. The terms on the right-hand side of Eq. (3.7), except the pressure gradient term, are explicitly computed at the n-th time step, which yields an intermediate velocity prediction $\boldsymbol{u}^*$ which does not satisfy the continuity equation (3.6) in general. Consequently, the pressure field p is implicitly solved from the pressure Poisson equation

$$\nabla \cdot \left(\frac{\varepsilon}{\rho}\nabla p\right) = -\frac{1}{\Delta t}\left(\frac{\Delta\varepsilon}{\Delta t} + \nabla \cdot (\varepsilon \boldsymbol{u}^*)\right) \tag{3.35}$$

and then a velocity correction based on the pressure gradient is performed.

Wall boundary motion

Finally, according to the IB method [12], the influence of the wall boundary is incorporated by locally averaging the fluid velocity $\boldsymbol{u}_f$ and the boundary velocity $\boldsymbol{u}_B$, from which the velocity at the $(n+1)$-th step is obtained:

$$\boldsymbol{u}^{n+1} = (1-\alpha)\boldsymbol{u}_f + \alpha\boldsymbol{u}_B \ . \tag{3.36}$$

Note that the geometry volume fraction α (Section 3.2.5) equals unity in wall domain, and thus the wall velocity is exactly prescribed therein.

3.3.3 Treatments near the IB

We remark on that, it is critical to take the effects of the IB geometry into consideration when calculating the fluid-particle interaction. Although the wall boundary shape and its motion are automatically handled by the IB approach, the IB is likely to interfere with the evaluation of drag force by rendering a fictitious flow state at least in two aspects: the local void fraction and flow velocity. Since the void fraction is determined by the ratio of the particle volume to the cut-cell volume other than the IB part, this computation may become inaccurate or unstable when the geometry fraction α is close to unity. Another problem arises when the flow velocity is to be determined in the vicinity of an IB, for which a naive interpolation of the velocity field using a stencil across the IB surface will contaminate the results by improperly introducing the wall velocity. Such errors generally stem from the discontinuity between a true fluid and a fictitious IB domain. Similar discussions also extend to other types of hydrodynamic forces that depend on local flow conditions.

In the present method, related problems are circumvented by carefully selecting and adapting the interpolation stencil close to the IB surface so that their influences are excluded effectively. A fluid cell with geometry fraction $\alpha > \alpha_0$ is considered to be a "small" cut-cell, and it is temporarily connected with surrounding cells and the void fraction ε is calculated within the imaginary "large" cell. This procedure is illustrated for a 2D configuration in Figure 3.2, in which the partial cell in the center is merged with adjacent eight cells (twenty-seven cells in 3D) as the area enclosed by the broken line. In this study, we have the constant threshold as $\alpha_0 = 0.2$, which is an adjustable parameter.

Similarly, the flow velocity interpolation also relies on the selective usage of data. As mentioned in Section 3.3.1, the flow velocity is obtained for a particle distant from IB by trilinear interpolation involving surrounding eight data points. Note that because the components of fluid velocity are staggered in space, the interpolation must be determined distinctively for all three dimensions. If any of these points is found to belong to the IB domain as indicated by $\alpha > \alpha_0$, it is then tagged and discarded from the stencil. The interpolation in that case falls back to a simple averaging among remaining valid points. If all eight points are tagged, the one with the smallest value of α is used. A typical 2D case for clarity is demonstrated in Figure 3.3, where the operation on the u-component velocity is shown. It is seen that among all four fluid points bounding the particle, the two on the left side are affected by the IB and thus get tagged as invalid points (white marker), while the other two are chosen as valid candidates (solid marker) to provide a reliable estimation to the local flow velocity.

Generally speaking, the treatment introduced here could be equivalently understood as the utilization of stencils biased to the fluid side near the IB surface, which is conceptually similar to the ghost fluid method (GFM) of multi-material flows [56]. It is critical for suppressing spurious particle motion and grid dependency of computational results, especially for simulations involving moving boundaries. In respect to this point, an example is discussed in Section 3.5.3.

3.3.4 time-stepping algorithm

The overall algorithm of the present DEM-VOF method is described in this section. It is assumed that at the current time step n, all variables, including the geometry profile, particle states, interface configuration and fluid field variables, are known.

1. If the geometry is moving, update its definition (geometry modeling in Section 3.2.4) and find the geometry fraction α^{n+1} and velocity $\boldsymbol{u}_B^{n+1}$ for the fluid mesh (Section 3.2.5).

2. Perform the DEM simulation of particle phase and compute the fluid-particle interaction force (Section 3.3.1) to have the particle velocity $\boldsymbol{v}^{n+1}$ and position $\boldsymbol{x}^{n+1}$.

3. According to the updated particle states, calculate the void fraction ε^{n+1} on the fluid mesh (Section 3.2.5). Simultaneously, the fluid-particle interaction force is gathered from the particle phase and transferred to the fluid phase (Section 3.3.2).

4. Perform VOF reconstruction and advection of the gas-liquid interface (Section 3.2.3), whose new configuration is known as ϕ^{n+1}. Fluid properties such as the density ρ^{n+1} and viscosity μ^{n+1} are also derived in this stage.

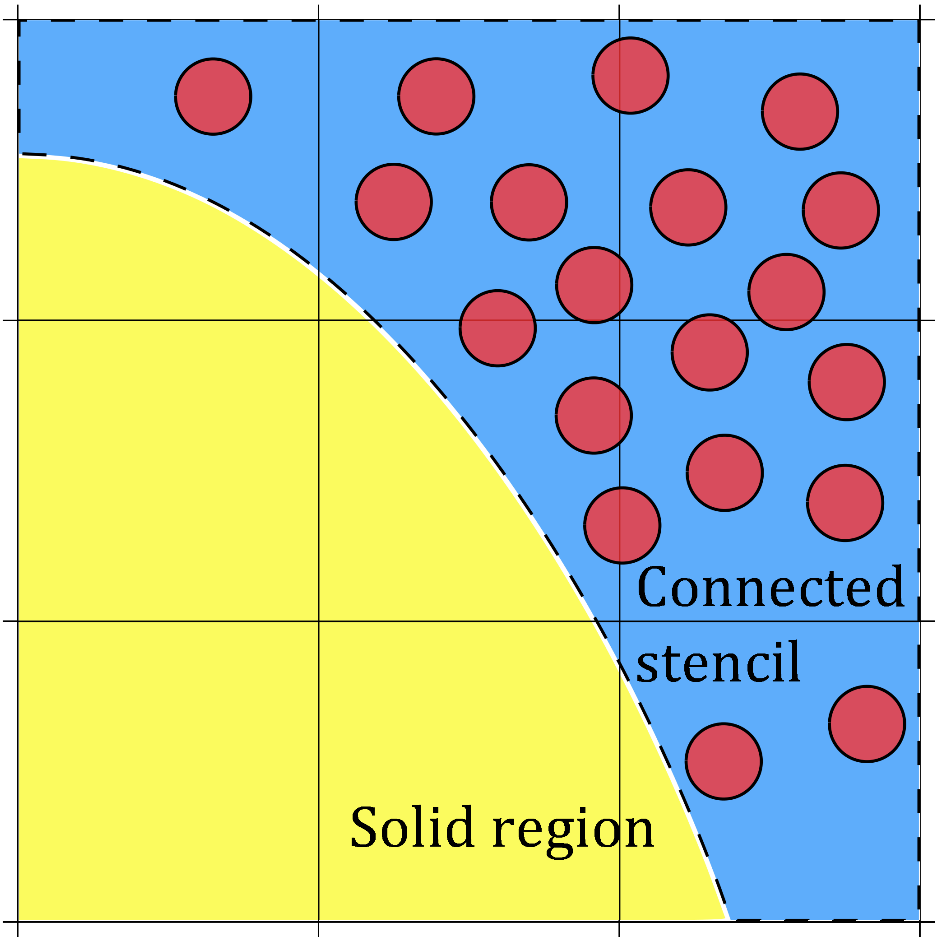

Figure 3.2: Stencil connected near the IB for evaluating void fraction.

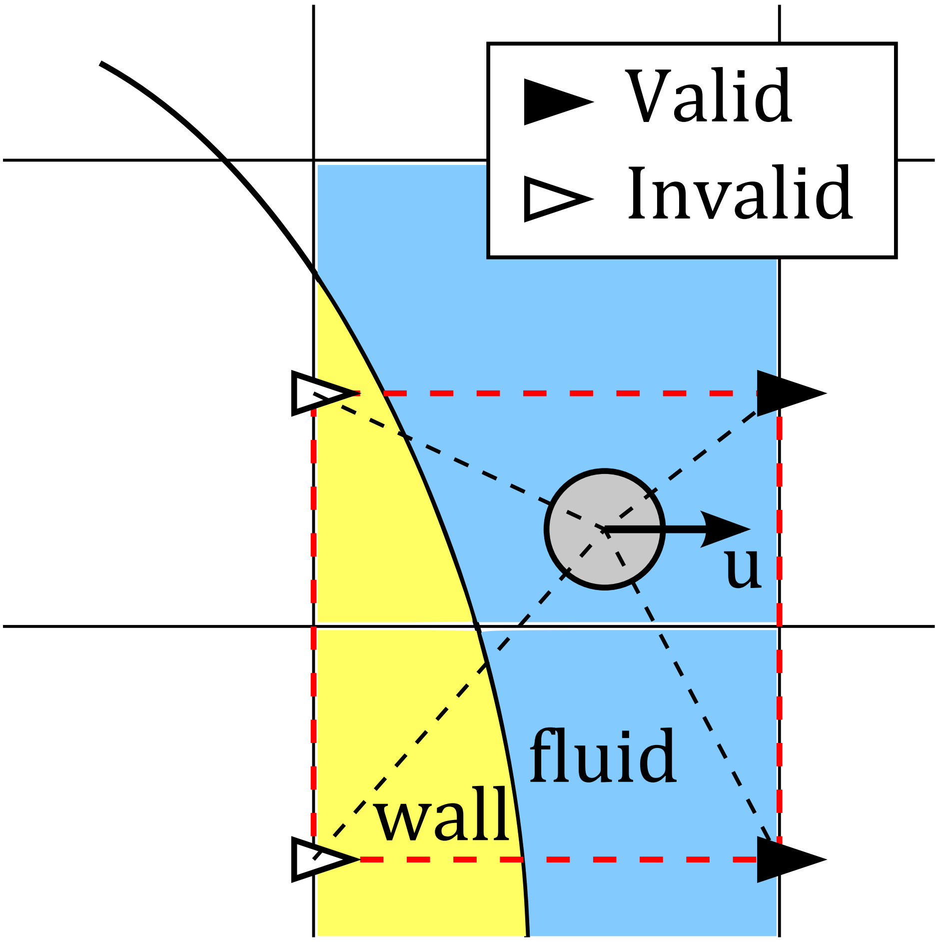

Figure 3.3: Stencil selected near the IB for velocity interpolation

5. Perform the fluid simulation and enforce the boundary velocity (Section 3.3.2), which finally yields the new fluid velocity $\boldsymbol{u}^{n+1}$ and pressure p^{n+1}. The gas-solid-liquid system is now fully updated to the next time step.

The time step Δt is limited by both particle and fluid sides. For the particle phase, the restriction mainly comes from the stiffness in the DEM contact model:

$$\Delta t^{particle} < 2\sqrt{\frac{m_p}{k}} \; . \tag{3.37}$$

At the same time, due to the explicit treatment of the convective, viscous and surface tension terms, the time step permissible in the fluid solver is given by

$$\Delta t^{fluid} < \min\left(\frac{\Delta x}{\|\boldsymbol{u}\|_{max}}, \frac{\rho_f \Delta x^2}{\mu_f}, \sqrt{\frac{\rho_f \Delta x^3}{2\pi\sigma}}\right) \; . \tag{3.38}$$

Basically, $\Delta t^{particle}$ tends to be more stringent than the fluid counterpart (typically smaller than Δt fluid by one order of magnitude in our tests) because of the stiff numerical parameter k and a relatively small particle mass m_p. Therefore the total stability condition is dominated by the particle simulation. In order to save computational time, it is feasible to adopt a sub-cycling methodology to run several iterations of particle computations and one sweep of fluid simulation sequentially in a single time step. During the particle iterations, the interphase coupling term is calculated based on a frozen flow state and it is integrated over those fine time intervals. When the sub-cycling comes to the end, the temporal average of the accumulated interaction force is passed to the fluid phase. This approach is similar to that used in [57, 58].

3.4 Model verification

In this section, verification of the proposed model is performed in simple problems. We will focus on the fluid-particle coupling by examining results of two problems: (a) single particle sedimentation and (b) flow passing through a fixed bed. In the first problem the particle behavior is dominated by the fluid action under dilute limitation and low-Re regime; in the second problem the flow state is influenced by the porous solid layer with dense packing and higher Re number. Through these "patch tests", we generally find good agreements between the computational results and analytical or empirical equations. The effects of some numerical parameters are also explored. Hence the proposed model could be applied with increased confidence.

We also note that, the underlying numerical framework has already been extensively tested and used for gas-solid fluidized beds, see e.g. [9, 10]. Tests for the multiphase model and complex geometries have already been provided in Chapter 2.

3.4.1 Single particle sedimentation

Sedimentation of a sphere is a basic and important problem for fluid-particle flows. Such particle settling problems are chosen here to examine the correct evaluation and integration of fluid force.

In a similar way like some other authors (see e.g. [59, 60]), a low-Re flow regime is assumed for simplicity, where the fluid remains almost quiescent and the Stokes' law of drag applies. Under this assumption, the particle motion is described by the following equation (with the gravity in the $-y$ direction):

$$\dot{v} = -\frac{\rho_p - \rho_f}{\rho_p} g - \frac{3\pi\mu_f d_p}{m_p} v \ , \tag{3.39}$$

which defines an initial value problem for the particle trajectory with the terminal velocity (if could be reached) derived as

$$v^\infty = -\frac{1}{18}\frac{(\rho_p - \rho_f) d_p^2 g}{\mu_f} \ . \tag{3.40}$$

For this problem, the Re number is calculated based on the fluid density, viscosity, particle diameter and terminal velocity, i.e.

$$Re = \frac{\rho_f d_p v^\infty}{\mu_f} \ . \tag{3.41}$$

Settling in one-fluid domain

We first consider the particle settling in a single fluid from static state. For this initial value problem provided that $v(t = 0) = 0$, it is easy to find the analytical solution given by

$$v(t)/v^{\infty} = 1 - \exp(-t/T) \tag{3.42}$$

where a characteristic time towards the final steady state is defined as

$$T = m_p/3\pi\mu d_p \ .$$

In the computational setup, the domain dimensions are 4 mm by 8 mm by 4 mm, for which all wall boundaries are set to non-slip. A particle is placed at 5 mm height. The whole fluid domain is covered by uniform grids with spacing of 0.25 mm and the particle diameter is 0.1 mm, which results in a size ratio of $\Delta x/d_p = 2.5$ times. The particle density is 2500 kg/m^3. The fluid density is fixed to 1000 kg/m^3, and its viscosity is varied in the simulations to achieve different Re numbers.

For this specific verification test with analytical assumption of the Stokes' law and ambient fluid, we consider the following factors that may bring in influences for simulation results.

Effect of the drag law adopted To better recover the predicted solution, one may hopefully use the analytical Stokes' law instead of the Gidaspow's correlation implemented for practical usage. It is thus necessary to investigate the difference when these two drag laws are used respectively. It is noted that for this single particle test, the void fraction is set to $\varepsilon = 1$ for drag calculation.

Effect of particle Re number Following the previous point, the Gidaspow's correlation is a function of finite Re numbers. It is also known that such empirical drag correlations should asymptotically approach the Stokes drag in the limit of zero Re number. Therefore, the fluid viscosity is changed from 0.001 Pa s to 0.01 Pa s to show the trend when approaching a Stokes flow regime. The Re numbers are approximately $Re = 0.818$ and 8.18×10^{-3} ("high" and "low") for those two cases, respectively.

Effect of fluid motion or coupling model Although they are considerably small, perturbations caused by settling particle can still affect the fluid motion, which may differ from the theoretical derivation within an inert fluid domain. In order to identify this effect, we perform regular

Table 3.1: Simulation cases for single particle settling in one-fluid domain.

	Case 1	Case 2	Case 3	Case 4
Drag model	Stokes	Stokes	Gidaspow	Gidaspow
Re number	High	High	High	High
Coupling model	1-way	2-way	1-way	2-way
	Case 5	Case 6	Case 7	Case 8
Drag model	Stokes	Stokes	Gidaspow	Gidaspow
Re number	Low	Low	Low	Low
Coupling model	1-way	2-way	1-way	2-way

"2-way" simulations as well as special "1-way" tests in which the fluid-particle interaction force is only acting on the particle but get switched off for the fluid side[2].

Table 3.1 lists all simulation cases. Figure 3.4 plots the dimensionless sedimentation velocity against time for all eight test cases together with the analytical solution. All cases adopting Stokes' law of drag generally agree well with the analytical curve, showing that the force acting on the particle is correctly evaluated and integrated. It is seen that, with relatively high Re number ($Re = 0.818$), the utilization of Gidaspow's correlation leads to a lower terminal velocity (Case 3 and 4). This is because that the drag force, as described in Section 3.3.1, boils down to the form like

$$F^{drag} = 3\pi\mu d_p v(1 + 0.15Re^{0.687}) \ ,$$

which is larger than the theoretical Stokes drag by a Re-related factor (≈ 1.13) in the parenthesis. Under the low Re number ($Re = 8.18 \times 10^{-3}$), the Gidaspow results can reproduce the analytical solution satisfactorily (Case 7 and 8). It seems that the drag-induced fluid motion in "2-way" simulations can cause slight perturbation in the final velocity, but this effect does not make an much appreciable difference.

Falling in air-water domain

Next a particle falling through an air-water interface is simulated. The computational setup is same as the one-fluid case, except that a horizontal interface is added in the center of the domain dividing it into an upper part

---

[2] Note that in "1-way" computations the fluid is still aware of the existence of the particle. Although the reaction force of fluid drag is set to zero, the system is still coupled via the void fraction, which works as a source term in the continuity equation to drive the fluid into motion.

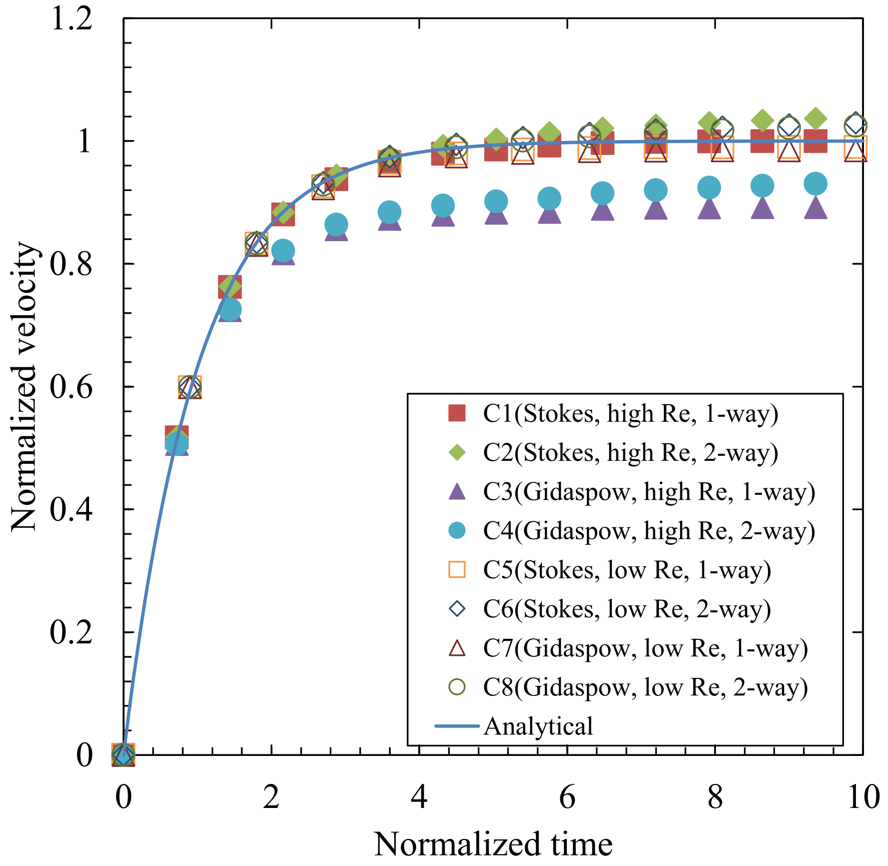

Figure 3.4: Plot of normalized sedimentation velocity against time.

Table 3.2: Simulation cases for single particle falling in air-water domain.

	Case 1	Case 2	Case 3	Case 4
Drag model	Stokes	Stokes	Gidaspow	Gidaspow
Coupling model	1-way	2-way	1-way	2-way

filled with air ($\rho_g = 1$ kg/m^3 and $\mu_g = 10^{-5}$ Pa s) and a lower part of water ($\rho_l = 1000$ kg/m^3 and $\mu_l = 10^{-3}$ Pa s).

The analytical solution is derived under the assumption that the particle experiences a free fall in the air phase and then settles obeying the Stokes' law in the water phase. The simulation cases deploying different drag laws and interphase coupling approaches are listed in Table 3.2.

In Figure 3.5 the temporal variations of particle position and velocity are plotted for each case. When falling in the air phase, the particle motion seems to be slightly delayed due to the air drag. After the water entry, the particle rapidly slow down to the predicted terminal velocity. It is seen that with the Gidaspow's drag correlation (Case 3 and 4), particle motion in the water is retarded more effectively, but in general the simulation results from all test cases reasonably match the analytical solution and tend towards the predicted terminal velocity.

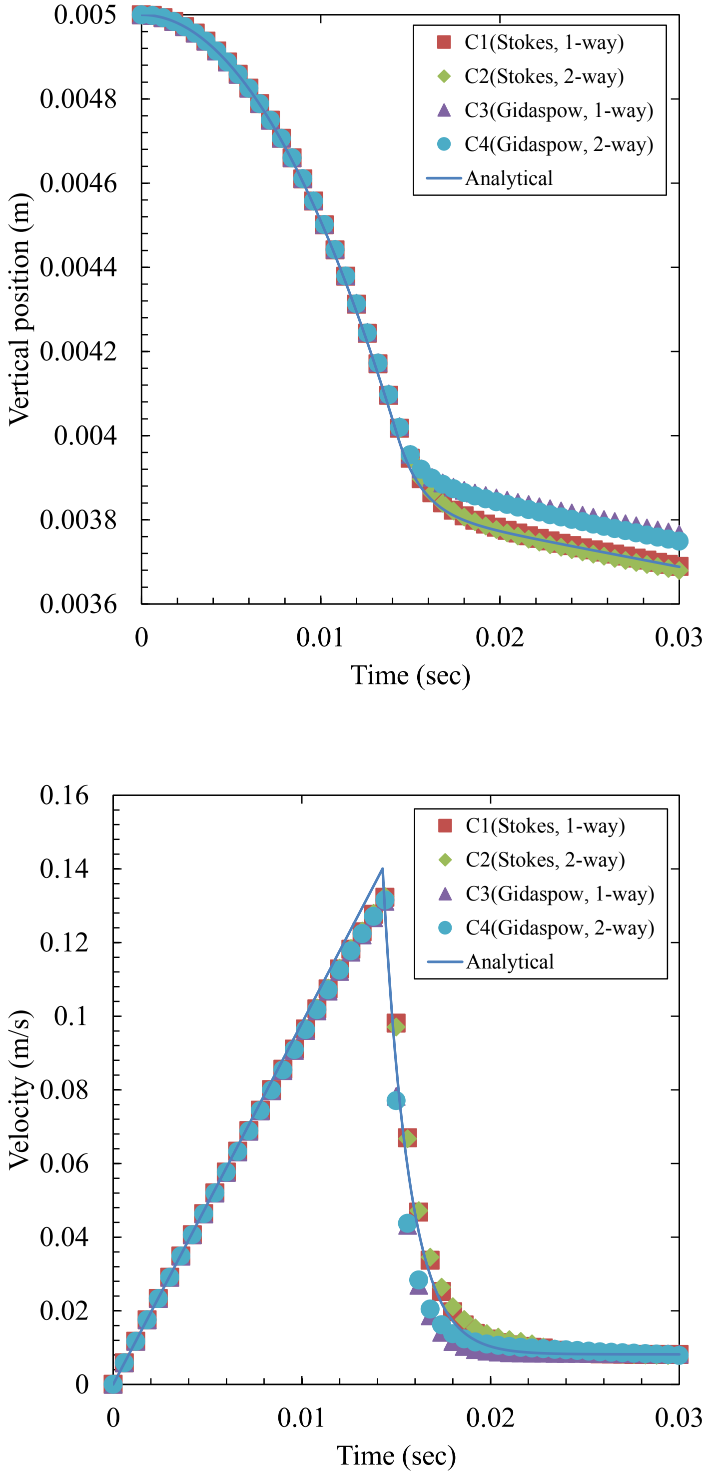

Figure 3.5: Plot of vertical position (a) and velocity (b) against time.

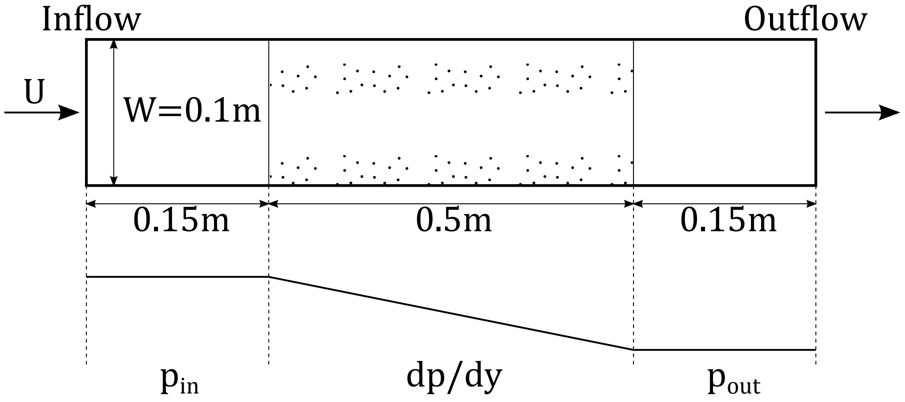

Figure 3.6: Schematic diagram of the flow through a fixed particle bed.

3.4.2 Flow through fixed particle bed

In another verification test for the fluid-particle coupling, the liquid flow passing through a fixed particle bed is simulated. In this test, the flow state is affected by the porous solid layer, through which a drop in pressure transpires as a result of the fluid-particle interaction.

The computational domain is a rectangular channel with a cross section of $W = 0.1$ m and a length of 0.8 m. The region between $0.15 < y < 0.65$ is filled with a fixed particle bed. The inflow velocity is $U = 0.1$ m/s. The fluid density is $\rho = 1000$ kg/m^3 and the viscosity is $\mu = 0.001$ Pa s. This configuration is similar to that in [30] but we left 0.15 m long free spaces at both the inlet and outlet zones to check the flow transition. The computational setup is illustrated in Figure 3.6.

Flow profile along central axis

All four channel walls are assumed to be free-slip boundary, so that there is no pressure loss due to friction and the pressure must remain constant in the free inlet/outlet zone. In the particle bed, the pressure drop rate could be predicted by using the Ergun's equation [46]:

$$\frac{\Delta p}{\Delta y} = 150\frac{(1-\varepsilon)^2}{\varepsilon^3}\frac{\mu U}{d^2} + 1.75\frac{1-\varepsilon}{\varepsilon^3}\frac{\rho U^2}{d} \ . \tag{3.43}$$

As the inlet velocity U is exactly equal to the superficial velocity passing through the channel, inside the particle bed the exact flow velocity is obtained

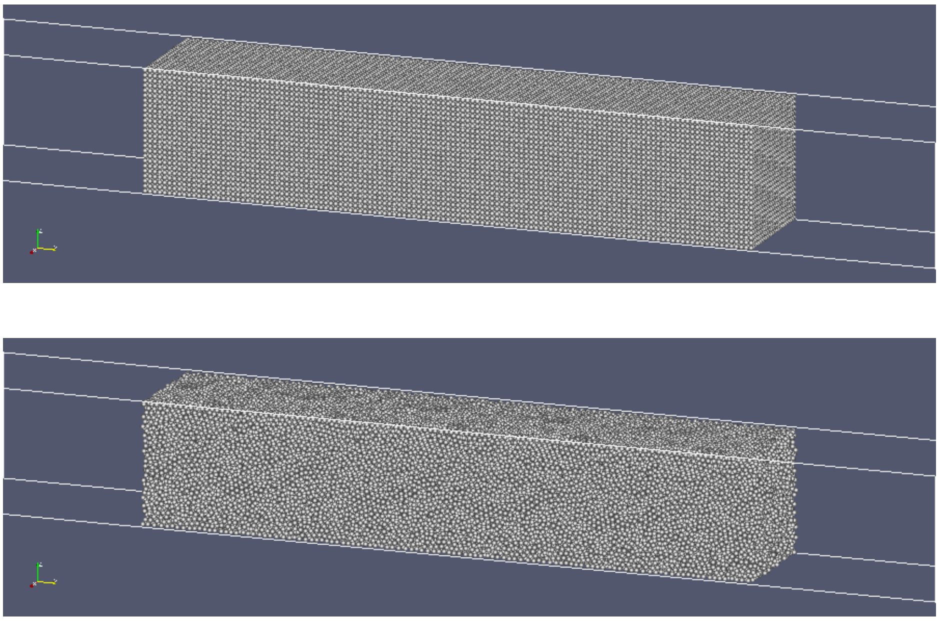

Figure 3.7: Fixed particle beds of regular (a) and random (b) packing.

via volume conservation:

$$u = U/\varepsilon \ . \tag{3.44}$$

It is known that the Gidaspow's correlation is actually an adaptation of the Ergun's equation for dense systems, so the agreement between simulation results and the prediction by Eq. (3.43) is determined critically by the calculation of three important factors: (a) void fraction, (b) flow velocity and (c) drag force feedback from particle bed to the flow.

The solid bed used in the simulation is regularly aligned on a 25 by 25 by 125 lattice as illustrated in Figure 3.7 (a), or 78125 particles in total. The particle diameter is $d = 3.95$ mm, from which a void fraction $\varepsilon = 0.496$ and flow velocity $u = 0.202$ m/s could be obtained. The pressure loss is thus expected to be 2.03×10^4 Pa/m. The fluid cell size is $\Delta x = W/10 = 10$ mm.

Figure 3.8 plots the profile of the void fraction, flow velocity and pressure on the central line of the channel. The sharp jump of ε is observed at $y = 0.15$ and 0.65, respectively. Between these two end points, the bed porosity is well calculated in comparison with the analytical value $\varepsilon = 0.496$ and an increased flow velocity is also confirmed. The pressure distribution obtained from simulation results agrees well with our analytical solution. By using a linear fitting, the pressure drop through the solid bed is found to be 2.03×10^4 Pa/m, and the relative error with the Ergun's equation is below 1%.

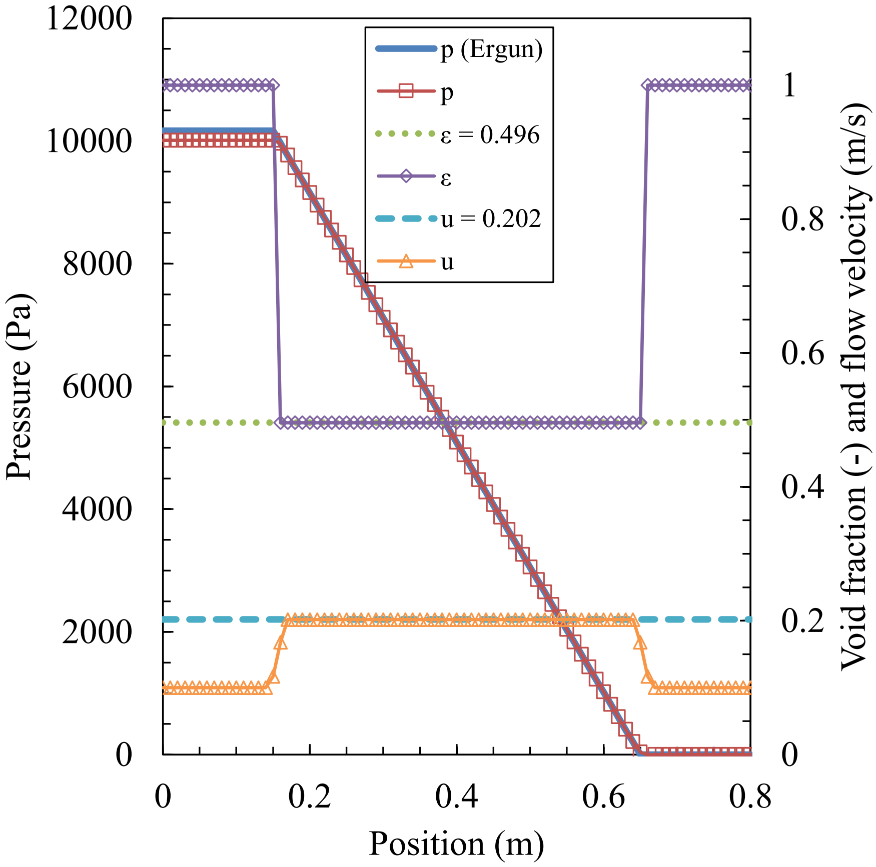

Figure 3.8: Void fraction, flow velocity and pressure along the channel.

Effect of grid size

Next we examine the computational dependency on grid size. The grid spacing used in the simulations is chosen as $\Delta x = W/8$, $W/10$, $W/12$ and $W/16$, respectively, or $3.16d$, $2.53d$, $2.11d$ and $1.58d$ measured in particle diameter. When using a refined grid size, it mainly brings in an impact on the calculation of void fraction, as illustrated in Figure 3.9. From its inset showing close-up of the ε values calculated on different grids, it seems that the $\Delta x = W/10$ or $2.53d$ grid gives the best results because particles are evenly fitted in each cell. The ε calculation is generally robust to larger or smaller cells ($\Delta x = 3.16d$ or $2.11d$) where the deviation is not very noticeable. A finer cell size ($\Delta x = 1.58d$) can lead to fluctuation and overshot values of ε, but the error is relatively small (about 1% relative error).

However, too much excessive refinement of the cell size might lead to unacceptable estimation of ε and consequently affect the fluid states such as velocity and pressure. Hence it is important to choose a grid size compatible with the particle diameter scale.

Effect of packing state

Besides the regular configuration of particles, a random packing state is also considered in this study. In order to avoid possible particle overlapping, the random bed of 78125 particles is generated by using a modified hard-sphere packing algorithm in [61], see Figure 3.7 (b). Figure 3.10 compares the void fraction and pressure profiles for these two packing states, from which reasonable agreements can be observed.

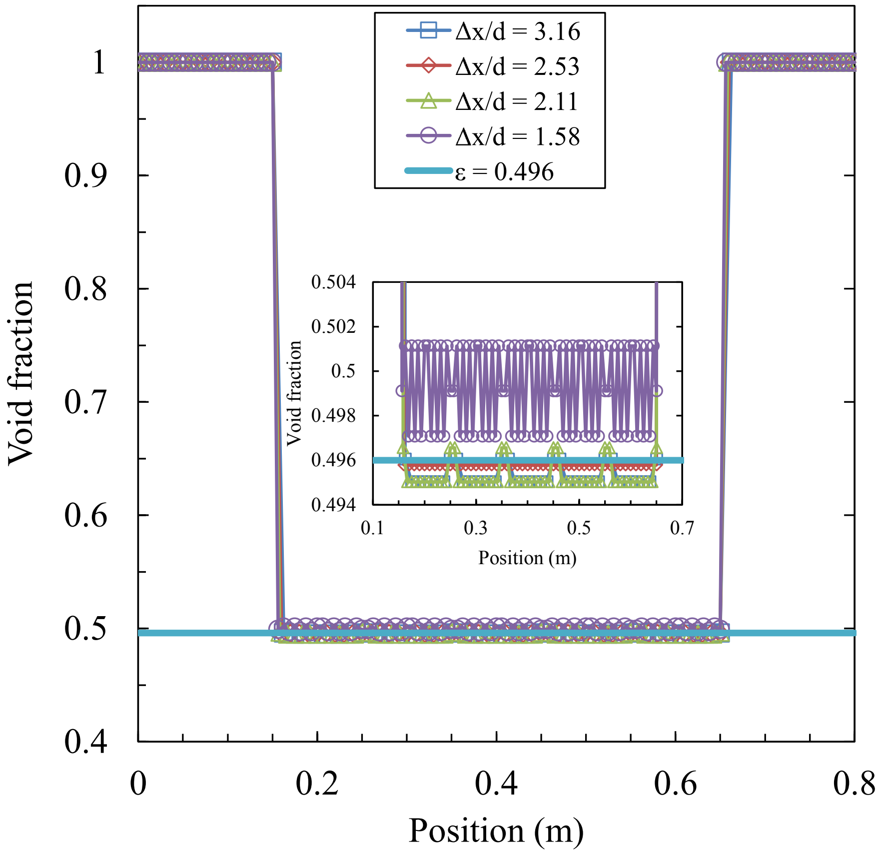

Figure 3.9: Plot of void fraction under different grid sizes.

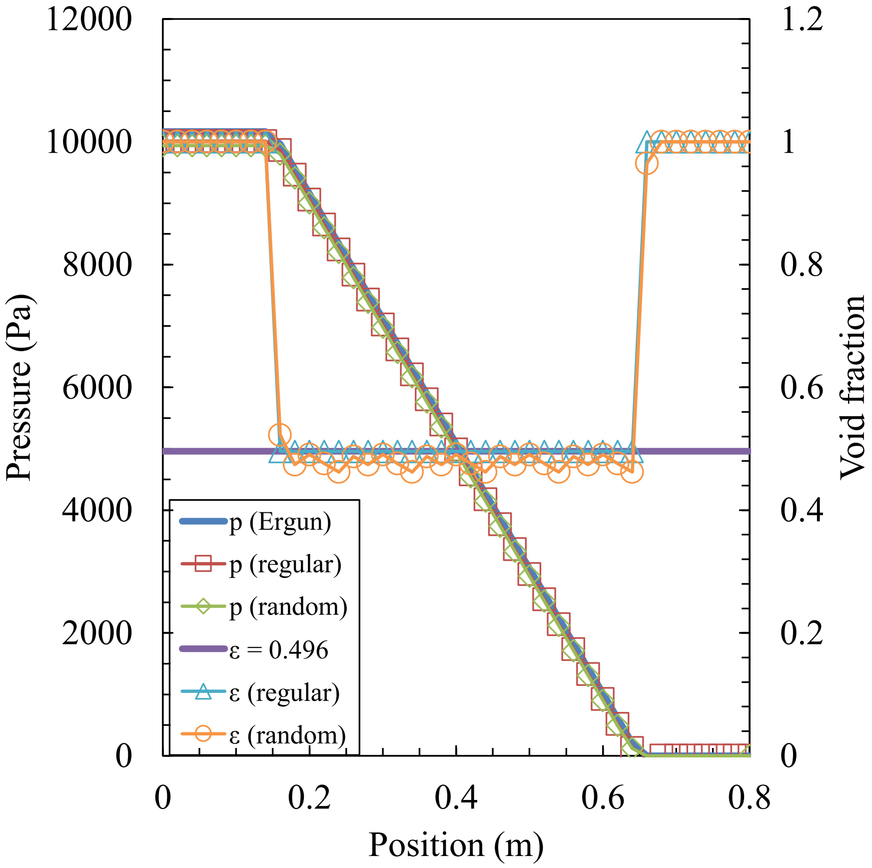

Figure 3.10: Comparison of void fraction and pressure for regular and random packing.

3.5 Numerical examples

Three-dimensional simulations of gas-solid-liquid flows are performed by using the DEM-VOF method. Some results are compared with available reference solutions, and some of them are validated against experimental data obtained in our laboratory measurement. When analyzing the results, we mainly focus on the macroscopic behaviors of the gas-solid-liquid flow system, e.g. the size, shape and motion of the free surface and the solid bed. The reason is twofold: firstly, such macroscopic behaviors are provided as the most evident criteria for justifying the simulation results from a phenomenological point of view; secondly, they can also be useful to characterizing flow regimes and determining key parameters such as particle loads in engineering practice.

3.5.1 Water entry of particle block

The water entry problem of solid objects is an interesting problem involving complex free surface motions and solid-liquid interactions. Particularly in a finite enclosure, the free surface must rise accordingly as the same amount of immersed solid volume. In this test, the sedimentation of a block of particles in an air-water column is simulated.

The computational domain size is 0.05 m by 0.20 m by 0.05 m, with the gravity $g = 9.8$ m/s^2 in the $-y$ direction. We use $16 \times 64 \times 16$ uniform cells to cover the entire domain. Non-slip wall boundary condition is enforced at all boundaries except the top boundary which is transparent. The free surface initially located at $y = 0.05$ m separates the domain into an air part ($\rho_g = 1.0$ kg/m^3 and $\mu_g = 10^{-5}$ Pa·s) and a water column ($\rho_l = 1000$ kg/m^3 and $\mu_l = 10^{-3}$ Pa·s).

Totally 10000 particles aligned on a $20 \times 25 \times 20$ lattice are placed just above the free surface. The particle diameter is $d_p = 2.0$ mm and the distance between their centers is 2.01 mm. Their density is set to $\rho_p = 2500$ kg/m^3. For numerical parameters used by the DEM, the spring constant is 500 N/m, the restitution coefficient is 0.9 and the friction coefficient is 0.3, respectively. It is noted that those numerical parameters are not necessarily the same as their physical counterparts. They are selected in the way based on our previous numerical studies using the DEM, see e.g. [43]. The computation is conducted with a fixed time step of $\Delta t = 2.0 \times 10^{-5}$ sec and runs up to $t = 2.0$ sec after the particles all get settled.

Particle and interface motion

Figure 3.11 shows a series of snapshots from the falling to final sedimentation, where the particles are colored by the magnitude of velocity and the free surface is rendered by the 0.5-contour of the VOF function. When the simulation begins, particles soon fall through the air-water interface under gravity in about $t = 0.1$ sec, which is close to the time predicted by a free falling. At the same time, the particle block expands laterally and fills the gap between the initial shape and the vertical wall. The water is also squeezed out of the original gap forming high jets climbing along the wall, especially at the four corners. After all particles are submerged beneath the free surface ($t > 0.2$ sec), it seems that their motions are generally found in two patterns: (a) the particles in the central part descend almost straightly and some of them reach the bottom in as early as $t < 0.4$ sec, but (b) the near-wall particles experience a rolling-up motion induced by the upward water flow, which causes that the particle block is stretched and fills up almost the whole water body. Such a motion is most noticeable near the corners and can last until $t = 0.6$ sec when the bulk of the particle bed has already get settled.

The images in Figure 3.12 are the same snapshots but the particles are labeled by their vertical positions in the initial block, from which the topological change of the particle block is easily observable. The bottom particles (colored blue and green) are partially flipped to the mixing region and they form two separated layers wrapping the original top particles (colored red) in the final deposits.

These patterns of particle motions could also be confirmed via Figure 3.13 where the trajectories of 250 out of 10000 particles are plotted by connecting their positions at different time steps. In principle, the dynamics presented here are analogous to a classical Rayleigh-Taylor instability (RTI), although the heavy fluid in RTI is replaced by the air-particle mixture and the perturbation is initiated with the impact on the free-surface in the current case.

We note that the coupling between fluid and particle phases is twofold: (a) the dynamic condition through the explicit interphase momentum exchange and (b) the kinematic condition in terms of local void fraction implicitly given by the continuity equation. It is thus critical for a numerical solver to resolve them simultaneously for such a three-phase flow problem, which is a remarkable demonstration of the capability of the DEM-VOF method.

Liquid displacement and volume conservation

The water entry simulation is also provided as a test to examine the volume conservation property for the DEM-VOF method, which is naturally a physical requirement for numerical modeling of gas-solid-liquid flow systems. From the snapshots in Figure 3.11, it is evident that the water entry of solid particles has caused the free surface to rise significantly. The advancement of water surface is theoretically 0.0168 m based on the total particle volume and sectional area of the column. This expected water level is compared with the last computational result at $t = 2.0$ sec.

As illustrated in Figure 3.14, the free surface lifted over its initial position runs across the analytical position and is sloshing weakly. The temporal variation of the total volume of the water phase is plotted in Figure 3.15. During the penetration of particles across the free surface, a tiny volume error (smaller than 1%) is observed which is generally acceptable for engineering applications. After that, the remaining volume is exactly conserved for the water phase without any loss. Hence it is shown that the proposed method can simulate the water displacement of solid particles correctly.

Although the water entry problem is designated as a fully numerical example due to the absence of theoretical solution and limited experimental conditions, it seems that these results are reasonable, especially with regard to the free surface deformation and rising. On the other hand, a qualitative likeness in flow pattern and particle motion has also been confirmed in our recent DNS study of a similar but substantially smaller problem setting-up (unpublished), which indirectly supported the reliability of current results. A critical comparison between DNS and volume-averaging simulations is beyond the scope of this study, but it will be pursued in a near future.

We also note that, although complex fluid-particle interactions and free surface deformations are successfully reproduced by using the present model, it is however unlikely to capture microscale phenomena smaller than the particle size scale such as the bubble entrainment and cavity attachment behind falling particles, which is an inherent drawback due to computational resolution of the fluid phase in a volume-averaging simulation.

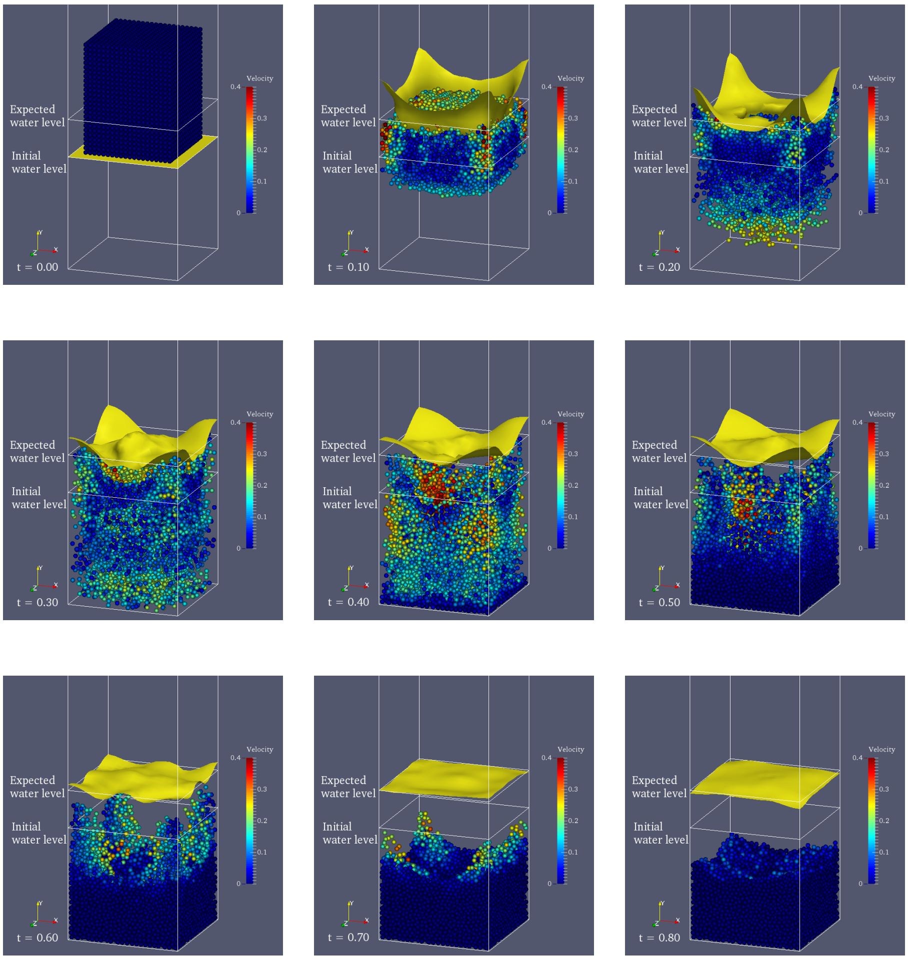

Figure 3.11: Snapshots of water entry of particles (colored by velocity).

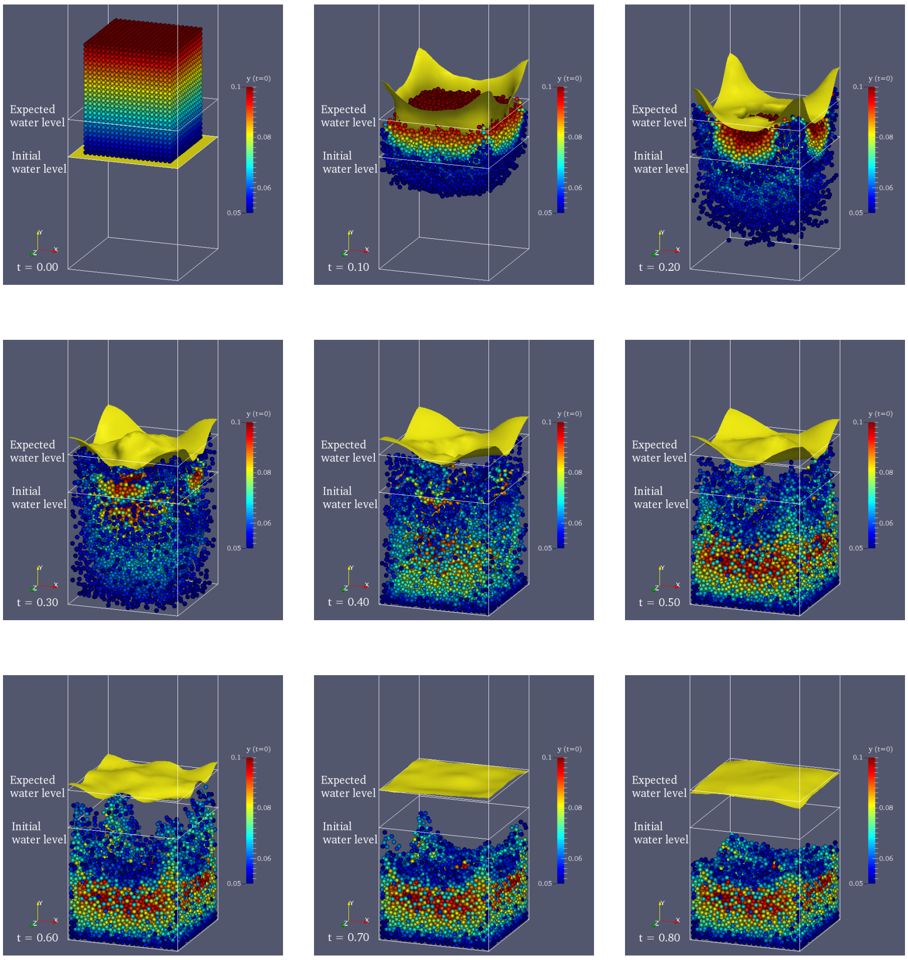

Figure 3.12: Snapshots of water entry of particles (colored by initial vertical position).

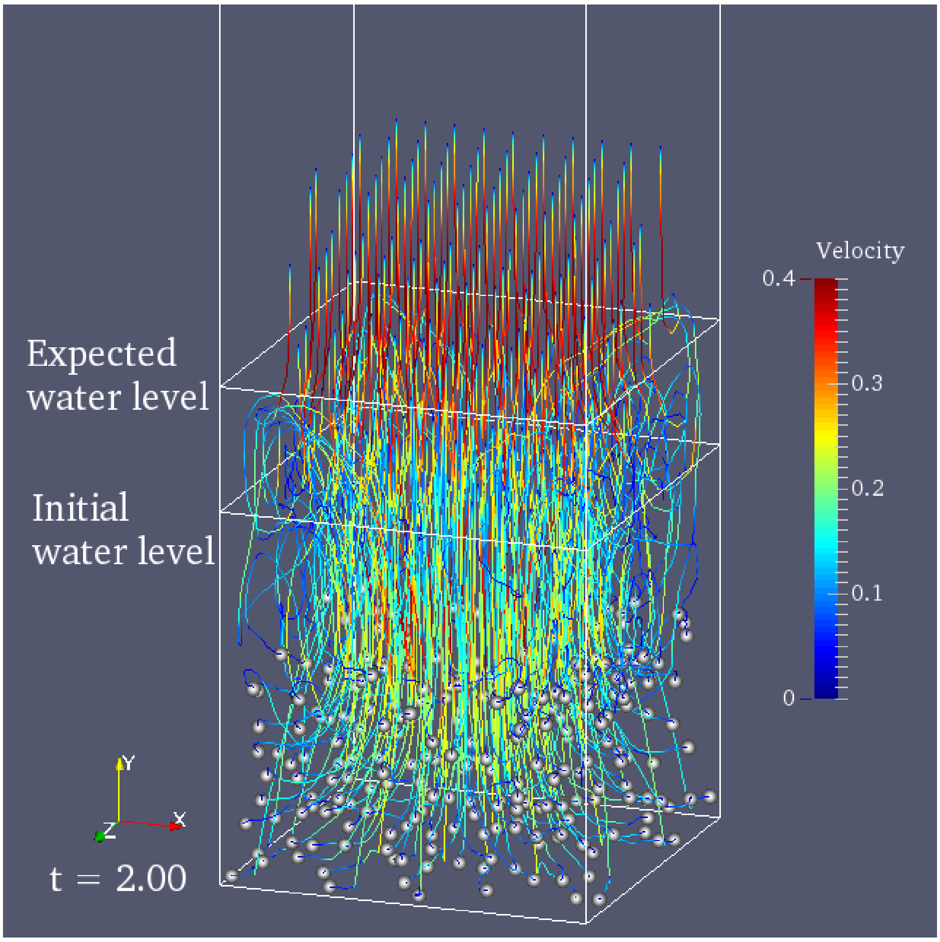

Figure 3.13: Water entry of particles: path-line of 250 representative particles.

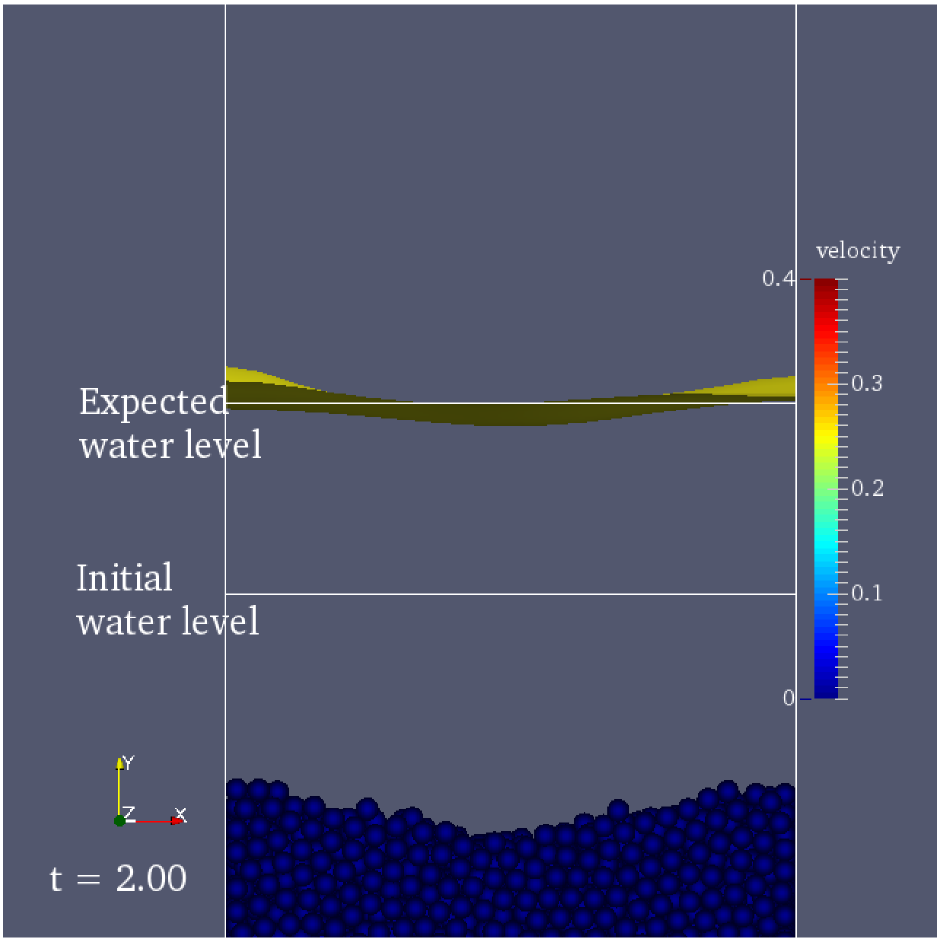

Figure 3.14: Water entry of particles: free surface at $t = 2.0$ sec.

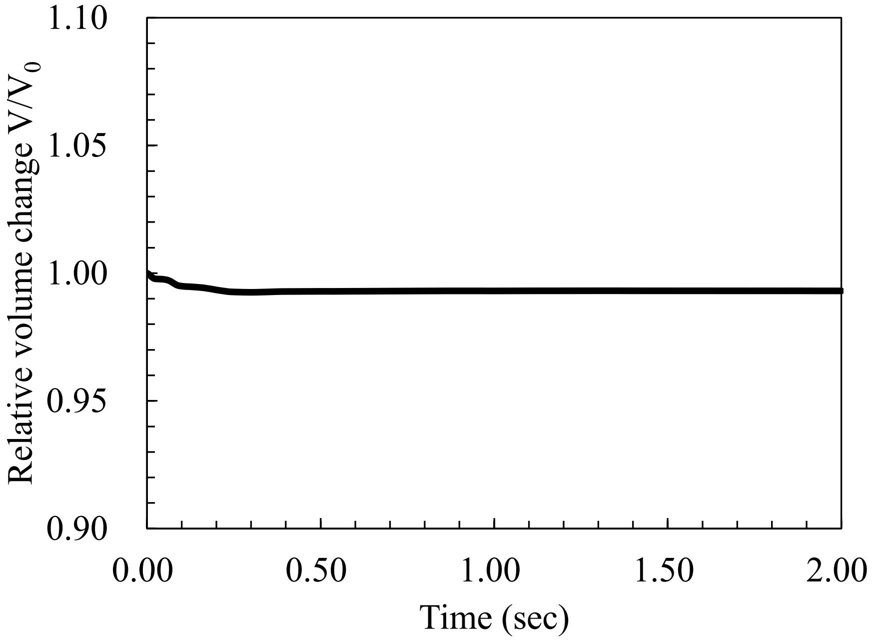

Figure 3.15: Water entry of particles: temporal variation of the volume of water phase.

3.5.2 Three-phase dam break flow

The dam break problem is a test case for incompressible two-phase or free surface flows, and it also has a wide application in ocean engineering. Although the classical gas-liquid dam break has been well studied in last decades which dates back to the experiment of [62], its three-phase version containing a particle bed has not been thoroughly discussed. Among limited literatures, some authors reported numerical results by using Lagrangian particle methods ignoring the gas phase motion, see [44, 63]. In this test, we simulate a dam break flow involving fully gas-solid-liquid three-phase dynamics and perform experiments for validation.

Similar to the typical setting-up of a dam break problem, initially a reservoir holding the water or solid-liquid mixture, whose length is a, and height is h, stands still in a tank. When released, the water dam will collapse under gravity and the wave propagation along the floor is simulated. As usual, the set of dimensionless time t^*, front z^* and height y^* is used to describe its motion:

$$t^* = t\sqrt{2g/a}$$
$$z^* = z/a \text{ and } y^* = y/a$$

in which z is the front position and y is the remaining height of the dam.

For the problem setting-up, the length, width and height of the computational domain are 0.2 m, 0.1 m and 0.3 m, respectively. Non-slip boundary condition is set at all vertical and horizontal walls including the top boundary to prevent the splashing water or particles from escaping. Since the air-water density ratio is as large as 1000 times and the domain is sufficiently high, our numerical tests show that results are not affected by the choice of boundary condition at the top of the domain. The reservoir with initial length $a = 0.05$ m holds a solid bed of glass beads. It is then filled up with water to a height of $h = 2a$. Totally 3883 glass beads are used in this test, and they are known have a mean diameter of 2.7 mm. The solid bed packed randomly from the reservoir bottom by using those particles is approximately 15 mm high. The rest of the computational domain is assumed to be air.

Table 3.3 lists the computational parameters for the dam break problem. The physical properties close to the air and water are used for the fluids and the surface tension is neglected in the simulation. The fluid cell size is $\Delta x = 5 \times 10^{-3}$ m. The particle density is 2500 kg/m^3. For the DEM contact parameters, the spring constant is 10^3 N/m and the coefficients of restitution and friction are 0.9 and 0.3, respectively. The time increment is 5.0×10^{-5} sec for the fluid and 1.0×10^{-5} sec for the solid. Hence five sub-iterations of the particle computation are executed per time step.

Table 3.3: Computational parameters for the three-phase dam break.

Liquid density (kg/m^3)	1000
Liquid viscosity (Pa s)	10^{-3}
Gas density (kg/m^3)	1
Gas viscosity (Pa s)	10^{-5}
Fluid cell size (m)	0.005
Fluid time step (s)	5×10^{-5}
Particle density (kg/m^3)	2500
Particle diameter (mm)	2.7
Spring constant (N/m)	1000
Restitution coefficient (-)	0.9
Friction coefficient (-)	0.3
Particle time step (s)	1×10^{-5}

Full-scale lab experiment is performed to obtain reference data. The tank is equipped with a shutter gate to lock the fluid-particle mixture. The gate is connected to weights through metal wire and it will be pulled up once the weights are released. The motion of the dam break flow is then recorded by a high-speed camera. From the pictures it is measured that the gate rises approximately at a constant velocity of 0.84 m/s. This effect of gate rising is also reflected in the simulation by adding an obstacle in front of the water column.

Three-phase dam break behavior

Snapshots of the gas-solid-liquid dam break flow are shown in Figure 3.16 for the physical time from $t = 0$ to 1.1 sec with intervals of 0.1 sec. The overall behavior is comparable with a classical dam break: as the gate is being removed, the mixture column flows through the opening gap between the gate and floor to form an elongating surge front. The remarkable point in these results is that the particle motion is also captured, as rendered by scattered dots with their velocity contour. It is seen that the particle bed moves more slowly than the water front does in early stages of the dam break for $t < 0.2$ sec. After that the particle layer slightly vibrates following the water sloshing. It is also interesting to observe that particles near the left corner are shoved aside, subject to the impact of water falling from the wall ($t = 0.5$ and 0.7 s), which implies an effective interaction between them.

Additionally, velocity vectors are presented for the central plane of the domain as well in Figure 3.16. They clearly describe the motion of the air phase in this system: the air flows over the gate to fill the cavity left empty behind the collapsing dam at $t = 0.1$ s; later strong vortices are generated from the free surface ($t = 0.4$ s) and spread to the entire air region ($t = 0.6$ s). It is known that the air can play important roles in dam break problems involving severe interface deformations and air cushion effects, see e.g. [64]. Those results turn out to be true proof for the three-phase nature of the DEM-VOF method.

Comparison with experimental observation

Figure 3.17 gives a detailed comparison of the simulation results with the experimental photographs for different time instants. As mentioned above, the locked gate is rising and the mixture dam is collapsing at $t = 0.1$ s, and the accelerating water and particle form a double-layer surge front. Consequently the front arrives at the opposite wall around $t = 0.2$ s. The solid particle bed expands over the floor of the tank and the water hits the vertical wall. The bulk of the water-particle mixture goes on moving forward and strongly impacts against the tank, which leads to a high water jet attached to the wall at $t = 0.3$ s. The solid layer also follows this motion, as it is found that at the left corner of the tank lies a pile of particles as well as some splashing ones. Finally at $t = 0.4$ s, a plunge wave is bounced back from the wall and most particles are again settled to be a solid bed that is thick at two ends and thin in the middle. In regard to the interface shape and particle bed configuration, the agreement between simulation results experimental data is apparent.

Water position and effect of solid phase

In addition, the normalized dam positions at the bottom floor (front z^*) and right wall (top y^*) are plotted against dimensionless time t^* to show the temporal variation of the dam shape. In order to examine the simulation results, Figure 3.18 compares the computed dam positions with those measured from the experimental photographs. They agree excellently before the front reaches the opposite wall.

Furthermore, simulations of a classical gas-liquid dam break (with the same aspect ratio of the initial shape) are performed independently and their results are presented together with the current gas-solid-liquid test in Figure 3.19. This is intended to emphasize the difference brought in by the solid phase. Compared with its gas-liquid counterpart, the gas-solid-liquid dam seems to move slower especially in terms of the front position, which is plausibly explained by the influence of solid particles.

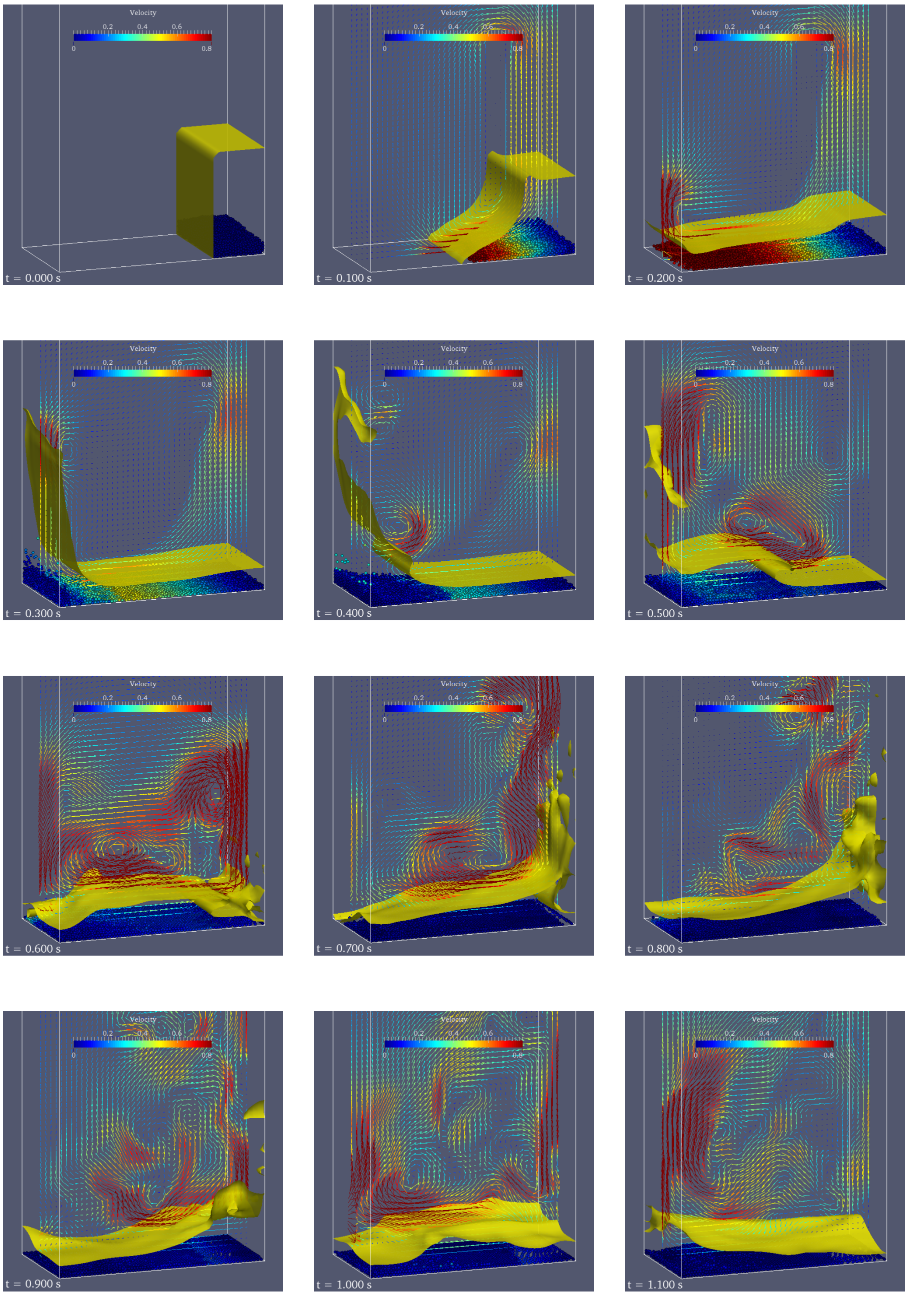

Figure 3.16: Snapshots of the three-phase dam break flow.

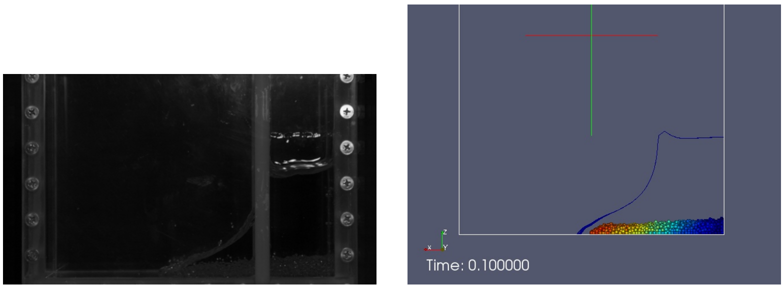

(a) $t = 0.1$ sec

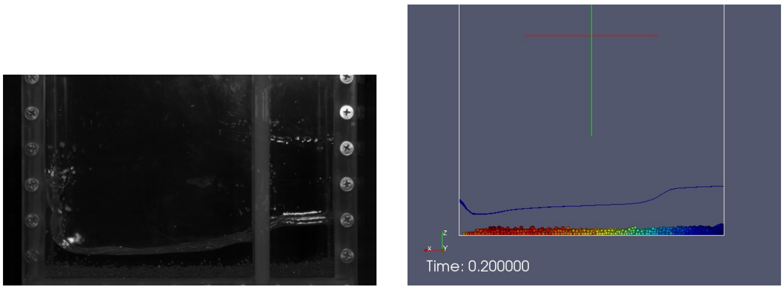

(b) $t = 0.2$ sec

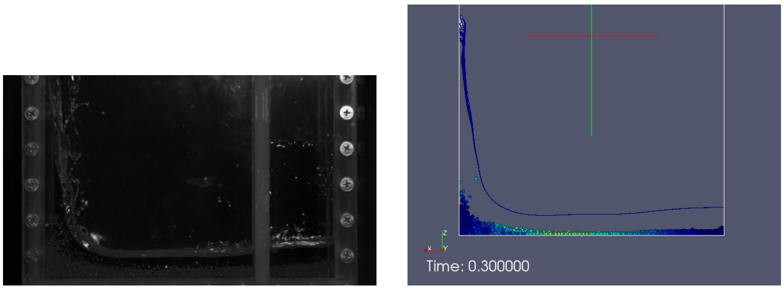

(c) $t = 0.3$ sec

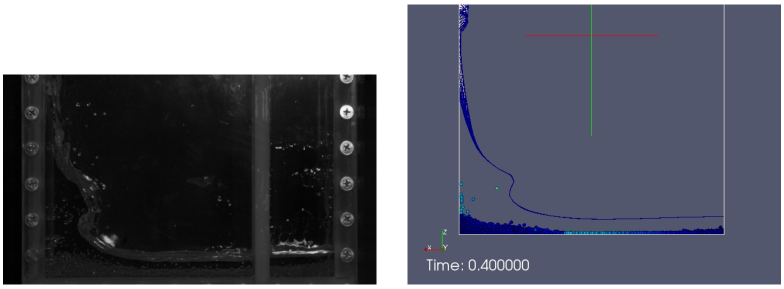

(d) $t = 0.4$ sec

Figure 3.17: Dam break flow: comparison of experimental photographs (left) and computational results (right).

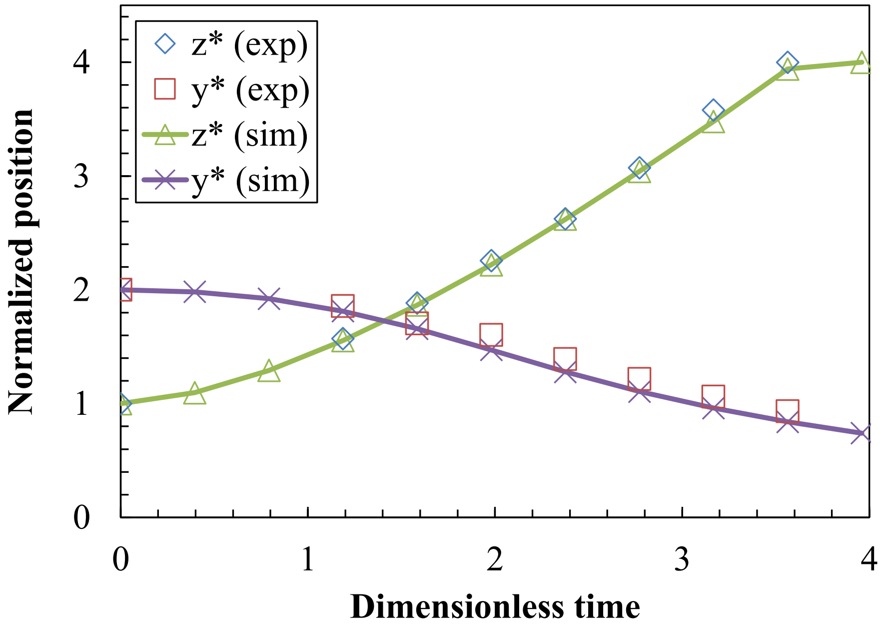

Figure 3.18: Three-phase dam break: comparison between simulation results and experimental data.

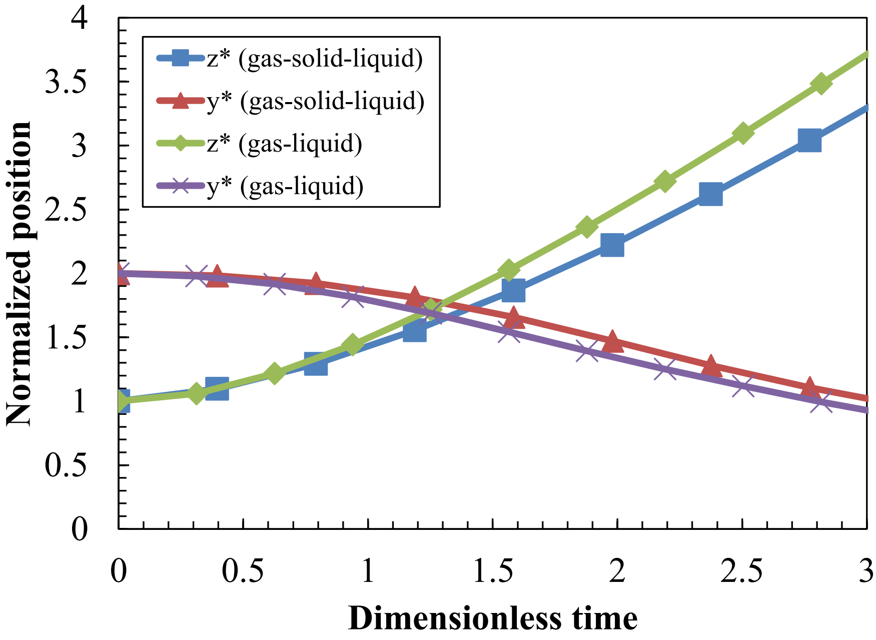

Figure 3.19: Three-phase dam break: comparison between three-phase and two-phase simulations.

3.5.3 Circulating flow in a rotating drum

The rotating cylindrical tank system, provided as a simplified model of powder devices such as a wet ball mill, is an important test case in the engineering context of grinding and mixing. In this study the circulating gas-solid-liquid flow is computed in such a rotating drum system as illustrated by Figure 3.20. Physically the cylindrical tank has an inner diameter of 120 mm and a depth of 100 mm. A mixture of water and glass beads fills the lower part of the partially-filled tank. The tank is driven by rollers and its speed of rotation is measured by a tachometer. We will mainly focus on the macroscopic aspects of the gas-solid-liquid flow at quasi-steady state, e.g. the shape and size of the solid bed.

A rectangular domain of $0.16 \times 0.16 \times 0.12$ m is used with uniform mesh size of $\Delta x = 0.004$ m in the simulation. The curved boundary of the cylindrical tank that does not conform to the grids is embedded in the center of the domain. As described in our numerical model, inside the tank is the true computational domain in which the motion of the gas-solid-liquid flow is solved, while the outer part represents the rotating geometry of the tank. This computational configuration is demonstrated in Figure 3.21. The solid bed is composed of totally 14555 glass beads with mean diameter of 2.7 mm. It is submerged in a water layer filling up to half the elevation of the tank. The physical properties and DEM parameters are the same as those used in the previous test problem. The time step of the DEM is 1.0×10^{-5} s and that of the continuum phase is five times larger.

Convergence towards quasi-steady state

The drum rotates at 63 rpm and the simulation runs until a quasi-steady state is reached. This point is ensured by examining the temporal evolution of the translational kinetic energy of the solid phase. Figure 3.22 shows that, during the first revolution ($t < 1$ s) the energy increases fast and traverses two sharp peaks as the solid bed is undergoing lifting and avalanche along the wall. The variation converges soon after two cycles of rotation except for some small fluctuations around the equilibrium energy density approximately equal to 0.008 J/kg. Hence in this test, simulation outputs obtained between the period of $3.0 < t < 4.0$ s will be presented as quasi-steady results. We note that this statement is consistent with our previous study on this problem, see [43].

Macroscopic behaviors at quasi-steady state

Figure 3.23 (a) depicts a representative snapshot from the simulation where a steady slope of solid bed has formed. Along the axial direction of the cylinder, the bed shape is almost flat and no local clumping of particles is observed near the front and back wall, which is also confirmed through our experiments. For a critical comparison of the bed shape, the experimental photograph is overlaid with the outline sketch of the computed slope in Figure 3.23 (b) in which the dashed line corresponds to the numerical solution. It is clearly seen that the bed shape is exactly recovered by simulation results.

Table 3.4 lists the bed width and height measured from the experiment and simulation, respectively. The relative error is below 2% and their agreement is also quantitatively satisfactory. Hence, it is shown that the proposed numerical model is able to accurately predict macroscopic behaviors in respect of solid bed shape and size for a three-phase flow system involving moving boundaries.

Effects of special IB treatments for fluid-particle interaction

Although the modeling of a moving boundary like the rotating tank seems to be straightforward, it is in fact non-trivial for a fluid-particle system where the computational reliability mainly depends on the validity of interphase coupling term. Here the rotating tank test case is utilized to show why the special treatments for the drag force calculation (Section 3.3.3) is necessary near the wall surface.

It is first investigated for the void fraction ε which is geometrically defined in a particle-in-cell manner regarding the local solid bed configuration. Figure 3.24 compares the ε values calculated for particles in a randomly packed bed with and without the corrective procedure of cell merging. The bright-yellow circle therein draws the outline of the tank and light-grey lattices depict the numerical cells surrounding the solid bed. For such a bed with equal-sized particles, as a matter of course, a rather homogeneous distribution of void fraction is expected inside the solid bed as well as in the vicinity of the rigid walls. This is well confirmed in Figure 3.24 (a) and (c) employing the ε correction for particles near the front surface and the curved bottom of the cylindrical tank, where the void fraction is reasonably close to the theoretical limit of random close packing of monodisperse spheres. If no correction is applied to the near-wall particles, noticeable deviation from our expectation is observed in both front and bottom views of Figure 3.24 (b) and (d), respectively. We note that, this is not a consequence of the physical confinement of the wall but a numerical artifact depending on the grid resolution and configuration.

Another strategy of near-wall correction is applied when determining the flow velocity at particle positions, as described by the biased interpolation procedure in Section 3.3.3. Its effectiveness is examined in a different rotating tank system. The dimensions of the tank are kept the same, but it revolves with a faster speed of 100 rpm. A loose, regular solid bed of 160000 particles with diameter of 1 mm is used instead. This solid bed is initially suspended in the lower part of the tank and does not touch the surrounding walls. The friction between particles and tank is set to zero. Modifications are made so to magnify the effect of fluid drag and to eliminate the frictional acceleration. Note that the treatment for the void fraction is always valid in this computation.

Figure 3.25 gives snapshots at $t = 0.005$ s of simulation results (a) with and (b) without the velocity correction. As indicated by the velocity contour in Figure 3.25 (b), the thin layer of particles adjacent to the front wall exhibits an abnormal azimuthal velocity distribution, which is mostly ascribable to the fluid drag since the wall friction is zero. According to the general form of drag force (3.24), the drag force is proportional to the flow velocity minus particle speed. Therefore a naive interpolation of the velocity field partially blending the contribution of a rapidly rotating boundary will inevitably overestimate the drag force and consequently lead to spurious behavior of the fluid-particle system.

Again, it turns out to be a nonphysical motion that explicitly depends on the grid configuration. Figure 3.26 provides a close-up view of near-wall particles and grids from the top without the correction. It is observed that the false acceleration due to uncorrected drag force is restricted to the two arrays of particles accommodated within the partial cells where the front wall is embedded. With the adoption of the correction based on biased velocity interpolation, those problems can be suppressed to a large extent, as implied by Figure 3.25 (b).

In this way, the problems caused by indiscriminate inclusion of boundary data have been revealed through our numerical tests and discussions. It is doubtlessly proved that the proposed treatments for the fluid-particle interaction is vital for gas-solid-liquid flow systems involving complex boundaries.

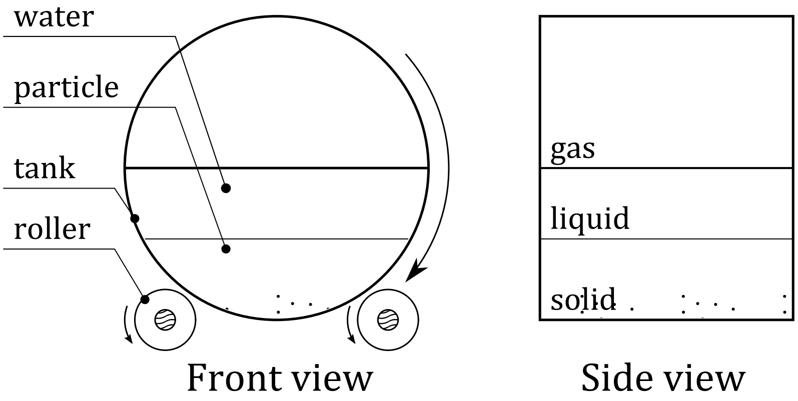

Figure 3.20: Schematic diagram of the rotating cylindrical tank.

Table 3.4: Rotating drum: comparison of the bed size.

	Bed width (mm)	Bed height (mm)
Experiment	93.9	67.8
Simulation	92.3	66.8
Relative error	1.70%	1.47%

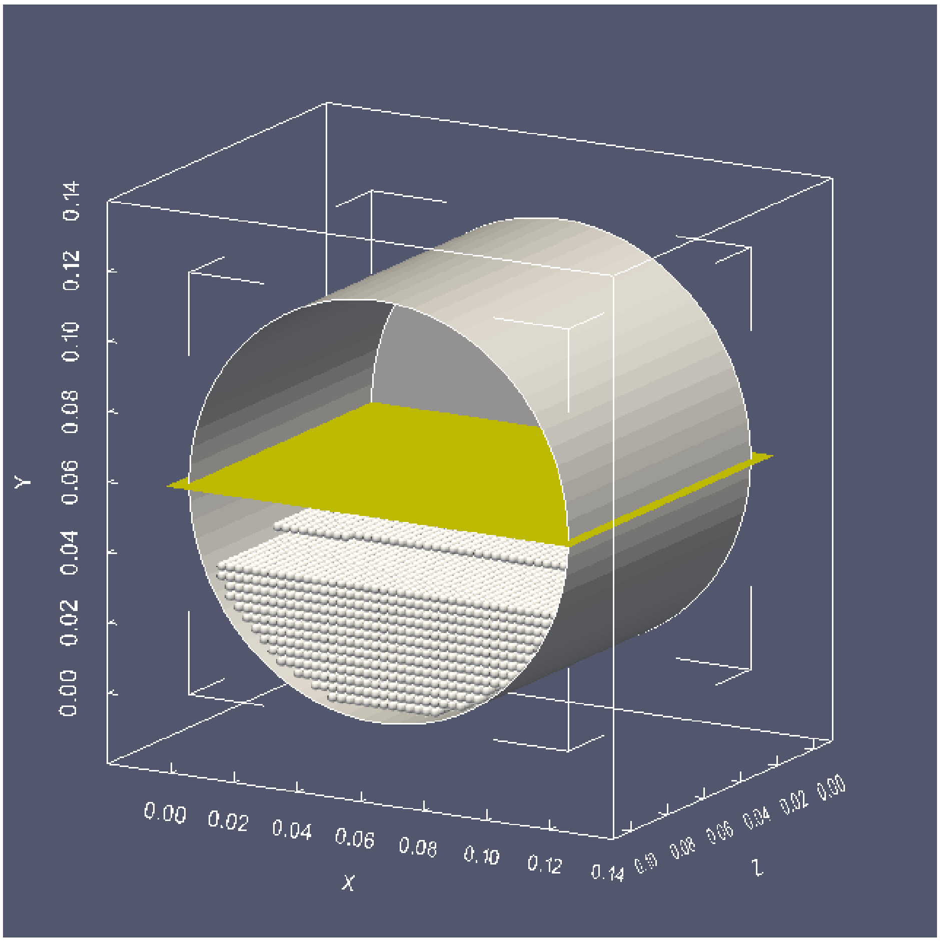

Figure 3.21: Computational setting-up of the rotating cylindrical tank.

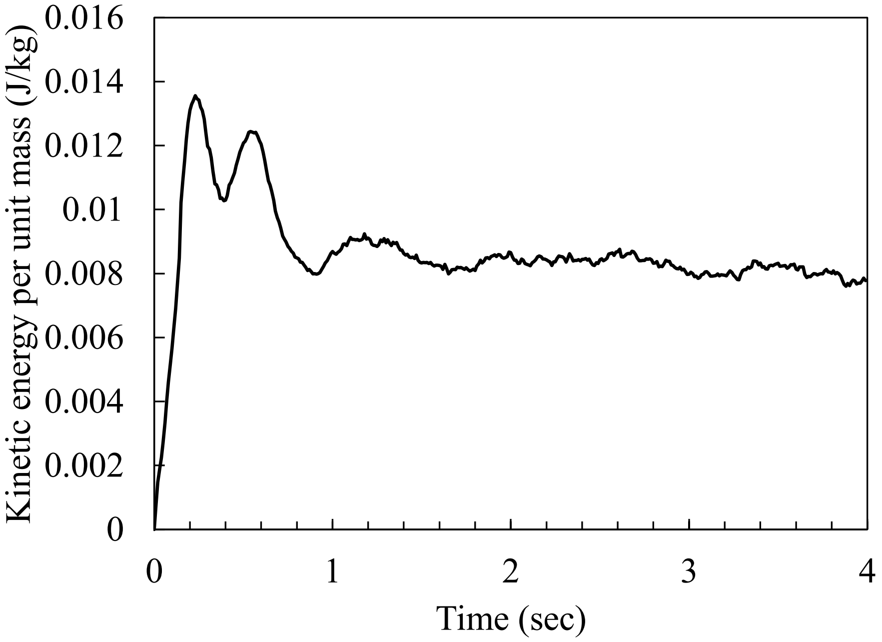

Figure 3.22: Rotating drum: evolution of the kinetic energy of the solid phase.

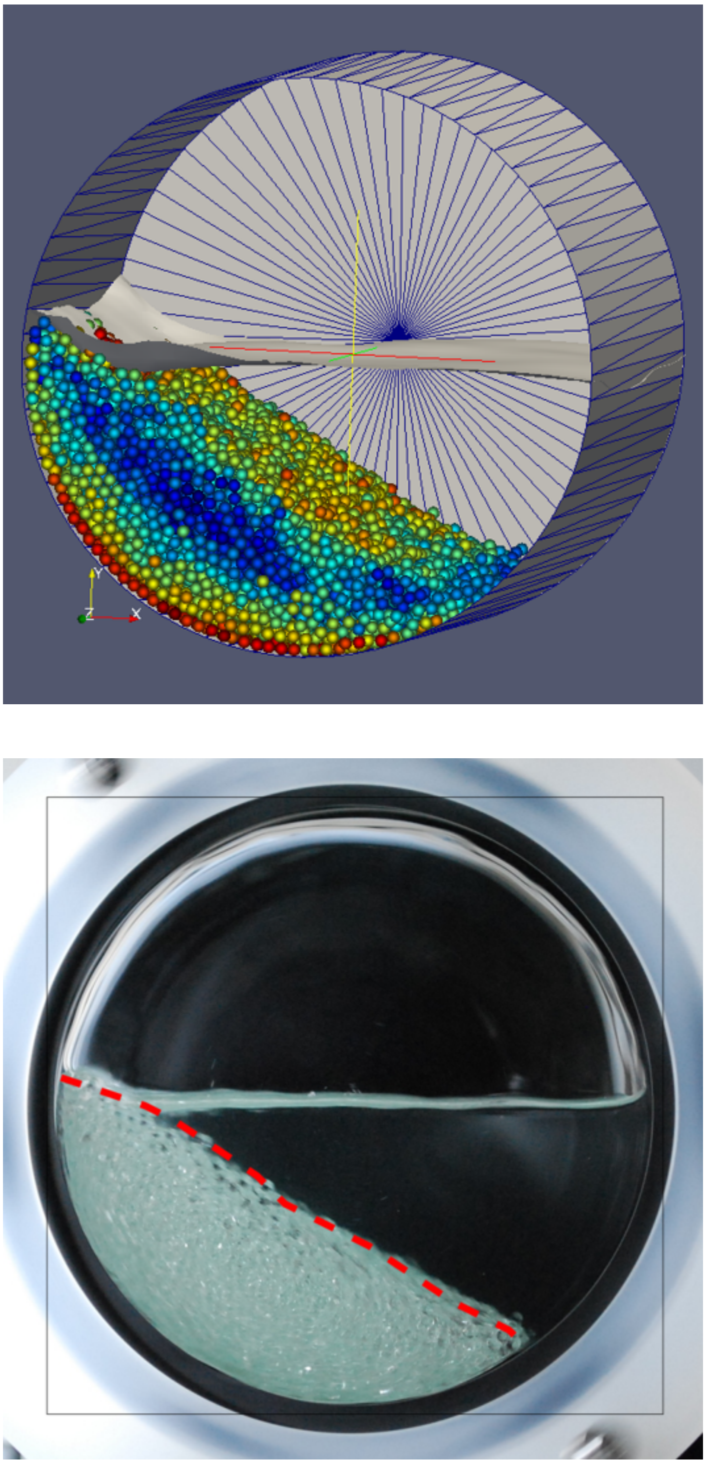

Figure 3.23: Rotating drum: (a) particles and free surface at quasi-steady state and (b) comparison of solid bed shape where the red dashed line shows the computed shape.

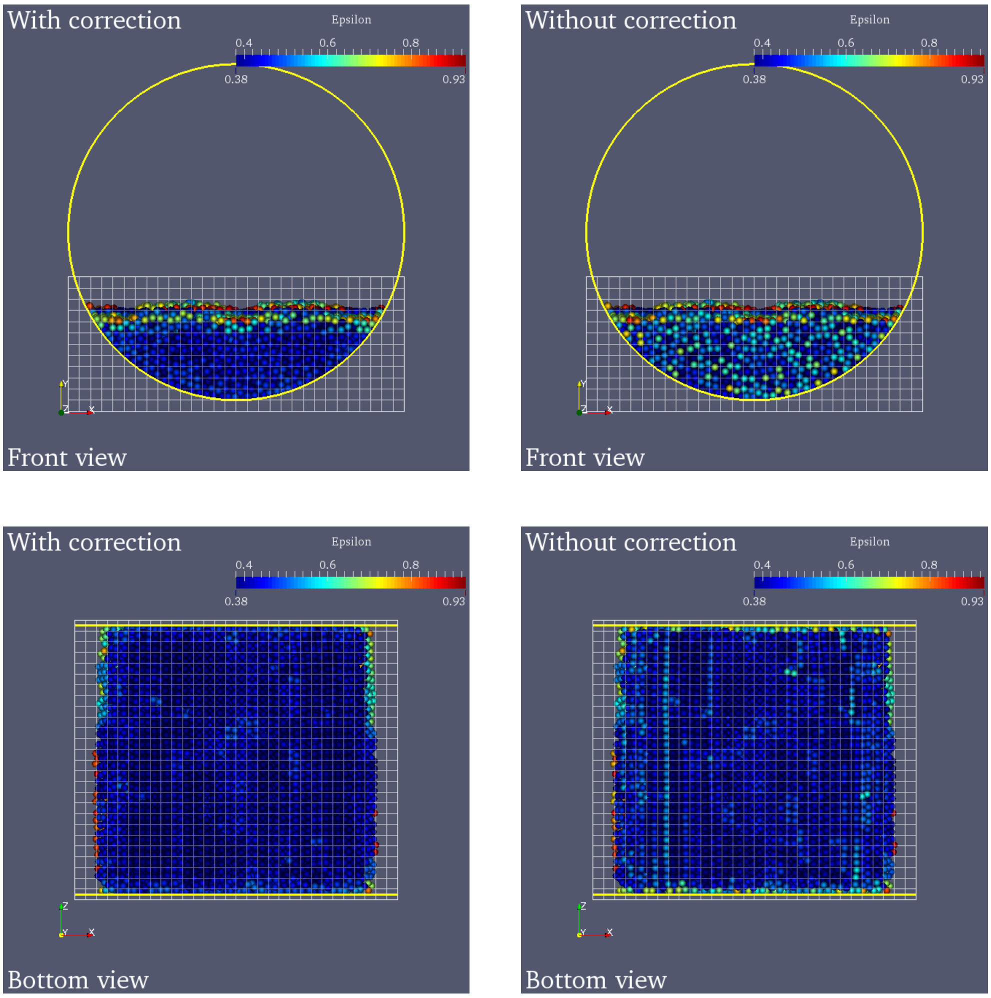

Figure 3.24: Effect of void fraction correction near the wall.

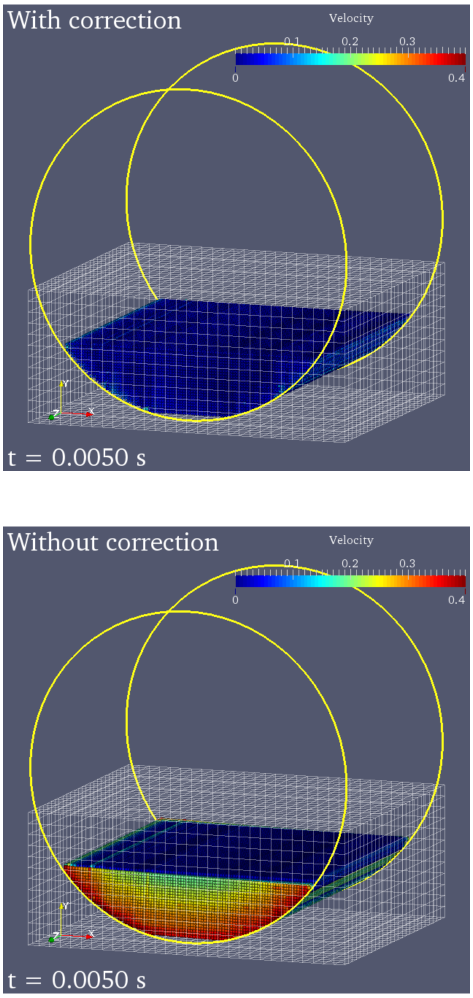

Figure 3.25: Effect of velocity interpolation correction near the wall.

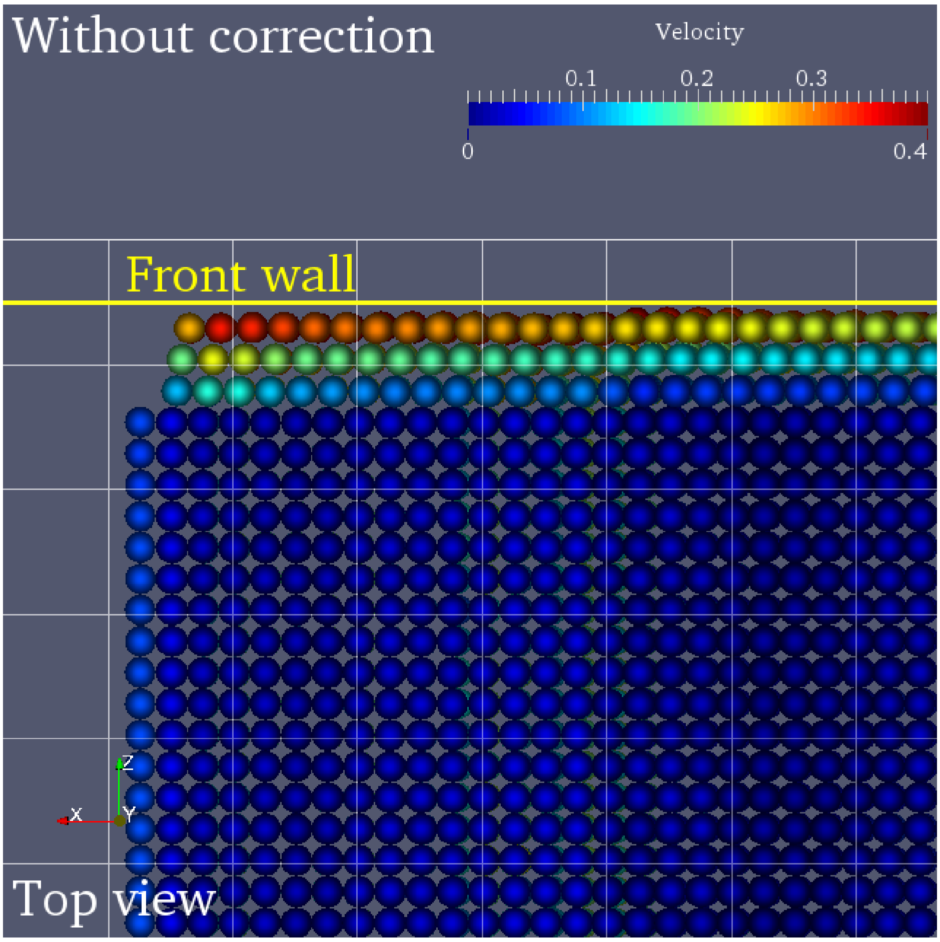

Figure 3.26: Close-up view of spurious velocity and near-wall grids.

3.6 Application to twin screw kneader (TSK)

In order to show the capability of the present method to model systems with extreme complexity, we present its application to 3D numerical simulations of a twin screw kneader (TSK). Nowadays the TSK plays a primary role in the chemical industry including processes of compounding and mixing. A picture of the laboratory apparatus of our TSK system is shown in Figure 3.27.

Calculating flow patterns in a TSK is not an easy job for its geometrical and physical complexities. Firstly, TSKs are, in general, composed of a fixed outer barrel and multiple screw elements or kneading blocks serialized and co-rotated around two axes. The shapes of these parts can be highly complicated, and what's more, the two sets of screw elements and kneading blocks are constantly moving asynchronously with respect to the barrel. It is thus extremely time-consuming and computationally demanding if one tries to model TSK system by generating body-fitted mesh and performing re-gridding during the simulation as the traditional CFD practice does. Secondly, in many applications the TSK features a multi-physics nature: for example, the free surface and particulate flows are frequently involved in popular TSK processing. This point further requires a versatile numerical solver able to treat the entire coupled system.

In the past, some attempts have been made to numerically explore the operation and performance of TSKs. In these known reports, the TSK is modelled by using unstructured moving meshes with complicated mesh superimposition techniques provided by commercial packages, see e.g. [65–68]. Besides the expensive punishment due to mesh manipulation, existing models are found only for single-phase continuum flow in TSK systems.

Targeting towards those two problems, we will present numerical results on two-phase and three-phase flows obtained by using fixed grid-based TSK simulations. It is shown that the TSK geometry and motion could be calculated with good efficiency, and complex flows involving free surface and solid particles can be treated as well. To the author's best knowledge, the present work is the first numerical model allowing for multiphase TSK computations.

3.6.1 Air-water flow in a TSK

In this study, such a case is carried out for our laboratory TSK system as illustrated in Figure 3.28. The TSK has a sealed barrel and is equipped with two screw elements that co-rotate in a counter-clockwise direction. The x-width (axial), y-height (vertical) and z-length (horizontal) of the outer barrel are 44 mm, 106 mm and 186 mm, respectively.

A single screw element is composed of four oblique disks arranged in a

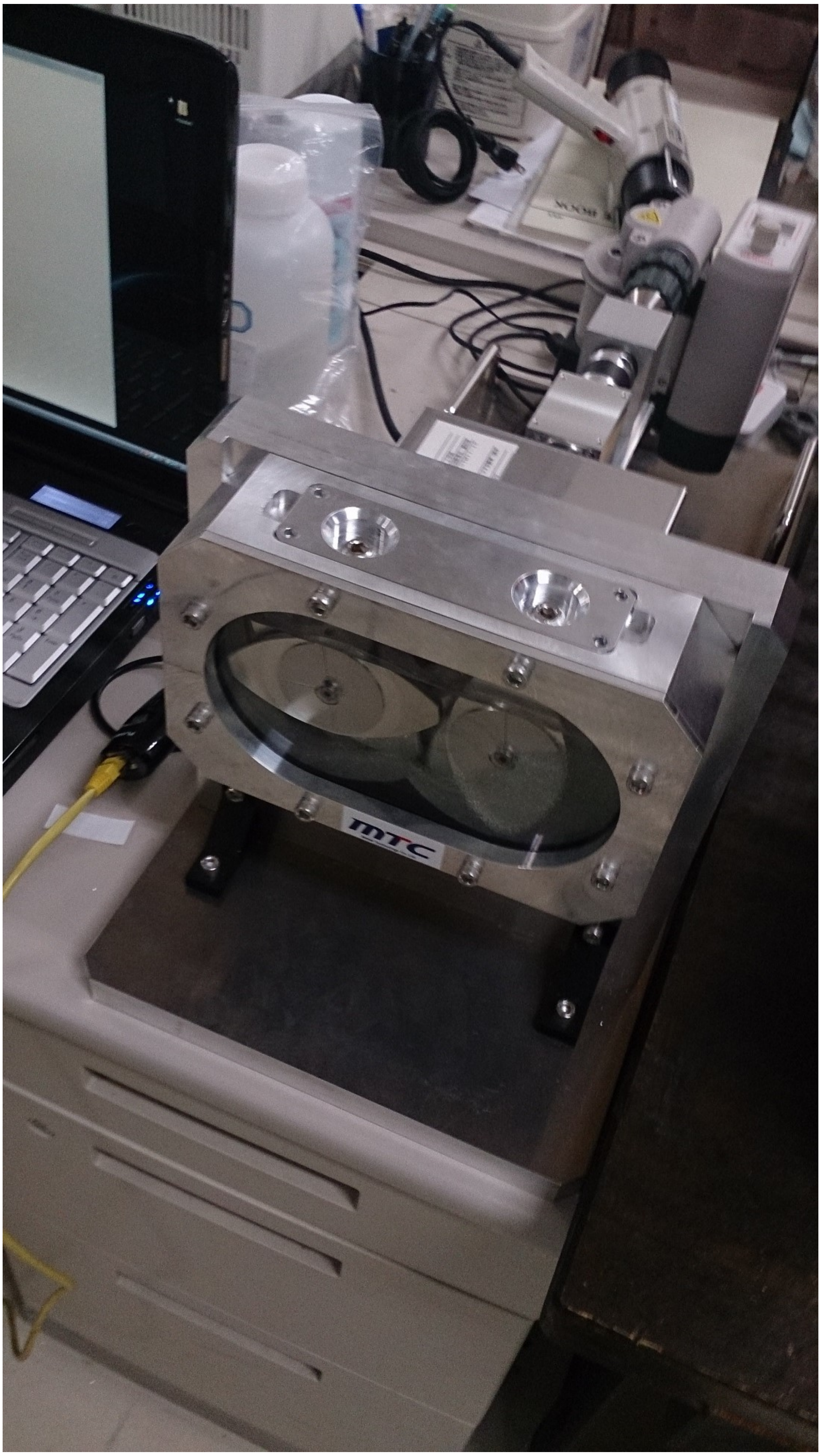

Figure 3.27: Photograph of the laboratory TSK apparatus.

Table 3.5: Computational conditions for the two-phase TSK problem.

Water density (kg/m^3)	1000
Water viscosity (Pa s)	10^{-3}
Air density (kg/m^3)	1
Air viscosity (Pa s)	10^{-5}
Surface tension (N/m)	0.075
Grid spacing (m)	2.0×10^{-3}
Time step (sec)	1.0×10^{-4}
Rotation speed (rpm)	30, 60 and 90

whorl with 45° advance angle. A disk is 7 mm thick and the gap between adjacent disks or barrel surfaces is about 3 mm. The screws outer diameter is 100 mm and the root diameter is approximately 50 mm. Center distance between the twin axes is equal to 80 mm. For the sake of brevity, information about the TSK design will not be further detailed here.

All the TSK parts, including the barrel and twin screws, are modeled by the SDF model and the IB method. Different from the primary shapes (e.g. spheres and cylinders) that are often discussed in past IB literatures or even the more complicated rotating ellipses problem (Section 2.6.5) for which one may still manage to find some analytical definition of the boundaries, it is almost impossible to represent the TSK geometry in a trivial way. This point highlights the good applicability and flexibility of our modeling for arbitrarily shaped boundaries.

For the initial setting-up, water level is set to half the barrel height. Fluid density, viscosity and surface tension are set equal to the physical properties of water and air under room temperature. The grid size is decided so that there is at least one fluid point in the narrow gap between two adjacent disks. The dilation approach introduced in Section 2.5.3 is used to treat the wall contact because boundaries can come very close in this problem.

Three simulation cases with screw speeds of $\Omega = 30$ rpm, 60 rpm and 90 rpm are considered in order to examine the effect of rotation speed. These computational conditions are summarized in Table 3.5. For this problem, the Reynolds number based on the tip speed U, disk cross-sectional length L and water kinematic viscosity ν is roughly estimated to be $Re \sim 5000$. In this study, turbulence models are not taken into account because of the complex wall shapes; the LES approach suggested by [42] may be considered in the future.

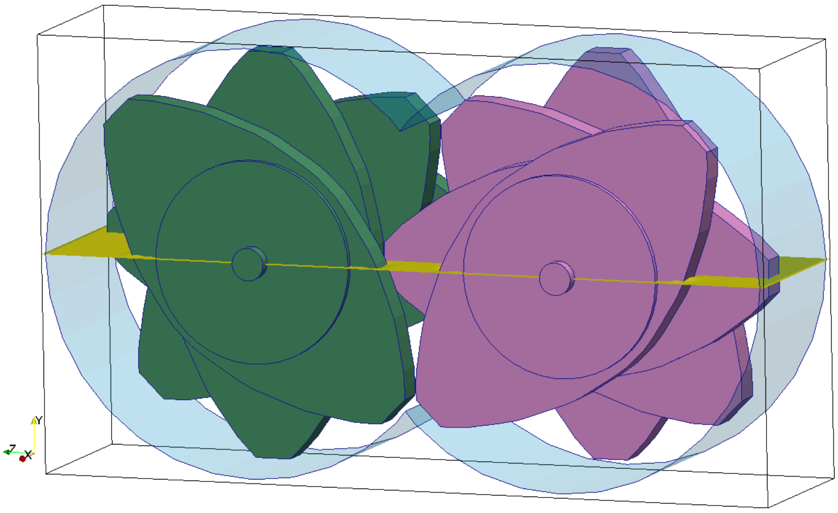

Figure 3.28: Two-phase TSK: initial setup.

Temporarl evolvement of the two-phase flow

We first present charts of the kinetic energy of the two-phase flow within the TSK as a function of time to depict the temporal evolvement of the system. Figure 3.29(a) plots the kinetic energy per unit fluid volume e against simulation time t to show the convergence towards quasi-steady states. From Figure 3.29(a) it is seen that the air-water mixture starts with a state of rest and reaches the quasi-steady state very soon under the agitation of screw paddles in all cases.

We have also noticed that, the relationship between temporal variation of kinetic energy and rotation speed can be more clearly revealed by plotting the normalized kinetic energy density $e^* = e/(\rho_m U^2/2)$ against the non-dimensional time $t^* = t/T$. Herein, ρ_m is the average fluid density which is equal to $\rho_m = 500.5$ kg/m^3 in the current TSK system and $T = 60/\Omega$ is the rotation period of the screw paddles. This relationship is shown in Figure 3.29(b) from which the flows in all three cases are known to reach quasi-steady states readily after one cycle of screw rotation, i.e. $t^* > 1$. After that, it seems that all simulation cases are shifted to a constant value of normalized kinetic energy density $e^* \sim 0.085$ which is almost independent of the rotation speed.

Besides the systematic behaviors from the viewpoint of energy, we have also examined the flow fields at three individual probes, whose positions are illustrated in Figure 3.30: the probes A and C are located beneath the screw paddles, and probe B is at the conjunction of the barrel. The coordinate is chosen that the x-axis is parallel to the axis of screw paddles, the y-axis is the vertical direction of gravity, and the z-axis runs along the line connecting the radial centers of the barrel. Figure 3.31 plots the fluid pressure subtracting the hydrostatic part at those probes $p_d = p - \rho g y$ as a function of time. Figures 3.32, 3.33 and 3.34 plot the temporal vairations of velocity components (u, v, w), respectively. In those charts, the pressure is rendered dimensionless by the dynamic pressure $\rho_m U^2/2$ and the velocity is normalized by the paddle velocity U. Similar to the overall kinetic energy, the values of different flow fields are well aligned by the normalization same factors. The flows are shown to be at quasi-steady states during the TSK agitation. No bifurcation has been excited by the current stirring effects.

Based on our observation of convergent behaviors, quasi-steady solutions of the TSK two-phase flow will be chosen from numerical results with simulation time $t > 2.0$ sec in the following sections.

Free surface motion in the TSK

Next for one to have an image of the flow behavior inside the TSK system, Figure 3.35 displays the configuration of the water surface during one single rotation of Case 3 with the largest rotation speed. As the screw disks periodically cut into and emerge from the water, they bring the fluid interface into motion and surface waves travel between two paddles. The water level in the right barrel is slightly higher than that in the left, due to the rotation direction. Those results seem reasonable. Again, we note that no re-gridding procedure is needed in this simulation.

In order to validate the simulations and demonstrate the effect of screw rotation, calculated results of Case 1 (30 rpm, the lowest rotation speed) and Case 3 (90 rpm, the highest rotation speed) are compared with experimental photographs taken by a high-speed camera. Figure 3.36 shows such comparisons of interface shapes for Case 1 (30 rpm) where the left column is experimental photograph and the right column is sketch of simulation result. The time interval between Figure 3.36(a) and (b) is a quarter of one rotation period. It is observed that the water surface remains almost flat in both simulation and experiment for the current rotation speed.

On the other hand, the disturbance of fluid interface is rather obvious for Case 3 (90 rpm) as shown by Figure 3.37. In Figure 3.37(a) the water level is ascending from the left to the right side of the TSK and some liquid near the central part is attached to the left paddle exiting the water, which have been satisfactorily recovered by simulation results. In Figure 3.37(b) the water level is higher in the middle part than other places. This is also captured by the simulation, except for that the height at the right wall is slightly over-

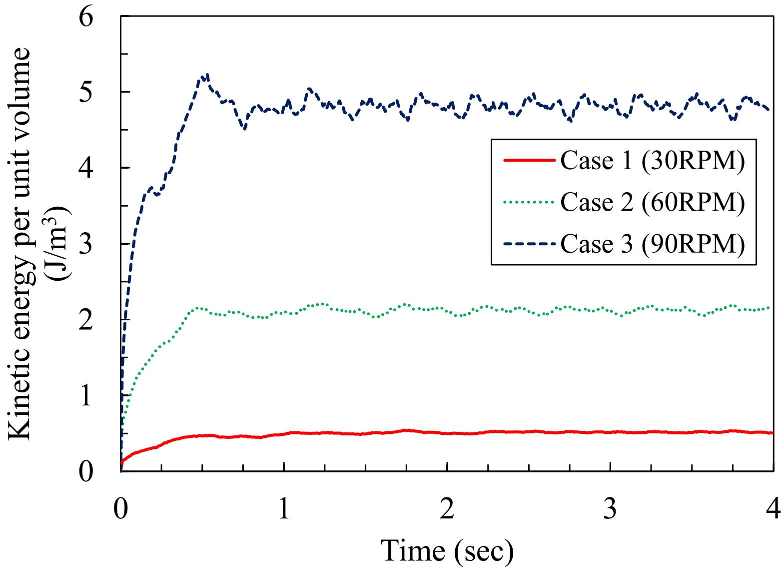

(a) Kinetic energy against time.

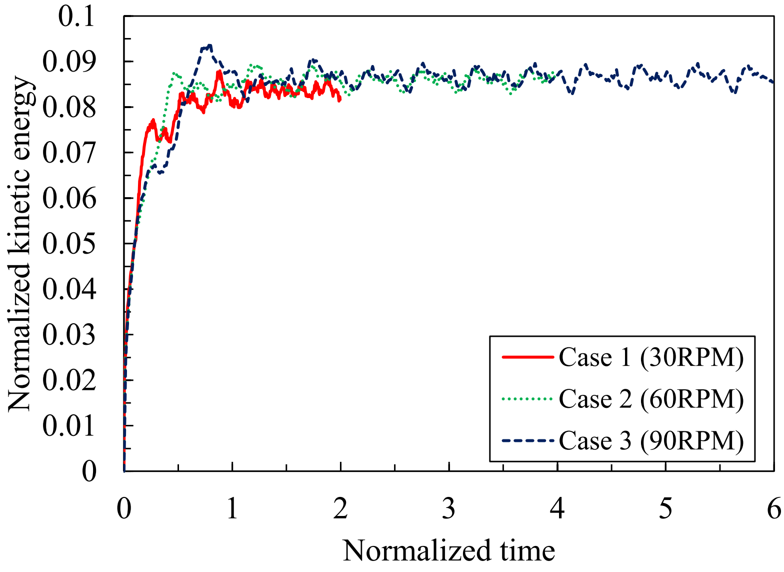

(b) Normalized kinetic energy against dimensionless time.

Figure 3.29: Plot of kinetic energy of two-phase flows in the TSK.

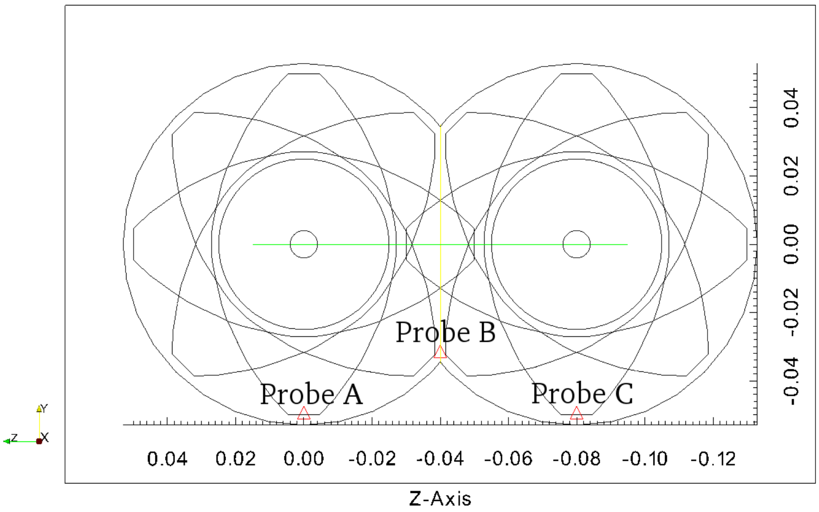

Figure 3.30: Probe positions A, B and C.

predicted. The air cavity entrained behind the left paddle entering the water is confirmed as well. Therefore, the simulation results are found in qualitative agreement with validation data, showing that the VOF-IB method is able to correctly reflect the influence of different rotation speeds on two-phase agitation.

To further examine and validate the simulation of energetic fluid-boundary interactions in Case 3 (90 rpm), the comparison of interface heights at the TSK front wall is carried out for seven gauge positions, named from P0 to P6 respectively, whose locations are elucidated in Figure 3.38 and Table 3.6. The horizontal line connecting the twin screw axes is chosen as the zero water level. The remainder fluctuation of the water height around the baseline is normalized by the radius of the TSK barrel. We note that experimental data is directly measured from the photographs because it is not realistic to install probes or sensors inside the TSK device. The series of water levels at different gauge positions are plotted against time in Figure 3.39. Those charts plot the surface fluctuation during a single rotation period T. Specifically, both simulation result and experiment data show a global periodic feature of $T/2$, which is due to the apparent symmetry of TSK disks. Apart from the global periodic mode, the local modes of surface fluctuation owns to the interface motion and interaction with moving paddles. Reasonable matches are found between the simulation and experiment in respects of the overall oscillation frequency and fluctuation pattern.

However, it seems that the calculated wave motions generally have greater amplitude than those measured. For example, the left gauges (P0, P1 and

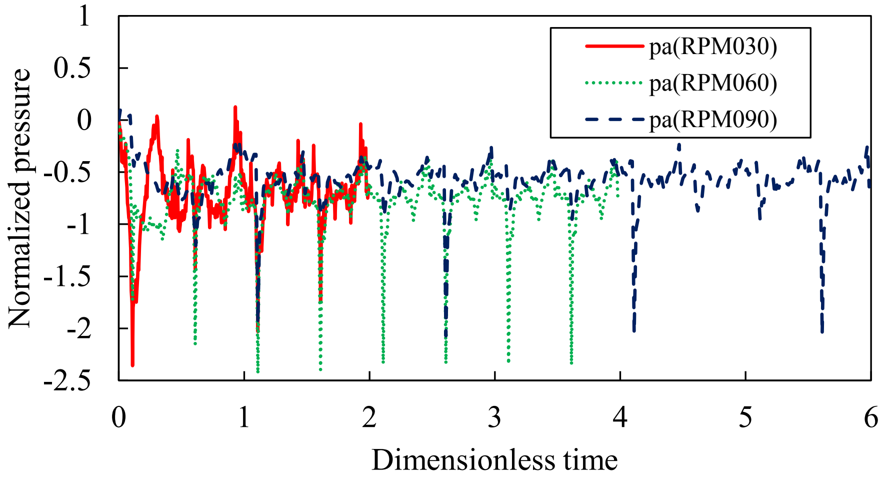

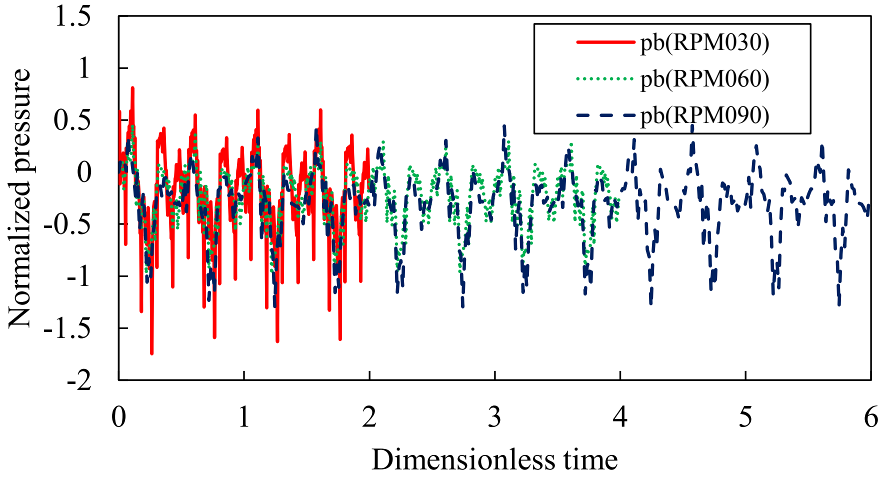

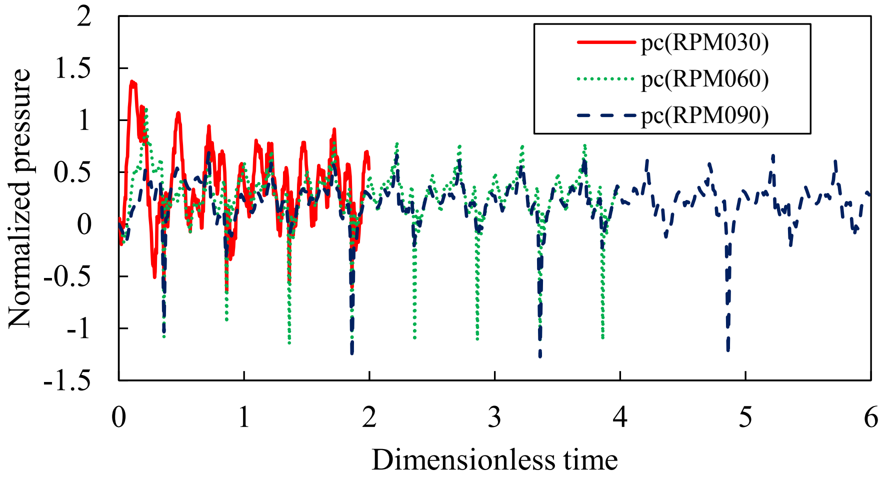

Figure 3.31: Plot of pressure $\frac{p}{\rho_m U^2/2}$ at probe positions A, B and C.

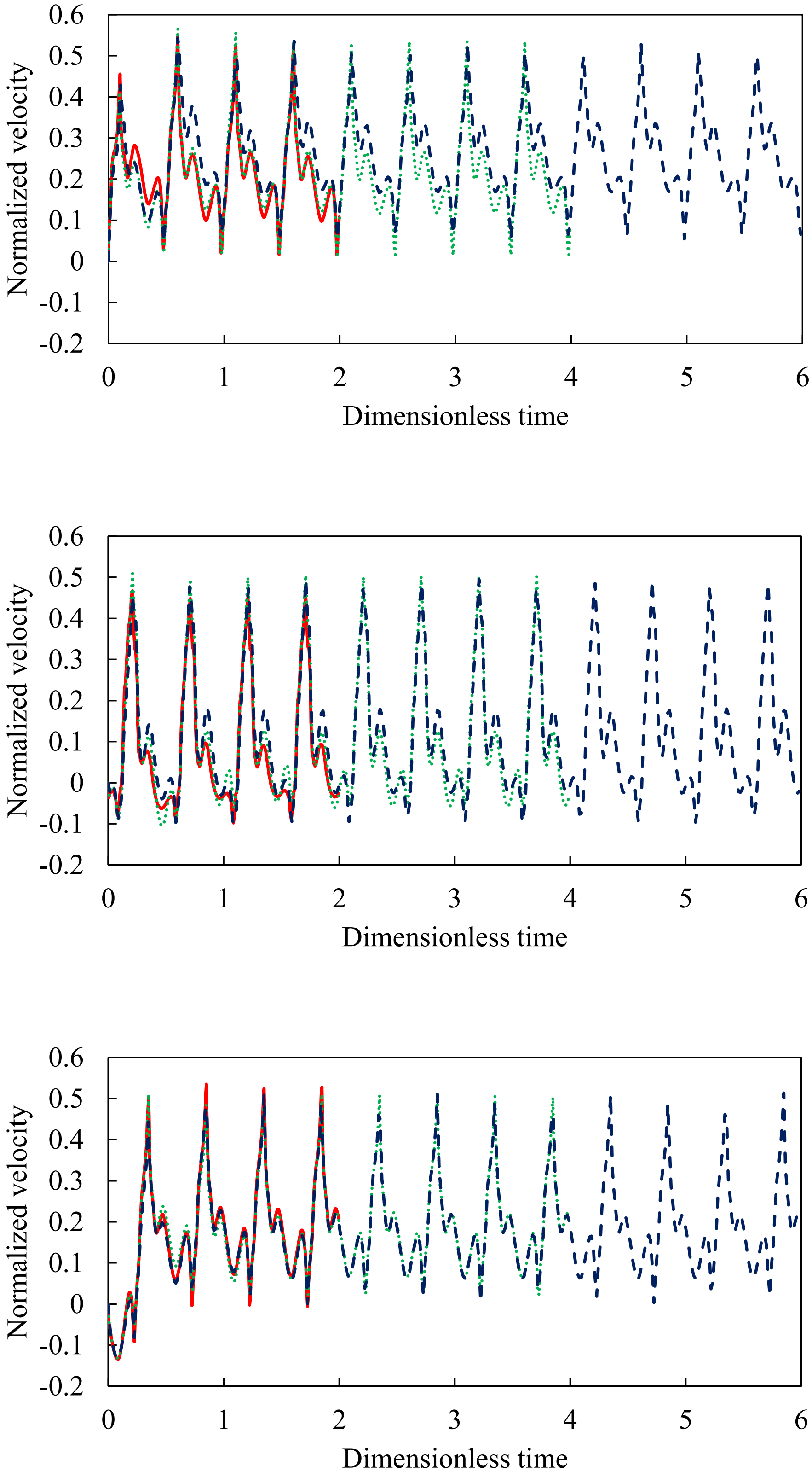

Figure 3.32: Plot of velocity component u/U at probe positions A, B and C.

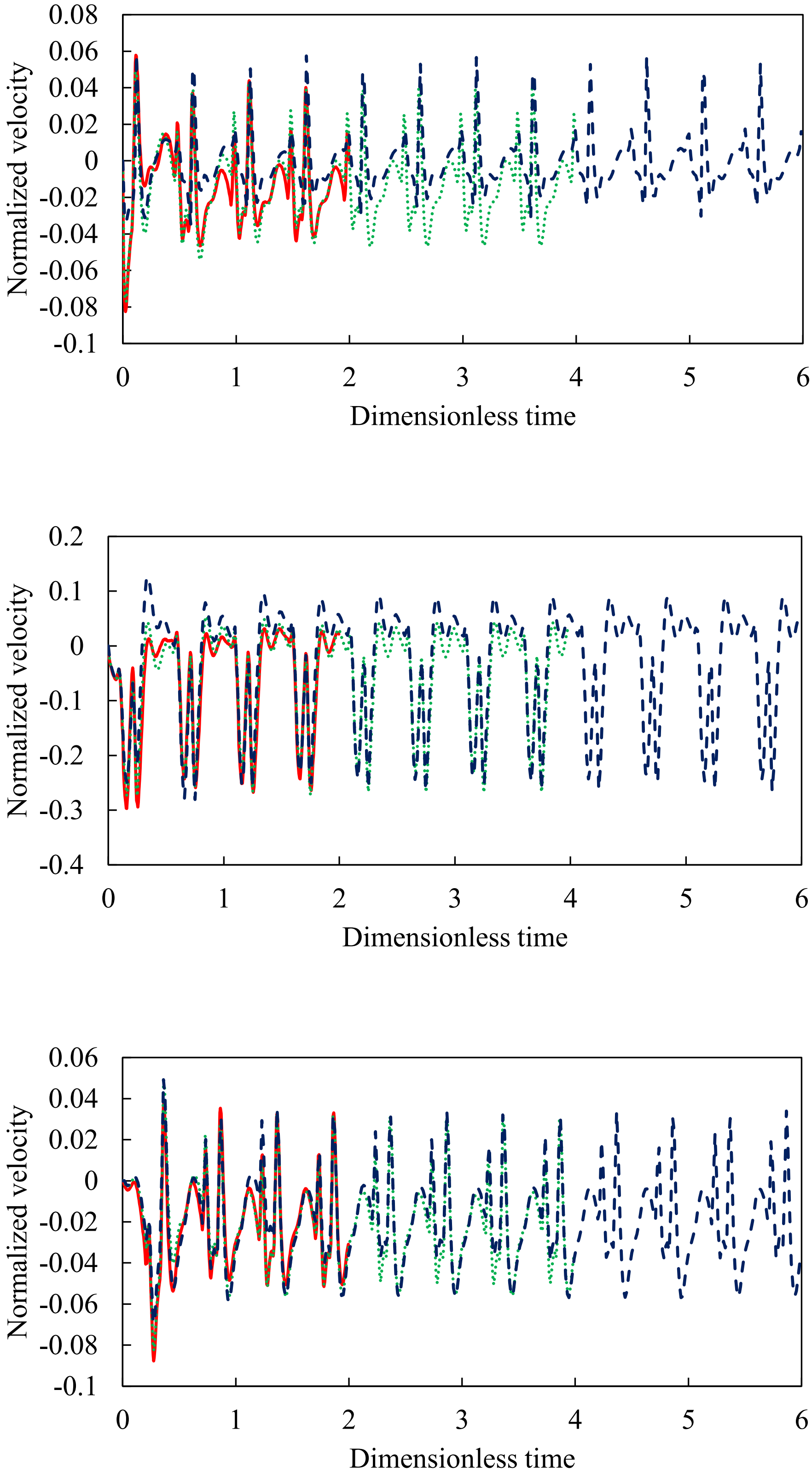

Figure 3.33: Plot of velocity component v/U at probe positions A, B and C.

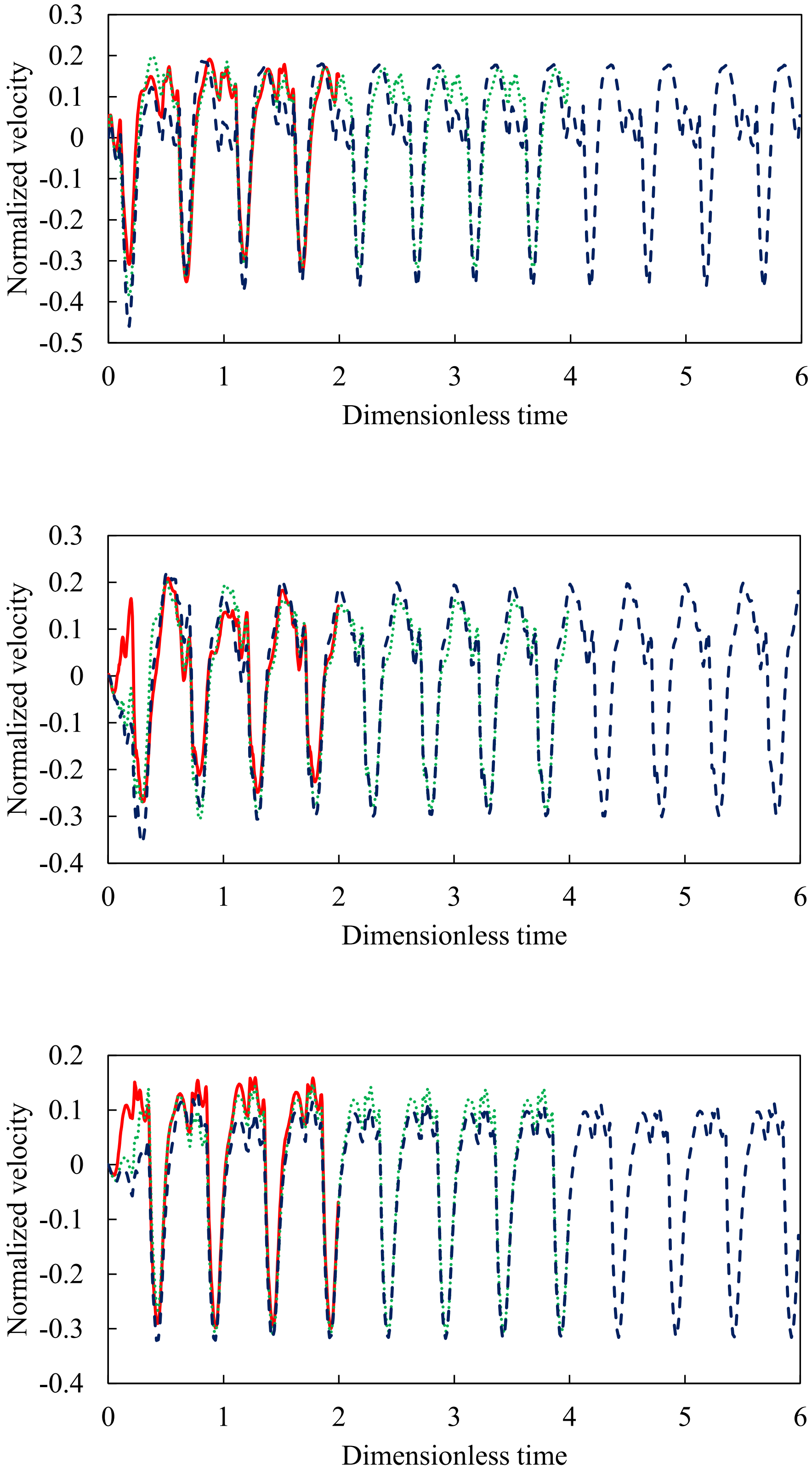

Figure 3.34: Plot of velocity component w/U at probe positions A, B and C.

Table 3.6: Gauge positions for interface height measurement.

Gauge name	Gauge position
P0	Left wall
P1	Midpoint between left wall and left screw axis
P2	Midpoint between left screw axis and TSK center
P3	TSK center
P4	Midpoint between TSK center and right screw axis
P5	Midpoint between right screw axis and right wall
P6	Right wall

P2) tend to be lower than their experimental counterparts whereas the right ones (P4, P5 and P6) are slightly higher. It is possibly explained by that the boundary layer is artificially thickened by the IB model and thus more liquid has been transported to the right barrel.

Shear effects induced by paddle rotation

The final part discussion is devoted to the investigation of screw-induced shear effects, which is generally considered to be dominant mechanism for a working TSK device. Particularly, strong shearing is expected for the interstitial slit region between counter-moving disks when they overlay each other.

Such a case is shown for the time instance when the second disk of the left paddle meets the third disk of the right paddle, as illustrated by the x-plane slice in Figure 3.40. Because two screw paddles co-rotate counter-clockwise, their interdigitated disk tips in the conjunction region tend to approach quickly and generate shear effects between them. Figure 3.40 shows the colored contour of the $(1,2)$-component of the strain rate tensor

$$\mathbf{D}_{xy} = \frac{1}{2}\left(\frac{\partial u}{\partial y} + \frac{\partial v}{\partial x}\right)$$

on the central plane perpendicular to the rotating axis. It is apparent that maximum shearing is found in the region sandwiched between the two grazing disks. Similarly, the distribution of shear strain rate $\mathbf{D}_{xy}$ is shown on the $y = -0.0168$ plane in Figure 3.41 from a bottom view, and on the plane connecting the left and right barrels in Figure 3.42.

Again, when the results obtained from different simulation cases (30, 60 and 90 rpm) are compared, values of $\mathbf{D}_{xy}$ (approximately 18.6, 37.0 and 55.0 sec^{-1}) are found almost proportional to the corresponding rotation speeds.

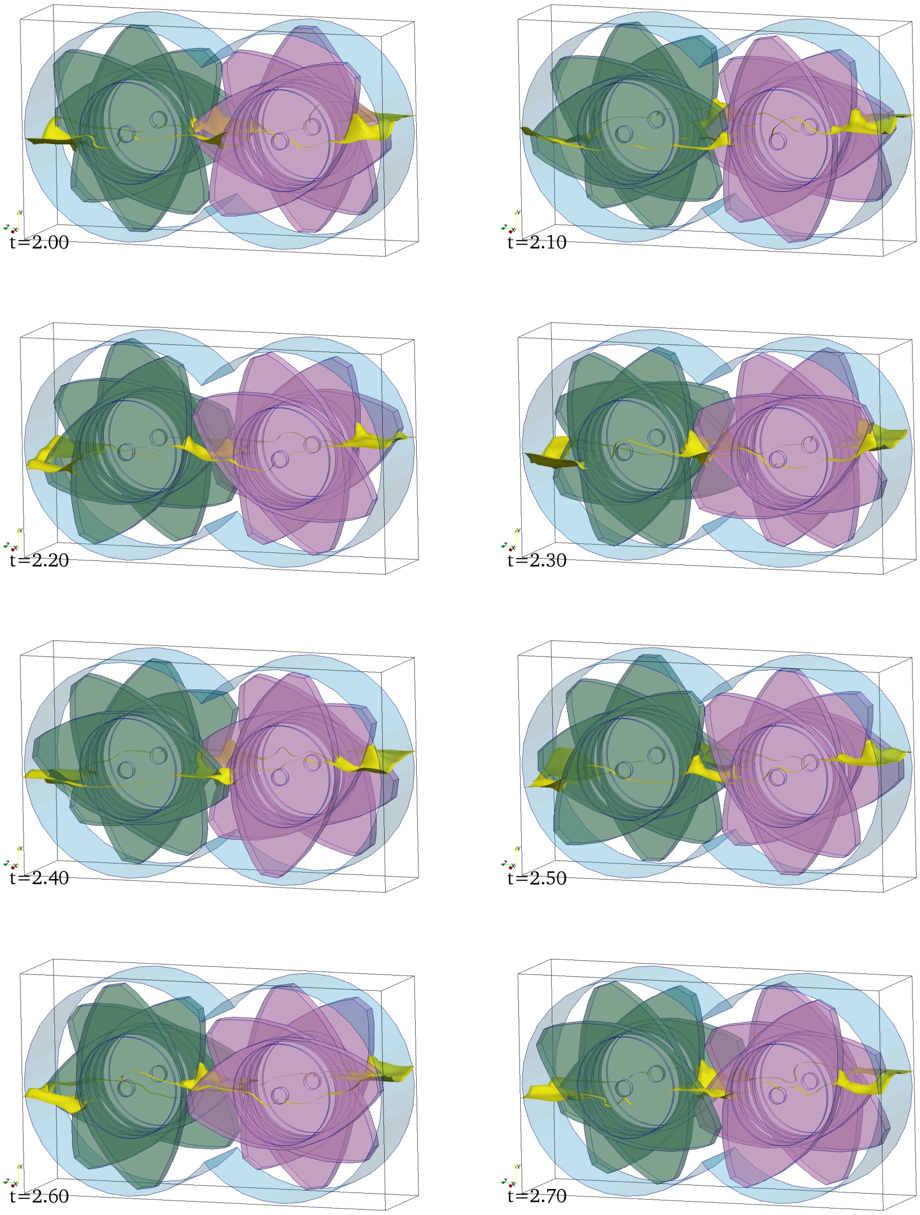

Figure 3.35: Two-phase TSK: water surface during one period of rotation (90 rpm).

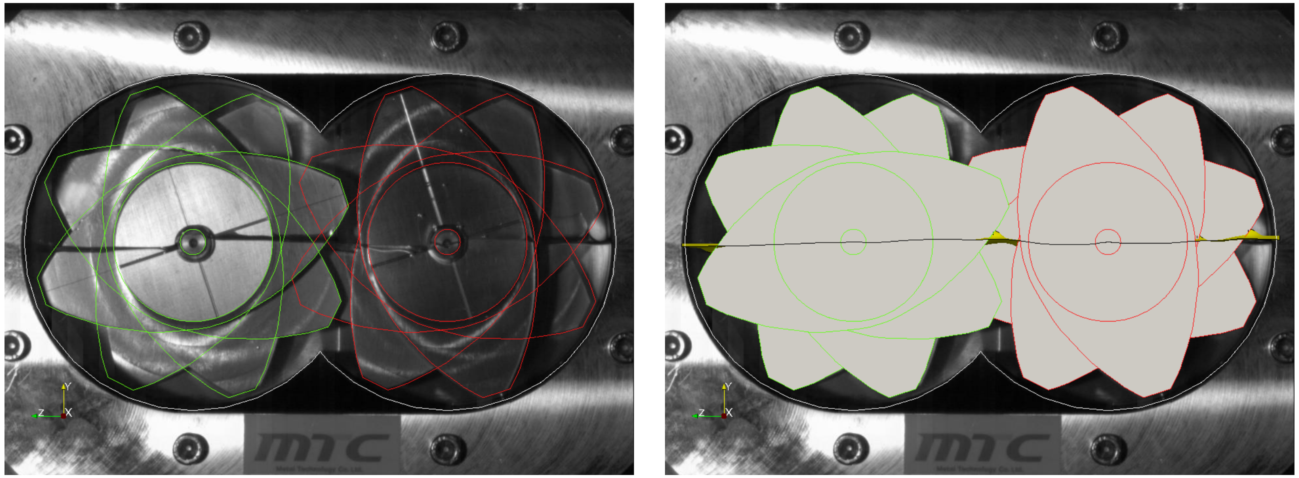

(a) Experiment (left) and simulation (right)

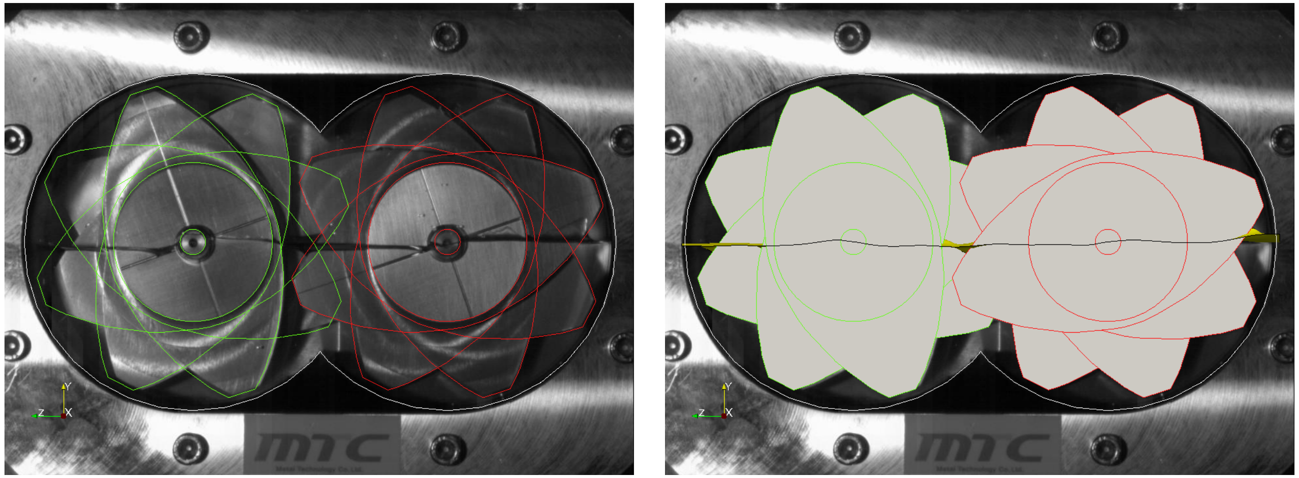

(b) After $T/4$ period

Figure 3.36: Comparison of interface shapes with rotation speed of 30 rpm. The time interval between the two images is approximately 1/4 rotation period.

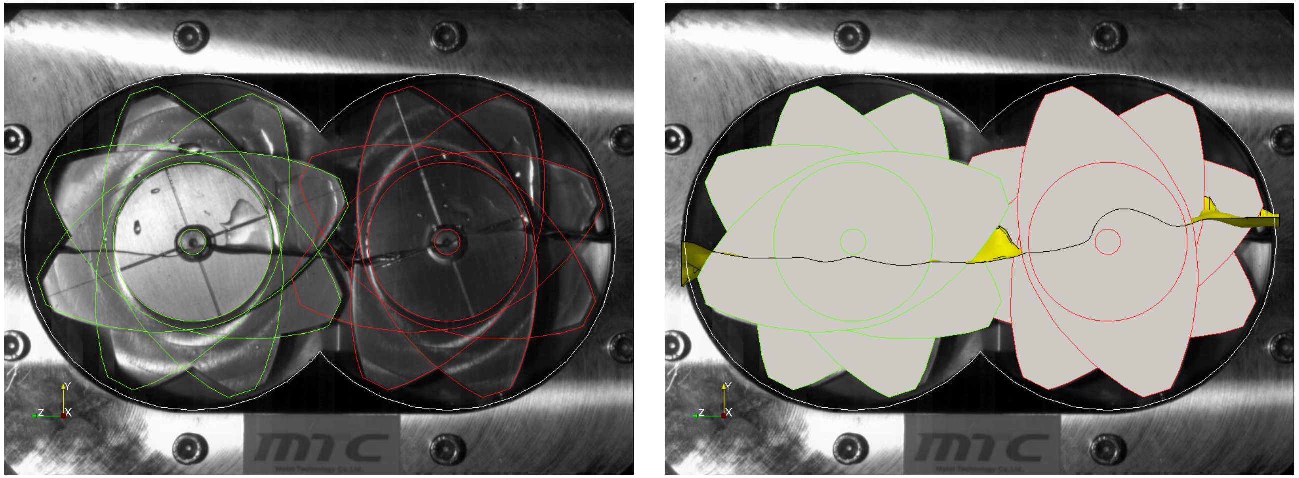

(a) Experiment (left) and simulation (right)

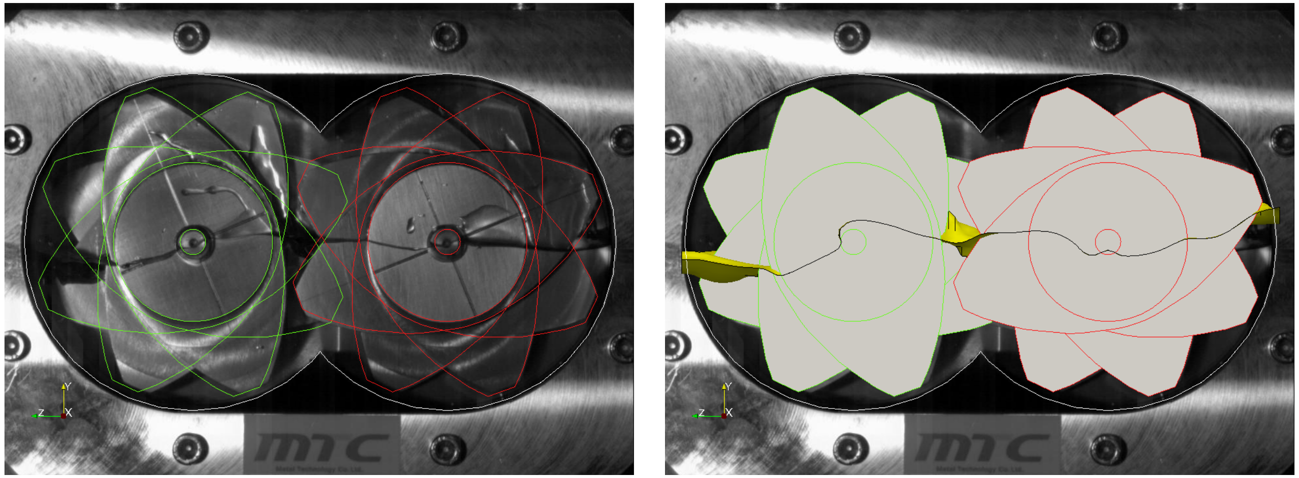

(b) After $T/4$ period

Figure 3.37: Comparison of interface shapes with rotation speed of 90 rpm. The time interval between the two images is approximately 1/4 rotation period.

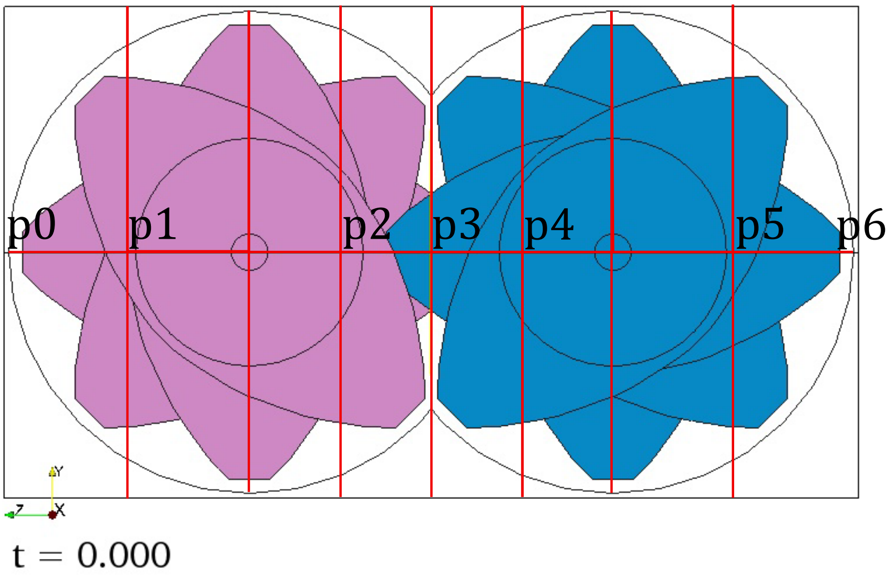

Figure 3.38: Gauge positions for interface height measurement.

This linear correlation owes to the Newtonian nature of water and it is plotted in Figure 3.43 with curve fitting.

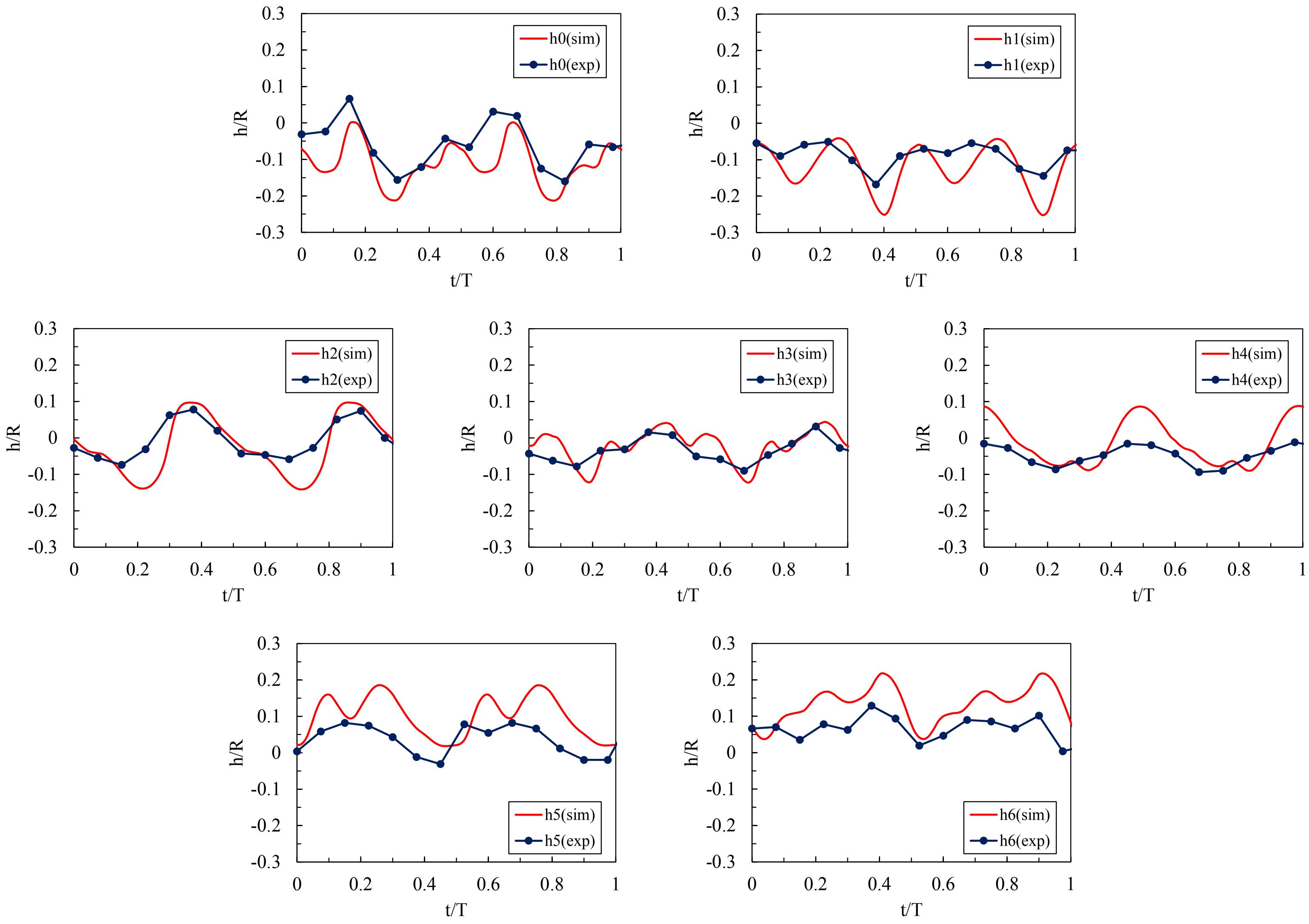

Figure 3.39: The normalized water level at gauge positions P0–P6. Charts are put in symmetrical places around the central gauge P3.

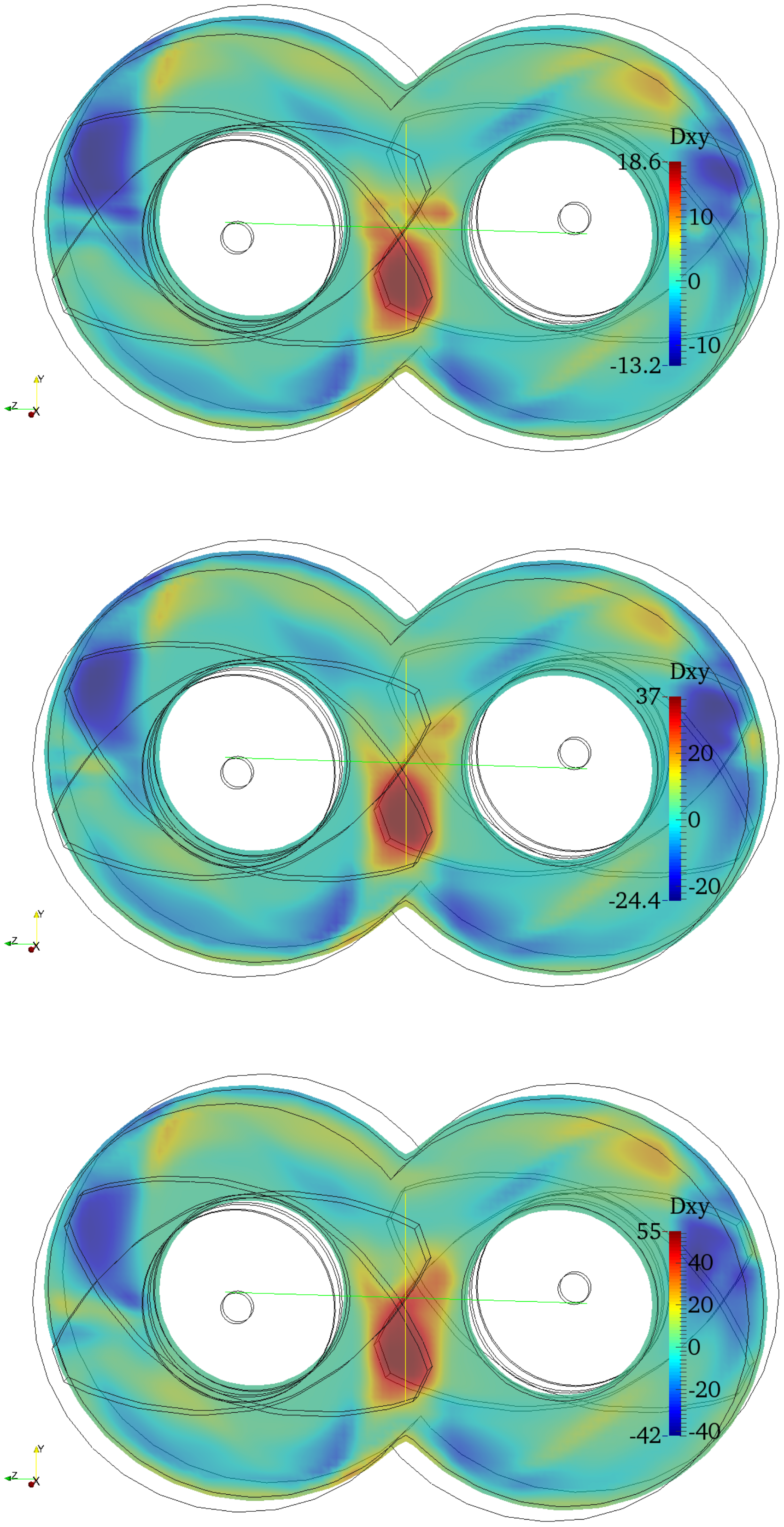

Figure 3.40: Strain rate tensor $\mathbf{D}_{xy}$ on $x = 0$ plane for Case 1 (top), Case 2 (middle) and Case 3 (bottom).

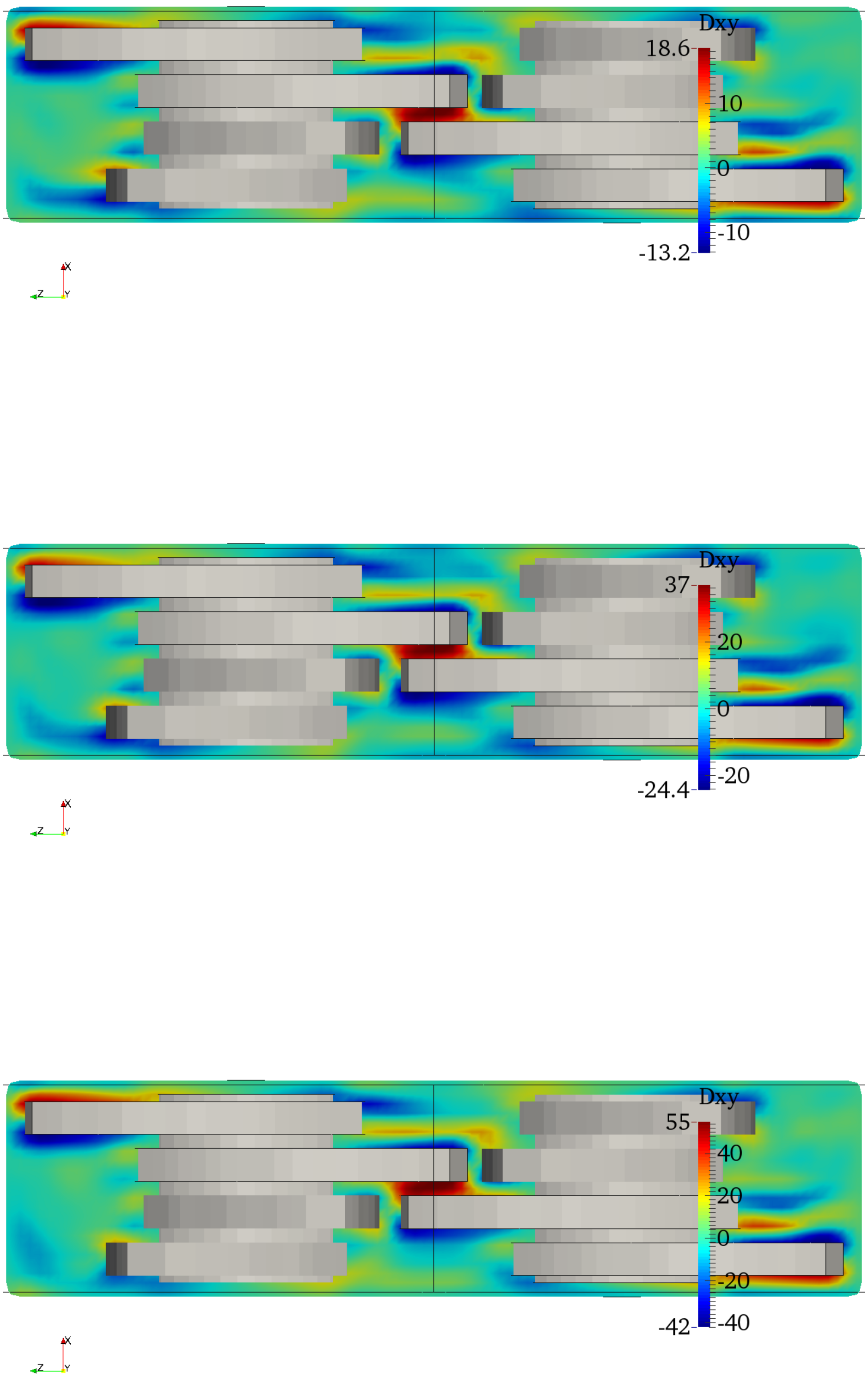

Figure 3.41: Strain rate tensor $\mathbf{D}_{xy}$ on $y = -0.0168$ plane for Case 1 (top), Case 2 (middle) and Case 3 (bottom).

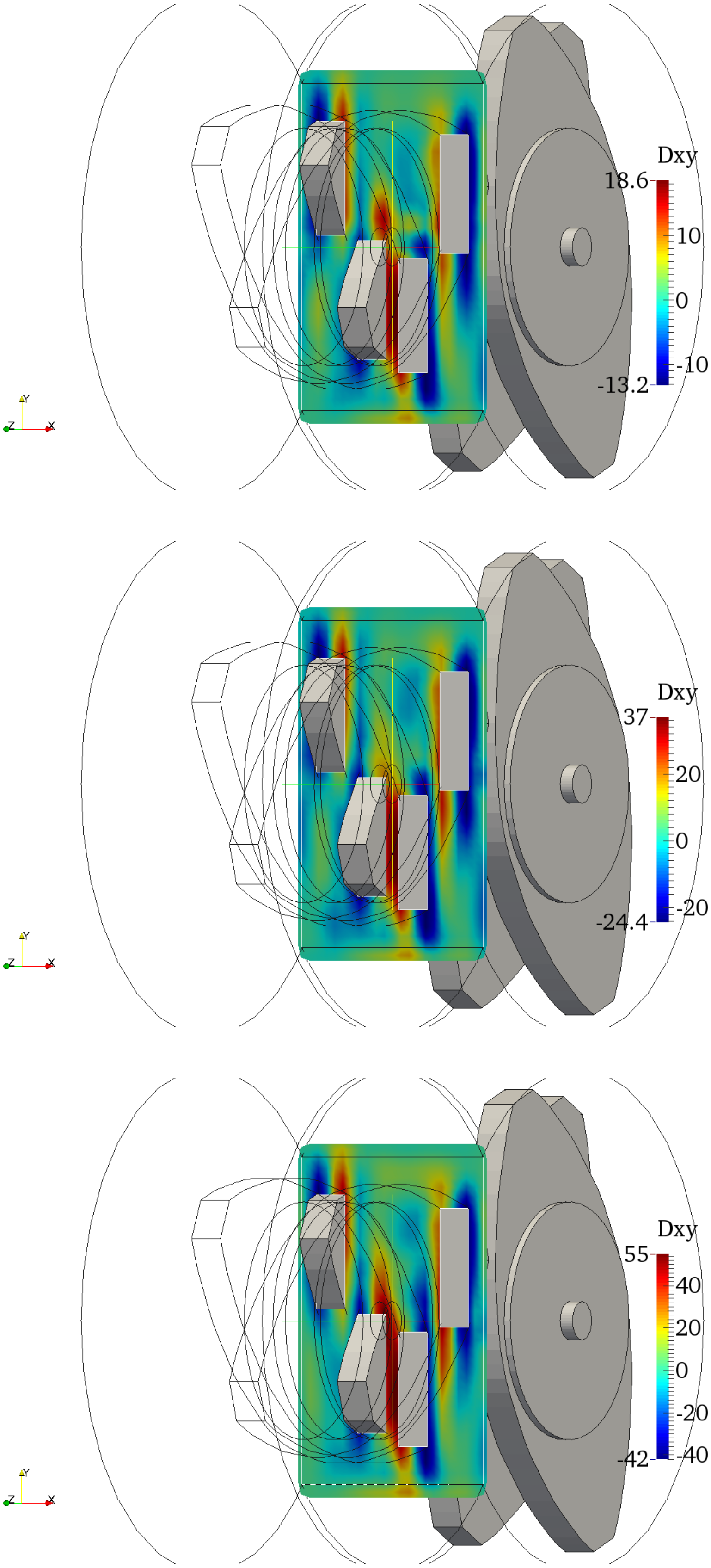

Figure 3.42: Strain rate tensor $\mathbf{D}_{xy}$ on $z = -0.04$ plane for Case 1 (top), Case 2 (middle) and Case 3 (bottom).

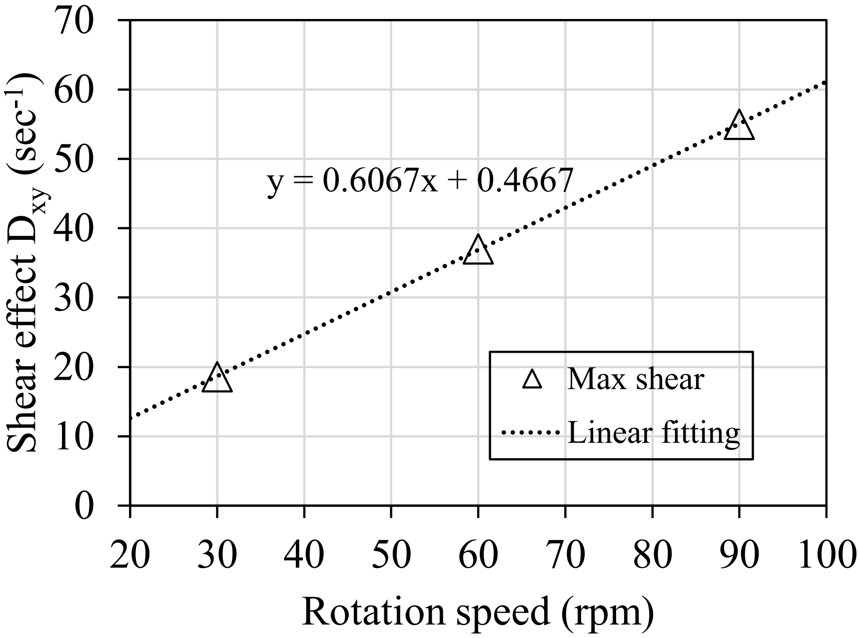

Figure 3.43: Maximum strain rate $\mathbf{D}_{xy}$ against rotation speed and linear fitting.

3.6.2 Three-phase flow in a TSK

In this section, the full-scale three-dimensional simulation of the gas-solid-liquid three-phase flow stirred by the TSK is performed. In addition to the gas-liquid free surface in the two-phase counterpart, a third solid particle phase is mixed into the system. Totally 200k particles are used in the simulation, or equivalently 261.8 g of glass beads for the lab experiment. These particles are let fall freely under gravity and reach a motionless, packed state owing to the inter-particle damping and friction. Water is filled into the barrel up to a height of 83 mm measured from the bottom, submerging approximately 80% of the TSK system. Initial configuration of the three-phase TSK simulation is shown in the Figure 3.44.

For the experiment, after the barrel is sealed, screw paddles are forced to rotate for several rounds so that entrapped gas bubbles are expelled and the particles are well mixed with the water phase. In our experiment, we noticed that some few particles may float on the water surface, which does not interfere with our experimental observation.

The simulated lab TSK is designed for a mean particle diameter $d_p = 1$ mm. With the same mesh resolution as the two-phase test, the ratio between grid spacing and particle size is close to $\Delta x/d_p = 2.0$, which is thought an appropriate choice for DEM-VOF computations. In this study, three simulation cases are conducted with different rotation speeds of 30, 60 and 90 rpm, respectively. Important computational parameters and a list of test cases can be found in Tables 3.7 and 3.8.

We note that, for Case 3 that rotates the fastest (90 rpm), the characteristic velocity based on the tip speed of the screw paddle ($D = 0.1$ m) is approximately $U \sim 0.5$ m/s. Then the particle Re number is estimated to be $Re \sim 500$. For such a moderate particle Re number and dense particle distribution, turbulent effect is known to be suppressed by the energy loss owing to fluid-particle interaction, see [69]. For this sake, turbulence modeling is not taken into account in the present study.

Early-time agitation of the TSK system

First some results describing the early-time movement, namely behaviors during the first revolution of TSK paddles by which the TSK has not yet arrived at a quasi-steady state, are presented. When the paddles begin to rotate, the initially quiescent mixture is agitated and transient movements transpire such as deformation of the solid bed and disturbance of the free surface. It is thus expected that the DEM-VOF simulation can recover such dynamical phenomena.

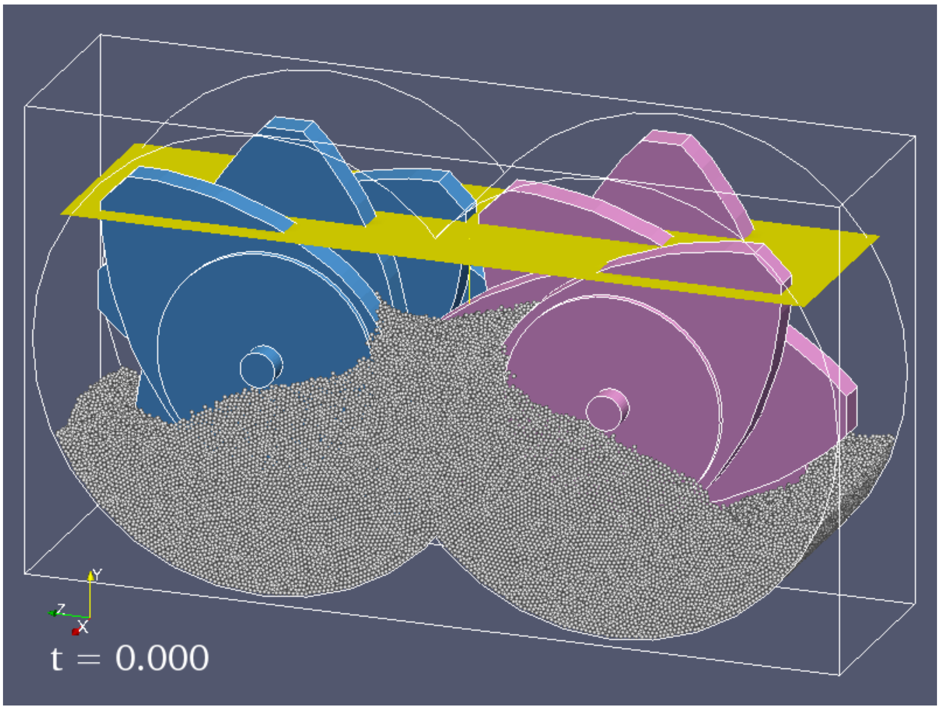

Figure 3.44: Initial configuration of the three-phase TSK simulation.

Table 3.7: Computational conditions for the three-phase TSK problem.

Water density (kg/m^3)	1000
Water viscosity (Pa s)	10^{-3}
Air density (kg/m^3)	1
Air viscosity (Pa s)	10^{-5}
Particle density (kg/m^3)	2500
Particle number (-)	200000
Particle size (m)	1.0×10^{-3}
Mesh size (m)	2.0×10^{-3}
Spring constant (N/m)	100
Restitution coefficient (-)	0.9
Friction coefficient (-)	0.3
DEM Δt (sec)	1.0×10^{-5}
CFD Δt (sec)	5.0×10^{-5}

Table 3.8: Simulation cases for the three-phase TSK problem.

	Case 1	Case 2	Case 3
Rotation speed (rpm)	30	60	90
Rotation period (s)	2.0	1.0	2/3

The image panels in Figures 3.45, 3.46, and 3.47 display the configurations of free surface and particle bed at dimensionless time $t/T = 1/4$, $1/2$, $3/4$ and 1 for three test cases, respectively. For all three cases, it is commonly observed that the left paddle suddenly cutting through the solid bed can generate a spalshing of particles in the middle of the TSK at $t/T = 1/4$. Futher stirring ($t/T = 1/2$ and $3/4$) of the screw paddles gradually conveys the solid bed from the left to right barrel. Then finally at $t/T = 1$ those particles rising with the right paddle begin to fall along its surface like an avalanche.

The free surface motions in response to the paddle rotation is also clear and self-explanatory: the water surface in Case 1 remains almost flat; on the contrary, break wave and overlapping of free surface can be observed in Case 3 where the motion is very energetic.

Evolution and convergence of systematic behavior

Through the visualization of simulation results, for all three cases the transitional behaviors described above tend to become steady in no more than two revolution periods, leading to a recurrent circulation between the left and right barrels.

In a similary manner to the rotating cylindrical tank test, the evolution and convergence to a quasi-steady state are checked by examining the temporal change of kinetic energy of the solid phase. As depicted in Figure 3.48(a), after a sharp increase, the kinetic energy very soon reaches a stable value around which small fluctuations are found in correspondence with the peroidic motion of the screw paddles.

Figure 3.48(b) plots the vertical position of mass center of the solid bed against time to show the temporal change of gravitational (potential) energy. In comparison with the kinetic energy, it is interesting to see that the potential energy increases almost monotonically during the transient stage, which indicates that the overall expansion of the solid bed in vertical direction is not significantly affected by the periodic entry and exit of the paddles.

From those charts, quasi-steady state solutions are extracted for time instants $t > 3.0$ sec.

Comparison with experiment at quasi-steady state

In this section, a comparison between simulation results and experimental data is presented at a phenomenological level. Our validation will mainly focus on some macroscopic behaviors of the gas-solid-liquid flow in the TSK

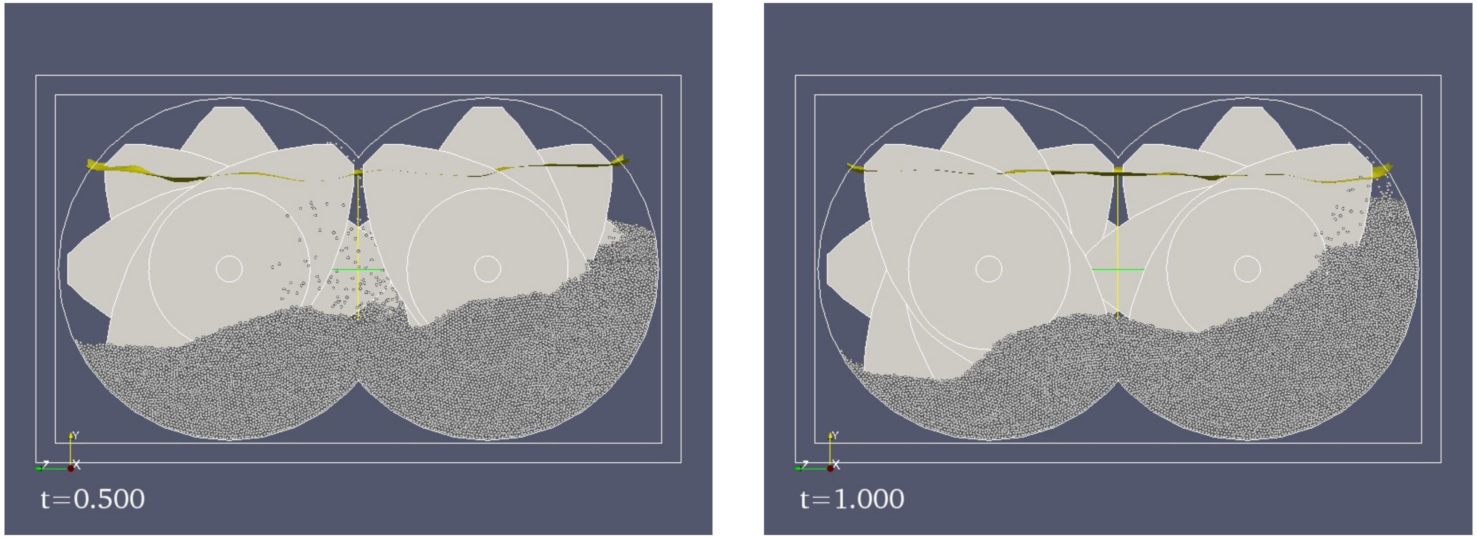

(a) $t/T = 1/4$

(b) $t/T = 1/2$

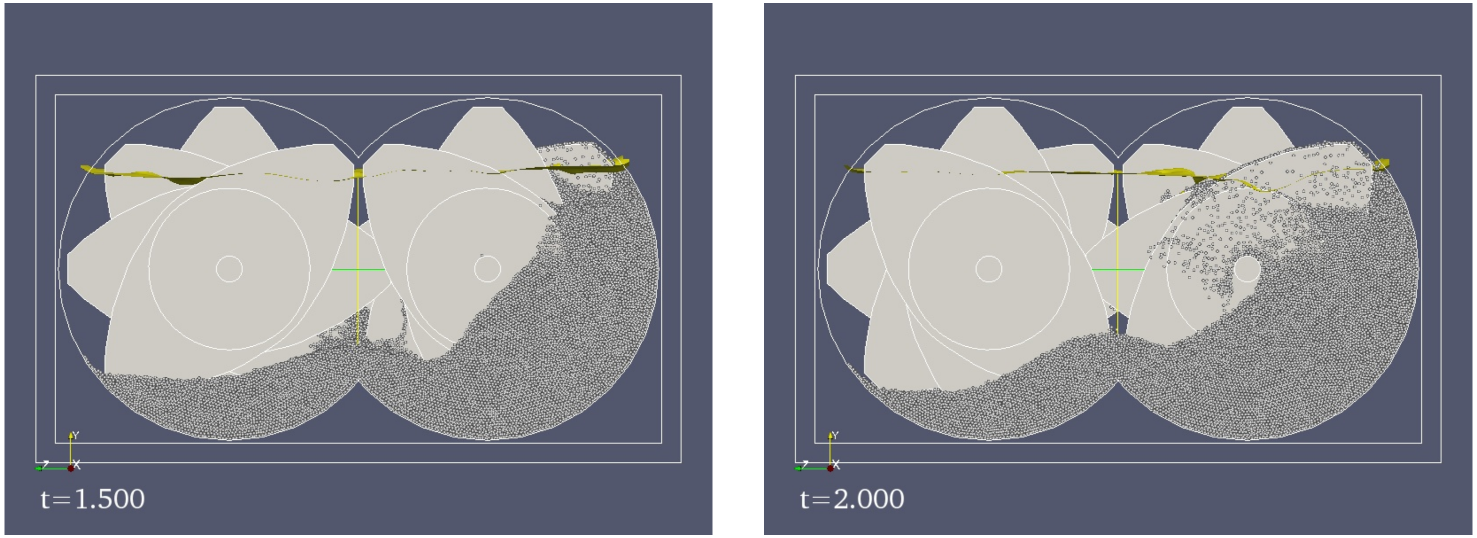

(c) $t/T = 3/4$

(d) $t/T = 1$

Figure 3.45: The first revolution of three-phase TSK: Case 1 (30 rpm).

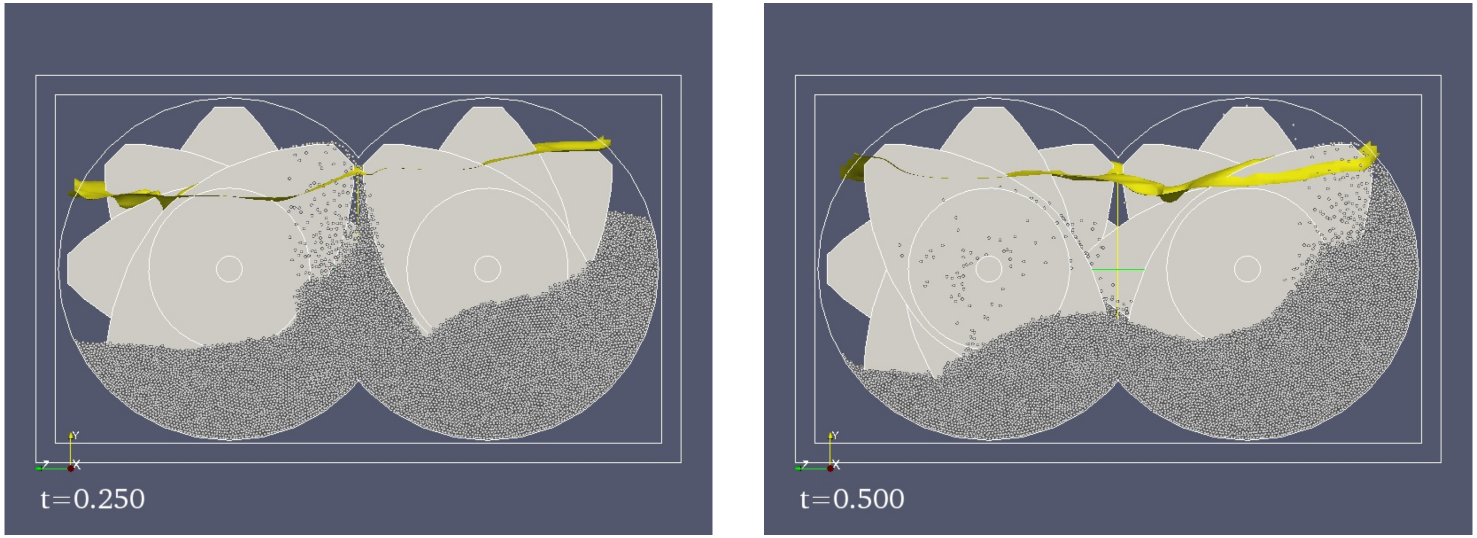

(a) $t/T = 1/4$ (b) $t/T = 1/2$

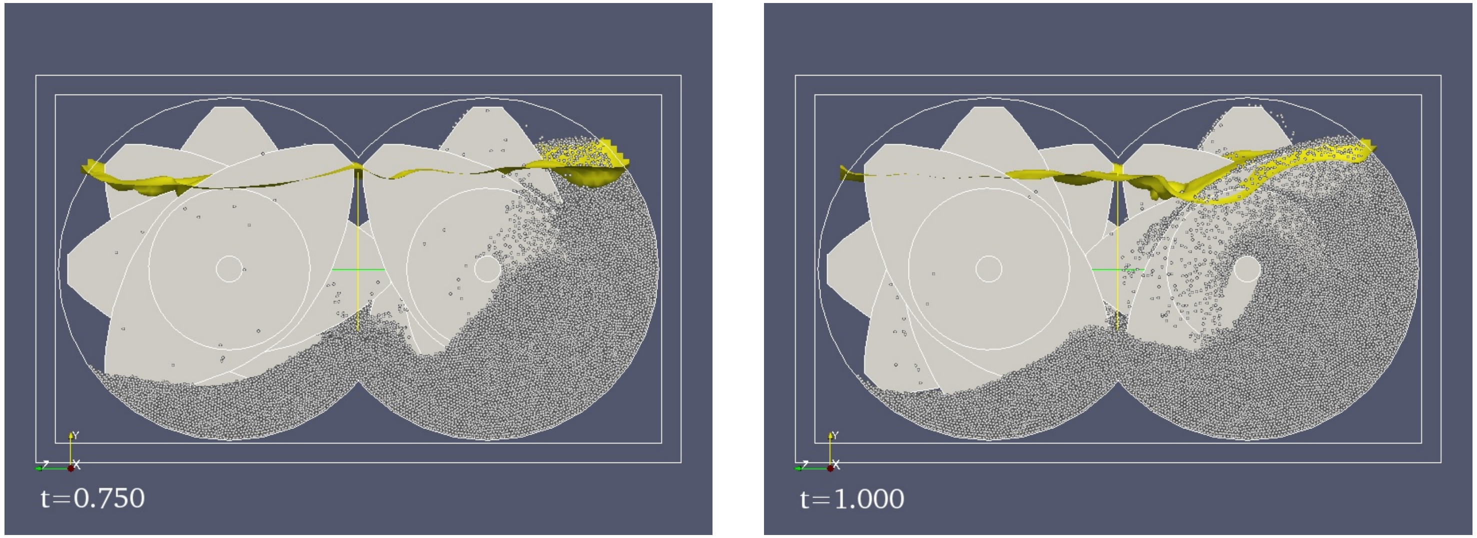

(c) $t/T = 3/4$ (d) $t/T = 1$

Figure 3.46: The first revolution of three-phase TSK: Case 2 (60 rpm).

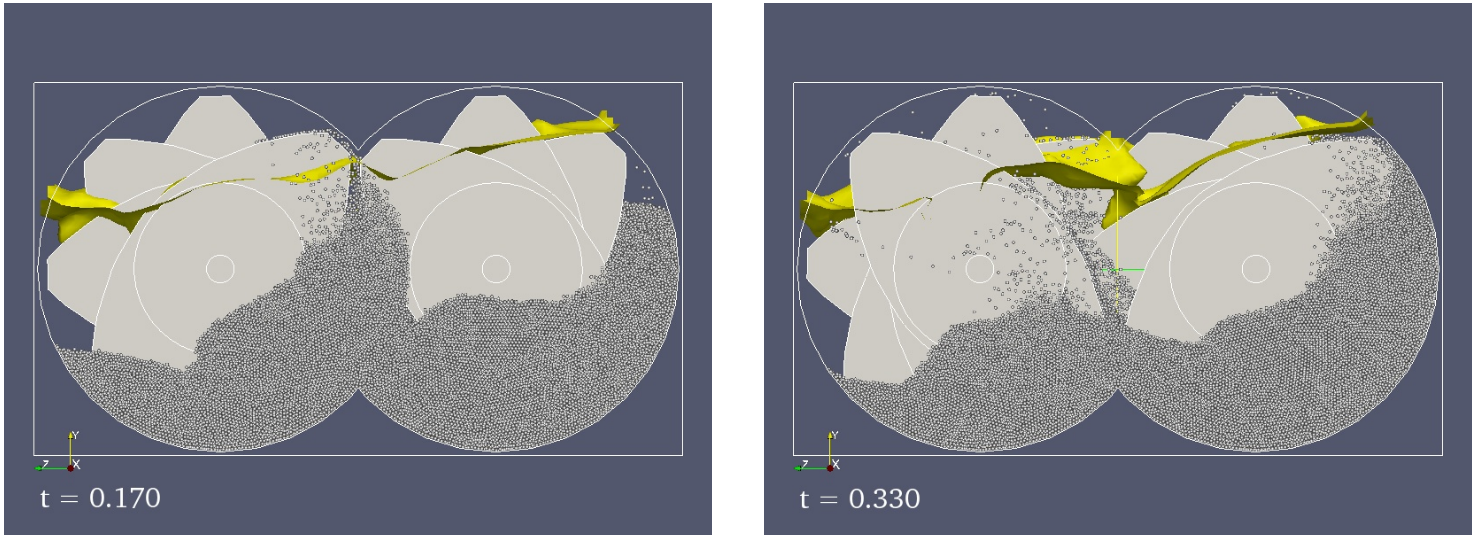

(a) $t/T = 1/4$

(b) $t/T = 1/2$

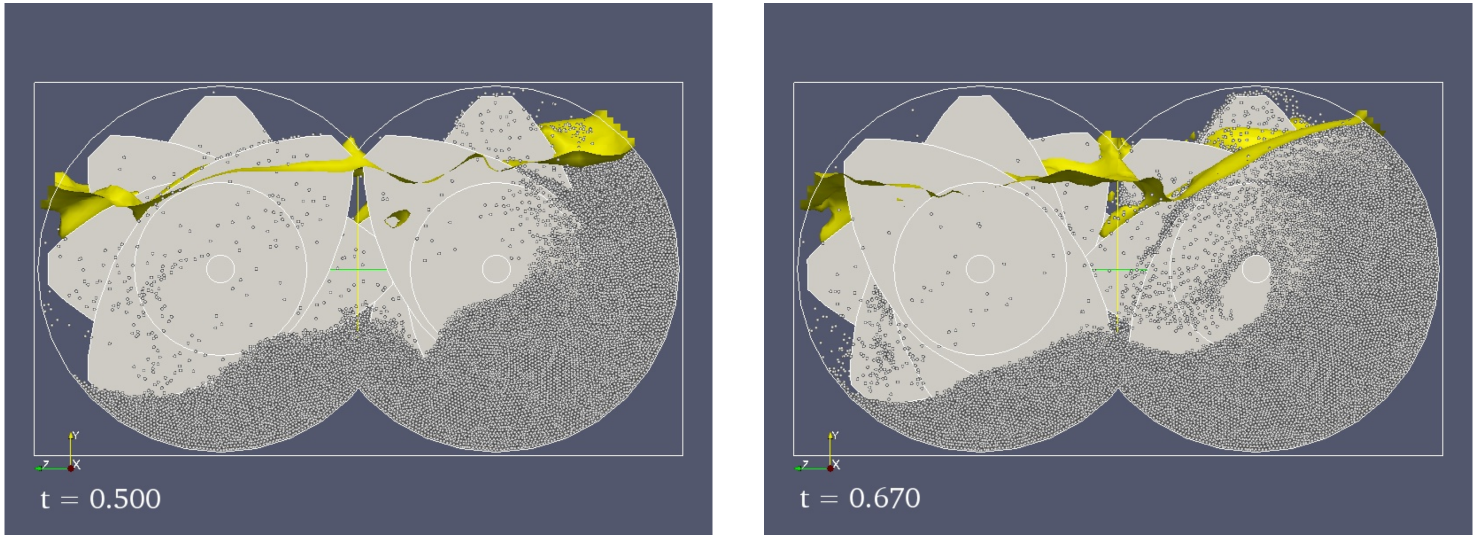

(c) $t/T = 3/4$

(d) $t/T = 1$

Figure 3.47: The first revolution of three-phase TSK: Case 3 (90 rpm).

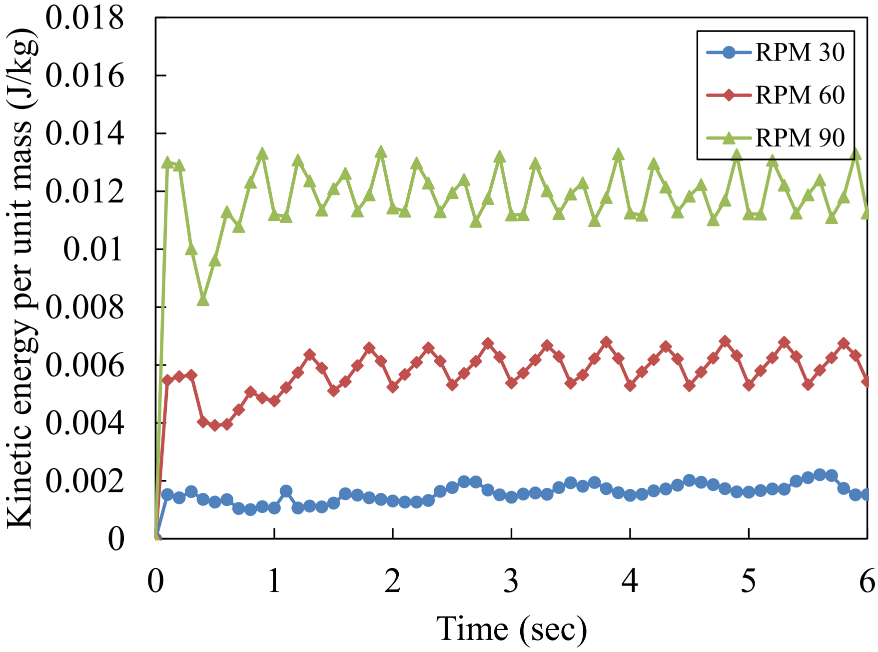

(a) Plot of translational kinetic energy of the solid phase.

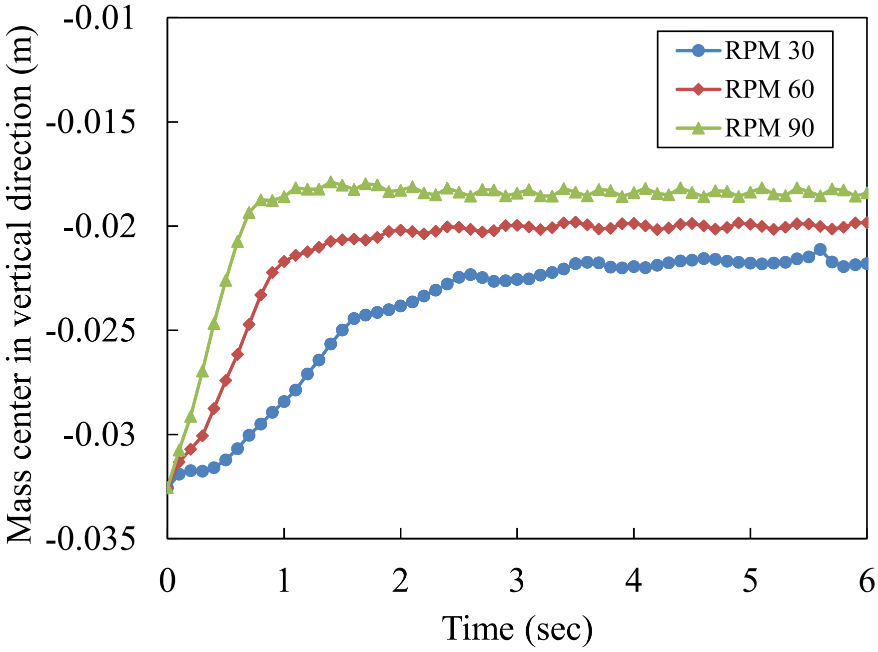

(b) Plot of vertical mass center of the solid phase.

Figure 3.48: Temporal variation of solid phase energy.

system. For the sake of brevity, only the results obtained from Case 3 (90 rpm) are discussed here.

Figure 3.49 juxtapose a simulation snapshot and experimental photograph with the same screw paddle configuration.

On the left side of the barrel, only a few particles are floating in the liquid, while the sedimentation stacking at the bottom forms a gradual ascent as indicated by the red lines in the figure. At the top left hand corner where a paddle blade has entered the water, the air cavity entrained at its back is well captured by the simulation (red circle).

Near the middle joint part of the barrel, scattered solid particles are settling within the space between two screw elements. From the animated movies, they are found to be released from the avalanche over the right paddle.

In the right part of the barrel, particle dispersions raised by the rotating paddle is visible. In fact, it is roughly estimated that solid particles cover the trapezoid area below the water surface and the red line running through the right axis. The water level also seems to be slightly lifted at the right shoulder.

In respect of interface shape and particle distribution, qualitative agreements have been confirmed between simulation results and experimental data. Figure 3.50 makes the comparison for an alternative paddle configuration, from which similar observations could be identified.

On the other hand, a noticeable discrepancy in the macroscopic behavior is the excessive particle gathering above the red line in the simulation result, which possibly implies too strong a rising effect has been generated locally. Provided that the slit between the paddle and front wall is considerably narrow ($\sim 1.5d_p$), it is likely to ascribe this problem to a numerical reason regarding the choice of friction coefficient for the DEM simulation. In some literatures, it is recommended to use a friction coefficient μ lower than the typical value of 0.3 for wet contacts, see e.g. [45]; otherwise the frictional effect will be overestimated. Based on this point, the value of friction coefficient μ is to be calibrated in order to hopefully improve the results. Besides that, we also noticed particle adherence caused by capillary liquid bridge, which is left as a future work to be considered in the proposed model.

Apart from these points, the current computational results are highly encouraging as a reasonable match to the experimental data in macroscopic aspects of the gas-solid-liquid flow in a complicated TSK system. In this study, our validation and investigation are based on visual comparisons due to the restricted experimental conditions. It is still planned to use a high-speed camera and particle image velocimetry (PIV) technique to facilitate detailed comparison of velocity profiles in the near future.

Time cost of the three-phase TSK simulation

The performance of the DEM-VOF solver is analysed in the TSK problem that involves considerably complicated conditions. Numerical simulations discussed in this section are carried out on a Windows workstation, which is equipped with Intel®Xeon®CPU E5-2699 v3 2.30GHz and 64.0 GB memory. The computation is parallelized by OpenMP technique using 36 cores.

For the current three-phase TSK simulation running up to $T^{max} \sim 6.0$ sec for a converged quasi-steady solution, the wall-clock time for each test case is approximately 25 hours on average. The differences among three cases is minor. Therefore, the proposed DEM-VOF method turns out to be a realistic choice that is able to yield meaningful results within acceptable computational time for practical engineering problems.

Concerning the runtime feature of the coupled DEM-VOF simulation, the CPU time cost by distinct computational stages is collected:

1. DEM phase: particle registration, contact detection and interaction force calculation;
2. CFD phase: explicit calculation of velocity predictor and implicit solution of pressure;
3. Miscellaneous functions: mainly the interface reconstruction and advection.

They are converted to percentages out of total execution time in order to locate the hotspots for the current computation.

Figure 3.51 gives such profiling information for TSK Cases 1 and 2 (Case 3 not measured). It is not surprising to find that the Lagrangian DEM simulation eats up over 70% of the total CPU time, owing to the relatively expensive contact detection which is not memory-friendly. We note as well, since sub-cycling has been performed for the DEM ($\Delta t^{CFD}/\Delta t^{DEM} = 5$), its actual iterations are five times as many as the CFD sweeps.

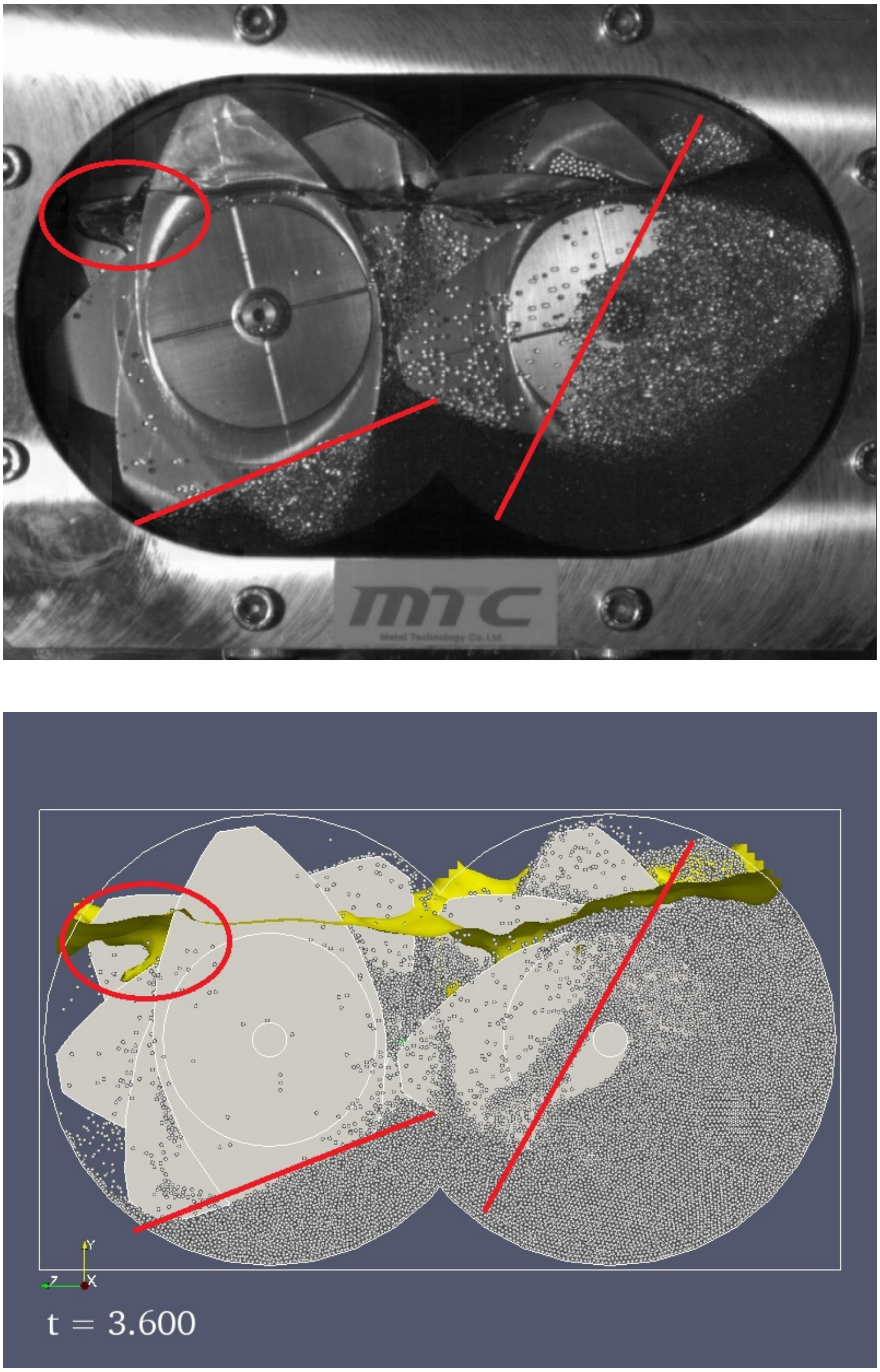

Figure 3.49: Comparison at quasi-steady state for Case 3 (90 rpm): state 1.

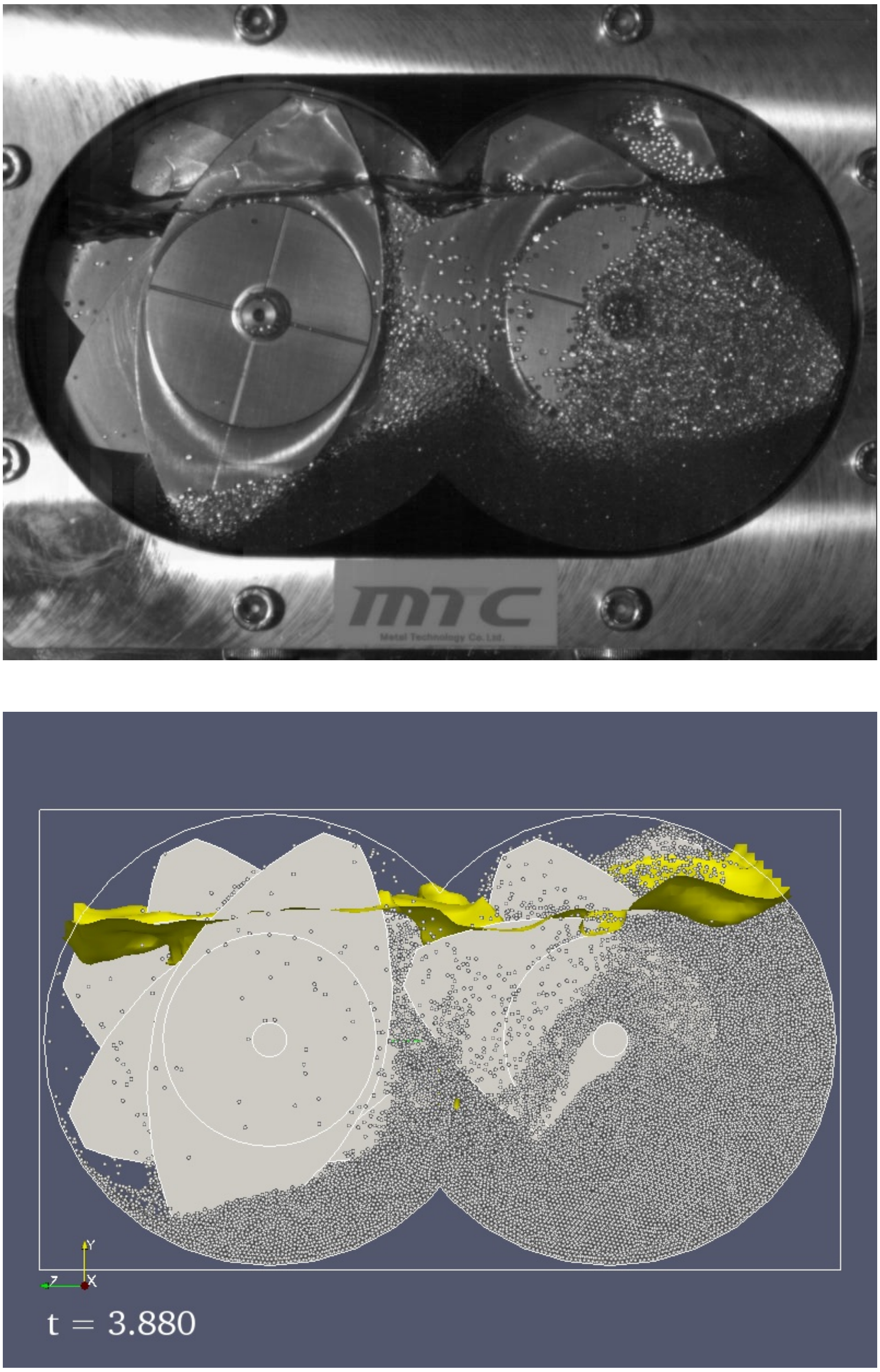

Figure 3.50: Comparison at quasi-steady state for Case 3 (90 rpm): state 2.

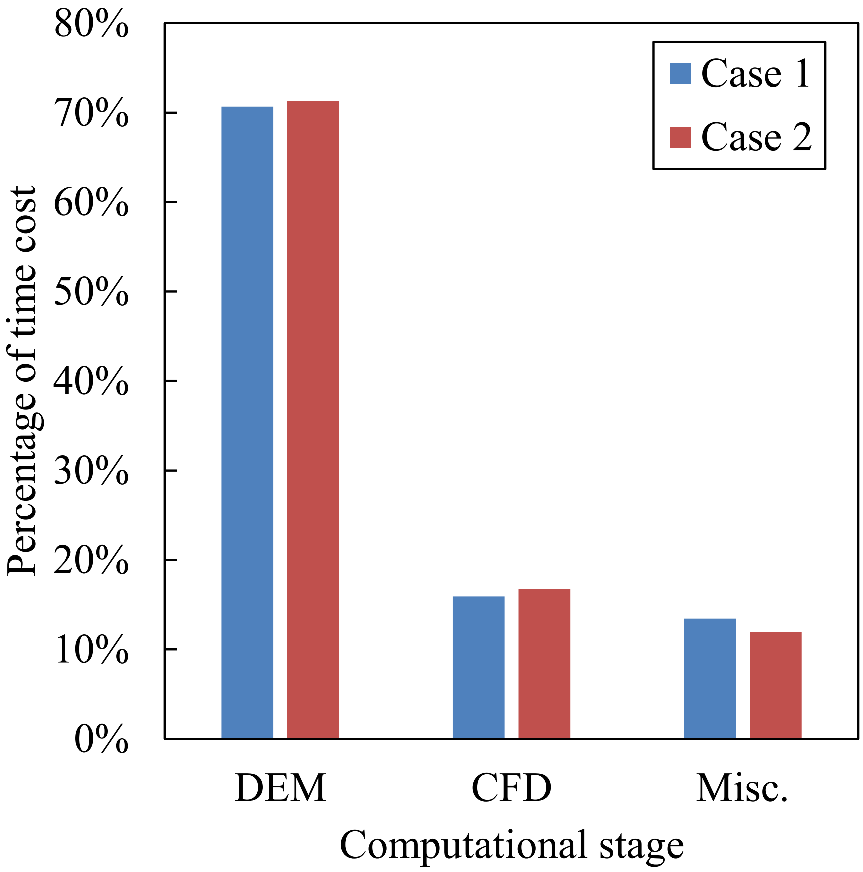

Figure 3.51: Percentage of computational cost by each stage. The miscellaneous fraction of computation (Misc.) is mainly due to the interface calculation.

3.7 Conclusions

In this study, we developed the DEM-VOF method based on an Eulerian-Lagrangian description for the three-dimensional simulation of gas-solid-liquid flows. The fluid and particle phases are computed by using the VOF method and the DEM, respectively, and they are coupled in the context of the volume-averaging approach. Curved walls and moving boundaries are efficiently simulated thanks to the adoption of the SDF and IBM with special treatments of near-wall interphase interactions. Compared with existing models, the proposed method adopts a consistent formulation of fluid-particle interaction and it can simulate complex three-phase flow behaviors involving large deformation of free surface and liquid displacement induced by the particle motion. Moreover, it has also enlarged the computational window by providing great freedom and ability to treat general geometries with ease.

Model verifications were conducted to justify the fluid-particle coupling in the problems of single particle sedimentation and flow passing through a fixed bed. It has been confirmed that the particle and flow behaviors match analytical predictions exactly; besides, effects of various computational conditions and parameters, such as the law of drag, particle Re number, coupling model, grid spacing and packing state, are also investigated targeting a comprehensive understanding of the numerical method.

The DEM-VOF method is then applied to several three-phase flow problems. In the first test, the water entry and subsequent sedimentation of a particle bed is simulated, in which complicated free surface deformation and particle motion comparable with a Rayleigh-Taylor instability have been observed. The water displacement of solid particles is also reproduced, implying a good volume conservation property of our model. The second test is the gas-solid-liquid wave propagation of a three-phase dam break problem. The violent motion of the water-glass beads mixture and vortex generated in the air phase are successfully computed and their dynamic snapshots agree well with experimental photographs at different stages. The temporal variations of the surge front and column height are also compared with experimental data. Finally, the gas-solid-liquid flow in a rotating cylindrical tank is considered as a test case involving curved, moving boundaries. The quasi-steady results are validated against an experiment. In respects of the macroscopic behaviors such as the solid bed shape and size, excellent agreement are found between them.

We finally apply the present method to a very challenging problem, namely the gas-liquid and gas-solid-liquid flows in a twin screw kneader and obtained reasonable predictions to this system. Through the numerical tests, we have demonstrated the flexibility and accuracy of the DEM-VOF method in performing high-fidelity simulations for gas-solid-liquid flows.

The proposed DEM-VOF method is designed to be a macroscopic model capable of predicting the behaviors of complicated gas-solid-liquid flows which is difficult to be achieved by existing numerical solvers even at a phenomenological level. At present its applications are mainly found for three-phase flows in various mixing and grinding process, and its potential for other engineering problems is promising.

As discussed previously, its major limitation lies in the macroscopic volume-averaging formulation which has introduced a strong coupling between the particle size and fluid grid spacing, that is, fluid cell Δx is required to be several times larger than the particle diameter d_p to sustain the essential prerequisite of locally-averaged approximation. It makes one difficult to freely adjust the spatial resolution for the continuum fluid phase, which is in fact the reason why it cannot be used to resolve flow behaviors at scales finer than d_p, e.g. air entrainment or liquid splash behind solid particles. Those microscale effects are generally considered unimportant in the scope of this study, but they may be of special interest when modeling certain three-phase problems such as spray coating/drying. For that purpose, subgrid-scale model can be introduced to describe the dispersed micro bubbles or droplets, see [70] for a recent example. Another problem related to the restricted computational resolution is that sharp edges and corners of wall boundaries may be smeared for fluid computation. This can be alleviated by defining special kernel functions to calculate void fraction and transfer interactive force between the fluid and particle phases. Those kernel functions will have support size determined by the original constraint of fluid cell-particle diameter ratio. Hence they can partly loosen the restriction and provide more degrees of freedom to better resolve the flow field and boundary shape.

Bibliography

[1] D. Gueyffier, J. Li, A. Nadim, R. Scardovelli, and S. Zaleski, "Volume-of-Fluid Interface Tracking with Smoothed Surface Stress Methods for Three-Dimensional Flows," *Journal of Computational Physics*, vol. 152, no. 2, pp. 423–456, 1999.

[2] M. Sussman, P. Smereka, and S. Osher, "A Level Set Approach for Computing Solutions to Incompressible Two-Phase Flow," *Journal of Computational Physics*, vol. 114, no. 1, pp. 146–159, 1994.

[3] M. Sussman and E. G. Puckett, "A Coupled Level Set and Volume-of-Fluid Method for Computing 3D and Axisymmetric Incompressible

Two-Phase Flows," *Journal of Computational Physics*, vol. 162, no. 2, pp. 301–337, 2000.

[4] S. O. Unverdi and G. Tryggvason, "A front-tracking method for viscous, incompressible, multi-fluid flows," *Journal of Computational Physics*, vol. 100, no. 1, pp. 25–37, 1992.

[5] T. Yabe, F. Xiao, and T. Utsumi, "The Constrained Interpolation Profile Method for Multiphase Analysis," *Journal of Computational Physics*, vol. 169, pp. 556–593, 2001.

[6] P. A. Cundall and O. D. L. Strack, "A discrete numerical model for granular assemblies," *Géotechnique*, vol. 29, no. 1, pp. 47–65, 1979.

[7] Y. Feng and J. Loughran, "On upscaling of discrete element models: similarity principles," *Engineering Computations*, vol. 26, pp. 599–609, 2009.

[8] M. Sakai and S. Koshizuka, "Large-scale discrete element modeling in pneumatic conveying," *Chemical Engineering Science*, vol. 64, no. 3, pp. 533–539, 2009.

[9] M. Sakai, M. Abe, Y. Shigeto, S. Mizutani, H. Takahashi, A. Viré, J. R. Percival, J. Xiang, and C. C. Pain, "Verification and validation of a coarse grain model of the DEM in a bubbling fluidized bed," *Chemical Engineering Journal*, vol. 244, pp. 33–43, 2014.

[10] M. Sakai, Y. Yamada, Y. Shigeto, K. Shibata, V. M. Kawasaki, and S. Koshizuka, "Large-scale discrete element modeling in a fluidized bed," *International Journal for Numerical Methods in Fluids*, vol. 64, no. 10 - 12, pp. 1319–1335, 2010.

[11] E. Fadlun, R. Verzicco, P. Orlandi, and J. Mohd-Yusof, "Combined Immersed-Boundary Finite-Difference Methods for Three-Dimensional Complex Flow Simulations," *Journal of Computational Physics*, vol. 161, pp. 35–60, 2000.

[12] T. Kajishima, S. Takiguchi, H. Hamasaki, and Y. Miyake, "Turbulence Structure of Particle-Laden Flow in a Vertical Plane Channel Due to Vortex Shedding," *JSME International Journal Series B*, vol. 44, pp. 526–535, 2001.

[13] C. S. Peskin, "Numerical analysis of blood flow in the heart," *Journal of Computational Physics*, vol. 25, pp. 220–252, 1977.

[14] Y. Shigeto and M. Sakai, “Arbitrary-shaped wall boundary modeling based on signed distance functions for granular flow simulations,” *Chemical Engineering Journal*, vol. 231, pp. 464–476, 2013.

[15] T. B. Anderson and R. Jackson, “Fluid Mechanical Description of Fluidized Beds. Equations of Motion,” *Ind. Eng. Chem. Fund.*, vol. 6, no. 4, pp. 527–539, 1967.

[16] D. Gidaspow, *Multiphase Flow and Fluidization: Continuum and Kinetic Theory Descriptions*. Academic Press, 1st ed., 1994.

[17] N. Deen, M. Van Sint Annaland, M. Van der Hoef, and J. Kuipers, “Review of discrete particle modeling of fluidized beds,” *Chemical Engineering Science*, vol. 62, pp. 28–44, 2007.

[18] H. Zhu, Z. Zhou, R. Yang, and A. Yu, “Discrete particle simulation of particulate systems: Theoretical developments,” *Chemical Engineering Science*, vol. 62, pp. 3378–3396, 2007.

[19] H. Zhu, Z. Zhou, R. Yang, and A. Yu, “Discrete particle simulation of particulate systems: A review of major applications and findings,” *Chemical Engineering Science*, vol. 63, pp. 5728–5770, 2008.

[20] X. Zhang and G. Ahmadi, “Eulerian—Lagrangian simulations of liquid—gas—solid flows in three-phase slurry reactors,” *Chemical Engineering Science*, vol. 60, pp. 5089–5104, 2005.

[21] J. Wen, P. Lei, and L. Huang, “Modeling and Simulation of Gas-Liquid-Solid Three-Phase Fluidization,” *Chemical Engineering Communications*, vol. 192, pp. 941–955, 2005.

[22] Y. Li, J. Zhang, and L.-S. Fan, “Numerical simulation of gas—liquid—solid fluidization systems using a combined CFD-VOF-DPM method: bubble wake behavior,” *Chemical Engineering Science*, vol. 54, pp. 5101–5107, 1999.

[23] Y. Li, G. Yang, J. Zhang, and L.-S. Fan, “Numerical studies of bubble formation dynamics in gas—liquid—solid fluidization at high pressures,” *Powder Technology*, vol. 116, pp. 246–260, 2001.

[24] J. Zhang, Y. Li, and L.-S. Fan, “Numerical studies of bubble and particle dynamics in a three-phase fluidized bed at elevated pressures,” *Powder Technology*, vol. 112, pp. 46–56, 2000.

[25] J. Zhang, Y. Li, and L.-S. Fan, "Discrete phase simulation of gas—liquid—solid fluidization systems: single bubble rising behavior," *Powder Technology*, vol. 113, pp. 310–326, 2000.

[26] K. Kafui, C. Thornton, and M. Adams, "Discrete particle-continuum fluid modelling of gas—solid fluidised beds," *Chemical Engineering Science*, vol. 57, pp. 2395–2410, 2002.

[27] C. Chen and L.-S. Fan, "Discrete simulation of gas-liquid bubble columns and gas-liquid-solid fluidized beds," *AIChE Journal*, vol. 50, pp. 288–301, 2004.

[28] Y. Ge and L.-S. Fan, "3-D direct numerical simulation of gas—liquid and gas—liquid—solid flow systems using the level-set and immersed boundary methods," *Advances in Chemical Engineering*, vol. 31, pp. 1–63, 2006.

[29] G. Yang, B. Du, and L. Fan, "Bubble formation and dynamics in gas—liquid—solid fluidization—A review," *Chemical Engineering Science*, vol. 62, pp. 2–27, 2007.

[30] M. van Sint Annaland, N. Deen, and J. Kuipers, "Numerical simulation of gas—liquid—solid flows using a combined front tracking and discrete particle method," *Chemical Engineering Science*, vol. 60, pp. 6188–6198, 2005.

[31] T. Can, L. Mingyan, and X. Yonggui, "3-D numerical simulations on flow and mixing behaviors in gas-liquid-solid microchannels," *AIChE Journal*, vol. 59, pp. 1934–1951, 2013.

[32] K. Washino, H. Tan, M. Hounslow, and A. Salman, "Meso-scale coupling model of DEM and CIP for nucleation processes in wet granulation," *Chemical Engineering Science*, vol. 86, pp. 25–37, 2013.

[33] K. Yokoi, "Efficient implementation of THINC scheme: A simple and practical smoothed VOF algorithm," *Journal of Computational Physics*, vol. 226, no. 2, pp. 1985–2002, 2007.

[34] T. Kajishima and S. Takiguchi, "Interaction between particle clusters and particle-induced turbulence," *International Journal of Heat and Fluid Flow*, vol. 23, pp. 639–646, 2002.

[35] Z. Y. Zhou, S. B. Kuang, K. W. Chu, and A. B. Yu, "Discrete particle simulation of particle—fluid flow: model formulations and their applicability," *Journal of Fluid Mechanics*, vol. 661, pp. 482–510, 2010.

[36] C. T. Crowe, M. Sommerfeld, and Y. Tsuji, *Multiphase Flows with Droplets and Particles.* Taylor & Francis, 1997.

[37] A. Di Renzo and F. P. Di Maio, "Homogeneous and bubbling fluidization regimes in DEM—CFD simulations: Hydrodynamic stability of gas and liquid fluidized beds," *Chemical Engineering Science*, vol. 62, pp. 116–130, 2007.

[38] M. Sakai, Y. Shigeto, X. Sun, T. Aoki, T. Saito, J. Xiong, and S. Koshizuka, "Lagrangian—Lagrangian modeling for a solid—liquid flow in a cylindrical tank," *Chemical Engineering Journal*, vol. 200-202, pp. 663–672, 2012.

[39] M. Abbas, M. Van der Hoef, and H. Kuipers, "Discrete Particle Model for simulating liquid-solid fluidization," in *7th International Conference of Multiphase Flows*, (Tampa, USA), 2010.

[40] Y. Feng and A. Yu, "Comments on " Discrete particle-continuum fluid modelling of gas—solid fluidised beds " by Kafui et al. [Chemical Engineering Scinece 57 (2002) 2395—2410]," *Chemical Engineering Science*, vol. 59, pp. 719–722, 2004.

[41] K. Kafui, C. Thornton, and M. Adams, "Reply to Comments by Feng and Yu on " Discrete particle-continuum fluid modelling of gas—solid fluidised beds " by Kafui et al.," *Chemical Engineering Science*, vol. 59, pp. 723–725, 2004.

[42] J. Yang and F. Stern, "Sharp interface immersed-boundary/level-set method for wave—body interactions," *Journal of Computational Physics*, vol. 228, pp. 6590–6616, 2009.

[43] X. Sun, M. Sakai, M.-T. Sakai, and Y. Yamada, "A Lagrangian—Lagrangian coupled method for three-dimensional solid—liquid flows involving free surfaces in a rotating cylindrical tank," *Chemical Engineering Journal*, vol. 246, pp. 122–141, 2014.

[44] X. Sun, M. Sakai, and Y. Yamada, "Three-dimensional simulation of a solid—liquid flow by the DEM—SPH method," *Journal of Computational Physics*, vol. 248, pp. 147–176, 2013.

[45] Y. Yamada and M. Sakai, "Lagrangian—Lagrangian simulations of solid —liquid flows in a bead mill," *Powder Technology*, vol. 239, pp. 105–114, 2013.

[46] S. Ergun, “Fluid flow through packed columns,” *Chem. Eng. Prog.*, vol. 48, pp. 89–94, 1952.

[47] C. Wen and Y. Yu, “Mechanics of fluidization,” *Chem. Eng. Prog. Symp. Ser.*, vol. 62, no. 62, p. 100, 1966.

[48] R. Di Felice, “The voidage function for fluid-particle interaction systems,” *International Journal of Multiphase Flow*, vol. 20, pp. 153–159, 1994.

[49] N. Sharma and N. A. Patankar, “A fast computation technique for the direct numerical simulation of rigid particulate flows,” *Journal of Computational Physics*, vol. 205, pp. 439–457, 2005.

[50] F. H. Harlow and J. E. Welch, “Numerical Calculation of Time-Dependent Viscous Incompressible Flow of Fluid with Free Surface,” *Physics of Fluids*, vol. 8, p. 2182, 1965.

[51] D. B. Spalding, “A novel finite difference formulation for differential expressions involving both first and second derivatives,” *International Journal for Numerical Methods in Engineering*, vol. 4, pp. 551–559, 1972.

[52] E. Olsson and G. Kreiss, “A conservative level set method for two phase flow,” *Journal of Computational Physics*, vol. 210, pp. 225–246, 2005.

[53] J. Brackbill, D. Kothe, and C. Zemach, “A continuum method for modeling surface tension,” *Journal of Computational Physics*, vol. 100, pp. 335–354, 1992.

[54] T. Yabe, K. Chinda, and T. Hiraishi, “Computation of surface tension and contact angle and its application to water strider,” *Computers & Fluids*, vol. 36, pp. 184–190, 2007.

[55] A. J. Chorin, “Numerical solution of the Navier-Stokes equations,” *Mathematics of Computation*, vol. 22, no. 104, pp. 745–745, 1968.

[56] R. P. Fedkiw, T. Aslam, B. Merriman, and S. Osher, “A Non-oscillatory Eulerian Approach to Interfaces in Multimaterial Flows (the Ghost Fluid Method),” *Journal of Computational Physics*, vol. 152, pp. 457–492, 1999.

[57] C. Kloss, C. Goniva, A. Hager, S. Amberger, and S. Pirker, “Models, algorithms and validation for opensource DEM and CFD—DEM,”

Progress in Computational Fluid Dynamics, an International Journal, vol. 12, no. 2, pp. 140–152, 2012.

[58] S.-Y. Lin and Y.-C. Chen, “A pressure correction-volume of fluid method for simulations of fluid—particle interaction and impact problems,” *International Journal of Multiphase Flow*, vol. 49, pp. 31–48, 2013.

[59] M. Robinson, M. Ramaioli, and S. Luding, “Fluid—particle flow simulations using two-way-coupled mesoscale SPH—DEM and validation,” *International Journal of Multiphase Flow*, vol. 59, pp. 121–134, 2014.

[60] J. Zhao and T. Shan, “Coupled CFD—DEM simulation of fluid—particle interaction in geomechanics,” *Powder Technology*, vol. 239, pp. 248–258, 2013.

[61] M. Skoge, A. Donev, F. Stillinger, and S. Torquato, “Packing hyperspheres in high-dimensional Euclidean spaces,” *Physical Review E*, vol. 74, p. 041127, 2006.

[62] J. C. Martin and W. J. Moyce, “Part IV. An Experimental Study of the Collapse of Liquid Columns on a Rigid Horizontal Plane,” *Philosophical Transactions of the Royal Society A: Mathematical, Physical and Engineering Sciences*, vol. 244, pp. 312–324, 1952.

[63] L. Guo and K. Morita, “Numerical simulation of 3D sloshing in a liquid-solid mixture using particle methods,” *International Journal for Numerical Methods in Engineering*, vol. 95, pp. 771–790, 2013.

[64] S. Muzaferija and M. Peric, “Computation of free-surface flows using interface-tracking and interface-capturing methods,” in *Nonlinear water wave interaction* (O. Mahrenholtz and M. Markiewicz, eds.), ch. 2, pp. 59–100, WIT Press, 1999.

[65] S. A. Jaffer, V. L. Bravo, P. E. Wood, A. N. Hrymak, and J. D. Wright, “Experimental validation of numerical simulations of the kneading disc section in a twin screw extruder,” *Polymer Engineering & Science*, vol. 40, pp. 892–901, 2000.

[66] X.-M. Zhang, L.-F. Feng, W.-X. Chen, and G.-H. Hu, “Numerical simulation and experimental validation of mixing performance of kneading discs in a twin screw extruder,” *Polymer Engineering & Science*, vol. 49, pp. 1772–1783, 2009.

[67] J. Wei, X. Liang, D. Chen, Y. Yang, and D. Zhou, “Evaluation of the mixing performance for one novel twin screw kneader with particle tracking,” *Polymer Engineering & Science*, pp. n/a–n/a, 2013.

[68] Y. Nakayama, E. Takeda, T. Shigeishi, H. Tomiyama, and T. Kajiwara, “Melt-mixing by novel pitched-tip kneading disks in a co-rotating twin-screw extruder,” *Chemical Engineering Science*, vol. 66, pp. 103–110, 2011.

[69] M. van der Hoef, M. van Sint Annaland, N. Deen, and J. Kuipers, “Numerical Simulation of Dense Gas-Solid Fluidized Beds: A Multiscale Modeling Strategy,” *Annual Review of Fluid Mechanics*, vol. 40, pp. 47–70, 2008.

[70] H. Marschall and O. Hinrichsen, “Numerical Simulation of Multi-Scale Two-Phase Flows Using a Hybrid Interface-Resolving Two-Fluid Model (HIRES-TFM),” *JOURNAL OF CHEMICAL ENGINEERING OF JAPAN*, vol. 46, pp. 517–523, 2013.

Chapter 4

A numerical method for the direct numerical simulation of three-phase problems

4.1 Introduction

Complex gas-solid-liquid flows involving free surface motion and solid particles transportation are widely encountered in industries. Especially in processes involving classification, dispersion and interfaces, it is known that the interactions among multi-fluids and granular particles can be relevant to the systematic account of complex phenomena and key parameter directing towards optimal operation conditions. Study of such problems based on numerical approaches is nowadays an active yet pressing topic for researchers and engineers.

So far, the complexity of gas-solid-liquid three-phase systems from its multi-physics and multi-scale nature has rendered the numerical study to fork in at least two levels: macroscopic methods based on averaged models and microscopic methods based on direct numerical simulation (DNS). For instance, the DEM-VOF method developed in our previous study belongs to the former category which is able to simulate large-scale engineering problems in practical applications. However, its actual performance may strictly depend on a number of core correlations for the description of unresolved terms, of which one considered the most important in fluid-particle flows is the interphase momentum transfer or the hydrodynamic force giving an effective fluid drag to furnish the coupling between continuum and dispersed phases. In the context of three-phase flows, there are still requirements for the closure defining the capillary force and liquid bridge force induced by local interface deformation. To some extent, the discovery and integration of various closure equations determine the validity and versatility of a numerical solver adopting macroscopic models.

In comparison with the macroscopic modeling of gas-solid-liquid flows discussed in the preceding chapter, the DNS-based approach is self-contained in the sense that all relevant flow structures and interaction terms at the continuum scale are solved without any empirical constitutions (as long as they are taken into consideration), including both hydrodynamic and capillary effects. It is certainly worth noting that, because of its constraint on computational cost, the requirement of DNS of multiphase problems is twofold from an engineering point of view:

(a) to directly simulate some microscopic systems, e.g. bubble floatation and self-assembly of colloidal particles on fluid interfaces and substrates;

(b) to provide scalable interaction models that can be used for large-scale problems, e.g. kneading, wet beads/ball milling and three-phase fluidized bed.

In both respects, the DNS approach would be helpful for understanding and improving the numerical modeling of gas-solid-liquid systems, which has motivated our development in this study of a three-phase DNS method that is able to correctly evaluate the fluid-particle interaction mainly owing to hydrodynamic and capillary forces.

4.1.1 Modeling of fluid-particle flows

The DNS modeling of fluid-particle flows is first reviewed briefly so as to provide a fundamental discretization of three-phase systems. A traditional approach is to use body-fitted moving mesh that conforms to the fluid-solid surface [1], which can be computationally complicated and expensive because of the grid generation and remeshing operations. In recent years, fixed Cartesian grid methods, e.g. the lattice Boltzmann method (LBM) [2], the fictitious domain (FD) method [3] and the immersed boundary (IB) method [4–6], have become popular for their great simplicity and efficiency in treating moving solid objects with arbitrary shapes. The most impressive applications of those fixed-grid methods are found in the DNS of fluidization systems [7–9].

The IB framework considered in this study is first proposed by [4] for fluid-structure interaction problems. In Peskin's IB method, the immersed interface is represented by marker points and their actions are distributed to surrounding fluids by a generalized delta-function, which is referred to as a continuous forcing approach. Sometimes, it can cause a considerable smearing of the fluid-solid surface. Later in the direct forcing IB method [10], the solid velocity is discretely prescribed on fluid points embedding the object surface by using geometrical interpolation. In the work of Kajishima et al. [11, 12], the direct forcing IB method is further simplified by mixing the fluid and solid velocities are explicitly blended by using the local solid volume fraction as a weighting factor. This method is easy to implement and particularly useful for dense suspensions. All these formulations of IB method have been successfully applied to the DNS of flows involving mobile particles or moving objects with necessary modifications and improvements, see e.g. [6, 13–17].

4.1.2 Modeling of three-phase flows

In the past, some studies have been contributed to the DNS of gas-solid-liquid flows by using fixed-grid type methods. The most common strategy is to incorporate an interfacial flow model such as the volume-of-fluid (VOF) method [18], the level-set (LS) method [19], the front-tracking (FT) method [20], and the constrained interpolation profile (CIP) method [21] into the fluid-particle solver to represent the continuum phase composed of a mixture of gas and liquid.

In [22] two-dimensional waves interacting with floating cylinders is computed. Iwata et al. [23] studied the trajectory of a single rising bubble through particle dispersions of comparable size, but their work is lacking in a detailed validation of the bubble-particle interaction model. Washino et al. [24] proposed models for fluid-particle interaction and gas-liquid contact line dynamics separately, but there were not any direct results illustrating the coupling among those three phases. Lin and Chen [25] simulated a three-phase dam break flow in which a submerged stack of spheres collapsed simultaneously with the water column. A series of water entry problems of spheres have been studied numerically with experimental backup in Jain et al. [26] and Mirzaii and Passandideh-Fard [27]. Based on DNS results of bubble-particle interference simulations, Baltussen et al. [28] tried to derive a closure for drag force on bubbles as a function of solid volume fractions.

However, we would like to emphasize that all of the above reports have only provided a partial modeling of three-phase flows as they generally neglect the particle-interface interaction which includes the contact angle on solid surface and the capillary effects exerted by the local meniscus. Therefore, it is no point that those “incomplete” models could ever be eligible for the target of this study, i.e. the fully-resolved DNS of gas-solid-liquid flows.

Existing models that are able to achieve a simultaneous resolution of hydrodynamic and capillary interactions in a three-phase system have been mostly achieved by using the multiphase LBM with special treatment to enforce the rigid motion of the solid phase. They have been applied to various three-phase problems featuring the lateral force between two-dimensional rods [29,30], solid particles suspension and wetting behavior [31,32], contact-line motions [33] and particle clustering driven by capillary interactions [34–36]. The major drawback of LBM is that the computation becomes unstable for flows with large density ratio, c.f. [37], so their application is severely restricted and may not be directly applicable to free surface flows with a typical air-water pairing. Additionally, for the mesoscopic nature of the LBM, the definition of contact angle cannot be directly designated but is introduced via an intermediate cohesive variable, see [34]. As mentioned by the authors, there arises an ambiguity of computational parameter, because no analytical correspondence could be found between the cohesive force parameter and the physical contact angle.

The Finite Element (FE) simulation by [38, 39] modeled the steady and unsteady motions of floating objects at fluid interface. A remarkable result of their work is the modeling of cubes and disks clipped to the free surface at sharp edges. However, the algorithm described in [38] is relatively complicated which might be prohibitive in treating systems with a large amount of particles. In fact, the number of spherical particles simulated is at most four in [39].

Washino et al. [40] proposed the continuum capillary force (CCF) model and proved its validity for the calculation of capillary force on solid particles. The description of fluid interface in their model is based on the CIP method, which is disadvantageous for the accurate representation of the interface and the computation of surface tension force.

According to the review of past studies, there are mainly three problems that would be addressed in order to achieve high-fidelity DNS of gas-solid-liquid flows:

(a) The algorithmic complexity and accuracy of the numerical framework to achieve fluid-particle coupling;

(b) An accurate representation of the interface which can also facilitate the calculation of surface tension and capillary force;

(c) The straightforward treatment of three-phase contact lines and contact angle boundary condition.

The section below will be talking about our solutions for these problems.

4.1.3 Developments in this work

In this study, we describe the DEM-VOF-DNS method to perform three-dimensional simulations of gas-solid-liquid flows at a micro-scale, i.e. a full resolution of fluid-particle interaction. The fluid phase consisted of gas and liquid is treated by our workhorse implementation of a multiphase flow solver based on the THINC/WLIC VOF scheme of [41]. The Newton dynamics of distinct particles are simulated by the discrete element method (DEM) [42]. The coupling of this system is realized by using the IB formulation suggested by [11].

Computational techniques have been developed within this DNS framework in order to address the numerical difficulties stemming from the complexity of gas-solid-liquid systems.

- With revising for the IB method, a new form of the fluid-particle interaction term is derived by considering the integral of a multiphase fluid stress over the solid surface. This revised model is provided as a unified interaction term for not only the hydrodynamic force as in conventional IB models for gas-solid and liquid-solid flows but also the capillary force due to the fluid interface in gas-solid-liquid flows. The numerical procedure enrolled in this new model is almost as simple as the original IB method so that the computational complexity is not increased.

- The modeling of the gas-liquid interface is based on a simplified coupled LS and VOF (CLSVOF) approach developed in this study. The VOF known to have good property of volume conservation is used to tracking the interface motion. From that an equivalent LS representation of the fluid interface is constructed by using the LS reinitialization operation [43]. Compared with a VOF method, the LS approach describes the interface as a smooth function and thus it is able to yield improved, convergent results for the calculation of surface tension and capillary force. Our simplified version of CLSVOF method is also more efficient than other existing ones [44,45] since it does not require explicit reconstruction of the interface shape.

- In order to treat contact angles, the extension approach proposed by [46] is adopted in the present model for spherical particles. In this method, the interface profile at the fluid side is extrapolated into the solid domain to implicitly satisfy the boundary condition of contact angle. Therefore, unlike some studies (see e.g. [47–49]), the position of the three-phase contact line need not be explicitly located.

In this way, the DEM-VOF-DNS method enables the fully-resolved simulation of gas-solid-liquid problems. Numerical tests have been performed to validate this model and to demonstrate its achievement in computational ability. It is further applied to the DNS of particles floating on the fluid interface which is a typical gas-solid-liquid system where the flow behavior can be dominated by hydrodynamic and capillary effects. The cases of single particle in equilibrium and capillary attraction among multiple particles ($\sim 10^2$) are simulated, showing that the proposed method can treat complex three-phase systems with ease. Thru our literature survey, we find this might be the first DNS method able to resolve the capillary interaction in an IB framework[1].

Additionally in the last part of this work, some DNS results are presented for the calculation of fluid drag when flows pass through an ordered or random particle bed within a range of solid fraction and Reynolds number. Those results are then put into comparison with some model equations obtained experimentally. Such drag correlations are the essential ingredient for numerical solvers based on volume-averaging approach such as the DEM-VOF method developed in the previous chapter. Hence, this might be helpful for establishing a connection between DNS and averaged models through which DNS results could be used to develop new subgrid constitutive laws or to find the validity domain of existing empirical equations.

4.2 Model description for three-phase flows

Consider a domain contains a continuum fluid phase and a dispersed solid phase V whose surface is denoted by S. The continuum phase is further separated by an immiscible interface into binary components (i.e. gas and liquid). The position where the gas-liquid interface intersects with the solid surface becomes the so-called contact line L.

---

[1] Very recently, Fujita et al. [50, 51] also described an immersed free surface method for colloidal particles behavior on a substrate with drying, which has got certain features in common with our DEM-VOF-DNS model. However, in their model the interface is tracked by using the LS method, which might suffer from loss of mass problem due to the difficulty in fixing conservation errors.

4.2.1 Fluid motion

The continuum phase motion is governed by a “one-fluid” Navier-Stokes equation written as

$$\rho \left(\frac{\partial \boldsymbol{u}}{\partial t} + \nabla \cdot (\boldsymbol{u}\boldsymbol{u}) \right) = -\nabla p + \nabla \cdot \tau + \rho \boldsymbol{g} + \gamma \kappa \delta \boldsymbol{n} \ , \tag{4.1}$$

which treats the fluid domain as a whole with varying physical properties. Herein, $\boldsymbol{u}$ and p are velocity and pressure, ρ is the density, τ is deviatoric stress tensor, $\boldsymbol{g}$ is the gravity, γ is the coefficient of surface tension, κ is local mean curvature, δ is a the delta-function non-zero at the fluid interface, and $\boldsymbol{n}$ is the unit normal vector of the fluid interface, respectively. For Newtonian fluids, the fluid stress is linked with the rate of deformation tensor $\mathbf{D}$ as

$$\tau = 2\mu \mathbf{D} \tag{4.2}$$

$$\mathbf{D} = \frac{1}{2}(\nabla \boldsymbol{u} + \nabla \boldsymbol{u}^T) \tag{4.3}$$

with μ the fluid viscosity. This system is complemented by the equation of mass conservation for which incompressible fluids are assumed:

$$\nabla \cdot \boldsymbol{u} = 0 \ , \tag{4.4}$$

which is the well-known divergence-free condition for fluid velocity.

They are then supplemented with a non-slip boundary condition for velocity on the solid surface S, which must be compatible with the rigid velocity:

$$\boldsymbol{u} = \boldsymbol{v} + \boldsymbol{\omega} \times \boldsymbol{r} \text{ on } S \ , \tag{4.5}$$

in which $\boldsymbol{v}$ is the velocity and $\boldsymbol{\omega}$ is the angular velocity of the solid object; $\boldsymbol{r}$ is the displacement vector from the mass center of the solid object.

4.2.2 Solid motion

The translational and rotational motions of the solid is governed by the Newton’s law of motion:

$$m_s \frac{\mathrm{d}\boldsymbol{v}}{\mathrm{d}t} = \boldsymbol{F}^C + m_s \boldsymbol{g} + \boldsymbol{F}^f \tag{4.6}$$

$$\frac{\mathrm{d}(\boldsymbol{I}_s \boldsymbol{\omega})}{\mathrm{d}t} = \boldsymbol{T}^C + \boldsymbol{T}^f \tag{4.7}$$

In the translational equation, m_s is solid mass, $\boldsymbol{F}^C$ is contact force, and $\boldsymbol{F}^f$ is the force due to fluid action. For the rotational equation, $\boldsymbol{I}_s$ is the moment of inertia tensor calculated as

$$\boldsymbol{I}_s = \int_V \rho_s \left[(\boldsymbol{r} \cdot \boldsymbol{r})\mathbf{I} - \boldsymbol{r} \otimes \boldsymbol{r} \right] dV \tag{4.8}$$

which is reduced to a single scalar

$$I_s = \frac{2}{5} m_s R^2 \tag{4.9}$$

for a single spherical particle. $\boldsymbol{T}^C$ and $\boldsymbol{T}^f$ are the torques of contact force and fluid actions, respectively.

In this study, the fluid action $\boldsymbol{F}^f = \boldsymbol{F}^d + \boldsymbol{F}^s$ comes from the contributions of fluid stress or the hydrodynamic force on the solid surface

$$\boldsymbol{F}^d = \int_S (-p\mathbf{I} + \tau) \cdot \boldsymbol{n}_S dS \ , \tag{4.10}$$

and the surface tension or the capillary force along the contact line

$$\boldsymbol{F}^s = \int_L \gamma \boldsymbol{n}_L dL \ . \tag{4.11}$$

Herein $\boldsymbol{n}_S$ is the unit normal vector of the solid surface, and $\boldsymbol{n}_L$ is a unit vector tangential to the fluid interface and perpendicular to the contact line indicating the orientation of pulling tension.

We would like to emphasize that, the current interaction model is also open to other effects, such as the lubrication effect for concentrated suspension [52], van der Waals force for adhesive particles, and thermal fluctuation or Brown motion in colloidal systems.

4.2.3 Interface description

The configuration of the gas and liquid phases are described by an indicator function dϕ coloring them differently, of which the advection equation gives the temporal advancement of the interface motion:

$$\frac{\partial \phi}{\partial t} + \boldsymbol{u} \cdot \nabla \phi = 0 \tag{4.12}$$

In this study, a static contact angle boundary condition is applied to contact lines to define the local shape of meniscus at the solid surface. With a prescribed contact angle θ_C, this condition is written as

$$- \boldsymbol{n} \cdot \boldsymbol{n}_S = \cos \theta_C \tag{4.13}$$

Again, recall that unit vector $\boldsymbol{n}$ is the interfacial normal pointing from the gas to the liquid phase, and $\boldsymbol{n}_S$ is the normal vector of the solid surface.

4.3 IB modeling of fluid-particle system

In this section, the numerical modeling of a fluid-particle system based on the IB method is discussed exclusively without any specific consideration for the fluid interface. It is intended to derive a general, accurate form for the fluid-particle interaction term within the IB framework.

4.3.1 Basic IB method

In the IB method, the fluid-particle motion is resolved in an integrated manner in which the fluid phase is extended to the entire computational domain including the solid region. For that purpose, the Navier-Stokes equation is augmented as

$$\frac{\partial \boldsymbol{u}}{\partial t} + \nabla \cdot (\boldsymbol{u}\boldsymbol{u}) = -\frac{1}{\rho}\nabla p + \frac{1}{\rho}\nabla \cdot \tau + \boldsymbol{g} + \frac{1}{\rho}\gamma\kappa\delta\boldsymbol{n} + \boldsymbol{f}_{IB} \ , \tag{4.14}$$

in which $\boldsymbol{f}_{IB}$ is a special body force to enforce the rigid motion. The solenoidal divergence-free condition

$$\nabla \cdot \boldsymbol{u} = 0 \tag{4.15}$$

now applies to the velocity field within the immersed solid region as well. An additional phase function α indicating the solid volume fraction is introduced to identify the solid domain. Its evolution is treated by a Lagrangian advection following the particle movement:

$$\frac{\mathrm{d}\alpha}{\mathrm{d}t} = 0 \ . \tag{4.16}$$

Those fluid equations are numerically solved by using a fractional-step method. Firstly, a velocity predictor is calculated with Adams-Bashforth scheme for the convective term and Crank-Nicolson scheme for the viscous term:

$$\begin{aligned}\frac{\boldsymbol{u}^* - \boldsymbol{u}^n}{\Delta t} = &-\left(\frac{3}{2}\nabla \cdot (\boldsymbol{u}\boldsymbol{u})^n - \frac{1}{2}\nabla \cdot (\boldsymbol{u}\boldsymbol{u})^{n-1}\right) \\ &+ \frac{1}{2\rho}(\nabla \cdot \tau^* + \nabla \cdot \tau^n)\end{aligned} \tag{4.17}$$

Next the jump terms due to gravity and surface tension are incorporated to give a provisional velocity field which does not satisfy the divergence-free condition:

$$\frac{\boldsymbol{u}^{**} - \boldsymbol{u}^*}{\Delta t} = \boldsymbol{g} + \frac{1}{\rho}\gamma\kappa\delta\boldsymbol{n} \ . \tag{4.18}$$

The following pressure Poisson equation (PPE) scaled by density is hence solved with proper boundary conditions to obtain the fluid pressure:

$$\nabla \cdot \left(\frac{1}{\rho} \nabla p \right) = \frac{\nabla \cdot \boldsymbol{u}^{**}}{\Delta t} \ . \tag{4.19}$$

For solid-liquid or solid-gas flows, the fluid density ρ remains constant and thus the PPE above is separable and can be efficiently solved by an FFT-based fast solver using the algorithm for boundary conditions treatment described in [53]. For gas-solid-liquid flows with variable fluid density, the resulting numerical system is solved by the multigrid preconditioned conjugate gradient (MGPCG) method provided by the HYPRE library.

Based on the pressure gradient, the velocity corrector is applied so that the divergence-free condition is satisfied:

$$\frac{\boldsymbol{u}^{***} - \boldsymbol{u}^{**}}{\Delta t} = -\frac{1}{\rho} \nabla p \ . \tag{4.20}$$

Finally the solid velocity is imposed for the pseudo-fluid in the immersed domain, which is performed by a linear interpolation based on the solid volume fraction function:

$$\boldsymbol{u}^{n+1} = (1 - \alpha) \boldsymbol{u}^{***} + \alpha \boldsymbol{v}^{n+1} \ . \tag{4.21}$$

From this equation, the IB forcing term could be found by

$$\boldsymbol{f}_{IB} = \frac{\boldsymbol{u}^{n+1} - \boldsymbol{u}^{***}}{\Delta t} = \frac{\alpha (\boldsymbol{u}_{IB} - \boldsymbol{u})}{\Delta t} \ . \tag{4.22}$$

In the original IB method by [11], $\boldsymbol{f}_{IB}$ is explained *a priori* as the interphase momentum transfer term, which directly leads to the following formulation of fluid action on solid particles, i.e. the fluid force

$$\boldsymbol{F}^f = -\int_V \rho \boldsymbol{f}_{IB} dV \ , \tag{4.23}$$

and its torque

$$\boldsymbol{T}^f = -\int_V \rho \boldsymbol{r} \times \boldsymbol{f}_{IB} dV \ . \tag{4.24}$$

Those integrals are simply replaced by the midpoint quadrature rule at the center of each numerical cell enclosed by the solid domain.

4.3.2 Revised IB force for mobile particles

In this section, the derivation of the fluid-particle interaction term is revised by considering its physical and mathematical definition owing to the integral of fluid stress over the particle surface. It is hence pursued on the end to derive a consistent equation for the fluid action.

Before that, the form of the singular surface tension is manipulated to facilitate the discussion. In the continuum surface stress (CSS) [54] formulation, it is shown that the surface tension can be recast into a tensorial form as

$$\boldsymbol{f}^s = \gamma\kappa\delta\boldsymbol{n} = -\nabla \cdot \Pi \tag{4.25}$$

with the capillary pressure tensor Π defined by

$$\Pi = -\gamma(\mathbf{I} - \boldsymbol{n} \otimes \boldsymbol{n})\delta \ . \tag{4.26}$$

Therefore it is possible to combine the hydrodynamic and capillary actions in a generalized "multiphase fluid stress",

$$\sigma = -p\mathbf{I} + \tau - \Pi \ . \tag{4.27}$$

The fluid force is thus by definition given by the surface integral of the total fluid stress σ on the solid surface. With the application of Gauss's divergence theorem, one obtains a volume integral instead:

$$\boldsymbol{F}^f = \int_S \sigma \cdot \boldsymbol{n} dS = \int_V \nabla \cdot \sigma dV \ . \tag{4.28}$$

In order to find this integral in an IB context, it is resorted to the pseudo-fluid motion within the IB domain which writes

$$\rho \frac{\mathrm{D}\boldsymbol{u}}{\mathrm{D}t} = \nabla \cdot \sigma + \rho \boldsymbol{g} + \rho \boldsymbol{f}_{IB} \ . \tag{4.29}$$

Integrate on both sides over the solid domain V and move terms, one can easily derive that

$$\begin{aligned} \boldsymbol{F}^f &= \int_V \nabla \cdot \sigma dV \\ &= -\int_V \rho \boldsymbol{f}_{IB} dV - \int_V \rho \boldsymbol{g} dV + \int_V \rho \frac{\mathrm{D}\boldsymbol{u}}{\mathrm{D}t} dV \ . \end{aligned} \tag{4.30}$$

From this form of $\boldsymbol{F}^f$, it is found that the total fluid force consists of three parts of contributions. Similar results can also be obtained for the fluid torque.

- The first part is the original IB forcing with a minus sign, indicating reaction to the solid phase.
- The second part is explicitly separated as hydrostatic buoyancy, which tends to cancel solid's gravity.
- The third part is a virtual force owing to the pseudo-fluid acceleration.

Now let us consider the motion of the immersed object, which is described by

$$m_s \dot{\boldsymbol{v}} = \boldsymbol{F}^f + m_s \boldsymbol{g} \ . \tag{4.31}$$

We insert the definition of $\boldsymbol{F}^f$ into the momentum equation and obtain the following one solved in the DEM-VOF-DNS method:

$$m_s \dot{\boldsymbol{v}} = \boldsymbol{F}_{IB} + (m_s - m_f)\boldsymbol{g} + \boldsymbol{F}_{virt} \ , \tag{4.32}$$

with

$$\boldsymbol{F}_{IB} = -\int_V \rho \boldsymbol{f}_{IB} dV \tag{4.33}$$

$$m_f = \int_V \rho dV \tag{4.34}$$

$$\boldsymbol{F}_{virt} = \int_V \rho \frac{\mathrm{D}\boldsymbol{u}}{\mathrm{D}t} dV \ . \tag{4.35}$$

We note that, the new formulation of fluid-particle interaction term has the following features in practical usage.

- It is consistent with the solution algorithm based on a fractional-step method. Note that in a fractional-step method, variables such as pressure and velocity generally come from different computational stages, which makes it difficult and uneconomical to directly calculate the integral of fluid pressure and viscous forces. This problem is circumvented in the present IB as only the fluid states at the end of a computational step is required.
- The calculation of all terms composing the interaction force is relatively straightforward; the virtual force term can also be easily computed by the original IB quadrature rule.
- As shown in its derivation, not only the hydrodynamic force but also the capillary force has been taken into account in the present model. It is thus shown to be potentially inclusive of other physics as long as they are continuous across the fluid-solid surface and can be integrated as a part of the total fluid stress σ.

We have also noticed that, the reduced-mass form of momentum equation used in many IB literatures (see e.g. [6]) can be recovered if the virtual term is moved to the left-hand side assuming that the rigid motion is perfectly satisfied within the solid domain, i.e.

$$\frac{1}{V}\int_V \boldsymbol{u} dV = \boldsymbol{v} \ . \tag{4.36}$$

In that case, the momentum equation becomes

$$(m_s - m_f)\frac{\mathrm{d}\boldsymbol{v}}{\mathrm{d}t} = \boldsymbol{F}_{IB} + (m_s - m_f)\boldsymbol{g} \ , \tag{4.37}$$

which is compatible with that adopted in [6]. However, the difference made by the present formulation is that the $\int \rho \frac{\mathrm{D}\boldsymbol{u}}{\mathrm{D}t}$ or the virtual force term actually comes from the previous fluid calculation as a historical acceleration rather than simultaneous effect at the current step. Moreover, it is known that the reduced-mass form allow the fluid-solid density ratio only for $\rho_s/\rho > 1.2$ [6]. On the other hand, the present model will remain stable even for $m_s \leq m_f$ so that light or neutrally buoyant particles could be simulated as well.

In comparison with the original IB [11, 12] method that uses a standard form standing for the momentum exchange based on only the IB forcing

$$m_s\frac{\mathrm{d}\boldsymbol{v}}{\mathrm{d}t} = \boldsymbol{F}_{IB} + m_s\boldsymbol{g} \ , \tag{4.38}$$

the virtual force term in the current model can be viewed as an enhancement for the transformation from the Eulerian fluid frame to the Lagrangian solid frame. Based on our numerical tests, it can improve the performance for time-dependent flows and naturally vanishes under steady flow cases.

In addition, it is noted that the current computational model suffices to resolve the multiphase action on a single particle and several particles at far and finite distances. However, the resolution may become insufficient for the interstitial fluid action as particle pairing comes as close as below several fluid grids. This also takes place when particles are in direct contact with each other. Usually in such cases it is considered that DNS results degenerate for those under-resolved regions and subgrid scale lubrication-like forces can be added for compensation. In past literatures, either lubrication models [8] or penalty forces [7] has ever been adopted for a pair of particles whose surface distance is smaller than one fluid grid spacing. The deployment of such subgrid scale models is accompanied by apparent arbitrariness as their role is to keep solid particles separated rather than to exactly tackle the interaction within narrow surface gap. Very recently, some advanced lubrication model attempts to perform scale separation between DNS-resolved part and subgrid scale-modeled part of fluid actions on solid particles, see e.g. [52]. In this study, the particle behavior at closed distance is out of our major concern and thus the subgrid scale lubrication is not taken into account, although it is straightforward to be incorporated. The contact and separation of solid particles are directly handled by the soft sphere model of the DEM.

4.3.3 time-stepping algorithm

This section describes the overall work flow of the DEM-VOF-DNS method to provide a understandable outline and close our discussion of IB modeling. At the beginning of the n-th computation step, all fluid variables and particle states including the fluid force are thought to be known. For the initialization of the fluid force at the first step, we perform $\sim$ 5 iterations of the fluid procedure without updating particle and interface states to obtain a quasi-steady solution.

1. Solid phase

   Calculate the particle collision force using the DEM and solve linear and angular momentum equations. After updating the particle velocity, the particle position is integrated by a mid-point rule as

   $$\boldsymbol{x}^{n+1} = \boldsymbol{x}^{n} + \Delta t \frac{\boldsymbol{v}^{n+1} + \boldsymbol{v}^{n}}{2} \ . \tag{4.39}$$

2. First sweep for coupling

   The updated solid position is projected to the fluid mesh to generate the solid volume fraction field. The updated solid velocity is also assigned to the solid domain.

3. Fluid interface

   Perform interface reconstruction and advection by using the VOF method. In order to facilitate the interface calculation, a LS-based interface representation is also built from the updated VOF function, see Section 4.4.

4. Fluid phase

   The fluid equations are solved by using the fractional-step methodology described above.

5. Second sweep for coupling

   For the fluid phase, the IB forcing is applied on the immersed mesh points to achieve desired solid motion. At the same time, we scan in solid domain for each immersed particle and calculate the fluid force based on the IB interaction model.

4.4 Simplified CLSVOF modeling of fluid interface

This part presents another important development made in this study, specifically the interface modeling and capillary action calculation based on a simplified CLSVOF technique. It is convenient and accurate to represent the fluid interface and contact line via the current approach; the capillary force acting on solid particles can also be obtained with ease.

4.4.1 LS-based interface representation

In addition to the VOF function ϕ corresponding to the phase volume fraction, a subsidiary interface representation based on LS field ψ is used in this study. Different from ϕ which has a sharp jump across the interfacial region, the LS field ψ is a smooth function indicating the shortest distance to the interface position. Following conventions in LS literatures [19], it is provided that the value of ψ is $\psi < 0$ in gas and $\psi > 0$ in liquid regions, and its zero-contour coincides with the interface.

To avoid sudden change of fluid properties across the interface, a smoothed Heaviside function is introduced to connect the gas and liquid regions, which writes

$$H^s(\psi;\chi) = \begin{cases} 0 & \text{if } \psi < -\chi, \\ 1 & \text{if } \psi > \chi, \\ \frac{1}{2}\left(1 + \frac{\psi}{\chi} + \frac{1}{\pi}\sin\frac{\pi\psi}{\chi}\right) & \text{otherwise,} \end{cases} \tag{4.40}$$

in which χ is a cutoff distance whose typical value is equal to the spacing of several numerical cells. The derivative of H^s with respect to ψ gives a generalized δ-function localized in the interfacial area:

$$\delta^s \equiv \frac{\mathrm{d}H^s}{\mathrm{d}\psi} = \begin{cases} \frac{1}{2\chi}\left(1 + \cos\frac{\pi\psi}{\chi}\right) & \text{if } |\psi| \leq \chi \\ 0 & \text{otherwise.} \end{cases} \tag{4.41}$$

Fluid properties of density and viscosity are determined based on the smoothed Heaviside function as

$$\rho = H\rho_l + (1 - H)\rho_g \tag{4.42}$$

$$\mu = H\mu_l + (1 - H)\mu_g \tag{4.43}$$

which commutes the VOF-based interpolation of fluid properties.

4.4.2 Construction of LS from VOF function

The present modeling is not a standalone application of the LS field ψ. It is, in fact, coupled to the primary VOF-based interface representation. We choose to construct ψ from the VOF function ϕ by using the following procedures.

After performing the interface reconstruction and advection using the VOF scheme as usual, we initialize the LS field ψ assuming the interface is the 0.5-contour of VOF function ϕ. Note that the VOF function $\phi \in [0, 1]$ is mapped to a distance space $\psi_0 \in [-0.5\Delta x, 0.5\Delta x]$ scaling according to the grid size,

$$\psi_0 = (2\phi - 1) \cdot 0.5\Delta x \ . \tag{4.44}$$

As a matter of course, this initial value ψ_0 does not satisfy the regularity condition as a well-defined LS field, i.e.

$$\|\nabla\psi_0\| \neq 1 \ . \tag{4.45}$$

Therefore, the LS reinitialization procedure [19] is invoked to generate a regularized distance function in the vicinity of the fluid interface. The reinitialization equation of ψ writes

$$\frac{\partial\psi}{\partial\tau} = \mathrm{sign}(\psi_0)(1 - \|\nabla\psi\|) \ , \tag{4.46}$$

which can be reformulated as a hyperbolic partial differential equation and treated by using upwind schemes. In this study, it is solved by using the TVD-RK algorithm described in [43] iteratively until a steady state

$$\|\nabla\psi\| = 1 \text{ in } |\psi| \leq \chi \tag{4.47}$$

has been reached. In this way, an equivalent representation of the interface based on ψ has been constructed, whose zero-contour should be, in principle, compatible with the original VOF interface. This hybrid interface modeling is referred to as the simplified CLSVOF method in this study.

Comparison with other approaches

The reinitialization procedure is an indispensable part of computations utilizing the LS field. However, it is known that the position of the free surface is not exactly preserved during the reinitialization operation and this can lead to volume error in LS-based methods. On the other hand, in the current simplified CLSVOF approach the interface is captured by the VOF method that conserves the phasic volume well, from which the LS is constructed as an auxiliary interface representation at each time step. Hence the error owing to LS reinitialization is reset periodically and it does not accumulate during the simulation.

Compared with Sussman's original CLSVOF [44] method that involves complicated procedures to locate the interface point with minimal distance, the current simplified version is much easier to implement. In addition, the VOF function is reversely coupled to the LS field in the original CLSVOF method by truncating its value according to the local signed distance to the interface, which may cause the problem of volume loss. On the other hand, the simplified CLSVOF in the present study is a "one-way" coupling in the sense that the VOF function is not affected by the LS side, so that the advantage of volume conservation of the VOF method is not violated.

Furthermore, in comparison with other CLSVOF variants (see e.g. [23, 45]), the present model does not require explicitly locating of the VOF 0.5-contour based on the PLIC VOF reconstruction or marching-cube algorithm. Hence it is more efficient and naturally connected with a WLIC VOF scheme or other type of interface-capturing methods.

4.4.3 Surface tension calculation

The calculation of surface tension force is based on the balanced continuous surface force (CSF) approach [45, 55, 56] utilizing the LS interface modeling. The surface tension force is given by

$$\boldsymbol{f}^s = \gamma \kappa \delta \boldsymbol{n} \ . \tag{4.48}$$

Notice that the generalized δ-function multiplied by the unit normal is an approximation of the spatial derivative of a smoothed Heaviside function across the interface, hence the following formulation

$$\boldsymbol{f}^s \approx \gamma \kappa \nabla H^s \tag{4.49}$$

is used to calculate fs in the interfacial region defined by $|\psi| \leq \chi$. The key element concerning the balance between the capillary and dynamic pressure in a “balanced” CSF approach is that, the same discretization scheme must be used for the gradient terms of H^s and pressure in the projection operation. On the MAC grid used in this study, they are both calculated by central difference at staggered positions.

Thanks to the LS representation of the interface, it is very straightforward to obtain the information required for the surface tension force. The unit normal vector $\boldsymbol{n}$ is replaced by the normalized gradient of the LS field,

$$\boldsymbol{n} = \frac{\nabla\psi}{\|\nabla\psi\|} \ . \tag{4.50}$$

Consequently, the local mean curvature κ is given by

$$\kappa = -\nabla \cdot \boldsymbol{n} \ . \tag{4.51}$$

4.4.4 Contact angle boundary condition

The contact angle boundary condition of the gas-liquid interface on the solid surface is written in terms of a static contact angle θ_C. This boundary condition is enforced by using the extension approach proposed by [46]. It has also been used by [45] to impose contact angle for droplet splashing on a dry plane.

In the extension approach, the contact angle BC is treated implicitly by extrapolating the LS function ψ along a selected direction into the solid region. The extension equation is written in a convective form

$$\frac{\partial\psi}{\partial\tau} + \boldsymbol{u}^{extend} \cdot \nabla\psi = 0 \tag{4.52}$$

for cells in solid domain $\psi \leq 0$ with the extension velocity $\boldsymbol{u}^{extend}$ subject to the expected capillary vector. The extension velocity is determined by

$$\boldsymbol{u}^{extend} = \begin{cases} \frac{\boldsymbol{n}_s - \cot(\pi-\theta_C)\boldsymbol{n}_2}{\|\boldsymbol{n}_s - \cot(\pi-\theta_C)\boldsymbol{n}_2\|} & \text{if } c < 0, \\ \frac{\boldsymbol{n}_s + \cot(\pi-\theta_C)\boldsymbol{n}_2}{\|\boldsymbol{n}_s + \cot(\pi-\theta_C)\boldsymbol{n}_2\|} & \text{if } c > 0, \\ \boldsymbol{n}_s & \text{if } c = 0, \end{cases} \tag{4.53}$$

in which a set of orthogonal vectors $\boldsymbol{n}_1$, $\boldsymbol{n}_2$ and direction index c are defined as

$$\boldsymbol{n}_1 = -\frac{\boldsymbol{n} \times \boldsymbol{n}_s}{\|\boldsymbol{n} \times \boldsymbol{n}_s\|} \ , \tag{4.54}$$

$$\boldsymbol{n}_2 = -\frac{\boldsymbol{n}_1 \times \boldsymbol{n}_s}{\|\boldsymbol{n}_1 \times \boldsymbol{n}_s\|} \ , \tag{4.55}$$

and

$$c = \boldsymbol{n} \cdot \boldsymbol{n}_2 \tag{4.56}$$

with $\boldsymbol{n}_s$ the unit normal vector of the solid surface.

The extension operation is furnished by using the back-tracing semi-Lagrangian scheme described in Chapter 2. After the extrapolation is completed, the VOF function in the solid domain is replaced by the smoothed Heaviside function, that is,

$$\phi = H^s(\psi) \quad \text{for } \psi \leq 0. \tag{4.57}$$

The major advantage of the extension method is that the contact angle boundary condition is satisfied automatically, which is independent of the local position and configuration of the contact line.

4.4.5 Evaluation of capillary force

When combined with the IB model, the present simplified CLSVOF method has the considerable merit of simply calculating the capillary force exerted on the solid particle. Note that a continuous fluid interface is constructed throughout the whole domain by the extension operation, and subsequently so is the surface tension force. Hence the IB forcing introduced in Section 4.3.2 is able to correctly evaluate the total fluid action as the integral of the generalized multiphase fluid stress.

Since already included in the total fluid action, explicit calculation of the capillary force is not necessary. If it is required to extract such information, summing up the surface tension term over the solid domain will give the capillary force estimated for the immersed object,

$$\boldsymbol{F}^s = \sum \alpha \boldsymbol{f}^s \Delta V \ . \tag{4.58}$$

4.5 Test of numerical models

In this section, the numerical models proposed for the computation of hydrodynamic force, surface tension and capillary force are tested. We show results of test problems including single particle settling, parasitic currents and drop attachment to show the capability and improvement made by the present modeling.

Table 4.1: Simulation cases for single particle settling in an enclosure.

	d_p (m)	ρ_p (kg/m^3)	ρ_f (kg/m^3)	μ_f (Pa s)	Re
Case 1	0.015	1120	970	0.373	1.5
Case 2			965	0.212	4.1
Case 3			962	0.113	11.6
Case 4			960	0.058	31.9

4.5.1 Sedimentation in enclosure

Single particle settling in an enclosure is simulated for the validation of the fluid-particle interaction term.

In a container whose size is 0.1 m by 0.16 m by 0.1 m, a spherical particle is initially suspended at a height of 0.12 m from its bottom to the floor. The particle diameter is 0.015 m. Basically 80 × 120 × 80 cells are used to discretize the computational domain, which results in a ratio of $d_p/\Delta x = 12$. Four different test cases with increasing fluid viscosity are simulated and compared with the experimental backup in [57]. Physical properties in these four cases are listed in Table 4.1, and the Reynolds number based on settling velocity varies in a range from 1 up to 30.

Validation against experiment

When the simulation starts, the particle is released and settles under its gravity, buoyancy and viscous friction from surrounding fluid. Figure 4.1 shows the snapshots particle position and flow velocity on the plane running through the particle center at time $t = 1.0$ sec. The effect of fluid viscosity is obvious: in Case 1 ($Re = 1.5$) the particle moves slowly and the flow velocity behind and in front of the particle is almost symmetric, while in Case 4 ($Re = 31.9$) the particle has advanced fast near the bottom with a long trail behind it.

The temporal changes of the sedimentation velocity and height (normalized by particle diameter) are plotted in Figure 4.2 together with the PIV measurement by [57]. It is seen that in Case 1 and 2 the particle moves with a steady sedimentation velocity for which the gravity and hydrodynamic force are well balanced, but in Case 3 and 4 the particle has already get settled to the bottom before such a terminal velocity could be reached. Such trend owing to the increasing Re number is well recovered by the current simulation and both the settling velocity and particle position compare very well with the experimental data.

It is worthy to note that, minor discrepancy is found when the particle approaches the enclosure bottom. Similar problems have been reported by other studies as well, see e.g. [9, 58]. In fact, in order to achieve closer fit to the experimental resutls, some authors (e.g. the LBM study of [57]) suggested to use a calibrated hydrodynamic diameter for the particle and add a lubrication force between the bottom. Such a calibration operation usually relies on some known analytical or experimental database and thus is inevitably problem-dependent. It is thus not considered in the present study.

Space-time convergence study

A convergence study has been conducted to examine the current numerical method. It is noted that both spatial and temporal steps are simultaneously refined to check the space-time convergence with the CFL number kept comparable, see e.g. [14, 59].

We will use the simulation conditions of Case 4 that has the highest Re number. Computational resolutions are prepared for cell number of $50 \times 80 \times 50$, $60 \times 96 \times 60$, $70 \times 112 \times 70$, $90 \times 144 \times 90$ and $100 \times 160 \times 100$. The result obtained on the finest grid of $120 \times 192 \times 120$ is used as reference solution. The particle sedimentation velocity, U, is selected and the error with respect to the reference velocity U^{ref} is calculated. Figure 4.3 plots the sedimentation velocity against time with space-time refinements.

In order to estimate the convergent behavior, Figure 4.4 shows the error in particle velocity at $t = 1.0$ sec. Similar to the report of [59], the convergence rate is better than first-order and very close to second-order, which essentially owes to the second-order schemes used for spatial and temporal discretization of fluid-particle system. We note that, this result is very close to the optimistic estimate of the present method because that the IB enforcing of rigid velocity is a first-order interpolation of local velocity.

Comparison with the basic IB results

We have also performed the simulation using the original IB method by disabling the virtual force term to emphasize their difference. The computations are conducted under a sufficiently converged resolution of $d_p/\Delta x = 12$ and $\Delta t = 0.4$ ms, which should well resolve the transient particle motion characterized by the particle relaxation time [60]

$$T_p = \frac{2(\rho_s + 0.5\rho_f)d_p^2}{\mu_f} \; . \tag{4.59}$$

For Case 1 (lowest Re), similar results have been obtained by using the present and original IB formulations (results not shown here). For Case 4

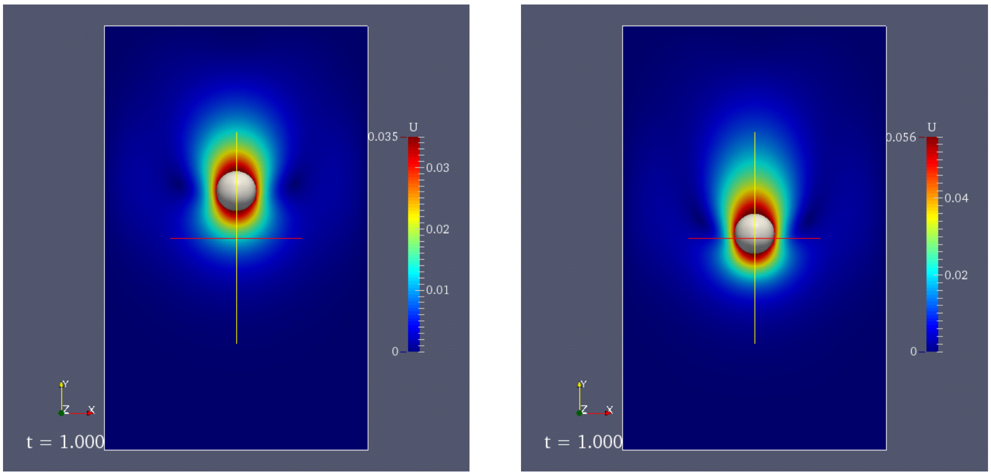

(a) Case 1 ($Re = 1.5$)

(b) Case 2 ($Re = 4.1$)

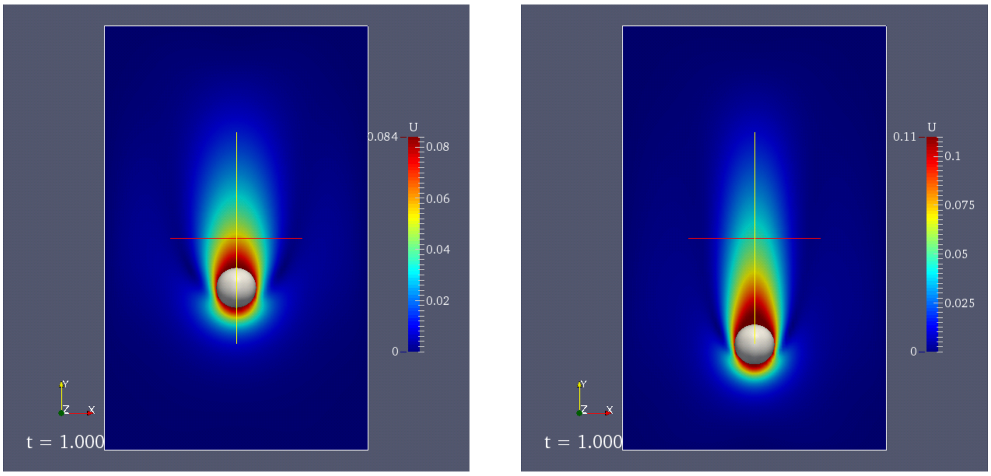

(c) Case 3 ($Re = 11.6$)

(d) Case 4 ($Re = 31.9$)

Figure 4.1: Snapshot of the settling particle and surrounding fluid velocity at $t = 1.0$ sec.

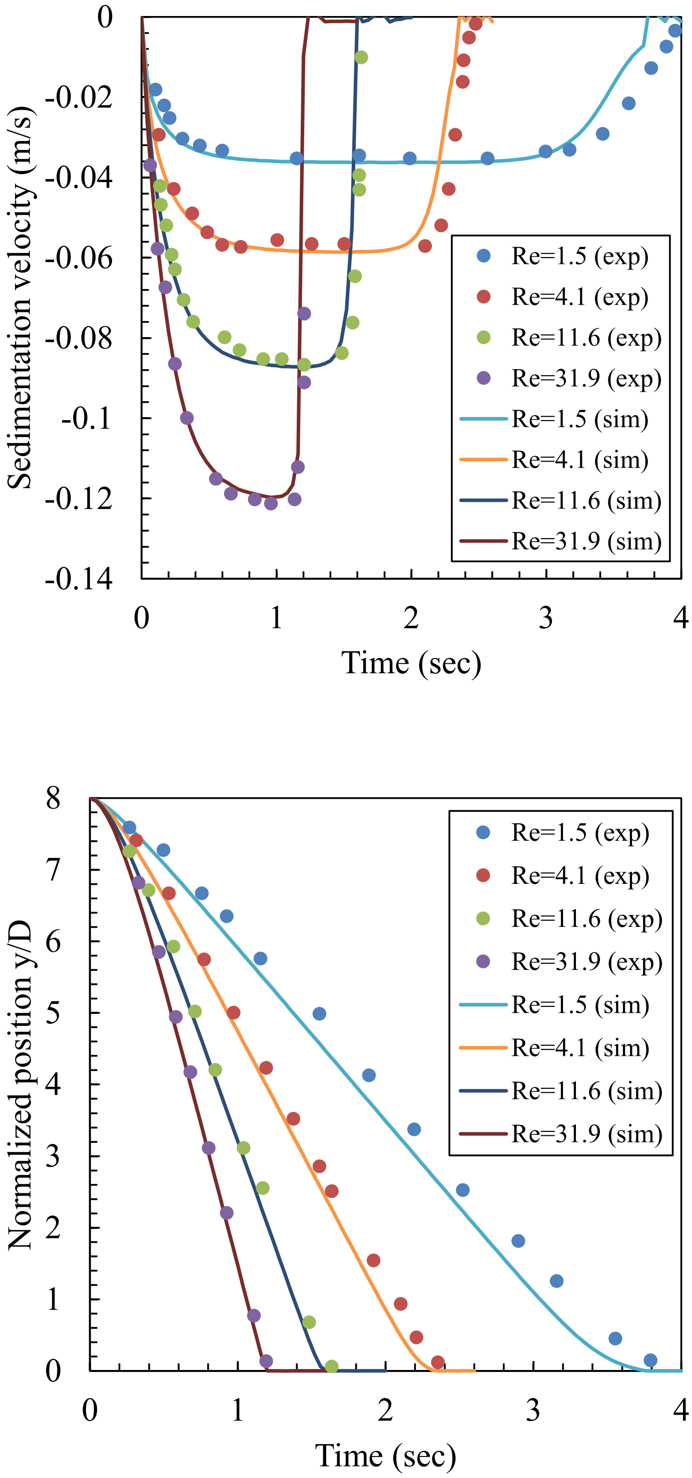

Figure 4.2: Plot of (a) sedimentation velocity and (b) normalized height of the settling particle.

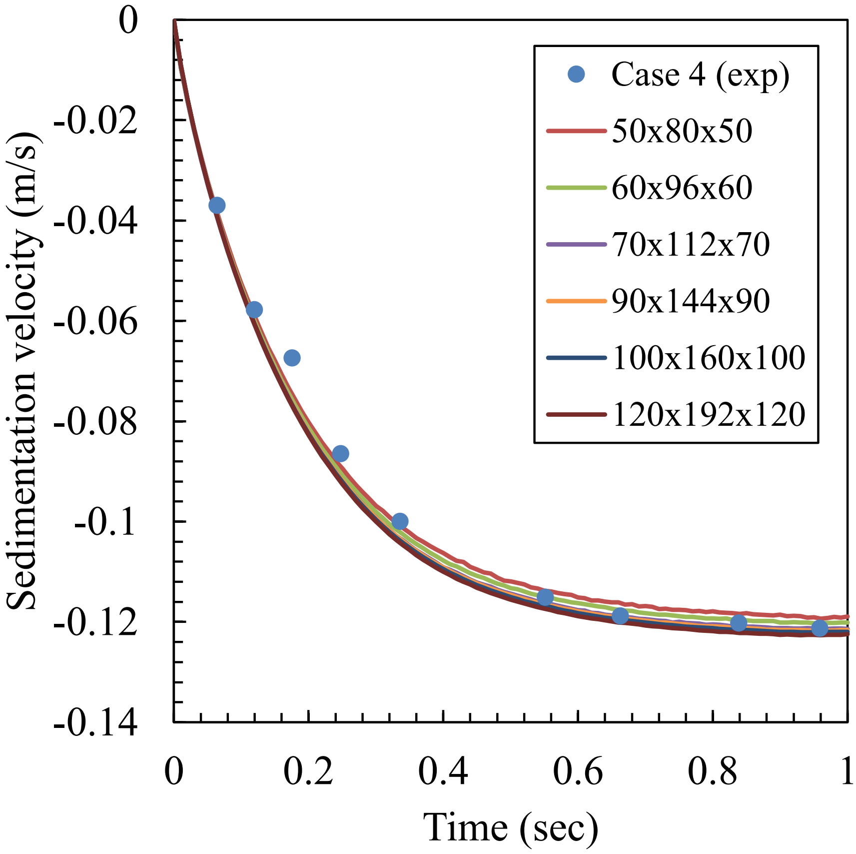

Figure 4.3: Plot of sedimentation velocity for Case 4 ($Re = 31.9$) with mesh refinements.

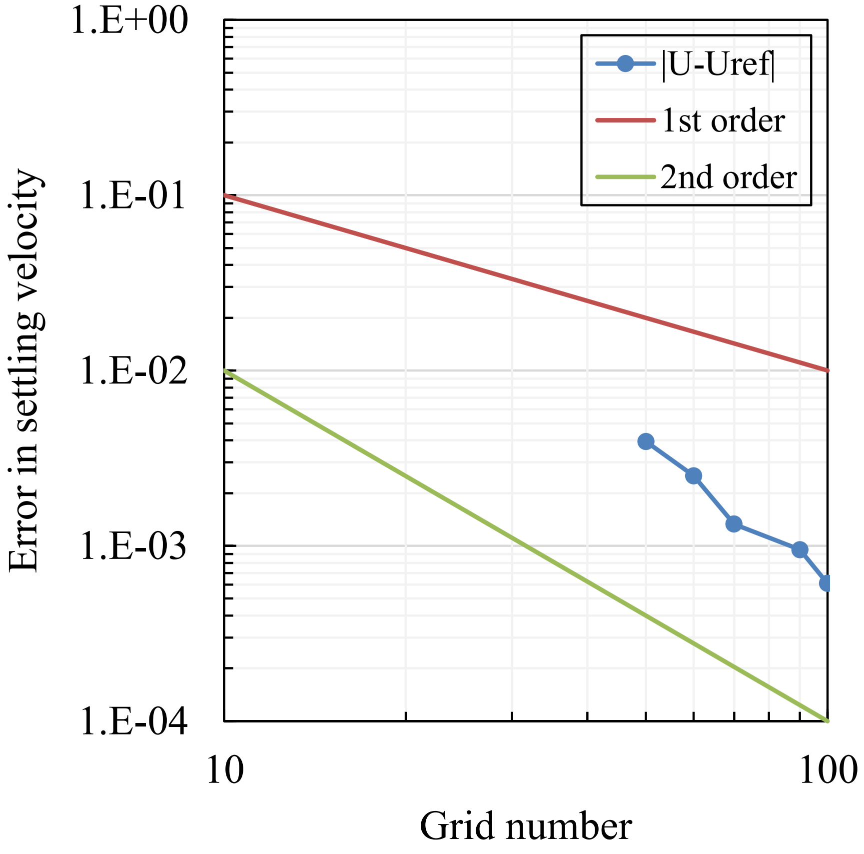

Figure 4.4: Convergence towards the reference velocity for Case 4 ($Re = 31.9$) with mesh refinements.

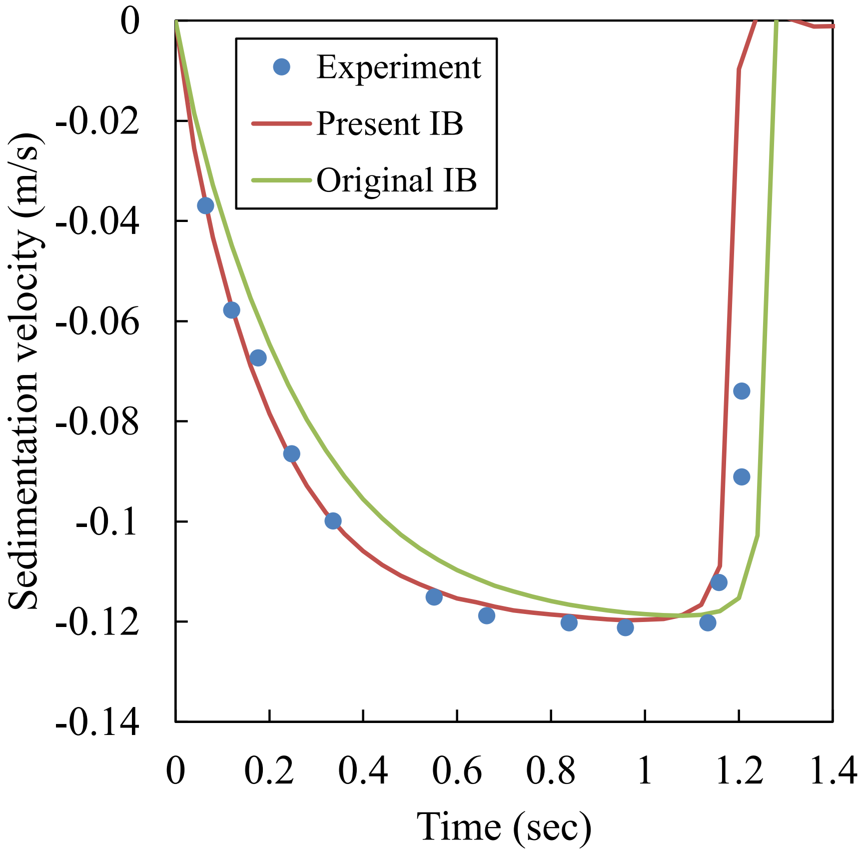

Figure 4.5: Comparison of sedimentation velocity for Case 4 between different IB formulation.

(highest Re), deviations are seen as the particle undergoes acceleration, see Figure 4.5. The present results clearly gives a better match to the experimental data. Therefore the proposed treatment of solid-fluid interaction is useful for unsteady particle-flow cases.

4.5.2 Parasitic current test

The parasitic current test is widely adopted to test the surface tension calculation in two-phase flow solvers. We will present results to check the simplified CLSVOF interface modeling and balanced CSF surface tension employed in this study.

Consider a spherical drop placed in the center of the domain with zero gravity. The fluid properties are set as $\rho = 1.0$ kg/m^3, $\mu = 0.01$ Pa s and

$\gamma = 1.0$ N/m. The diameter of the drop is $D = 1.0$ m. The characteristic Laplace-Ohnesorge number indicating the ratio between surface tension and viscous force for this system is

$$La = \frac{1}{Oh^2} = \frac{\gamma \rho D}{\mu^2} = 10000 \; . \tag{4.60}$$

Theoretically the flow velocity is zero everywhere, but in simulations parasitic currents can occur around the drop surface due to numerical error in calculating the surface tension. Hence, the magnitude of the parasitic velocity is provided as a direct measurement of numerical errors.

In this study, the velocity errors are obtained for varied grid resolutions at $t = 0.1$ sec by using the following error norms:

- The L^∞ error

$$e^\infty = \max \|\boldsymbol{u}\| \tag{4.61}$$

- L^2 error

$$e^2 = \sqrt{\frac{\sum \boldsymbol{u}^2}{N_x N_y N_z}} \tag{4.62}$$

- L^1 error

$$e^1 = \frac{\sum \|\boldsymbol{u}\|}{N_x N_y N_z} \tag{4.63}$$

From their definitions, L^∞ error corresponds to the maximum error, while L^1 and L^2 errors give the averaged global error in different norm spaces. The local slope in error convergence can also be calculated as an estimation of convergence rate,

$$s = -\frac{\log e^{fine} - \log e^{coarse}}{\log N^{fine} - \log N^{coarse}} \; , \tag{4.64}$$

where N is proportional the reciprocal of mesh spacing Δx.

Figure 4.6 (a) shows the measured numerical error in this convergence study. The distribution of L^∞ error is non-uniform and generally follows the first-order slope because CSF-type surface tension models adopt first-order modeling of the fluid interface. Its magnitude is also found to be larger than L^1 and L^2 errors by orders, showing a localization of numerical error near the interface. On the other hand, the convergence rate of L^1 and L^2 errors is found between 1 and 2. For example, a power law-based fitting of the L^2 error (dashed line in Figure 4.6 (a)) implies that the exponent for the order is approximately 1.67, and the local slopes of $L2$ error (Figure 4.6 (b)) also fall in that range. It is a reasonable result because errors are averaged out in a global sense for L^1 and L^2 norms, and thus the strongest ones are partially compensated by the low velocity region far away from the interface. This observation is very similar to the LS study by [61].

In this way, convergent results have been obtained for the surface tension calculation by using the simplified CLSVOF method. In fact, it is reported that VOF-based calculation does not converge with mesh refinement [62,63]. Hence, it is expected that the present model can substantially improve the computation of surface tension in fluid phase and capillary force on solid particles.

4.5.3 Drop attached to a particle

In this test, a liquid drop attached to a fixed particle with specified contact angle is simulated. It serves as a test of the capillary force calculation newly introduced in the current method.

The dimensions of the computational domain is 2 mm by 4 mm by 2 mm. A solid particle with diameter of 2 mm is fixed at the position of $(1.0, 1.5, 1.0) \times 10^{-3}$. A spherical drop whose radius is 0.5 mm is centered at $(1.0, 2.823, 1.0) \times 10^{-3}$. The fluid density is 1000 kg/m^3, the viscosity is 0.02 Pa s, and the surface tension is 0.04 N/m. The contact angle on the particle surface is set to $120\,^\circ$. According to the geometrical configuration of the drop and solid, the capillary force acting on the particle stemming from pulling surface tension can be analytically calculated, see [64]. A typical snapshot of this drop-particle systems is shown in Figure 4.7.

The relative error in the calculated capillary force is plotted as a function of grid resolution in Figure 4.8. It is seen that the relative error decreases below 5% when using a mesh spacing of $d_p/\Delta x > 30$. The convergence rate is at best first-order, as indicated by Figure 4.9, which is naturally consistent with the accuracy of surface tension calculation.

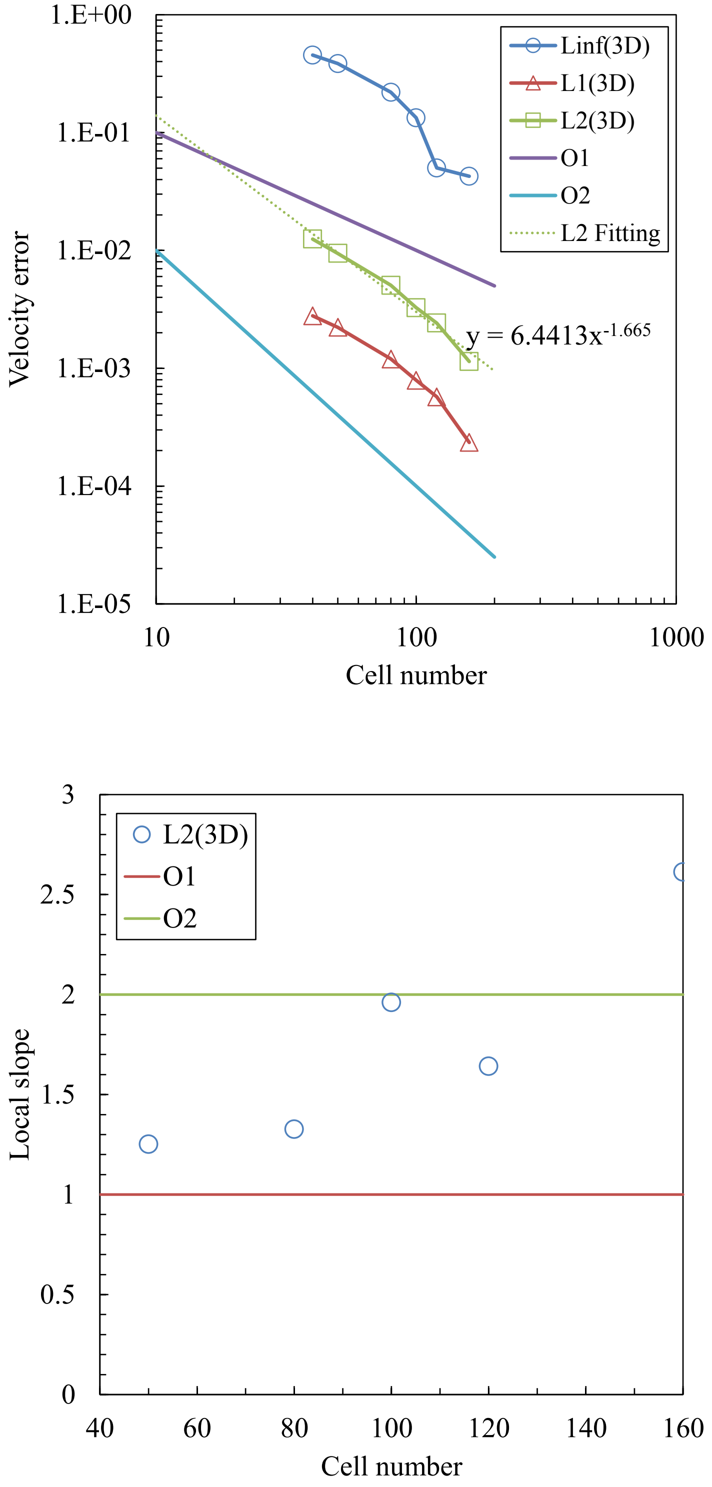

Figure 4.6: Parasitic current test: (a) error convergence and (b) L^2 local slope with mesh refinement.

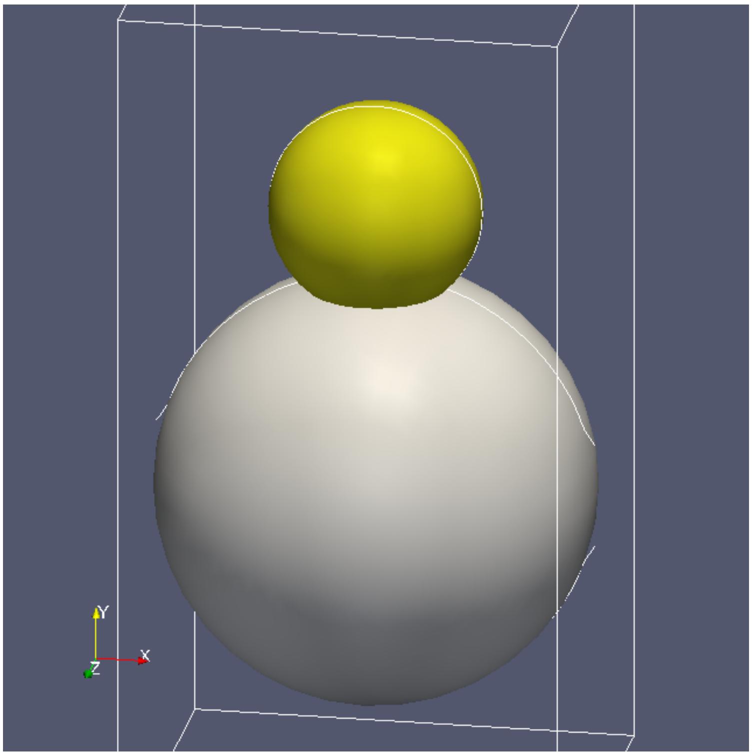

Figure 4.7: Drop placed on the particle surface.

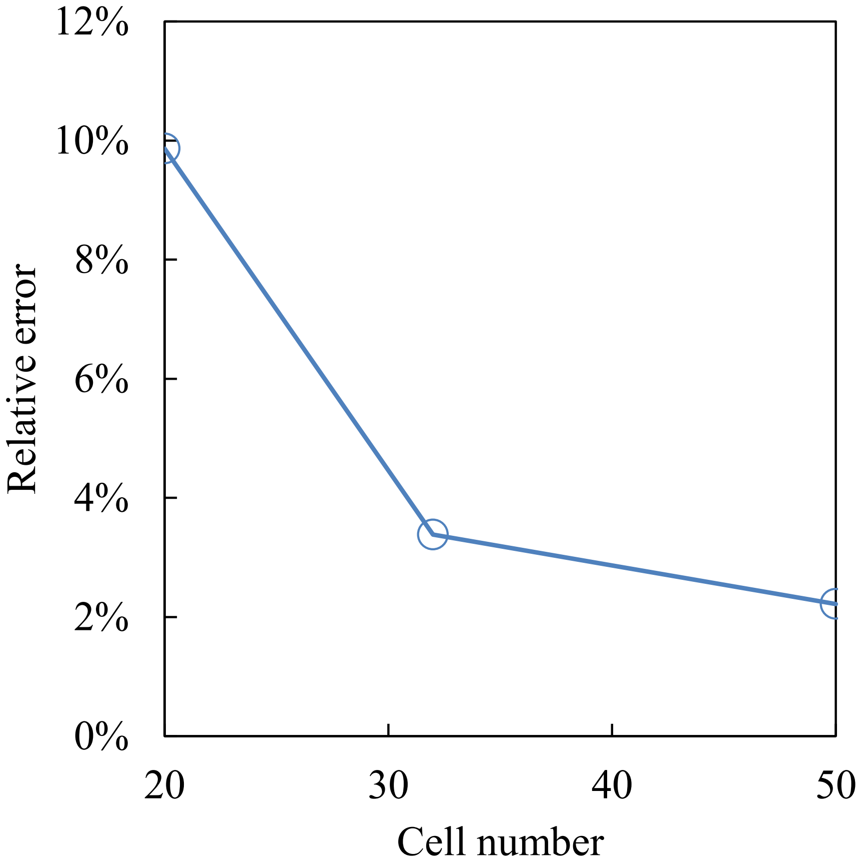

Figure 4.8: Relative error in capillary force calculation with mesh refinements.

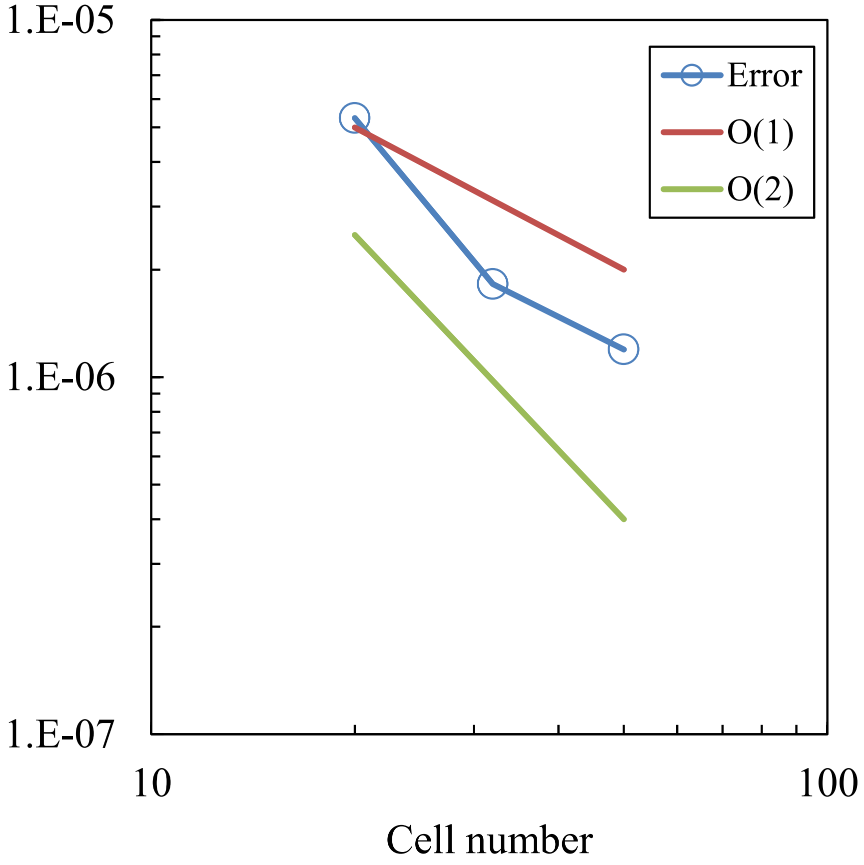

Figure 4.9: Convergence of the capillary force calculation with mesh refinement.

4.6 DNS of floating particles

Solid particles floating on free surface are widely observed in daily life and powder processes, which is a typical gas-solid-liquid three-phase system where the flow behavior is mainly dominated by the hydrodynamic and capillary forces. In this section, the dynamics of floating particles are performed by using the present DNS method. The computational results are first validated thoroughly under various conditions and contact angles for a single floatation system similar to that discussed in [38]. Next the problem is further extended to the cases of dual and multiple particles among which capillary actions arise causing a spontaneous clustering of particles. The present results show that the DEM-VOF-DNS method can simulate a complex three-phase system involving coupled interaction between particle and fluid interface with ease.

4.6.1 Equilibrium of a floating sphere

Under certain conditions, a solid particle can be “clipped” to the free surface, even if its density is heavier than surrounding fluids. The dynamics and equilibrium of such a problem are discussed in this section to justify the proposed three-phase DNS model.

For such a sphere embedded between binary fluids, its steady state is found by the balance of its gravity, buoyancy from surrounding fluid, and capillary force stemming from the local contact line intersecting on its surface. For the sake of simplicity, constant density and viscosity are assumed for the two fluids separated by the interface. As the geometry illustrated in Figure 4.10 (a), the balance of forces in vertical direction gives

$$F^s = (m_s - m_f)g \tag{4.65}$$

where the capillary force F^s along the contact ring is

$$F^s = \gamma \cdot 2\pi R \cos\theta \cdot \cos\left(\frac{\pi}{2} - \theta + \frac{\pi}{2} - \theta_C\right) \ , \tag{4.66}$$

in which θ subtends the angle between the horizontal orientation and the contact ring. Therefore the balance equation yields a relationship between the subtending angle θ and known physical conditions,

$$\cos\theta \cdot \cos(\theta + \theta_C) + \frac{2}{3}Bo = 0 \ , \tag{4.67}$$

in which Bo is the modified Bond number based on density difference, particle radius, gravity, and surface tension,

$$Bo = \frac{(\rho_s - \rho_f)R^2 g}{\gamma} \ . \tag{4.68}$$

Note that the Bond number can be possibly negative for light particles.

If Eq. (4.67) is to be satisfied with a meaningful solution for θ, a necessary condition is clearly that

$$|Bo| \leq \frac{3}{2} . \tag{4.69}$$

Since the dimensionless Bond number indicates the ratio between gravitational and surface tension forces in the floating system, this condition is straightforwardly explained as an upper limit for the buoyant weight of the particle beyond which the balance owing to capillary force is broken down.

For a neutral 90° contact angle (see Figure 4.10 (b)), Eq. (4.67) further simplifies to

$$\theta = \frac{1}{2} \arcsin \left(\frac{4}{3} Bo \right) , \tag{4.70}$$

for which it is required for the Bond number that

$$|Bo| \leq \frac{3}{4} . \tag{4.71}$$

Case of neutral contact angle

The simpler case with a neutral contact angle condition is first simulated. A spherical particle is placed at the center of a cubic domain whose size is 4 mm. The particle diameter is $D = 2$ mm. Uniform meshes are used with a spacing of $\Delta x = 1/16$ mm, resulting in a size factor of $D/\Delta x = 32$. The fluid density is 1000 kg/m^3 and viscosity is 0.1 Pa s. Two types of solid particles are chosen for density of 937.5 (light) or 1062.5 (heavy) kg/m^3. A constant gravitational body force equal to 10.0 m/s^2 is applied in the vertical direction. A fixed time step $\Delta t = 5 \times 10^{-5}$ sec is used to advance the system.

The simulation simply starts with a quiescent state, where particle is placed at the domain center with the interface filling up to half the domain height. Then it is released and allowed to move freely and reach a steady state, see Figure 4.11.

Figure 4.12 shows representative snapshots of particles with different densities floating at the interface. For non-neutrally buoyant particles (either lighter or heavier than the surrounding fluid), the interface deforms to counteract the gravity effect so that they are captured thereby. From the simulation results, the subtending angle θ is measured. Figure 4.13 plots the angle θ obtained with varying Bond number together with the analytical correlation (4.70). It is seen that simulation results agree well with our prediction.

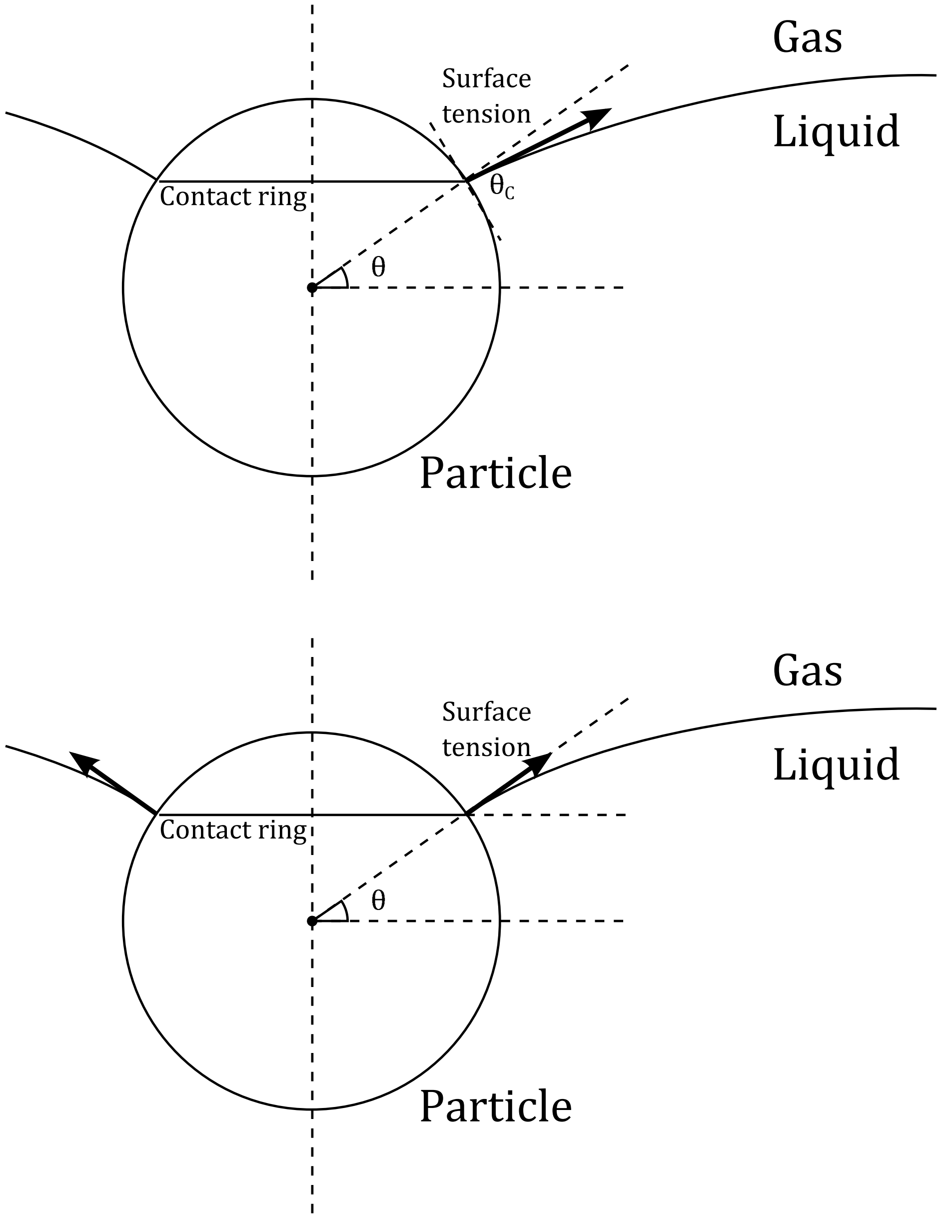

Figure 4.10: Schematic diagram of the floating particle with (a) general and (b) neutral contact angle.

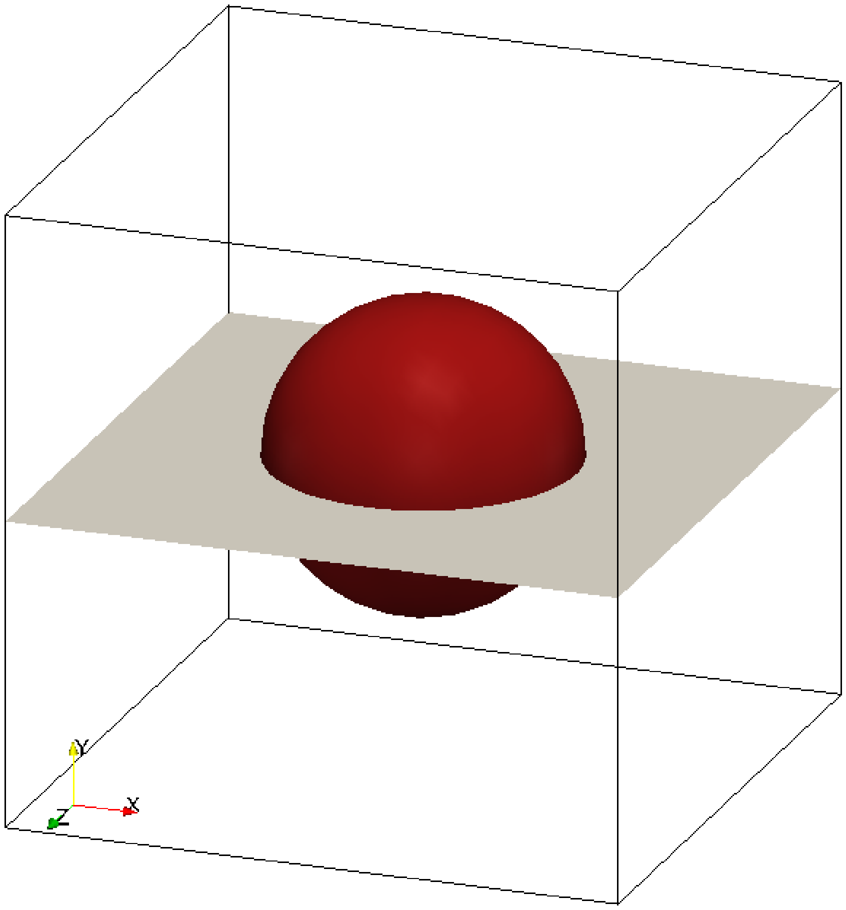

Figure 4.11: Initial configuration of the floating particle and fluid interface.

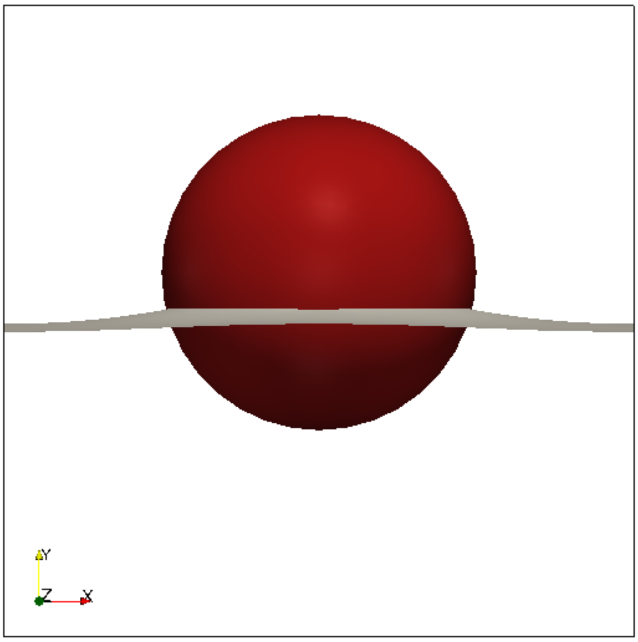

(a) Light particle, $\theta = -15\,^{\circ}$

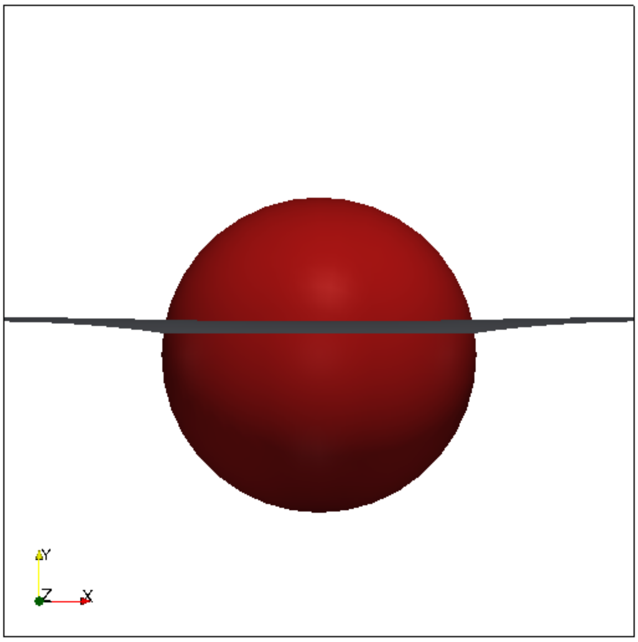

(b) Heavy particle, $\theta = 10\,^{\circ}$

Figure 4.12: Embedded particle with neutral contact angle.

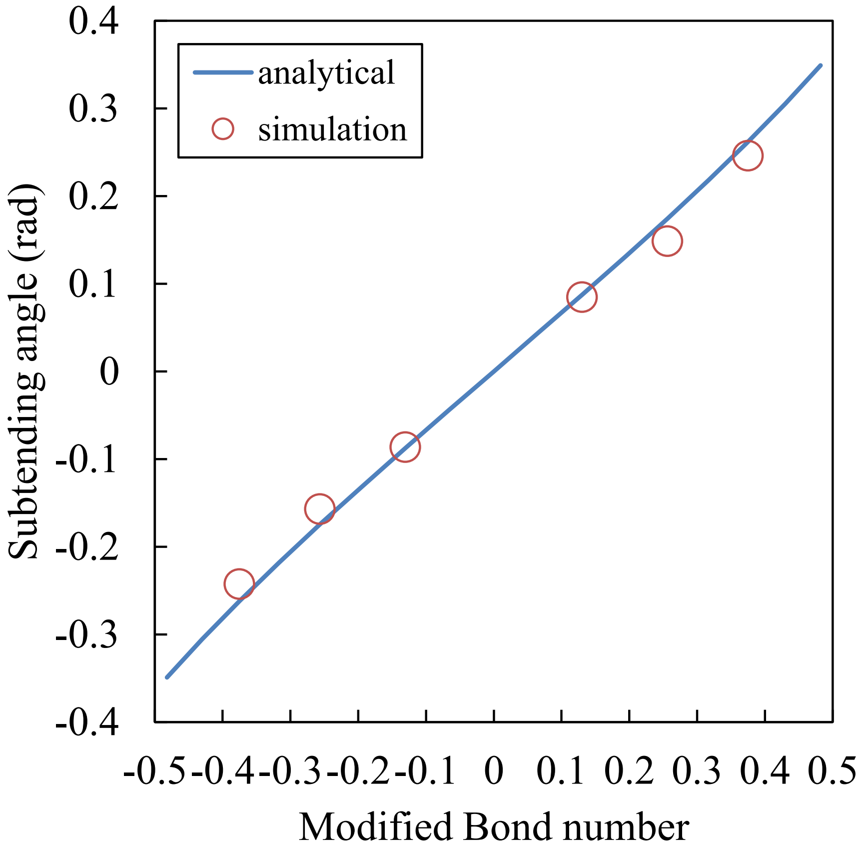

Figure 4.13: The correlation for the subtending angle θ with 90° contact angle.

Table 4.2: Computational results of the subtending angle θ.

	Bo	θ_C	Analytical	Calculated	Abs. err.	Rel. err
Case 1	0.417	$120\,^\circ$	$-13.4\,^\circ$	$-14.3\,^\circ$	$0.9\,^\circ$	6.72%
Case 2		$135\,^\circ$	$-26.9\,^\circ$	$-28.2\,^\circ$	$1.3\,^\circ$	4.83%

Case of general contact angle

Next simulations are performed for non-neutral contact angles. In that case, the solution for angle θ in the nonlinear equation (4.67) must be found numerically. By using the same computational setting-up and resolutions as the preceding test, we choose the Bond number equal to $Bo = 0.417 > 0$ so that the solid particle tends to sink and the meniscus must bend concavely to cancel its weight. Two test cases with hydrophobic contact angles of $\theta_C = 120\,^\circ$ and $135\,^\circ$ are computed.

Figure 4.14 plots the variation of particle velocity against time. At the initial state, particles gain a sudden acceleration owing to the hydrodynamic effects induced by the sliding contact line. The maximum velocity is approximately two times higher in Case 2 ($\theta_C = 135\,^\circ$) than that observed in Case 1 ($\theta_C = 120\,^\circ$). This motion decays very soon under the viscous damping of surrounding fluids in both cases. The particle adjusts its vertical position and finally comes to a state of rest. Figure 4.15 shows the terminal states of floating particles with different contact angles. Generally speaking, the larger the contact angle is, the stronger hydrophobic effect should be generated by the interface. Hence it is confirmed in those snapshots that the particle is pushed to a more migrated position above the interface in Case 2. The values of subtending angle θ measured from simulation results are summarized in Table 4.2. They grees well with the analytical prediction, from which the absolute error is approximately $1\,^\circ$.

Similarly, we have also performed simulations of particle flotation with hydrophilic wetting conditions, i.e. $\theta_C < 90\,^\circ$. The dimensionless Bond number is $Bo = -0.417$ and contact angles are set to $\theta_C = 45\,^\circ$ and $60\,^\circ$, respectively. These conditions simulate solid particles lighter than surrounding fluids and the interface shape at equilibrium state shall coincides with the reflection of previous hydrophobic tests about the domain center. Figure 4.16 illustrates the floating particles at steady states with two different contact angles. As expected, the interface has deformed in a way to defeat the rising trend of light particles. In particular, for the current computation with light particles, the simulation very soon becomes unstable if the original IB formulation is used. The proposed IB model benefits from the stabilization of the virtual momentum term and thus is able to overcome this problem.

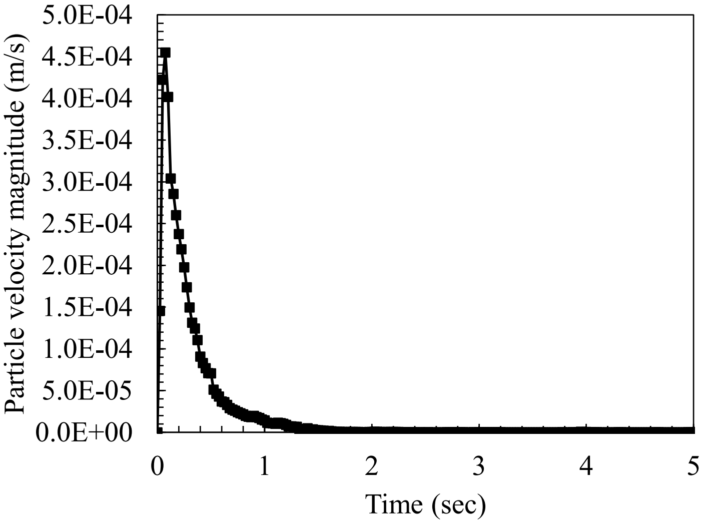

(a) $\theta_C = 120\,^\circ$

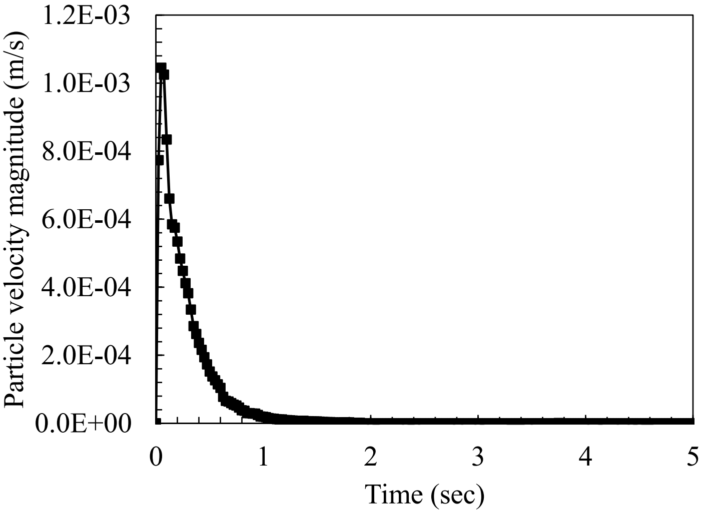

(b) $\theta_C = 135\,^\circ$

Figure 4.14: Temporal change of the particle velocity.

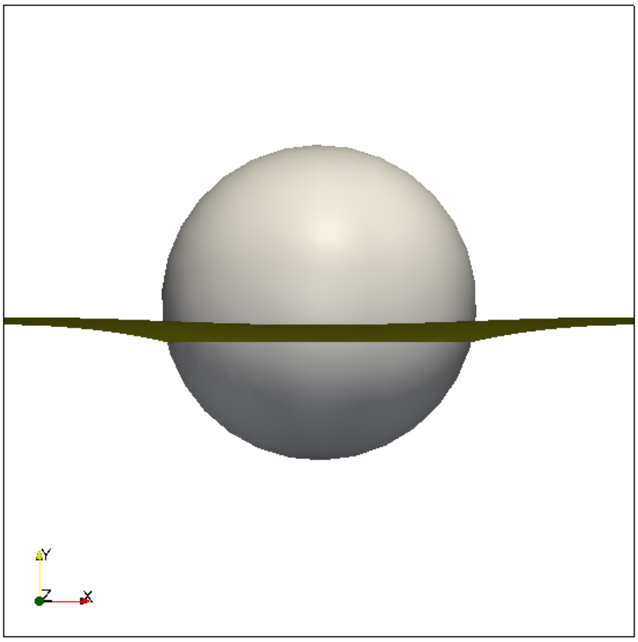

(a) $\theta_C = 120\,^\circ$

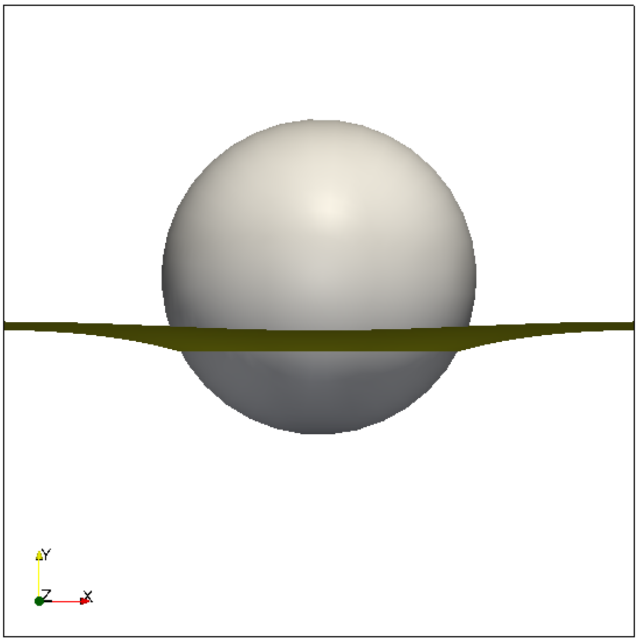

(b) $\theta_C = 135\,^\circ$

Figure 4.15: Embedded particle with hydrophobic contact angle.

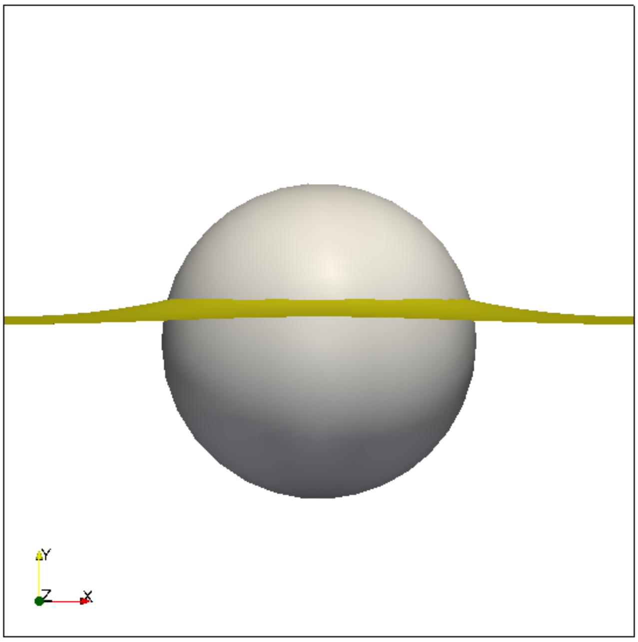

(a) $\theta_C = 60^\circ$

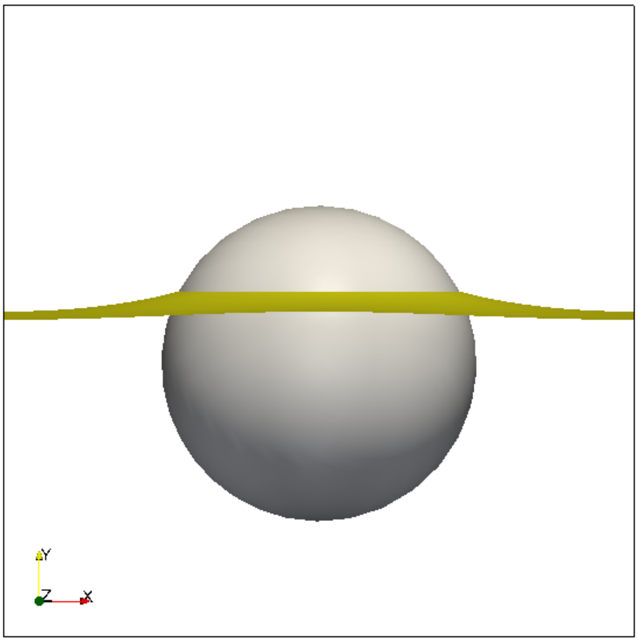

(b) $\theta_C = 45^\circ$

Figure 4.16: Embedded particle with hydrophilic contact angle.

4.6.2 Interaction between floating particle pair

In comparison with a single floating particle whose motion is limited in vertical direction, the capillary interaction between a pair of solid particles can further lead to lateral motions, which has been analyzed and studied numerically in [34, 38]. This section presents results for dual particles floating on free surface in order to demonstrate this special inter-particle effect.

The length, width and height of the computational domain are 8 mm by 4 mm by 4 mm. Two spherical particles with diameter $D = 2.0$ mm are placed at $(2.75, 2.0, 2.0) \times 10^{-3}$ and $(5.25, 2.0, 2.0) \times 10^{-3}$, respectively. The initial height of the free surface is 2.5 mm, immersing most part of the particles. The liquid density is $\rho_l = 1000$ kg/m^3 and the gas density is $\rho_g = 10$ kg/m^3 which gives a density ratio of $\rho_l/\rho_g = 1000$. The values of their viscosity are set to $\mu_l = 0.1$ Pa s and $\mu_g = 0.001$ Pa s. The surface tension between them is $\gamma = 0.01$ N/m and a 90° contact angle is prescribed for the solid surface. The solid density is $\rho_s = 1050$ kg/m3 in this test. Simulation is performed with grid number of $100 \times 50 \times 50$ and time step fixed to $\Delta t = 0.25 \times 10^{-4}$ sec.

Figure 4.17 illustrates the initial and final states of the pair of floating particles. Compared with their initial separation, particles have come close and get in touch with each other. Figure 4.18 plots their relative distance and velocity against time to show the transient behavior. Similar to the single particle case, the beginning stage brings a sudden change in particle velocity and position as the local contact line is being adjusted to keep compatible with the prescribed contact angle boundary condition. Unlike the single particle case, the existence of particle paring breaks the symmetry of meniscus shape around them and causes the lateral motion driven by capillary effects. These results are in qualitative agreement with the reports of [38].

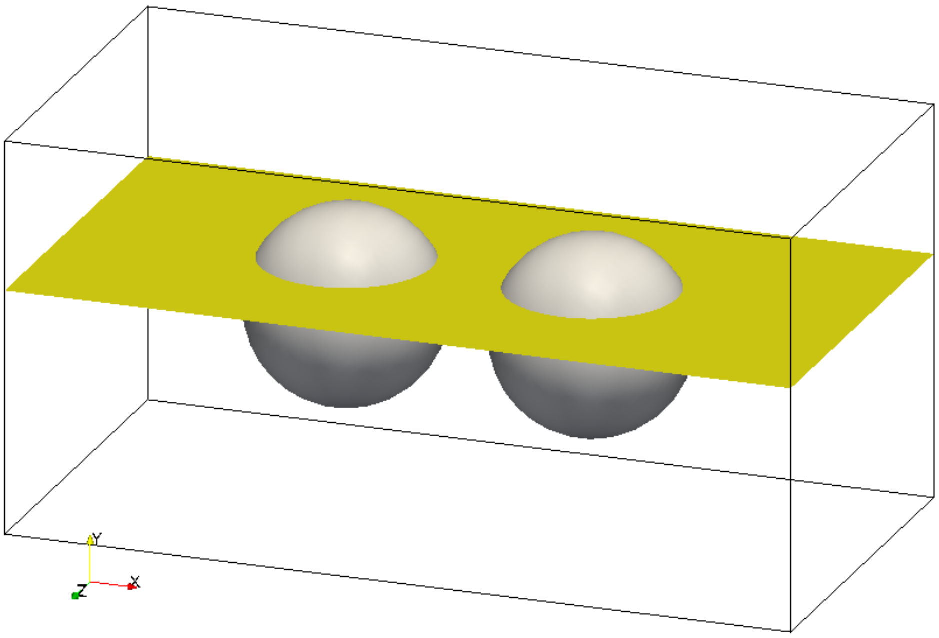

(a) Initial state

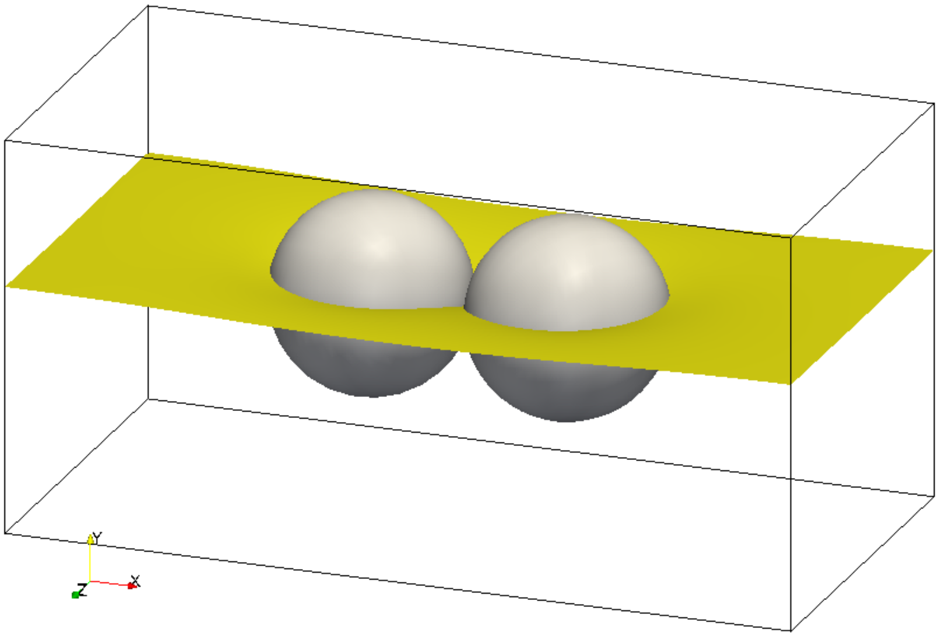

(b) Final state

Figure 4.17: A pair of particles floating on the fluid interface.

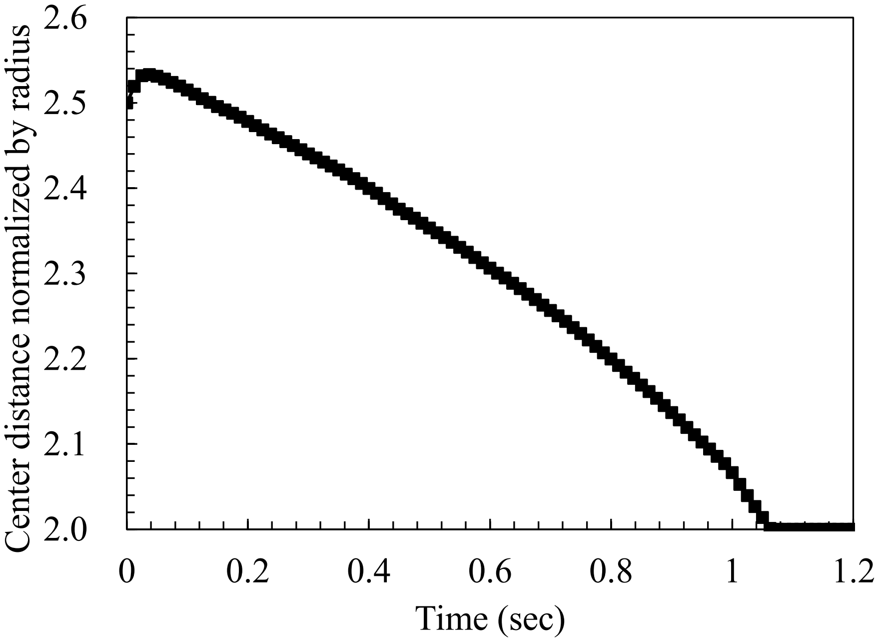

(a) Relative distance

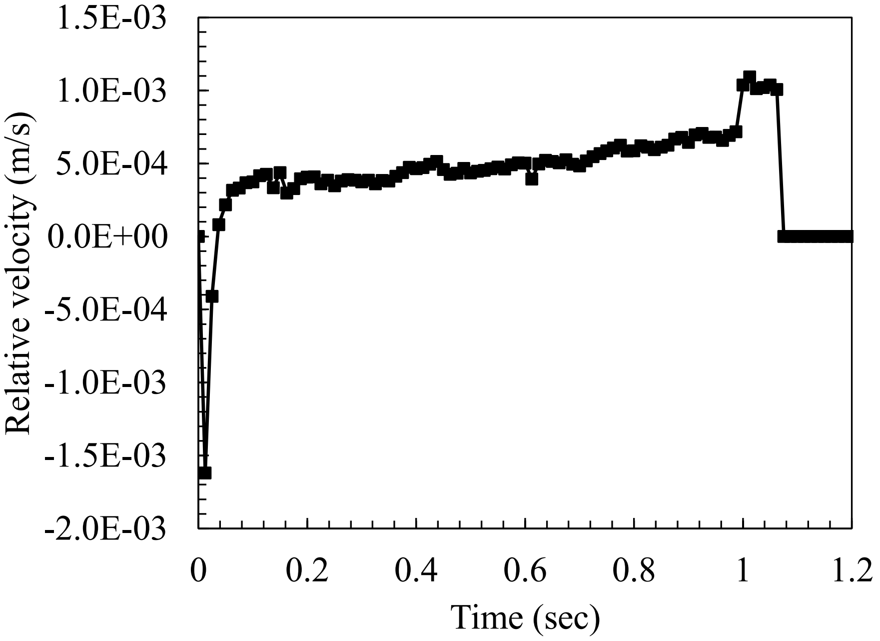

(b) Relative velocity

Figure 4.18: Relative motion between two floating particles.

Table 4.3: Computational conditions for the particles self-assembly.

Particle radius (mm)	1.2
Particle density (kg/m^3)	1050
Liquid density (kg/m^3)	1000
Liquid viscosity (Pa s)	0.1
Gas density (kg/m^3)	10
Gas viscosity (Pa s)	0.001
Surface tension (N/m)	0.015
Contact angle	90 °
Grid size (mm)	15/64
Spring coefficient (N/m)	1000
Restitution coefficient	0.9
Friction coefficient	0.3

4.6.3 Self-assembly among multiple floating particles

Finally we have extended the discussion to the problem of multiple ($\sim 10^2$) particles behavior on a fluid interface by showing their motion driven by capillary interaction. For the initial configuration, 100 particles are placed in a 10 by 10 lattice with some random perturbation on the fluid interface. The computational domain is periodic in horizontal directions. Other computational parameters are summarized in Table 4.3.

Figure 4.19 shows a series of snapshots of the particle configurations during the simulation. The capillary attraction transpires among particles caused by the deformation of the free surface. From the images, it is observed that particles that are close to each other first gather in pairs ($t = 2.0$) and then cluster in blocks ($t = 4.0$). Those clusters further attempt to establish links through single arrays of particles ($t = 6.0$ and 8.0) and finally a stable two-dimensional network structure is formed on the free surface during this self-assembly process.

Effect of frictional force

It is remarkably noticed that in our previous results, the final structure contains a large amount of tetragonal configurations of particles rather than the most stable hexagonal ones. The reason is attributed to that a finite frictional force was taken into account for the contact force between particles via the friction coefficient $\mu = 0.3$, see Table 4.3. When particles come close, this fictional effect will prevent the relative sliding of contact surface and lead to a lock of gathered structures. The effect of the friction coefficient

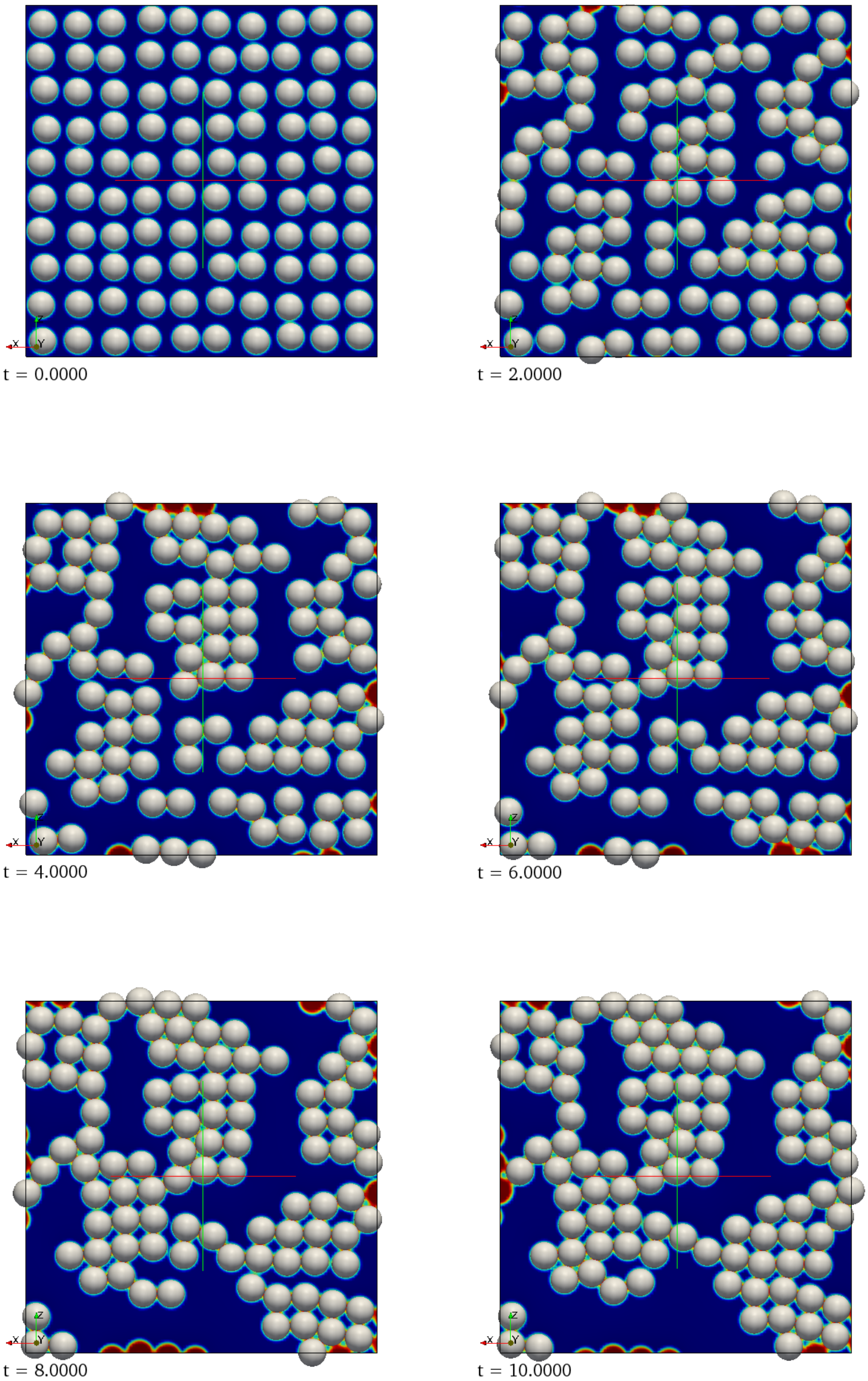

t = 0.0000

t = 2.0000

t = 4.0000

t = 6.0000

t = 8.0000

t = 10.0000

Figure 4.19: Top-view snapshots of particle configuration.

is thus investigated by setting its value to zero. Figure 4.20 displays the particle structure obtained. It is confirmed that only the stable hexagonal configuration will be visible in the final result if the friction is excluded.

The influence of friction on particle gathering behavior is also examined by calculating the particle coordination number, C, which is defined as the number of neighbors in direct contact with the central one. For the present two-dimensional structure, $C \in [0, 6]$. The temporal change of mean coordination number and its standard deviation are plotted in Figure 4.21 (a). From this chart, the different systems with and without friction forces bifurcate after $t > 4.0$ sec, which is identified as the time instant when distinct particle pairs begin to gather in larger clusters. The friction effect has effectively prevented the formation of more inter-particle contacts. As a result, in the histogram of coordination number by Figure 4.21 (b), the distribution without friction is shifted to the right side, showing a denser network in the final structure. Especially a significant increase has been found for the bulk coordination number $C = 6$ from the histogram. These results imply that the surface roughness might be an important factor for the self-assembly behavior of particles.

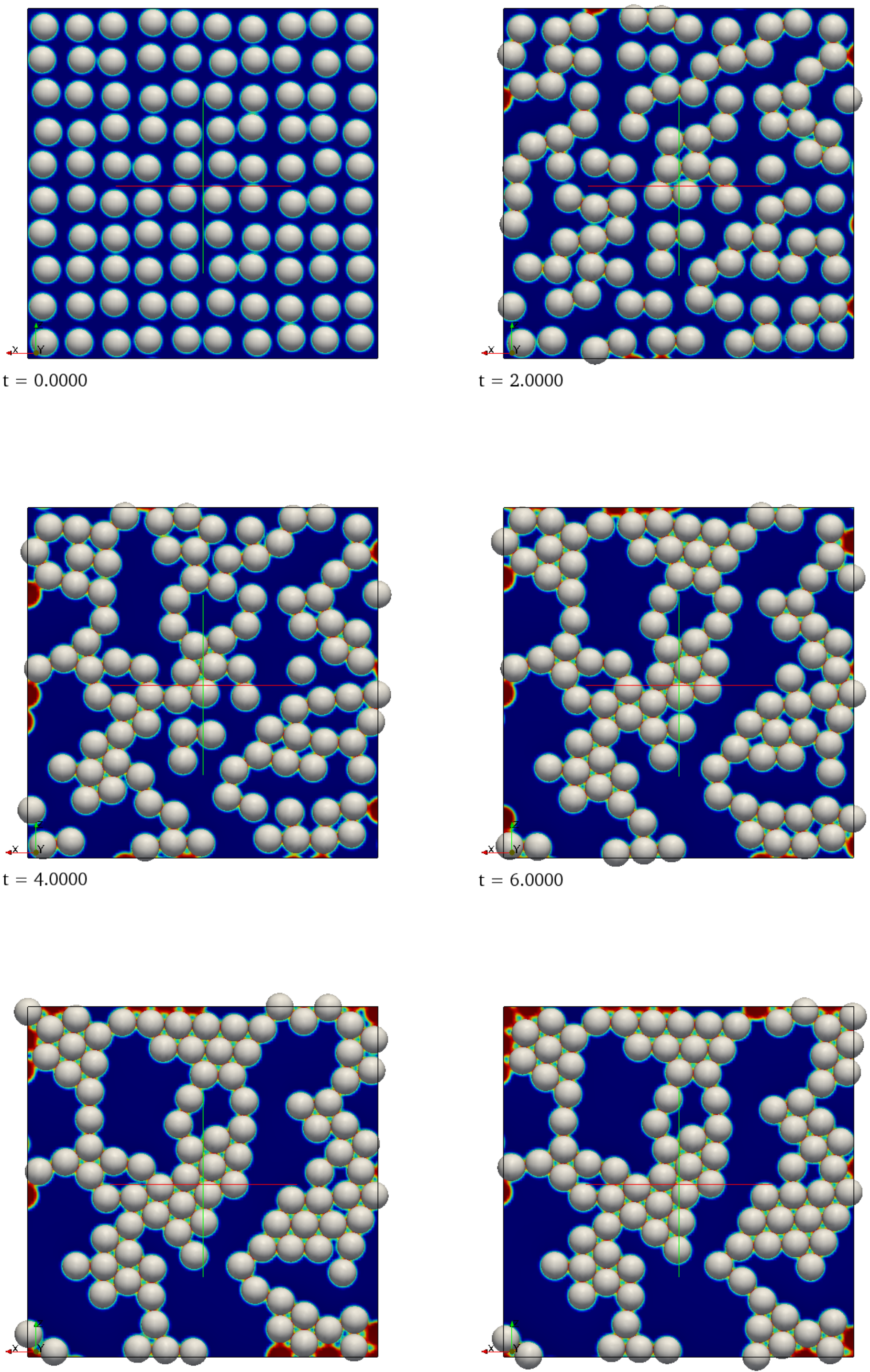

t = 0.0000

t = 2.0000

t = 4.0000

t = 6.0000

t = 8.0000

t = 10.0000

Figure 4.20: Top-view snapshots of particle configuration (no friction).

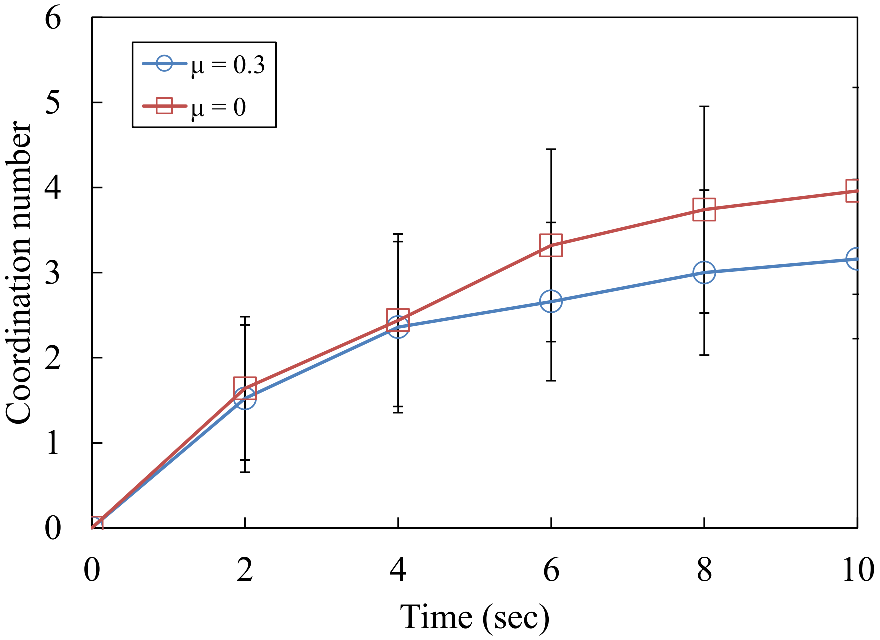

(a) Temporal change of average coordination number

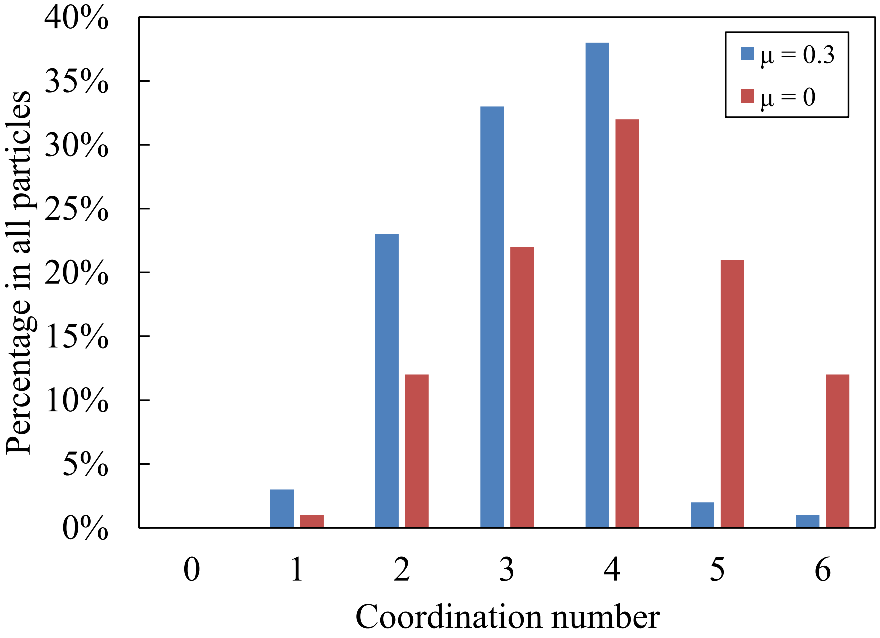

(b) Histogram of coordination number in final state

Figure 4.21: Effect of frictional force in formation of self-assembly structures.

4.7 Connecting DNS and averaged models

As mentioned in the introductory remarks of this work, DEM-VOF type methods and the current DNS method actually come from different hierarchies in multi-scale modeling of fluid-particle flows. The review paper by [65] well addressed the relationship and difference between DNS and averaged models. Macroscopic methods critically relies on various constitutive laws and empirical closures for the description of unresolved terms, of which the foremost is the drag law to calculate the hydrodynamic interaction between fluid and particles. On the other hand, microscopic DNS methods are able to play the role to provide such model equations or to put them to the test under broad range of flow conditions unreachable in experiments.

We will focus on the *a priori* DNS study of drag correlations for their importance in defining the interphase momentum exchange for Eulerian and Eulerian-Lagrangian modeling of fluid-particle systems. In the past, discoveries of drag laws have been attempted by using the Lattice Boltzmann method (LBM) [66–68] and the IB method [69–71]. Unlike those previous studies making efforts to derive novel correlations based on numerical approach, we are more interested in examining existing empirical equations such as the Gidaspow model utilized in the DEM-VOF method in order to justify their applications.

In this part, we will present numerical results of fixed bed simulations of different particle packing states and flow conditions. First the (nearly) creeping flow in a simple cubic (SC) array of fixed spheres is simulated and the fluid force is validated against a semi-analytical solution. Next the hypothetical flow driven by body force in a face-centered cubic (FCC) cell is calculated and the fluid drag is compared with the equations of Ergun and Wen-Yu with different parameters of the particle Reynolds number and void fraction. In the last, a more realistic case in which the flow passing through a random bed is simulated, which is a matter of common occurrence in fluidization systems. The pressure drop is directly compared with the Ergun's equation as well as that derived from the Wen-Yu drag correlation. In this way, the connection between DNS and averaged models can be established in the perspective of fluid-particle coupling.

4.7.1 Drag force in an SC solid bed

Following [24, 60, 72], the flow around a simple cubic (SC) array of fixed spheres is simulated in the Stokes regime. The computational domain is a unit SC cell with length $L = 1.0$ m and fully periodic boundary condition on all six sides. The diameter of the sphere placed at the center of the domain

Table 4.4: Convergence of non-dimensional drag force.

$L/\Delta x$ (-)	U_m (m/s)	F (-)	F_{ana} (-)	Relative error
10	0.007901	28.84		55.74%
20	0.01062	22.21		15.90%
30	0.01146	20.58	19.16	7.380%
40	0.01192	19.77		3.191%
50	0.01214	19.42		1.366%

is $d = 0.9$ m, resulting in a solid volume fraction equal to $\varepsilon_s = 0.3817$. The fluid filling up the gap between particle surfaces has density $\rho = 1.0$ kg/m^3 and viscosity $\mu = 0.05$ Pa s. A constant body force $g = 0.1$ N/kg is applied along x-axis as an average pressure gradient. For this body force-driven flow, the Reynolds number based on the diameter d and mean velocity U_m (found in the whole cell) is approximately $Re \sim 0.2$, which is close to a creeping flow. Simulations are performed on gradually refined grids of $L/\Delta x = 10$, 20, 30, 40 and 50 with a fixed time step $\Delta t = 0.2$ ms. Figure 4.22 illustrates the velocity contour and streamlines on vertical and diagonal slices of this SC cell.

The convergence of results is examined by calculating the non-dimensional drag force F exerted on the central sphere, which is defined as

$$F = \frac{F^D}{3\pi\mu d U_m} \ .$$

Note that the total drag force F^D here includes both a periodic part and the mean pressure gradient, see [73].

According to the Stokes solution by [73] and the curve fitting of [72], the reference value of the dimensionless drag force is $F_{ana} = 19.16$. Table 4.4 gives our results of mean velocity U_m and the resulting dimensionless drag F, whose values converge to F_{ana} as the grid resolution increases. This space convergence behavior is plotted in Figure 4.23 together with that of [72] obtained by a continuous-forcing IB method [6]. Compared with their results, the present results have a comparable rate of convergence close to second-order of the best estimate based on the discretization schemes. Under low resolutions, the current simulation generally yields smaller error, which might owe to that the IB model of [11] is able to keep sharp fluid-solid surface with less smearing than the others; when the grids are sufficiently fine, accuracy of the result is satisfactory. Similar trend has been reported by [24] who has adopted the same IB model.

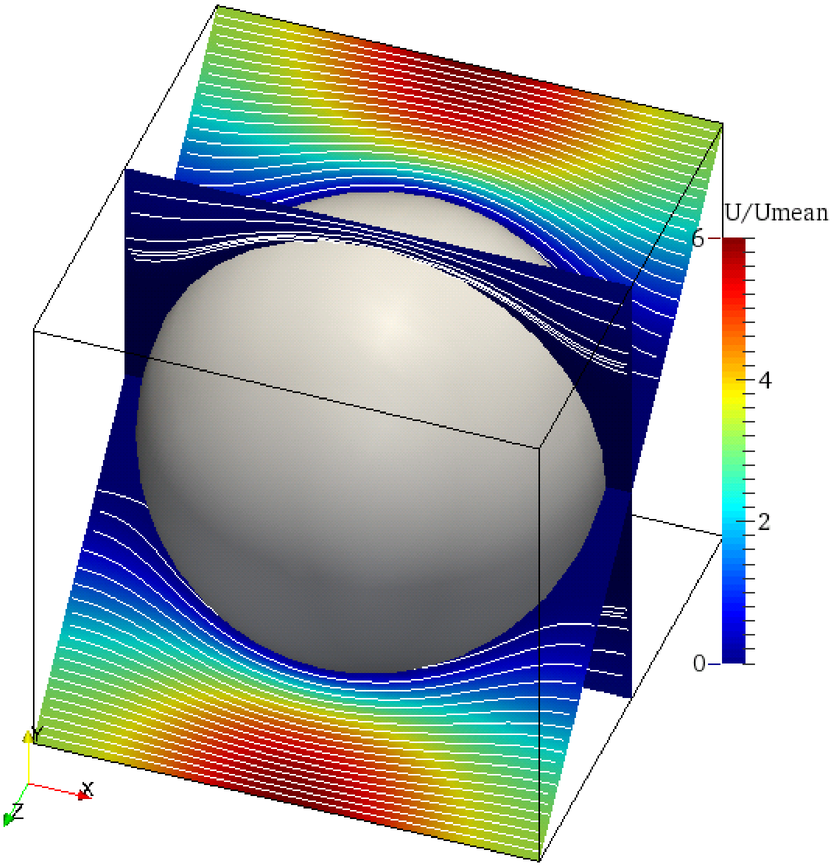

Figure 4.22: Velocity contour and streamlines in the SC array of spheres.

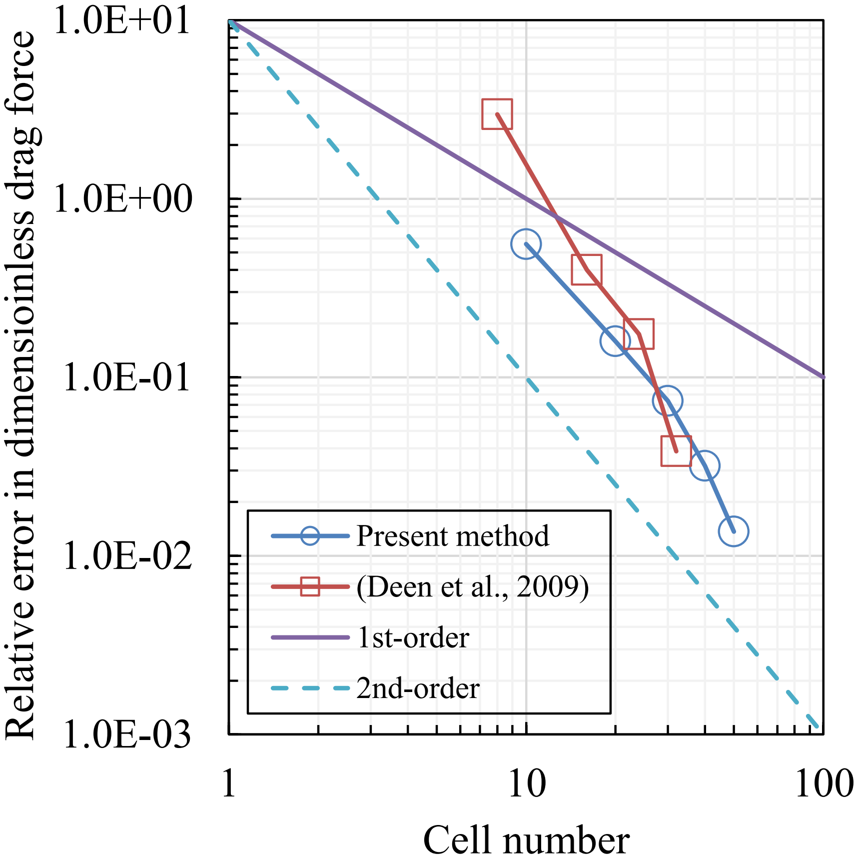

Figure 4.23: Spatial convergence of non-dimensional drag force.

4.7.2 Drag force in an FCC solid bed

A unit cell with FCC arrangement of particles is displayed in Figure 4.24. The size of the cell is $L = 1$, and totally $N = 4$ particles are contained. The relationship between particle diameter and solid volume fraction is given as

$$\varepsilon_p = \frac{2}{3}\frac{\pi D^3}{L^3} \tag{4.72}$$

and here comes the void fraction

$$\varepsilon = 1 - \varepsilon_p \ . \tag{4.73}$$

The physical properties of the fluid filling up the void between solid particles are $\rho = 1.0$ kg/m^3 and $\mu = 0.05$ Pa s.

Fully periodic boundary conditions are prescribed at all boundaries, and a body force, g, is added in x-direction as a mean pressure gradient to drive the flow motion. When the flow reaches steady state, the body force on the fluid phase must be exactly balanced by the resistant force from the solid particles, which gives the value of the drag force as

$$F^d = \frac{\varepsilon \rho L^3 g}{N} \ . \tag{4.74}$$

At the same time, the mean velocity U_m in the domain is estimated by

$$U_m = \frac{1}{L^3}\int u dV \ . \tag{4.75}$$

Consequently, Reynolds number based on fluid density, viscosity, particle diameter and mean flow velocity Um in the cell is obtained:

$$Re = \frac{\rho D U_m}{\mu} \ . \tag{4.76}$$

From this problem setting-up, we know that the value of fluid drag is exactly prescribed in the simulation, while the flow condition indicated by Reynolds number is indirectly controlled by the magnitude of external force. Hence this approach is thought to be a force-based evaluation of drag correlations.

Recall that the expression of the fluid drag is generally written by

$$\boldsymbol{F}^d = \beta \frac{V_p}{\varepsilon_p}(\boldsymbol{u} - \boldsymbol{v}) \ . \tag{4.77}$$

In the current FCC cell, this becomes

$$F^d = \frac{1}{\varepsilon(1-\varepsilon)} \beta U_m V_p \ , \tag{4.78}$$

for which the relationship $U_m = \varepsilon u$ between local and mean velocity is used. The multiplier β is specifically defined by different drag laws. It is, in most cases, a function of the void fraction ε and the particle Reynolds number. Therefore in this test, values of void fraction $\varepsilon = 0.9$, 0.8, 0.7, 0.6 and 0.5 are tested for particle suspensions from dilute to dense regimes. The value of body force g is varied simultaneously to achieve a range of Re numbers. A uniform grid spacing $\Delta x = L/80$ is used, except for the densest case $\varepsilon = 0.5$ where $\Delta x = L/100$. The flow behavior is calculated with a fixed time step $\Delta t = 10^{-4}$ sec until the expected drag force is obtained for solid particles.

In our test, the simulation results are compared to the empirical equations of Ergun and Wen-Yu with the same void fraction and Re number. In addition, another correlation frequently used in averaged models namely the Hill-Koch-Ladd drag [66, 67] is also considered for reference. The HKL drag coefficient is given in a simplified form by

$$\beta = \frac{18\mu\varepsilon^2(1-\varepsilon)}{d_p^2}(F_0 + 0.5F_3 Re) \tag{4.79}$$

in which

$$F_0 = \begin{cases} \frac{1+3\sqrt{\varepsilon_p/2}+\frac{135}{64}\varepsilon_p\ln\varepsilon_p+16.14\varepsilon_p}{1+0.681\varepsilon_p-8.48\varepsilon_p^2+8.14\varepsilon_p^3} & \text{if } \varepsilon_p < 0.4, \\ \frac{10\varepsilon_p}{\varepsilon^2} & \text{if } \varepsilon_p \geq 0.4, \end{cases} \tag{4.80}$$

and

$$F_3 = 0.0673 + 0.212\varepsilon_p + \frac{0.0232}{\varepsilon^5} \tag{4.81}$$

The resulting mean velocity obtained in each case with different void fraction and driving force is summarized in Tables 4.5-4.9. Figure 4.25 depicts the velocity contour on a middle slice parallel to the flow direction of the FCC cell with void fraction $\varepsilon = 0.8$. The effect of the Reynolds number is apparent: for lower $Re = 0.16$, the velocity profile around solid surface is almost symmetric, while for higher $Re = 76.3$, the flow is stretched and wake regions behind particle are found. As the void fraction increases, separation of boundary layers can occur as shown by the streamline around $\varepsilon = 0.9$ solid phase in Figure 4.26, in which the vortex attached to the rear of the particles is visible. On the other hand, lower void fraction leads to stronger damping due to viscous friction and thus suppresses the flow separation.

The trend is more clearly demonstrated by flow simulations at $Re \approx 36$ in Figure 4.27, for which the data is provided in Table 4.10. From the plot, at low solid volume fraction (or high void fraction) the DNS results are close to the Wen-Yu's correlation. As the solid volume fraction approaches dense packing, the agreement with Ergun's equation is more remarkable.

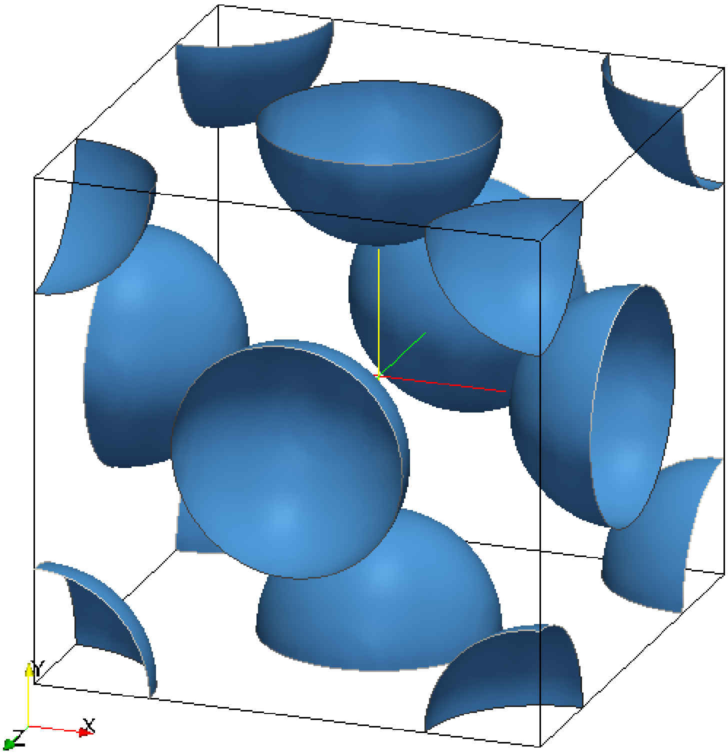

Figure 4.24: A face-centered cubic (FCC) configuration of particles.

This observation is reasonable according to the knowledge of those drag laws and their validity domains. In fact, the Ergun's equation is based on a derivation of pressure drop through a close-packed random bed and the Wen-Yu's is obtained by fluidization experiments of solid particles. Later in the Gidaspow model, they are combined for different flow regimes between which a threshold based on void fraction is used to switch. Hence the application of their hybrid model to general flow conditions seems to be sound and is well supported by our DNS study.

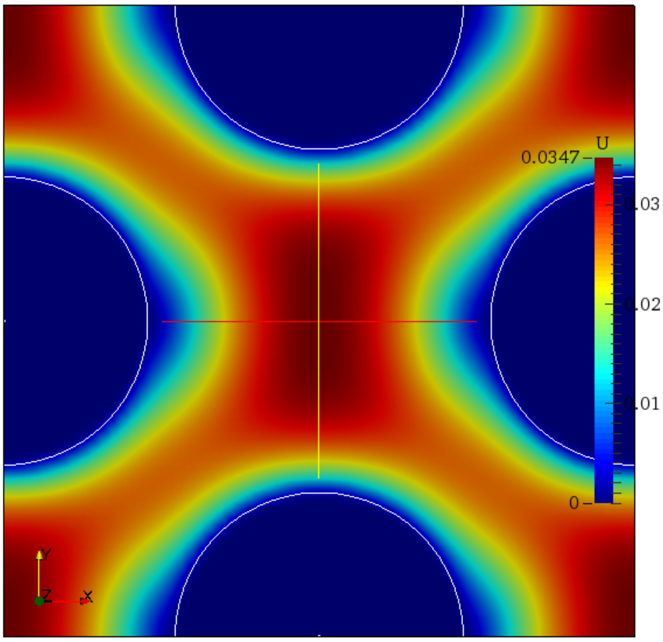

(a) $Re = 0.16$

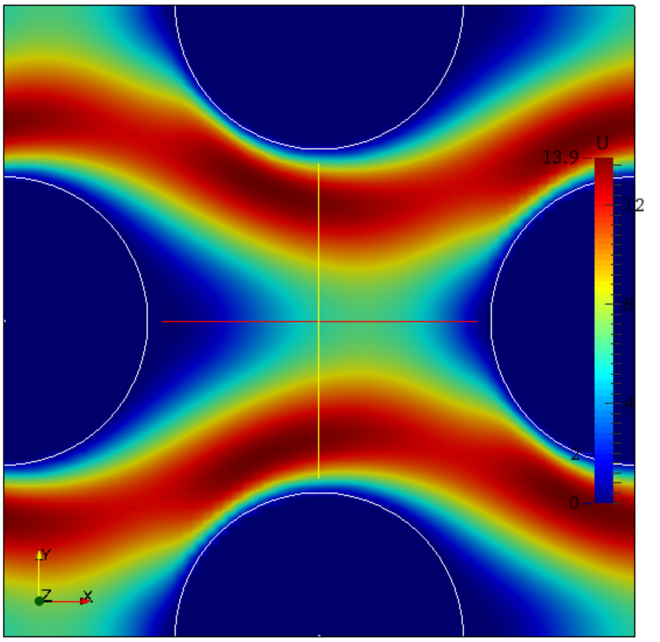

(b) $Re = 76.3$

Figure 4.25: Flow velocity on central slice of FCC cell $\varepsilon = 0.8$.

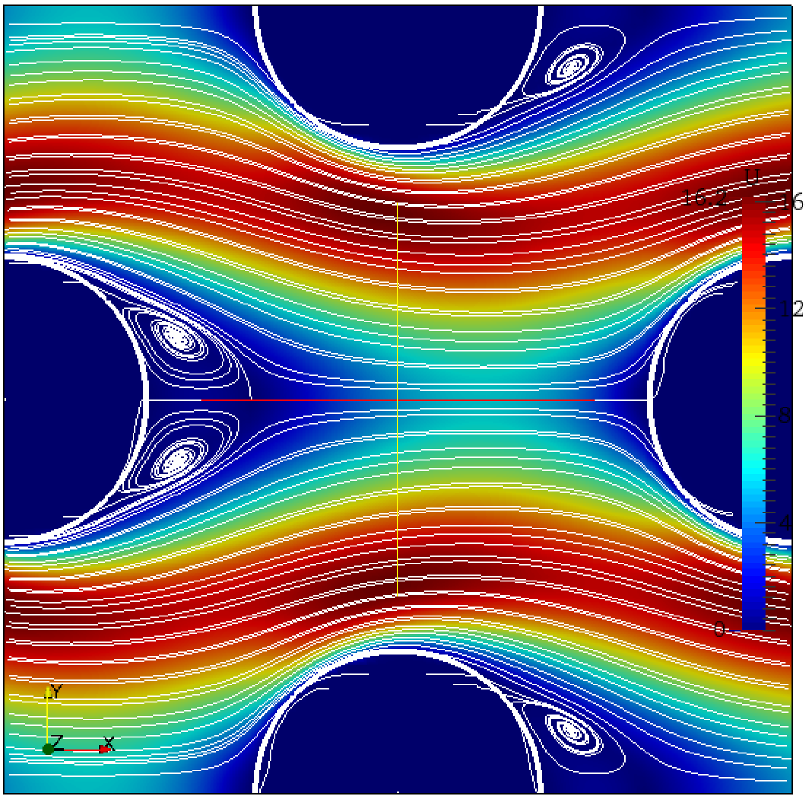

Figure 4.26: Velocity and streamline on central slice of $\varepsilon = 0.9$ and $Re = 82.1$.

Table 4.5: Prescribed body force and resulting average velocity for $\varepsilon = 0.9$.

Body force (N/kg)	Mean velocity (m/s)	Re
0.5	0.191	1.39
5	1.66	12.0
10	2.99	21.7
20	5.34	38.8
50	11.3	82.1

Table 4.6: Prescribed body force and resulting average velocity for $\varepsilon = 0.8$.

Body force (N/kg)	Mean velocity (m/s)	Re
0.1	0.0181	0.165
0.5	0.0904	0.827
5	0.860	7.86
8	1.32	12.0
15	2.20	20.1
25	3.21	29.3
40	4.74	43.3
60	6.62	60.5
80	8.35	76.3

Table 4.7: Prescribed body force and resulting average velocity for $\varepsilon = 0.7$.

Body force (N/kg)	Mean velocity (m/s)	Re
0.5	0.0395	0.413
5	0.390	4.08
10	0.760	7.96
20	1.45	15.2
50	3.26	34.1
80	4.83	50.5
100	5.80	60.7

Table 4.8: Prescribed body force and resulting average velocity for $\varepsilon = 0.6$.

Body force (N/kg)	Mean velocity (m/s)	Re
0.5	0.0213	0.246
5	0.191	2.20
10	0.378	4.36
20	0.736	8.48
50	1.72	19.9
100	3.21	37.0
150	4.55	52.4
200	5.78	66.5

Table 4.9: Prescribed body force and resulting average velocity for $\varepsilon = 0.5$.

Body force (N/kg)	Mean velocity (m/s)	Re
0.5	0.00910	0.113
5	0.0909	1.13
10	0.181	2.25
20	0.358	4.45
50	0.854	10.6
100	1.60	19.9
150	2.30	28.6
200	2.97	36.9

Table 4.10: Prescribed body force and resulting Reynolds number for $Re \approx 36$.

Void fraction	Solid volume fraction	Body force (N/kg)	Re
0.9	0.1	20	38.8
0.8	0.2	32	36.6
0.7	0.3	50	34.1
0.6	0.4	100	37.0
0.5	0.5	200	36.9

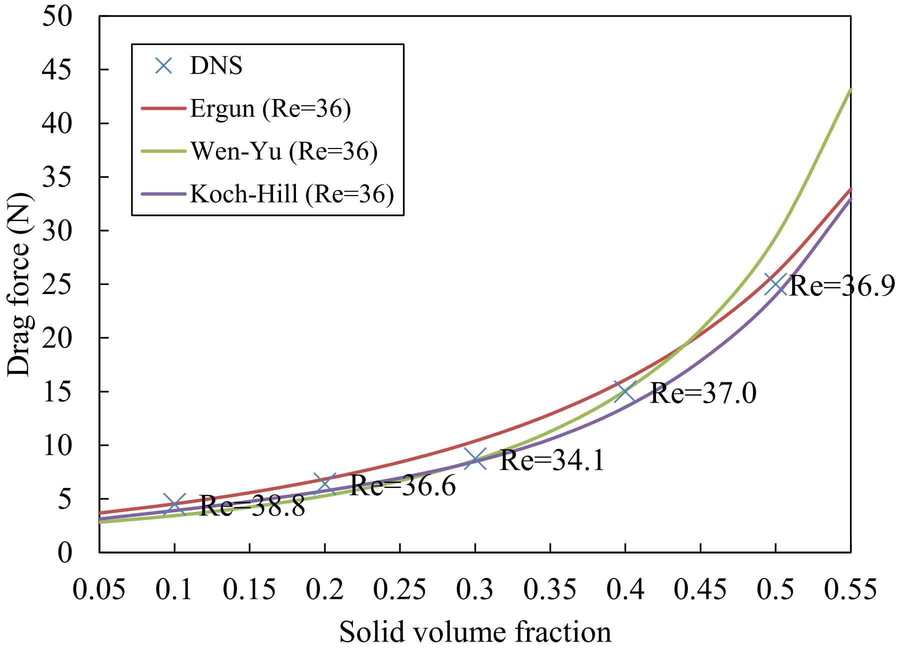

Figure 4.27: Comparison of FCC drag force obtained for $Re \approx 36$.

4.7.3 Pressure drop through a random solid bed

Different from the regular FCC arrangement, in this test we consider the fluid drag on a random configuration of solid particles. From a perspective of fluid mechanics, the pressure gradient driving the flow must be balanced by the total drag force on the solid bed, and for many industrial problems including fluidization processes, it is also an important issue to find the pressure drop when flowing through the bed at a given superficial velocity. Such correlation is best known as the one attributed to Ergun. Hence, we will directly compare the pressure drop obtained in simulations with Ergun's equation.

On the other hand, we would also like to consider the possibilities offered by other drag correlations. For a pressure gradient-driven uni-directional flow in the domain V containing a homogeneous bed composed of N particles, the balance of force indicates that

$$-\frac{\Delta p}{\Delta y} \cdot V = -\frac{\Delta p}{\Delta y} \cdot \sum_N V_p + \sum_N F_p^{drag} \ ,$$

in which the LHS is the total pressure drop, the first term on the RHS is the pressure force on particles and the second term on the RHS is the total drag force. By using the volumetric relation $\sum_N V_p = (1-\varepsilon)V$, it is easy to derive that

$$-\frac{\Delta p}{\Delta y} = \frac{1}{\varepsilon} \frac{\sum_N F_p^{drag}}{V} \ .$$

Recall that the general form of the fluid drag is given by

$$F_p^{drag} = \frac{V_p}{\varepsilon(1-\varepsilon)} \beta U \ ,$$

for which the relationship $U = \varepsilon(u - v_p)$ is used. Inserting this definition into the balance between pressure gradient and fluid drag, an equation relating the drag law and total pressure drop is obtained as

$$-\frac{\Delta p}{\Delta y} = \frac{U}{\varepsilon^2} \beta \ .$$

If the drag law of Ergun is adopted, it directly recovers the well-known Ergun's equation of pressure drop through a particle bed,

$$\left(-\frac{\Delta p}{\Delta y}\right)_{\text{Ergun}} = 150 \frac{(1-\varepsilon)^2}{\varepsilon^3} \frac{\mu}{d^2} U + 1.75 \frac{1-\varepsilon}{\varepsilon^3} \frac{\rho}{d} U^2 \ .$$

Similarly, a prediction of pressure drop based on the drag law of Wen-Yu is

$$\left(-\frac{\Delta p}{\Delta y}\right)_{\text{WenYu}} = \frac{3}{4} C_d \frac{1-\varepsilon}{\varepsilon^2} \frac{\rho}{d} \varepsilon^{-2.65} U^2 \ .$$

The current computation is thus intended to provide *quantitative comparison* between the predictions of pressure drop by the Ergun's and the Wen-Yu's correlations, via the numerical calculation by DNS.

The computational domain is a rectangular channel whose width is 1 m and length is 3 m. In its axial range of $[0.5, 2.5]$, $N = 64$ particles are randomly generated to form a close-packed solid bed with three types of void fraction $\varepsilon = 0.55$, 0.60 and 0.65. At the near end to the solid bed, a constant inlet velocity U is prescribed and the fluid is allowed to exit the domain from the opposite end with pressure $p = 0$. Periodic boundary condition is set on other four sides. This problem setting is illustrated in Figure 4.28.

The fluid density is $\rho = 1.0$ kg/m^3 and viscosity is $\mu = 0.01$ Pa s. Notice that the inflow velocity U is equal to the superficial velocity passing through the bed at a steady state, so the particle Reynolds number characterizing the current system is defined as

$$Re = \frac{UD}{\mu/\rho} \tag{4.82}$$

with D the particle diameter calculated from the solid volume fraction ε. The range of Re is selected to vary from 0 to 100 by changing the superficial velocity U. Their values for each simulation case are summarized in Table 4.11.

In order to check the convergence of DNS results, simulations are performed on uniform grids with mesh refinements of $64 \times 192 \times 64$ cells ($\Delta x = 1/64$), $80 \times 240 \times 80$ cells ($\Delta x = 1/80$) and $100 \times 300 \times 100$ cells ($\Delta x = 1/100$). Note that for finer meshes, only results with $U > 2.0$ m/s are shown, as their difference with low-resolution results at smaller Reynolds number is not significant. The time step Δt is adjusted to achieve a Courant number CFL ~ 0.2.

The pictures in Figure 4.29 show the velocity and pressure on the mid-plane of the channel at conditions of $\varepsilon = 0.65$ and $U = 3.0$ m/s for which $Re = 82.6$. The detached flow behind some particles can be clearly identified. As for the pressure profile, a gradual loss can be observed from the inflow to the outflow boundaries.

In Figure 4.30, the pressure drop measured at the two ends of the channel is plotted for all cases with respect to the Reynolds number. Basically, the pressure drop grows nonlinearly as the superficial velocity rises. Among different packing ratios, the dense packing of $\varepsilon = 0.55$ causes the most significant drop in pressure. For the DNS results, those obtained with the finest grid ($\Delta x = 1/100$) are considered to be sufficiently convergent. At lower void fractions ($\varepsilon = 0.65$ and 0.60), the DNS results lie between those of Ergun's and Wen-Yu's equations. At this stage, it seems that the predictions of total

Table 4.11: Superficial velocity and corresponding Reynolds number in each test case.

Superficial velocity (m/s)	Case 1 ($\varepsilon = 0.65$)	Case 2 ($\varepsilon = 0.60$)	Case 3 ($\varepsilon = 0.55$)
0.1	2.75	2.88	2.99
0.5	13.8	14.4	15.0
1.0	27.5	28.8	29.9
1.5	41.3	43.2	44.9
2.0	55.1	57.6	59.9
2.5	68.9	72.0	74.9
3.0	82.6	86.4	89.8
3.5	96.4	100.8	104.8
4.0	110.2	115.2	119.8

pressure drop (or mean drag force) are within an uncertainty domain that is transitional between the two empirical correlations compared. However, due to the nonlinearity of the flow behavior, at high solid volume fraction ($\varepsilon = 0.55$) the DNS results have been heading upwards to be in good agreement with the correlation by Ergun. On the other hand, the prediction based on the Wen-Yu drag model deviates from them with underestimation of the pressure loss.

Through the comparison by Figure 4.30, it is elucidated for the validity and applicability of different drag laws in the current dense random packing system. The two empirical drag laws involved in Gidaspow's model are likely to be discriminated at a considerably dense fraction of solids ($\varepsilon > 0.4$ for the current test). This seems to corroborate Gidaspow's claim of connecting them at some threshold void fraction ε_0, although the exact choice of its value is still arguable. Finally, it is also important to note that the present comparative study is not qualitative but quantitative focusing on the overall trend of fluid-particle interaction under specific conditions. For random beds, many factors may more or less influence the prediction of pressure drop effect, such as the different random packing of particles, size of computational domain, and the negative pressure region formed at the exit from the solid bed. Hence more detailed studies are to be investigated for this topic.

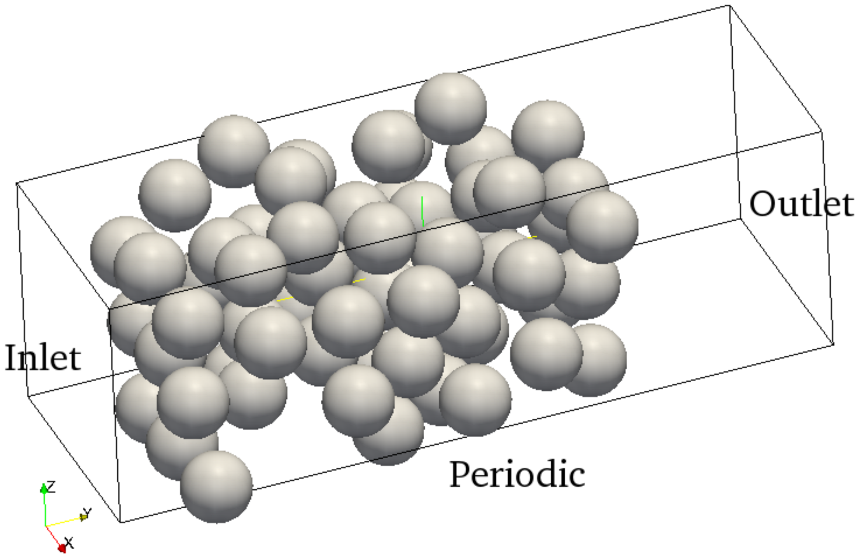

Figure 4.28: Randomly packed solid bed to measure pressure drop ($\varepsilon = 0.6$).

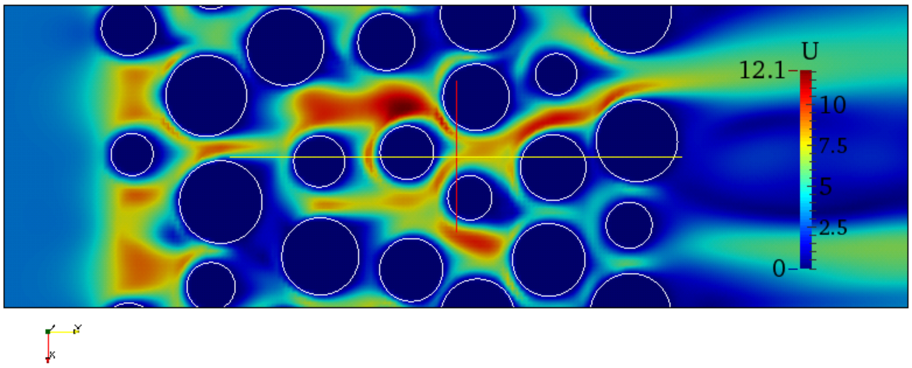

(a) Velocity

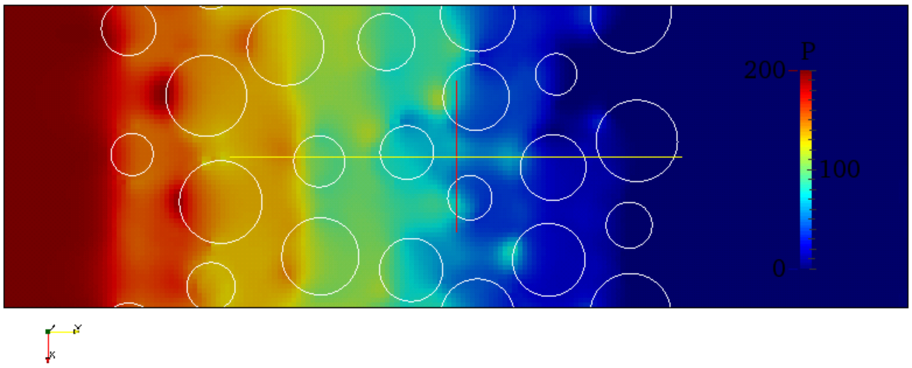

(b) Pressure

Figure 4.29: Flow passing through the random bed: $\varepsilon = 0.65$, $U = 3.0$ m/s.

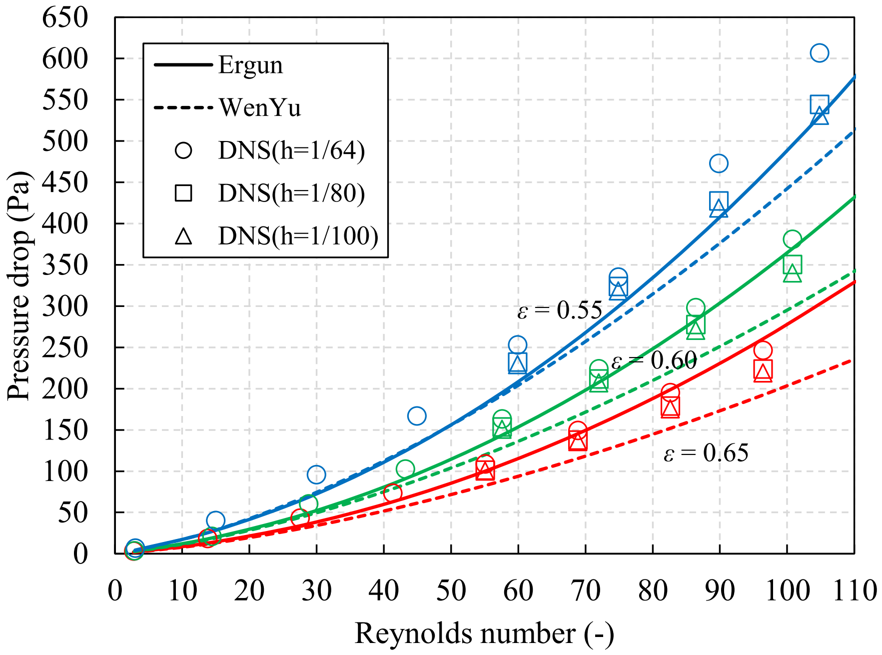

Figure 4.30: Pressure drop as a function of Reynolds number for flow passing through the random bed.

4.8 Conclusions

In this study, we described the DEM-VOF-DNS method for the direct numerical simulation of gas-solid-liquid flows, in which the VOF two-phase flow simulation and the DEM particle tracking is coupled by using the IB method. The foremost of our interest of research is an accurate and efficient modeling of the interphase coupling term involving the major contributions from flow-particle hydrodynamic force and particle-interface capillary actions in a typical three-phase system.

To realize this objective, a revised model inclusive of general fluid actions is proposed within the existing IB framework. Numerical test of particle sedimentation shows that this model can correctly predict the solid behavior and bring in considerable improvements for unsteady particle motions. Another development in this study is made by using a simplified CLSVOF technique for the modeling of the fluid interface and capillary action, together with which an iterative extension method is employed to prescribe general contact angle boundary conditions on particle surfaces. Through our test of parasitic currents and drop attachment, this technique can largely facilitate the interface representation and outperform a conventional VOF method in the calculation of surface tension.

The present DNS method is applied to the three-dimensional simulation of particles floating on an interface, which is a representative three-phase phenomenon where the hydrodynamic and capillary actions dominate the systematic behavior. It is first thoroughly investigated for the equilibrium state of a single particle. In terms of the position of the contact ring on the particle surface, satisfactory agreements have been obtained between the simulation results and analytical solutions under various physical conditions and capillary contact angles. After that the capillary attraction among multiple particles floatation is simulated by using the proposed method. The pairing of two particles and the self-assembly gathering of 10^2 particles are successfully computed. It is hence shown that the DEM-VOF-DNS method is able to capture the complex motions of three-phase systems, and fully resolve the fluid-particle interactions of hydrodynamic and capillary forces with good accuracy and simplicity in comparison with existing methods.

In the final part, efforts have been made to establish some preliminary connection between the DNS and averaged model of fluid-particle flows. DNS studies of the interphase momentum transfer or the drag correlation are performed to compare with the empirical equations employed in the volume-averaging approach. The results are very encouraging: (a) for the (nearly) creeping flow in the SC array of spheres, the calculated drag force accurately reproduces the Stokes solution when fluid grids are gradually refined, (b) in an ordered, periodic FCC fluid cell, our DNS results of fluid drag is generally compatible with the Wen-Yu correlation, and (c) for the pressure drop through a close-packed random bed the results agree well with the Ergun equation. This validates the application of Gidaspow's hybrid model combining those two equations for their adaptation at different solid fractions and flow regimes. Further investigations based on DNS will be conducted to extract model equations of capillary and liquid bridge forces that can be adopted in large-scale simulation of wet particle beds.

Bibliography

[1] H. H. Hu, N. Patankar, and M. Zhu, "Direct Numerical Simulations of Fluid—Solid Systems Using the Arbitrary Lagrangian—Eulerian Technique," *Journal of Computational Physics*, vol. 169, pp. 427–462, 2001.

[2] A. J. C. Ladd and R. Verberg, "Lattice-Boltzmann Simulations of Particle-Fluid Suspensions," *Journal of Statistical Physics*, vol. 104, no. 5-6, pp. 1191–1251, 2001.

[3] R. Glowinski, T. Pan, T. Hesla, D. Joseph, and J. Périaux, "A Fictitious Domain Approach to the Direct Numerical Simulation of Incompressible Viscous Flow past Moving Rigid Bodies: Application to Particulate Flow," *Journal of Computational Physics*, vol. 169, pp. 363–426, 2001.

[4] C. S. Peskin, "Numerical analysis of blood flow in the heart," *Journal of Computational Physics*, vol. 25, pp. 220–252, 1977.

[5] C. S. Peskin, "The immersed boundary method," *Acta Numerica*, vol. 11, pp. 479–517, 2002.

[6] M. Uhlmann, "An immersed boundary method with direct forcing for the simulation of particulate flows," *Journal of Computational Physics*, vol. 209, pp. 448–476, 2005.

[7] T.-W. Pan, D. D. Joseph, R. Bai, R. Glowinski, and V. Sarin, "Fluidization of 1204 spheres: simulation and experiment," *Journal of Fluid Mechanics*, vol. 451, pp. 169–191, 2002.

[8] J. J. Derksen and S. Sundaresan, "Direct numerical simulations of dense suspensions: wave instabilities in liquid-fluidized beds," *Journal of Fluid Mechanics*, vol. 587, pp. 303–336, 2007.

[9] S. Vincent, J. C. Brändle de Motta, A. Sarthou, J.-L. Estivalezes, O. Simonin, and E. Climent, “A Lagrangian VOF tensorial penalty method for the DNS of resolved particle-laden flows,” *Journal of Computational Physics*, vol. 256, pp. 582–614, 2014.

[10] E. Fadlun, R. Verzicco, P. Orlandi, and J. Mohd-Yusof, “Combined Immersed-Boundary Finite-Difference Methods for Three-Dimensional Complex Flow Simulations,” *Journal of Computational Physics*, vol. 161, pp. 35–60, 2000.

[11] T. Kajishima, S. Takiguchi, H. Hamasaki, and Y. Miyake, “Turbulence Structure of Particle-Laden Flow in a Vertical Plane Channel Due to Vortex Shedding,” *JSME International Journal Series B*, vol. 44, pp. 526–535, 2001.

[12] T. Kajishima and S. Takiguchi, “Interaction between particle clusters and particle-induced turbulence,” *International Journal of Heat and Fluid Flow*, vol. 23, pp. 639–646, 2002.

[13] J. Keating and P. D. Minev, “A fast algorithm for direct simulation of particulate flows using conforming grids,” *Journal of Computational Physics*, vol. 255, pp. 486–501, 2013.

[14] T. Kempe and J. Fröhlich, “An improved immersed boundary method with direct forcing for the simulation of particle laden flows,” *Journal of Computational Physics*, vol. 231, pp. 3663–3684, 2012.

[15] S.-Y. Lin, Y.-H. Chin, J.-J. Hu, and Y.-C. Chen, “A pressure correction method for fluid-particle interaction flow: Direct-forcing method and sedimentation flow,” *International Journal for Numerical Methods in Fluids*, vol. 67, pp. 1771–1798, 2011.

[16] K. Luo, Z. Wang, and J. Fan, “A modified immersed boundary method for simulations of fluid—particle interactions,” *Computer Methods in Applied Mechanics and Engineering*, vol. 197, pp. 36–46, 2007.

[17] Y. Yuki, S. Takeuchi, and T. Kajishima, “Efficient Immersed Boundary Method for Strong Interaction Problem of Arbitrary Shape Object with the Self-Induced Flow,” *Journal of Fluid Science and Technology*, vol. 2, pp. 1–11, 2007.

[18] C. Hirt and B. Nichols, “Volume of fluid (VOF) method for the dynamics of free boundaries,” *Journal of Computational Physics*, vol. 39, pp. 201–225, 1981.

[19] M. Sussman, P. Smereka, and S. Osher, "A Level Set Approach for Computing Solutions to Incompressible Two-Phase Flow," *Journal of Computational Physics*, vol. 114, no. 1, pp. 146–159, 1994.

[20] S. O. Unverdi and G. Tryggvason, "A front-tracking method for viscous, incompressible, multi-fluid flows," *Journal of Computational Physics*, vol. 100, no. 1, pp. 25–37, 1992.

[21] T. Yabe, F. Xiao, and T. Utsumi, "The Constrained Interpolation Profile Method for Multiphase Analysis," *Journal of Computational Physics*, vol. 169, pp. 556–593, 2001.

[22] S. Vincent, T. N. Randrianarivelo, G. Pianet, and J.-P. Caltagirone, "Local penalty methods for flows interacting with moving solids at high Reynolds numbers," *Computers & Fluids*, vol. 36, pp. 902–913, 2007.

[23] R. Iwata, S. Takeuchi, and T. Kajishima, "Large-scale analysis of interactive behaviors of bubbles and particles in a liquid by a coupled immersed boundary and VOF technique," *Multiphase Science and Technology*, vol. 22, no. 3, pp. 233–246, 2010.

[24] K. Washino, H. Tan, A. Salman, and M. Hounslow, "Direct numerical simulation of solid—liquid—gas three-phase flow: Fluid—solid interaction," *Powder Technology*, vol. 206, pp. 161–169, 2011.

[25] S.-Y. Lin and Y.-C. Chen, "A pressure correction-volume of fluid method for simulations of fluid—particle interaction and impact problems," *International Journal of Multiphase Flow*, vol. 49, pp. 31–48, 2013.

[26] D. Jain, N. G. Deen, J. Kuipers, S. Antonyuk, and S. Heinrich, "Direct numerical simulation of particle impact on thin liquid films using a combined volume of fluid and immersed boundary method," *Chemical Engineering Science*, vol. 69, pp. 530–540, 2012.

[27] I. Mirzaii and M. Passandideh-Fard, "Modeling free surface flows in presence of an arbitrary moving object," *International Journal of Multiphase Flow*, vol. 39, pp. 216–226, 2012.

[28] M. Baltussen, L. Seelen, J. Kuipers, and N. Deen, "Direct Numerical Simulations of gas—liquid—solid three phase flows," *Chemical Engineering Science*, vol. 100, pp. 293–299, 2013.

[29] H. Shinto, D. Komiyama, and K. Higashitani, "Lateral capillary forces between solid bodies on liquid surface: a lattice Boltzmann study.,"

Langmuir : the ACS journal of surfaces and colloids, vol. 22, pp. 2058–64, 2006.

[30] H. Shinto, D. Komiyama, and K. Higashitani, “Lattice Boltzmann study of capillary forces between cylindrical particles,” *Advanced Powder Technology*, vol. 18, pp. 643–662, 2007.

[31] A. S. Joshi and Y. Sun, “Multiphase lattice Boltzmann method for particle suspensions,” *Physical Review E*, vol. 79, p. 066703, 2009.

[32] A. S. Joshi and Y. Sun, “Wetting dynamics and particle deposition for an evaporating colloidal drop: A lattice Boltzmann study,” *Physical Review E*, vol. 82, p. 041401, 2010.

[33] A. Kawasaki, J. Onishi, Y. Chen, and H. Ohashi, “A lattice Boltzmann model for contact-line motions,” *Computers & Mathematics with Applications*, vol. 55, pp. 1492–1502, 2008.

[34] J. Onishi, A. Kawasaki, Y. Chen, and H. Ohashi, “Lattice Boltzmann simulation of capillary interactions among colloidal particles,” *Computers & Mathematics with Applications*, vol. 55, pp. 1541–1553, 2008.

[35] G. Liang, Z. Zeng, Y. Chen, J. Onishi, H. Ohashi, and S. Chen, “Simulation of self-assemblies of colloidal particles on the substrate using a lattice Boltzmann pseudo-solid model,” *Journal of Computational Physics*, vol. 248, pp. 323–338, 2013.

[36] G. Liang, Z. Zeng, Y. Chen, H. Ohashi, and S. Chen, “Simulaiton of self-assemblies of colloidal particles with different sized by using a lattice Boltzmann pseudo-solid model,” *International Journal of Modern Physics C*, vol. 24, p. 1340002, 2013.

[37] H. Zheng, C. Shu, and Y. Chew, “A lattice Boltzmann model for multiphase flows with large density ratio,” *Journal of Computational Physics*, vol. 218, pp. 353–371, 2006.

[38] P. Singh and D. D. Joseph, “Fluid dynamics of floating particles,” *Journal of Fluid Mechanics*, vol. 530, pp. 31–80, 2005.

[39] P. Singh, D. D. Joseph, S. K. Gurupatham, B. Dalal, and S. Nudurupati, “Spontaneous dispersion of particles on liquid surfaces.,” *Proceedings of the National Academy of Sciences of the United States of America*, vol. 106, pp. 19761–4, 2009.

[40] K. Washino, H. Tan, M. Hounslow, and A. Salman, "A new capillary force model implemented in micro-scale CFD—DEM coupling for wet granulation," *Chemical Engineering Science*, vol. 93, pp. 197–205, 2013.

[41] K. Yokoi, "Efficient implementation of THINC scheme: A simple and practical smoothed VOF algorithm," *Journal of Computational Physics*, vol. 226, no. 2, pp. 1985–2002, 2007.

[42] P. A. Cundall and O. D. L. Strack, "A discrete numerical model for granular assemblies," *Géotechnique*, vol. 29, no. 1, pp. 47–65, 1979.

[43] M. Sussman, E. Fatemi, P. Smereka, and S. Osher, "An improved level set method for incompressible two-phase flows," *Computers & Fluids*, vol. 27, no. 5, pp. 663–680, 1998.

[44] M. Sussman and E. G. Puckett, "A Coupled Level Set and Volume-of-Fluid Method for Computing 3D and Axisymmetric Incompressible Two-Phase Flows," *Journal of Computational Physics*, vol. 162, no. 2, pp. 301–337, 2000.

[45] K. Yokoi, "A practical numerical framework for free surface flows based on CLSVOF method, multi-moment methods and density-scaled CSF model: Numerical simulations of droplet splashing," *Journal of Computational Physics*, vol. 232, pp. 252–271, 2013.

[46] M. Sussman, "An Adaptive Mesh Algorithm for Free Surface Flows in General Geometries," in *Adaptive Method of Lines* (A. Vande Wouwer, P. Saucez, and W. Schiesser, eds.), Chapman and Hall/{CRC}, 2001.

[47] T. Yabe, K. Chinda, and T. Hiraishi, "Computation of surface tension and contact angle and its application to water strider," *Computers & Fluids*, vol. 36, pp. 184–190, 2007.

[48] H. S. Yoon, C. H. Jeon, J. H. Jung, B. Koo, C. Choi, and S. C. Shin, "Simulation of two-phase flow-body interaction problems using direct forcing/fictitious domain-level set method," *International Journal for Numerical Methods in Fluids*, vol. 73, pp. 250–265, 2013.

[49] K. W. Connington, T. Lee, and J. F. Morris, "Interaction of fluid interfaces with immersed solid particles using the lattice Boltzmann method for liquid—gas—particle systems," *Journal of Computational Physics*, vol. 283, pp. 453–477, 2015.

[50] M. Fujita, O. Koike, and Y. Yamaguchi, “Computation of Capillary Interactions among Many Particles at Free Surface,” *Applied Physics Express*, vol. 6, p. 036501, 2013.

[51] M. Fujita, O. Koike, and Y. Yamaguchi, “Direct simulation of drying colloidal suspension on substrate using immersed free surface model,” *Journal of Computational Physics*, vol. 281, pp. 421–448, 2015.

[52] S. Gallier, E. Lemaire, L. Lobry, and F. Peters, “A fictitious domain approach for the simulation of dense suspensions,” *Journal of Computational Physics*, vol. 256, pp. 367–387, 2014.

[53] U. Schumann and R. A. Sweet, “A direct method for the solution of poisson’s equation with neumann boundary conditions on a staggered grid of arbitrary size,” *Journal of Computational Physics*, vol. 20, pp. 171–182, 1976.

[54] B. Lafaurie, C. Nardone, R. Scardovelli, S. Zaleski, and G. Zanetti, “Modelling Merging and Fragmentation in Multiphase Flows with SURFER,” *Journal of Computational Physics*, vol. 113, pp. 134–147, 1994.

[55] M. Boger, J. Schlottke, C.-D. Munz, and B. Weigand, “Reduction of parasitic currents in the DNS VOF code FS3D,” *12th Workshop on Two-Phase Flow Predictions*, 2010.

[56] M. M. Francois, S. J. Cummins, E. D. Dendy, D. B. Kothe, J. M. Sicilian, and M. W. Williams, “A balanced-force algorithm for continuous and sharp interfacial surface tension models within a volume tracking framework,” *Journal of Computational Physics*, vol. 213, pp. 141–173, 2006.

[57] A. ten Cate, C. H. Nieuwstad, J. J. Derksen, and H. E. A. Van den Akker, “Particle imaging velocimetry experiments and lattice-Boltzmann simulations on a single sphere settling under gravity,” *Physics of Fluids*, vol. 14, p. 4012, 2002.

[58] Z.-G. Feng and E. E. Michaelides, “Proteus: a direct forcing method in the simulations of particulate flows,” *Journal of Computational Physics*, vol. 202, pp. 20–51, 2005.

[59] S. V. Apte, M. Martin, and N. A. Patankar, “A numerical method for fully resolved simulation (FRS) of rigid particle—flow interactions in

complex flows," *Journal of Computational Physics*, vol. 228, pp. 2712–2738, 2009.

[60] G. Pianet, A. Ten Cate, J. Derksen, and E. Arquis, "Assessment of the 1-fluid method for DNS of particulate flows: Sedimentation of a single sphere at moderate to high Reynolds numbers," *Computers & Fluids*, vol. 36, pp. 359–375, 2007.

[61] R. Croce, M. Griebel, and M. A. Schweitzer, "Numerical simulation of bubble and droplet deformation by a level set approach with surface tension in three dimensions," *International Journal for Numerical Methods in Fluids*, pp. n/a–n/a, 2009.

[62] Y. Renardy and M. Renardy, "PROST: A Parabolic Reconstruction of Surface Tension for the Volume-of-Fluid Method," *Journal of Computational Physics*, vol. 183, pp. 400–421, 2002.

[63] D. Lörstad, M. Francois, W. Shyy, and L. Fuchs, "Assessment of volume of fluid and immersed boundary methods for droplet computations," *International Journal for Numerical Methods in Fluids*, vol. 46, pp. 109–125, 2004.

[64] K. Washino, H. Tan, M. Hounslow, and A. Salman, "Meso-scale coupling model of DEM and CIP for nucleation processes in wet granulation," *Chemical Engineering Science*, vol. 86, pp. 25–37, 2013.

[65] M. van der Hoef, M. van Sint Annaland, N. Deen, and J. Kuipers, "Numerical Simulation of Dense Gas-Solid Fluidized Beds: A Multiscale Modeling Strategy," *Annual Review of Fluid Mechanics*, vol. 40, pp. 47–70, 2008.

[66] R. J. Hill, D. L. Koch, and A. J. C. Ladd, "Moderate-Reynolds-number flows in ordered and random arrays of spheres," *Journal of Fluid Mechanics*, vol. 448, pp. 243–278, 2001.

[67] R. J. Hill, D. L. Koch, and A. J. C. Ladd, "The first effects of fluid inertia on flows in ordered and random arrays of spheres," *Journal of Fluid Mechanics*, vol. 448, pp. 213–241, 2001.

[68] R. Beetstra, M. A. van der Hoef, and J. A. M. Kuipers, "Drag force of intermediate Reynolds number flow past mono- and bidisperse arrays of spheres," *AIChE Journal*, vol. 53, pp. 489–501, 2007.

[69] S. Tenneti, R. Garg, and S. Subramaniam, “Drag law for monodisperse gas—solid systems using particle-resolved direct numerical simulation of flow past fixed assemblies of spheres,” *International Journal of Multiphase Flow*, vol. 37, pp. 1072–1092, 2011.

[70] S. Tenneti and S. Subramaniam, “Particle-Resolved Direct Numerical Simulation for Gas-Solid Flow Model Development,” *Annual Review of Fluid Mechanics*, vol. 46, pp. 199–230, 2014.

[71] Y. Tang, E. A. J. F. Peters, J. A. M. Kuipers, S. H. L. Kriebitzsch, and M. A. van der Hoef, “A new drag correlation from fully resolved simulations of flow past monodisperse static arrays of spheres,” *AIChE Journal*, vol. 61, pp. 688–698, 2015.

[72] N. G. Deen, M. v. S. Annaland, and J. Kuipers, “Direct numerical simulation of complex multi-fluid flows using a combined front tracking and immersed boundary method,” *Chemical Engineering Science*, vol. 64, pp. 2186–2201, 2009.

[73] A. A. Zick and G. M. Homsy, “Stokes flow through periodic arrays of spheres,” *Journal of Fluid Mechanics*, vol. 115, pp. 13–26, 1982.

Chapter 5

Conclusions

5.1 Summary of main work

In this thesis, a numerical framework has been presented to simulate three-phase problems that are relevant in many natural and industrial flows such as those in the wet ball milling and twin screw kneading processes, for which the prime and central aim is the development of an accurate, robust and efficient numerical solver able to predict the macroscopic behavior of gas-solid-liquid flows interacting with complex geometries. The main contents and results of this work are summarized as follows.

In Chapter 1 the key elements required to achieve our main purpose of research are first analyzed and some fundamental numerical techniques suitable for solving reduced aspects in a typical gas-solid-liquid system have been extensively reviewed and compared. Consequently, we made up the mind to adopt an integrated strategy that couples the VOF method (description of fluid interface and movement), the DEM (Lagrangian tracking of particles), the IB method (modeling of general boundaries on regular grids) and the SDF model (representation of arbitrary-shaped walls and rigid motions) as necessary building-blocks in the present computational framework. Next for the modeling of three-phase flows, revelations based on our literature survey of current status have figured out three problems to be addressed for a practical and self-contained numerical methodology: (a) the effective computation of two-phase flows within complex geometries for real situations, (b) the appropriate modeling of gas-solid-liquid three-phase flows with complex geometries and correct resolution of the macroscopic flow behaviors from an engineering perspective and (c) the numerical functionality of direct simulation of gas-solid-liquid problems serving for the validation and development of closure correlations and subgrid models to supplement the preceding macroscopic modeling.

As a point of departure, Chapter 2 describes a numerical method namely the VOF-IB method to perform three-dimensional simulations of two-phase flows in general geometries. This method adopts a VOF approach to capture and advance the fluid interface, and it integrates the fluid solver with the IB modeling of arbitrary-shape walls and moving bodies. The shape and movement of solid geometries are efficiently represented by an auxiliary SDF field with local coordinate transformation. Various validation tests have been conducted using the present method, and the computational results are in good agreements with reference solutions and experimental data. Hence, the adequacy and suitability of the present VOF-IB method are shown to successfully simulate complicated two-phase flows interacting with general geometries.

In Chapter 3, an Eulerian-Lagrangian numerical model, specifically the DEM-VOF method, is presented for three-dimensional simulations of gas-solid-liquid flows. The treatment of the fluid motion in general comes from our previous attempts. The particle phase is tracked by the DEM as discrete entities. The fluid-particle coupling is achieved by the volume-averaging technique wherein a well-established empirical closure is adopted for the description of hydrodynamic forces. In particular, the modeling of arbitrary-shaped walls and moving boundaries that can influence both the fluid phase and the particle phase are tackled by the introduction of SDF representation and IB method, which is tailored to be an efficient approach unified for gas-solid-liquid systems interacting with complex geometries. Special attentions when computing fluid-particle interactions near those boundaries are raised and their treatments are also discussed, with which the enhanced performance and realistic flow behavior obtained are remarkable. Various model verifications and validation tests are performed in this study to show the validity and capability of the DEM-VOF method. By comparing with analytical solutions and experimental data, we generally find good agreements from the simulation results in the macroscopic respects of free surface deformation, water displacement, and the shape of solid beds, thereby highlighting its promising potential in accurately modeling complicated gas-solid-liquid flows in engineering problems. The DEM-VOF method is also successfully applied to the simulation of a laboratory twin screw kneader system yielding satisfactory predictions of the agitation of gas-solid-liquid mixture by the stirring paddles. To the best of our knowledge, the proposed method is the first report that successfully couples the DEM to a VOF solver with non-trivial wall boundaries.

The work of Chapter 4 developed a DNS method for microscopic modeling of gas-solid-liquid flows. The discretization of the fluid-particle systems is accomplished by an improved IB method accounting for increased accuracy in unsteady flows and generalized fluid actions. A simplified CLSVOF calculation takes care of the particle-interface capillary interaction with general static contact angles. This DNS method can fully resolve the gas-solid-liquid interaction inclusive of both hydrodynamic and capillary forces and open to other effects as well, without any empirical constitutive models. Numerical tests are performed to show the validity of proposed models; in particular the motions of floating particles on fluid interface are studied as a system dominated by hydrodynamic and capillary interactions that can be solved by using this DNS method with ease. In the last part of this chapter, the usage of the DNS approach to evaluate the applicable domain of empirical drag correlations adopted in the DEM-VOF method closes the current framework by establishing a preliminary connection between microscopic and macroscopic levels of numerical modeling.

In this way, the implementation of proposed numerical methods has shed some light on the modeling of gas-liqluid and gas-solid-liquid flows in complex geometries. Different new technologies for the simulations of industrial multiphase flows have been developed, namely the VOF-IB method, the DEM-VOF method and the DEM-VOF-DNS method. The author believes that the present computational techniques have filled many gaps and would be a versatile tool to deepen our knowledge of complex three-phase systems encountered in scientific and industrial applications.

5.2 Future work

Further developments are to be investigated in two directions. For the application of the DEM-VOF method to engineering problems, improvements in computational efficiency and robustness are desirable. For example, the adaptive mesh refinement (AMR) technique can be implemented to save simulation time and resource, the implicit calculation of the fluid-particle interaction force by iterative procedures will make the scheme more stable for larger time steps, and the coarse grain model (CGM) [1] is effective for DEM simulations with large amounts of solid particles. For some industrial problems, it is also important to treat heat transfer in a gas-solid-liquid system, which may require the modeling of fluid-particle heat convection, interparticle heat conduction and heat radiation.

On the other hand, it is expected in the DNS approach for its contribution to the advancement of model developments of fluid-particle interactions. This may involves the innovative correlations of drag force taking into account the granular temperature (suggested by [2–4] but still not realized) and the additional capillary stress when the free surface penetrates into the solid layer (see [5]). Those effective models could be important in some certain situations. Our focus has been recently spotted on the DNS-based calculation and modeling of the liquid bridge force among multiple particles. Figure 5.1 depicts our preliminary results in twin and triple particle systems with a 15 ° contact angle, where the arrows indicate the liquid bridge force (i.e. the sum of the capillary force and pressure force) computed numerically, which is however extremely difficult to be derived analytically.

Bibliography

[1] M. Sakai, M. Abe, Y. Shigeto, S. Mizutani, H. Takahashi, A. Viré, J. R. Percival, J. Xiang, and C. C. Pain, "Verification and validation of a coarse grain model of the DEM in a bubbling fluidized bed," *Chemical Engineering Journal*, vol. 244, pp. 33–43, 2014.

[2] S. Tenneti, R. Garg, C. Hrenya, R. Fox, and S. Subramaniam, "Direct numerical simulation of gas—solid suspensions at moderate Reynolds number: Quantifying the coupling between hydrodynamic forces and particle velocity fluctuations," *Powder Technology*, vol. 203, pp. 57–69, 2010.

[3] S. Kriebitzsch, M. van der Hoef, and J. Kuipers, "Fully resolved simulation of a gas-fluidized bed: A critical test of DEM models," *Chemical Engineering Science*, vol. 91, pp. 1–4, 2013.

[4] S. Tenneti and S. Subramaniam, "Particle-Resolved Direct Numerical Simulation for Gas-Solid Flow Model Development," *Annual Review of Fluid Mechanics*, vol. 46, pp. 199–230, 2014.

[5] K. Washino, H. Tan, M. Hounslow, and A. Salman, "Meso-scale coupling model of DEM and CIP for nucleation processes in wet granulation," *Chemical Engineering Science*, vol. 86, pp. 25–37, 2013.

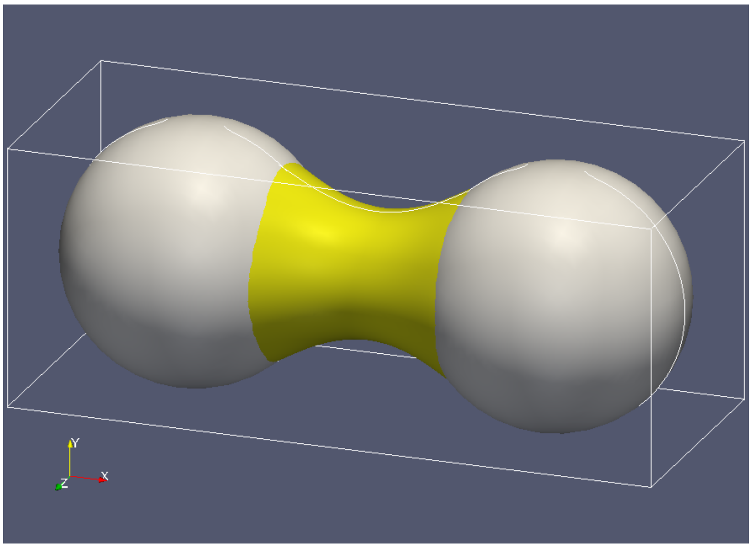

(a) Dual liquid bridge

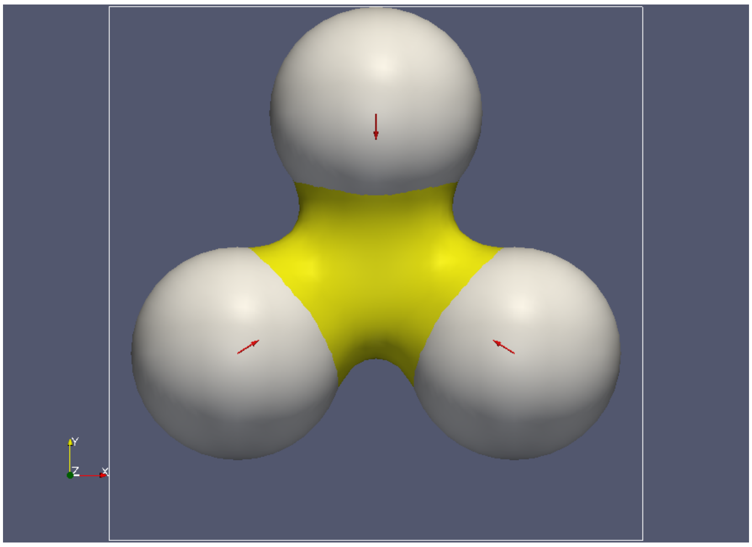

(b) Triple liquid bridge

Figure 5.1: Formation of particle-particle liquid bridges.

Acknowledgements

Firstly the immense gratitude goes to my supervisor, Prof. M. Sakai, for his professional guidance, valuable suggestion and warm help throughout my study. I would also like to send my best regards to the Ph.D. defense committee that comprises Prof. K. Ishikawa, Prof. N. Kasahara, Prof. S. Takagi (The University of Tokyo) and Prof. T. Kajishima (Osaka University) for their inspiring discussions and pertinent comments to help improve the quality of this thesis.

The author is financially supported by the Japan Society for the Promotion of Science (JSPS) DC1 fellowship. The study on multiphase flows has benefited from the lectures and papers provided by Prof. M. Ohta (Tokushima University). Prof. S. Koshizuka (The University of Tokyo) has generously made available the photographs of dam break experiments for comparison and validation. Kurimoto Ltd. and Metal Technology Co. Ltd. are acknowledged for designing and manufacturing the laboratory TSK device used in the study of gas-solid-liquid flows. Dr. O. Koike (The University of Tokyo) has provided some state-of-the-art literatures on the DNS of three-phase flows. I am very grateful to Prof. G. Tryggvason and his colleagues during my short visit to the University of Notre Dame where I have learned a lot about their modeling of bubbly flows. It is the kind recommendation by Prof. S. Honma (Saitama University) and the support by Prof. H. Takahashi (The University of Tokyo) and Prof. K. Ishihara that offered me this opportunity.

The present work owns much to the discussions with the members of Computational Granular Dynamics Group run by Prof. M. Sakai, particularly with Dr. Y. Shigeto for his outstanding work on the DEM and SDF models, Dr. G. Basinskas for his assistance in preparing, testing and recording the TSK experiments, and Dr. Y. Yamada, Dr. T. Watanabe, Dr. S. Mizutani, Dr. Y. Tsunazawa and Dr. M-T. Sakai for their numerous helps. Our respected administrative secretaries and technical assistants Mrs. Y. Asahi, Mrs. Y. Iijima, Mrs. C. Iguchi and Mrs. T. Ichinose have also provided a lot of arrangement of academic affairs. I always feel at home in my

life as a Ph.D. student in the University of Tokyo thanks to the support from the Department of Nuclear Engineering and Management.

I am deeply indebted to all my friends here in my life. Your friendship has changed me into a better person. Most of all, I would like to dedicate this work to my parents and family for all efforts they have done as best they could.

`Xiaosong SUN`
`The University of Tokyo`
`July 30, 2015`

Appendix A

Momentum equation for a solid particle in ambient flow

In this section, the momentum equation that governs the particle motion as considered in the DEM-VOF method (Chapter 3) is explained. We note that, the model formulation of the DEM-VOF method generally falls within the class of methodology of Eulerian-Lagrangian volume-averaging approach, which has already been well established in some past studies, see e.g. [1]. For the sake of brevity, they will not be repeated here. Instead of that, we will focus on some necessary physical considerations, in particular the role of the viscous force, and show its consistency by examining particle behaviors in several hypothetical flow conditions. The discussions in this section is gratefully attributed to our private communication with Prof. Takeo Kajishima (The Osaka University) and Prof. Shu Takagi(The University of Tokyo).

The Navier-Stokes equation is written for a viscous fluid as follows:

$$\frac{\mathrm{D}\boldsymbol{u}}{\mathrm{D}t} = -\frac{1}{\rho}\nabla p + \frac{1}{\rho}\nabla \cdot \tau + \boldsymbol{g} \ , \tag{A.1}$$

in which p is pressure and τ is the viscous stress. Now we consider a small solid particle moving in that fluid, for which the motion is described by

$$m_p \frac{\mathrm{d}\boldsymbol{v}_p}{\mathrm{d}t} = -V_p \nabla p + V_p \nabla \cdot \tau + \boldsymbol{F}^f + m_p \boldsymbol{g} \ . \tag{A.2}$$

On the RHS of this equation, the first two terms correspond to "far-field" pressure gradient and viscous forces [2] under the assumption that the ambient flow field does not change suddenly around the particle position, and the third term represents an effective fluid action based on the local flow condition. In the fluid-particle flow numerically studied in this work, the effective drag force $\boldsymbol{F}^d$ makes the dominant contribution, which is usually written in terms of the slipping velocity between phases,

$$\boldsymbol{F}^d = \beta(\boldsymbol{u} - \boldsymbol{v}) \ . \tag{A.3}$$

The fluid-particle interaction is also inclusive of lift and added-mass forces and it writes

$$\boldsymbol{F}^f = \boldsymbol{F}^d + \boldsymbol{F}^l + \boldsymbol{F}^{am} \ . \tag{A.4}$$

In fact, by substitution of the NS equation to eliminate the ambient forces, one can easily obtain that

$$m_p \frac{\mathrm{d}\boldsymbol{v}_p}{\mathrm{d}t} = \rho V_p \frac{\mathrm{D}\boldsymbol{u}}{\mathrm{D}t} + \boldsymbol{F}^d + \boldsymbol{F}^l + \boldsymbol{F}^{am} + (m_p - \rho V_p)\boldsymbol{g} \ , \tag{A.5}$$

which is consistent and equivalent with the fluid force derived for inviscid flow in [3] (see their Eq. (3.13)), except for the drag term owing to viscous friction on solid surface. It is also important to note the difference between the operators of $\frac{\mathrm{d}(\bullet)}{\mathrm{d}t}$ and $\frac{\mathrm{D}(\bullet)}{\mathrm{D}t}$, of which the former follows the particle frame and the latter is in the fluid frame.

Remarks on difference model formulations A special topic on modeling fluid-particle flows concerns the choice of particle equations with different formulations like Eq. (A.2) or Eq. (A.5). Theoretically both of them are, as a matter of course, the same, whereas subtle difference may exist in a numerical sense. Eq. (A.2) is clearly a pure relation of fluid actions (pressure gradient and viscous stress) and it is related to the volume-averaged form of fluid-particle momentum equations, indicating an explicit conservation of momentum. On the other hand, Eq. (A.5) recasts the explicit force-based interaction into an implicit form depending on the change of local fluid momentum (fluid density and acceleration).

Both model formulations have been historically adopted. A rather new and thorough comparison has been made in [1]. Basically, Eq. (A.2) corresponds to their “Set I” or “II”, and the Eq. (A.5) corresponds to their “Set III”. They have critically figured out that, since the action of fluid stress is directly calculated, the model formulation of “Set I/II” (and equivalently Eq. (A.2)) can better predict the particle behaviors under complicated dynamic situations, especially for those cases with pressure fluctuations or non-uniform pressure gradients, while “Set III” (or Eq. (A.5)) is usually problematic. This becomes an evidence for the present choice of model formulation targeting better generality and performance for complicated multiphase flows.

In the sections that follow, several thought experiments are presented to illustrate the problem of such an equation of motion applied to some test particles in steady, hypothetical systems. Note that only the fluid drag among the effective forces is considered hereinafter.

A.1 Sedimentation in infinite, quiescent fluid

In this case (Figure A.1 (a)), according to the assumption of the inert surrounding fluid (i.e. $u = 0$), a simple relationship between hydrostatic pressure and the buoyant force is yielded,

$$- V_p \nabla p = -\rho V_p \boldsymbol{g} \ . \tag{A.6}$$

Hence the momentum equation (A.2) becomes

$$m_p \frac{\mathrm{d}v_p}{\mathrm{d}t} = \boldsymbol{F}^d + (m_p - \rho V_p)\boldsymbol{g} \ . \tag{A.7}$$

If a proper drag correlation is adopted for $\boldsymbol{F}^d$, e.g. the Stokes' drag law, then a terminal velocity for the particle sedimentation could be calculated from the steady state of this equation. In this case, the viscous force does not contribute to the particle motion.

A.2 Transportation in horizontal channel flow

Next the transportation of a neutrally buoyant particle in a horizontal channel is considered, see Figure A.1 (b), which should simply follow the flow at a steady state. In this Poiseuille-like flow, the pressure gradient applied along the channel is balanced by the viscous shear, giving that

$$- \nabla p + \nabla \cdot \tau = 0 \ . \tag{A.8}$$

Therefore for a particle at steady motion it is obtained that

$$\boldsymbol{F}^d = 0 \ , \tag{A.9}$$

which implies that $v_p = u$ as our expectation. On the other hand, if the viscous force is neglected, it happens that the pressure gradient force must be balanced by the effective drag instead, which leads to a non-physical result that $v_p > u$.

In numerical simulations, it is also common to generate a periodic channel by adding an external body force. The analysis of such body force-driven flows is similar to our discussion above.

A.3 Motion in vertical channel flow

This case is illustrated in Figure A.1 (c), for which the particle might be moving upwards, downwards, or keeping motionless in the frame of the channel wall. In any case, the NS equation (A.1) for fluid motion at steady state indicates that

$$-\nabla p + \nabla \cdot \tau + \rho \boldsymbol{g} = 0 \ . \tag{A.10}$$

Inserting this into the particle momentum equation (A.2), one arrives at a simple expression,

$$m_p \frac{\mathrm{d}\boldsymbol{v}_p}{\mathrm{d}t} = \boldsymbol{F}^d + (m_p - \rho V_p)\boldsymbol{g} \ , \tag{A.11}$$

which is a familiar restatement of the balance between the fluid drag and buoyant weight of an immersed object. Again, reasonable result cannot be obtained if the viscous force is neglected.

A.4 Discussion and recap

As commented in Chapter 3, it is a common practice to drop the ambient viscous force exerted on solid particles because of its negligible effect compared to other forces in many engineering applications, e.g. fluidized bed [4, 5] and beads mill [6]. In this section, however, we discussed some cases where this force cannot be ignored or incorrect particle behavior could be deduced. As a matter of course, such steady, hypothetical cases are rather “rare” in real-world problems, but they are still able to provide a critical examination of the validity of our numerical modeling of fluid-particle systems.

In particular, we would like to discuss why the viscous term could be reasonably neglected in many engineering problems. The reason is basically twofold. Firstly, the fluid carriers often considered such as water and air are generally low-viscosity ones. In many mesoscale and large-scale applications, Reynolds number is thus sufficiently high so that the (ambient) viscous effect never distinguishes so strongly as the others, e.g. the pressure gradient as driving force.

What’s more, it merely has a lesser influence in comparison with the effective fluid drag $\boldsymbol{F}^d$, which is naturally a result of the scale separation between ambient flow and flow around particles. As the characteristic scale of particle size is typically one order smaller than that of the flow system, thus so is the particle Reynolds number Re_p compared with the flow Reynolds number Re. In other words, the effective skin friction or drag force is more dominant than the far-field viscous term in most cases. This can be elucidated by the verification example of flow through fixed particle bed calculated in Section 3.4.2.

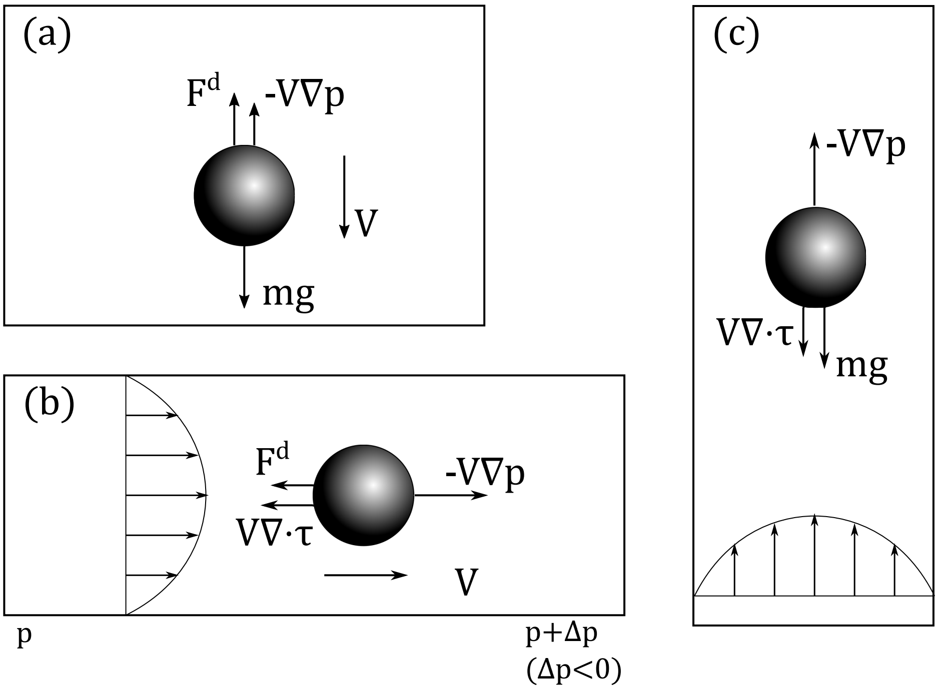

Figure A.1: Schematic diagram of particle motion in different flow cases.

As mentioned, the pressure drop in this porous layer is approximately 2×10^4 Pa/m based on empirical equation. Based on our numerical test, deviation from this value will be below 10% if one sets the boundaries to be non-slip (viscous term is very small since the flow is uniform at average scale). The viscous effect is even smaller if we only consider the pressure loss of a laminar flow through the same channel, which is roughly 0.1 Pa/m. Therefore, for many problems of interest, the role of the viscous term is not important. We also note that, this may not be true for fluid-particle flows at microscales, for instance, those found in microchannels, which requires a well-balanced state between the driving pressure gradient and viscous force.

Bibliography

[1] Z. Y. Zhou, S. B. Kuang, K. W. Chu, and A. B. Yu, "Discrete particle simulation of particle—fluid flow: model formulations and their applicability," *Journal of Fluid Mechanics*, vol. 661, pp. 482–510, 2010.

[2] C. T. Crowe, M. Sommerfeld, and Y. Tsuji, *Multiphase Flows with Droplets and Particles.* Taylor & Francis, 1997.

[3] T. R. Auton, J. C. R. Hunt, and M. Prud'Homme, "The force exerted on a body in inviscid unsteady non-uniform rotational flow," *Journal of Fluid Mechanics*, vol. 197, pp. 241–257, 1988.

[4] Y. Tsuji, T. Kawaguchi, and T. Tanaka, "Discrete particle simulation of two-dimensional fluidized bed," *Powder Technology*, vol. 77, pp. 79–87, 1993.

[5] K. Kafui, C. Thornton, and M. Adams, "Discrete particle-continuum fluid modelling of gas—solid fluidised beds," *Chemical Engineering Science*, vol. 57, pp. 2395–2410, 2002.

[6] Y. Yamada and M. Sakai, "Lagrangian—Lagrangian simulations of solid —liquid flows in a bead mill," *Powder Technology*, vol. 239, pp. 105–114, 2013.